

AD-A238 933



2

PL-TR-91- 2062

MODELING REGIONAL SEISMIC WAVES

Donald V. Helmberger  
David G. Harkrider

California Institute of Technology  
Seismological Laboratory  
Pasadena, CA 91125

25 March 1991

Scientific Report No. 1

DTIC  
SELECTED  
AUG 01 1991  
S B D

APPROVED FOR PUBLIC RELEASE; DISTRIBUTION UNLIMITED

91-06570



PHILLIPS LABORATORY  
AIR FORCE SYSTEMS COMMAND  
HANSCOM AIR FORCE BASE, MASSACHUSETTS 01731-5000

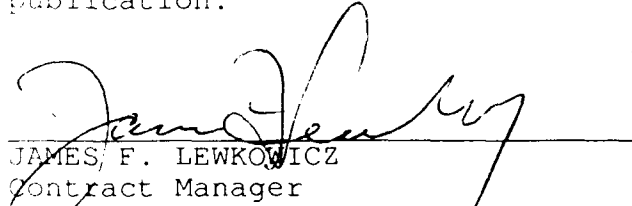
91 06570 002

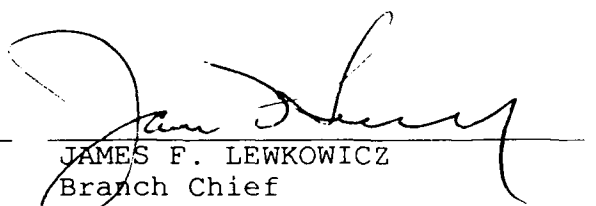
SPONSORED BY  
Defense Advanced Research Projects Agency  
Nuclear Monitoring Research Office  
ARPA ORDER NO. 5299

MONITORED BY  
Phillips Laboratory  
Contract F19628-89-K-0028

The views and conclusions contained in this document are those of the authors and should not be interpreted as representing the official policies, either expressed or implied, of the Defense Advanced Research Projects Agency or the U.S. Government.

This technical report has been reviewed and is approved for publication.

  
JAMES F. LEWKOWICZ  
Contract Manager  
Solid Earth Geophysics Branch  
Earth Sciences Division

  
JAMES F. LEWKOWICZ  
Branch Chief  
Solid Earth Geophysics Branch  
Earth Sciences Division

FOR THE COMMANDER

  
DONALD H. ECKHARDT, Director  
Earth Sciences Division

This report has been reviewed by the ESD Public Affairs Office (PA) and is releasable to the National Technical Information Service (NTIS).

Qualified requestors may obtain additional copies from the Defense Technical Information Center. All others should apply to the National Technical Information Service.

If your address has changed, or if you wish to be removed from the mailing list, or if the addressee is no longer employed by your organization, please notify PL/IMA, Hanscom AFB, MA 01731-5000. This will assist us in maintaining a current mailing list.

Do not return copies of this report unless contractual obligations or notices on a specific document requires that it be returned.

UNCLASSIFIED

SECURITY CLASSIFICATION OF THIS PAGE

## REPORT DOCUMENTATION PAGE

1a. REPORT SECURITY CLASSIFICATION UNCLASSIFIED			1b. RESTRICTIVE MARKINGS	
2a. SECURITY CLASSIFICATION AUTHORITY			3. DISTRIBUTION/AVAILABILITY OF REPORT Approved for public release: distribution unlimited	
2b. DECLASSIFICATION/DOWNGRADING SCHEDULE				
4. PERFORMING ORGANIZATION REPORT NUMBER(S)			5. MONITORING ORGANIZATION REPORT NUMBER(S) PL-TR-91-2062	
6a. NAME OF PERFORMING ORGANIZATION California Institute of Tech. Seismological Laboratory		6b. OFFICE SYMBOL (If applicable)	7a. NAME OF MONITORING ORGANIZATION Phillips Laboratory	
6c. ADDRESS (City, State and ZIP Code) Pasadena, California 91125			7b. ADDRESS (City, State and ZIP Code) Hanscom Air Force Base, Massachusetts 01731-5000	
8a. NAME OF FUNDING/SPONSORING ORGANIZATION Defense Advanced Research Projects Agency		8b. OFFICE SYMBOL (If applicable) NMRO	9. PROCUREMENT INSTRUMENT IDENTIFICATION NUMBER F19628-89-K0028	
8c. ADDRESS (City, State and ZIP Code) 1400 Wilson Boulevard Arlington, Virginia 22209-2308			10. SOURCE OF FUNDING NOS.	
			PROGRAM ELEMENT NO.	PROJECT NO.
			61101E	9A10
			TASK NO.	WORK UNIT NO.
			DA	AD
11. TITLE (Include Security Classification) Modeling Regional Seismic Waves				
12. PERSONAL AUTHOR(S) Donald V. Helmberger and David G. Harkrider				
13a. TYPE OF REPORT Scientific No. 1		13b. TIME COVERED FROM 3/24/89 TO 7/31/90		14. DATE OF REPORT (Yr., Mo., Day) 25 March 1991
				15. PAGE COUNT 184
16. SUPPLEMENTARY NOTATION				
17. COSATI CODES			18. SUBJECT TERMS	
FIELD	GROUP	SUB GR.	Tibetan Plateau, Southeastern China, upper mantle, shear velocity structure	
			broadband modeling, Generalized Ray Method (GRM), Mode Summation Method (MSM),	
			reflectivity, S-waves from off-center explosions	
19. ABSTRACT (Continue on reverse if necessary and identify by block number)				
<p>The research performed under the contract, during the period 24 May 1989 through 31 July 1990, can be divided into four main topics; modeling the shear-velocity structure of the crust and upper mantle beneath Tibetan Plateau and Southeastern China using Love waves and S and SS arrivals, broadband modeling along a regional shield path where the strengths of the surface waves can be compared with the crustal body phases, broad-band modeling of local earthquakes, and the wave fields from an off center explosion in a embedded sphere.</p>				
20. DISTRIBUTION/AVAILABILITY OF ABSTRACT UNCLASSIFIED/UNLIMITED <input checked="" type="checkbox"/> SAME AS RPT. <input type="checkbox"/> DTIC USERS <input type="checkbox"/>			21. ABSTRACT SECURITY CLASSIFICATION UNCLASSIFIED	
22a. NAME OF RESPONSIBLE INDIVIDUAL James Lewkowicz			22b. TELEPHONE NUMBER (Include Area Code) (617) 377-3028	22c. OFFICE SYMBOL PL/LWH

In section 1, we present a study which addresses the velocity structure of the crust and upper mantle in Southern China with special emphasis on the Tibet region. Velocity constraints on the crust are derived from modeling regional Love waves and  $P_{nl}$  waves in the time domain with observed waveforms. An average crustal thickness of 70 km is obtained beneath the Tibetan Plateau with a modest increase of velocity with depth. The lithospheric and upper-mantle structure is deduced from modeling S and SS triplication waveform data and relative travel times. S-SS seismograms chosen with bounce-points directly under Tibet allow remote sensing of this inaccessible region. We conclude that the upper-mantle structure in the entire region is basically shield-like below 200 km (SNA). However, the velocity of the lithosphere is abnormally slow, roughly 5% beneath Tibet. Modeling two station  $P_{nl}$  waveform data conforms the crustal and upper mantle model. The model for Tibet derived does not have a distinct lid, and has a positive velocity gradient in the crust, suggesting crustal shortening.

In section 2, broad-band modeling along a regional shield path was done for the Harvard recording of the Saguenay earthquake. The Saguenay earthquake, November 25, 1988, is one of the first large shield type events recorded by a broadband - high dynamic range instrument, the Streckeisen system, installed at Harvard station (HRV). The event is sufficiently large to be well recorded teleseismically and thus the source characteristics can be determined by independent means and considered known. This allows a detailed study of the propagational effects along this path, at an epicentral distance of 625 km, where the strengths of the surface waves can be compared with the crustal body phases. Broadband modeling using standard analytical techniques and flat layered models works amazingly well over the period range of 0.5 to 20 seconds. A detailed strategy for modeling broadband regional phases is given in terms of a decomposition of the vertical and radial seismograms into three segments:  $P_{nl}$  (containing  $P_n$ ,  $pP_n$ ,  $sP_n$ ,  $P_mP$ ,  $P$  coupled  $PL$  waves);  $S_{nl}$  (containing  $S_n$ ,  $sS_n$ ,  $S_mS$ , etc.); and the fundamental Rayleigh waves. Information about the upper crust is obtained from the fundamental Rayleigh waves while crustal thickness and velocity gradients in the mantle are obtained from  $P_{nl}$  and  $S_{nl}$ . This Particular crustal model has a thickness of 35 km with a sharp mocho and a substantial gradient in the top 20 km of the mantle, 0.01 km/sec per km for both P and S velocities. The mantle velocities,  $\alpha=8.2$  and  $\beta=4.55$  km/sec are slower than expected for a shield environment. Attenuation is not required for waveform modeling or for absolute amplitude estimation.

In section 3, three component broad-band waveforms of two small earthquakes near Upland, California recorded on the Pasadena broad-band high dynamic range instrument, were forward modeled to obtain useful Green's functions. The sensitivity of the synthetic seismograms to differing layered structure, boundary sharpness, and two-dimensional structures was also investigated. We assumed that the sources of these events were both simple and known, as determined from the Caltech-USGS array first-motions. A trapezoidal time function was chosen such that the width of the direct S-wave was well modeled. The waveforms were forward modeled using Generalized Rays, Reflectivity, and Finite-Difference techniques. In addition, estimates of moment, fault dimension, and stress drop were computed.

The results of the modeling exercise indicate that a simple layer over a half-space model is a adequate approximation of the upper crust along this profile. In particular, the waveforms are controlled by a relatively slow surficial layer. The sensitivity analyses indicate that the details of boundary sharpness, and deep crustal structure are not very important at frequencies less than 1 Hz, and at ranges less than 50 km. The thickness of the surface layer was constrained to be greater than 3 km and less than 5 km thick. The boundary sharpness sensitivity study indicated that the contact between the surficial material, and underlying material can be smoothed to 2 km without adversely affecting the synthetic waveform shapes. A number of two-dimensional finite-difference calculations were performed, and it was found that a ridge structure beneath the recorder, acted as a lowpass filter, and the lower frequency phases were largely unaffected. Other two-dimensional models with ridges between the source to receiver clearly did not fit the data however, the extended duration of these synthetic waveforms may be important in modeling more complicated waveforms observed in data from events south of this study. Synthetic seismograms computed for the best fitting model were used to estimate a long period moment of  $6 \times 10^{22}$  dyne-cm ( $M_L=4.6$ ) and  $1 \times 10^{22}$  dyne-cm ( $M_L=3.7$ ) with identical triangular source time durations of 0.3 seconds. Assuming the same fault dimension of 0.4 km from standard scaling, stress drop estimates of 410 and 70 bars are obtained. Generally, we found that it is possible to model local waveforms to frequencies of 1 Hz., without a complete understanding of fine structural detail. Resulting Green's functions can be useful in studying historic events, and in simulation of large events from a given source region.

In section 4, we present analytic and numerical wave fields from an off-center explosion in an embedded solid sphere. This study investigates the effects of explosions in asymmetric source regions on the excitation of seismic body waves. We give an analytic formulation for determining the wave fields from an off-center explosion in an embedded solid sphere in an elastic whole-space. As expected, this geometry generates shear as well as compressional body waves. The calculated wave fields show that the SV and SH wave generation is determined by the asymmetry of the source region. The results are compared with the known analytic solutions of an explosion in an elastic whole-space and at the center of an elastic sphere embedded in the whole-space. The radiation patterns at different periods for different parameters of the media suggest that the asymmetry of the source region has significant effects on shorter period, but has only minor effects on long periods. The long period P to S wave maximum amplitude results are in agreement with that for explosions in axisymmetric cavities.

**ANNUAL TECHNICAL REPORT**  
**24 May 1989 - 31 July 1990**

ARPA Order No.:

Name of Contractor: California Institute of Technology

Effective Date of Contract: 24 March 1989

Contract Expiration Date: 31 July 1991

Contract Number: F19628-89-K-0028

Principal Investigators: Donald V. Helmberger  
(818) 356-6998

David G Harkrider  
(818) 356-6910

Program Manager: James F. Lewkowicz  
(617) 861-3028

Short Title of Work: Modeling Regional Seismic Waves

The views and conclusions contained in this document are those of the authors and should not be interpreted as necessarily representing the official policies, either expressed or implied, of the Defense Advanced Research Projects Agency or the U. S. Government

Sponsored by  
Defense Advanced Research Projects Agency (DoD)  
Nuclear Monitoring Research Office  
ARPA Order No.  
Issued by the Air Force Geophysics Laboratory under  
Contract# F19628-89-K-0028

Seismological Laboratory  
Division of Geological and Planetary Sciences  
California Institute of Technology  
Pasadena, California 91125



Accession For	
NTIS GRA&I	<input checked="checked" type="checkbox"/>
DTIC TAB	<input type="checkbox"/>
Unannounced	<input type="checkbox"/>
Justification	
By	
Distribution/	
Availability Codes	
Dist	Avail and/or Special
A-1	

## TABLE OF CONTENTS

	Summary_____	V	.
1.	Shear-velocity structure of the crust and upper mantle beneath Tibetan Plateau and Southeastern China_____	1	.
2	Broadband modeling along a regional shield path, Harvard recording of the Saguenay Earthquake_____	51	
3.	Broad-band modeling of local earthquakes_____	97	
4.	Wave fields from an off-center explosion in an embedded solid sphere_____	125	

## Summary

The research performed under the contract, during the period 24 May 1989 through 31 July 1990, can be divided into four main topics; modeling the shear-velocity structure of the crust and upper mantle beneath Tibetan Plateau and Southeastern China using Love waves and S and SS arrivals, broadband modeling along a regional shield path where the strengths of the surface waves can be compared with the crustal body phases, broad-band modeling of local earthquakes, and the wave fields from an off-center explosion in a embedded sphere.

In section 1, we present a study which addresses the velocity structure of the crust and upper mantle in Southern China with special emphasis on the Tibet region. Velocity constraints on the crust are derived from modeling regional Love waves and  $P_{nl}$  waves in the time domain with observed waveforms. An average crustal thickness of 70 km is obtained beneath the Tibetan Plateau with a modest increase of velocity with depth. The lithospheric and upper-mantle structure is deduced from modeling S and SS triplication waveform data and relative travel times. S-SS seismograms chosen with bounce-points directly under Tibet allow remote sensing of this inaccessible region. We conclude that the upper-mantle structure in the entire region is basically shield-like below 200 km (SNA). However, the velocity of the lithosphere is abnormally slow, roughly 5% beneath Tibet. Modeling two station  $P_{nl}$  waveform data conforms the crustal and upper mantle model. The model for Tibet derived does not have a distinct lid, and has a positive velocity gradient in the crust, suggesting crustal shortening.

In section 2, broad-band modeling along a regional shield path was done for the Harvard recording of the Saguenay earthquake. The Saguenay earthquake, November 25, 1988, is one of the first large shield type events recorded by a broadband - high dynamic range instrument, the Streckeisen system, installed at Harvard station (HRV). The event is sufficiently large to be well recorded teleseismically and thus the source characteristics can be determined by independent means and considered known. This allows a detailed study of the propagational effects along this path, at an epicentral distance of 625 km, where the strengths of the surface waves can be compared with the crustal body phases. Broadband modeling using standard analytical techniques and flat layered models works amazingly well over the period range of 0.5 to 20 seconds. A detailed strategy for modeling broadband regional phases is given in terms of a decomposition of the vertical and radial seismograms into three segments:  $P_{nl}$  (containing  $P_n$ ,  $pP_n$ ,  $sP_n$ ,  $P_mP$ ,  $P$  coupled  $PL$  waves);  $S_{nl}$  (containing  $S_n$ ,  $sS_n$ ,  $S_mS$ , etc.); and the fundamental Rayleigh waves. Information about the upper crust is obtained from the fundamental Rayleigh waves while crustal thickness and velocity gradients in the mantle are obtained from  $P_{nl}$  and  $S_{nl}$ . This Particular crustal model has a thickness of 35 km with a sharp mocho and a substantial gradient in the top 20 km of the mantle, 0.01 km/sec per km for both P and S velocities. The mantle velocities,  $\alpha=8.2$  and  $\beta=4.55$  km/sec are slower than expected for a shield environment. Attenuation is not required for waveform modeling or for absolute amplitude estimation.

In section 3, three component broad-band waveforms of two small earthquakes near Upland, California recorded on the Pasadena broad-band high dynamic range instrument, were forward modeled to obtain useful Green's functions. The sensitivity of the synthetic seismograms to differing layered structure, boundary sharpness, and two-dimensional structures was also investigated. We assumed that the sources of these events were both simple and known, as determined from the Caltech-USGS array first-motions. A trapezoidal time function was chosen such that the width of the direct S-wave was well

modeled. The waveforms were forward modeled using Generalized Rays, Reflectivity, and Finite-Difference techniques. In addition, estimates of moment, fault dimension, and stress drop were computed.

The results of the modeling exercise indicate that a simple layer over a half-space model is a adequate approximation of the upper crust along this profile. In particular, the waveforms are controlled by a relatively slow surficial layer. The sensitivity analyses indicate that the details of boundary sharpness, and deep crustal structure are not very important at frequencies less than 1 Hz, and at ranges less than 50 km. The thickness of the surface layer was constrained to be greater than 3 km and less than 5 km thick. The boundary sharpness sensitivity study indicated that the contact between the surficial material, and underlying material can be smoothed to 2 km without adversely affecting the synthetic waveform shapes. A number of two-dimensional finite-difference calculations were performed, and it was found that a ridge structure beneath the recorder, acted as a lowpass filter, and the lower frequency phases were largely unaffected. Other two-dimensional models with ridges between the source to receiver clearly did not fit the data however, the extended duration of these synthetic waveforms may be important in modeling more complicated waveforms observed in data from events south of this study. Synthetic seismograms computed for the best fitting model were used to estimate a long period moment of  $6 \times 10^{22}$  dyne-cm ( $M_L=4.6$ ) and  $1 \times 10^{22}$  dyne-cm ( $M_L=3.7$ ) with identical triangular source time durations of 0.3 seconds. Assuming the same fault dimension of 0.4 km from standard scaling, stress drop estimates of 410 and 70 bars are obtained. Generally, we found that it is possible to model local waveforms to frequencies of 1 Hz., without a complete understanding of fine structural detail. Resulting Green's functions can be useful in studying historic events, and in simulation of large events from a given source region.

In section 4, we present analytic and numerical wave fields from an off-center explosion in an embedded solid sphere. This study investigates the effects of explosions in asymmetric source regions on the excitation of seismic body waves. We give an analytic formulation for determining the wave fields from an off-center explosion in an embedded solid sphere in an elastic whole-space. As expected, this geometry generates shear as well as compressional body waves. The calculated wave fields show that the *SV* and *SH* wave generation is determined by the asymmetry of the source region. The results are compared with the known analytic solutions of an explosion in an elastic whole-space and at the center of an elastic sphere embedded in the whole-space. The radiation patterns at different periods for different parameters of the media suggest that the asymmetry of the source region has significant effects on shorter period, but has only minor effects on long periods. The long period P to S wave maximum amplitude results are in agreement with that for explosions in axisymmetric cavities.



## **SECTION 1**

**Shear-Velocity Structure of the Crust and Upper Mantle  
Beneath Tibetan Plateau and Southeastern China**

# **Shear-Velocity Structure of the Crust and Upper Mantle Beneath Tibetan Plateau and Southeastern China**

*Lian-She Zhao, Donald V. Helmberger and David G. Harkrider*

Seismological Laboratory,  
California Institute of Technology,  
Pasadena, CA91125.

# Shear-Velocity Structure of the Crust and Upper Mantle Beneath Tibetan Plateau and Southeastern China

*Lian-She Zhao, Donald V. Helmberger and David G. Harkrider*

Seismological Laboratory,  
California Institute of Technology,  
Pasadena, CA91125.

## SUMMARY

This study addresses the velocity structure of the crust and upper mantle in Southern China with special emphasis on the Tibet region. Velocity constraints on the crust are derived from modeling regional Love waves and  $P_{nl}$  waves in the time domain with observed waveforms. An average crustal thickness of 70 km is obtained beneath the Tibetan Plateau with a modest increase of velocity with depth. The lithospheric and upper-mantle structure is deduced from modeling  $S$  and  $SS$  triplication waveform data and relative travel times.  $S$ - $SS$  seismograms chosen with bounce-points directly under Tibet allow remote sensing of this inaccessible region. We conclude that the upper-mantle structure in the entire region is basically shield-like below 200 km (SNA). However, the velocity of the lithosphere is abnormally slow, roughly 5% beneath Tibet. Modeling two station  $P_{nl}$  waveform data conforms the crustal and upper mantle model. The model for Tibet derived does not have a distinct lid, and has a positive velocity gradient in the crust, suggesting crustal shortening.

**Key words:** Tibetan Plateau, Southeastern China, upper mantle, shear velocity structure

## INTRODUCTION

China is a part of the Eurasian plate, but the margins of the Indian and

Philippine plates are involved in the Himalayas and in the coastal ranges of Taiwan, respectively. Relative to the north of China, the Indian plate is moving NNE, and the Philippine plate is moving NW (Minster et al, 1974). The arrows in Figure 1 show the directions of the motions of the plates surrounding China (Wang and Xu, 1985). China is composed mainly of four major tectonic provinces, the Tarim Basin, Sino-Korea Craton, Yangtze Craton and the Tibetan Plateau. The Tarim basin, Sino-Korea craton, and northern part of Yangtze craton are precambrian massives (Yang et al, 1986; Zhang et al, 1984). The provinces are characterized by large variations in crustal thickness as indicated in the isopach map presented in Figure 2. The thickness of the crust of the eastern part of China is about 35 km, that of northern China is 45 km, and that of the Tibetan Plateau is more than 50 km. Thus, we would expect the crustal and upper mantle velocity distributions beneath these four tectonic provinces to be much different.

The dynamic processes that lead to the formation and maintenance of a mean elevation of 5 km over the Tibetan Plateau are not well understood and are controversial. Because of its obvious importance for constraining these deep processes, the seismic velocity structure of the Tibetan Plateau has been the subject of many studies.

The three-year Sino-Franco joint research program (1980-1982) contributed significantly to both the geology and geophysics of the Tibetan Plateau. P-wave velocity profile of a 600 km line (from  $(28.5^{\circ}N, 89.0^{\circ}E)$  to  $(32.2^{\circ}N, 91.7^{\circ}E)$ ) was obtained from seismic soundings. The thickness of the crust changes from about 40 km to 75 km along this profile. The results of the program are published in a series of papers (see for example Hirn et al, 1984; Teng, 1987).

Some studies of the seismic velocity structure of the Tibetan Plateau used group and phase velocities of fundamental mode surface waves (e. g. Chen and Molnar, 1981; Romanowicz, 1982; 1984; Brandon and Romanowicz, 1986; Feng, 1982). Other studies used  $P_n$  and  $S_n$  waves (Barazangi and Ni, 1982; Ni and Barazangi, 1983, Holt and Wallace, 1989) to derive the velocity of the lid beneath the crust of the plateau. Recently, Lyon-Caen (1986) used the travel times and

waveforms of long period *SH* wave data recorded at distances of 10-30 degrees and some *SS-S* waveforms to constrain the upper mantle velocities down to a depth of 400 km beneath the plateau. She argues that the Indian plate is not underthrusting the whole of the Tibetan Plateau at the present time.

For the other parts of China, there are fewer studies reported in English. For the Yangtze Craton, there are surface wave studies ( Wier, 1982; Feng, 1982 ). Shedlock and Roecker ( 1987 ) used travel time inversion to study the elastic wave velocity structure of the crust and upper mantle beneath the Sino-Korea craton.

Wang and Yao ( 1989 ) gave one upper mantle shear velocity model for the Tibetan Plateau, and one upper mantle shear velocity model for North China ( Tarim basin and Sino-Korea craton ) by modeling the long-period *SS-S* waveforms recorded at distances of 30-60 degrees.

The purpose of this study is to constrain the upper mantle shear velocity structure of southern China by using the travel times and waveforms of Love waves recorded at distances of 7-23 degrees; long-period *S* waves recorded at distances of 15-30 degrees; and long-period *SS-S* waves recorded at distances of 30-60 degrees. Recent work using long-period body wave data have demonstrated that the travel times and waveforms of *SH* waves recorded at distances up to 30 degrees and of *SS-S* waves recorded between 30 and 60 degrees can provide some constraints on the large-scale velocity structure of the upper 670 km of the mantle and particularly of the upper 400 km ( Grand and Helmberger, 1984a; 1984b; Rial et. al, 1984 ). In this distance range the waveforms are controlled by the interference of phases whose turning points are in the regions above the 400 km discontinuity, between the 400 km and 670 km discontinuities, and below the 670 km discontinuity. The differential travel times of *SS* waves and *S* waves are controlled mainly by the velocity structure of the neighborhood of the bounce points of the *SS* phases. This property makes it possible to constrain the shear velocity structure of an area not big enough for the pure path data. The search of models can be achieved by comparing the synthetics with the data. The *WKBJ* method ( Chapman, 1978 ), which is discussed at length by Grand and Helmberger ( 1984a

), was used for constructing synthetic  $S$  and  $SS$  waves, and the mode summation method ( Harkrider, 1964; 1970 ) was used in studying Love waves.

## DATA AND METHODS

In this study, we used travel times and waveforms of long-period  $SH$  wave data from 44 earthquakes, magnitude 4.5 or larger, from 1965 to 1985, within or around China ( Table 1 ), as recorded at the  $WWSSN$  stations around China ( ANP, BAG, HKC, KBL, LAH, MAT, MSH, NDI, NIL, QUE, SEO, SHL, SHK ) and along with some Chinese stations ( GYA, GZH, LZH, XAN ). In Table 1, the source information is from Bulletin of the International Seismological Centre ( ISC ), otherwise indicated. The seismograms have high signal to noise ratios, and are not necessarily from earthquakes with known source mechanisms. There are only a limited number of Tibetan earthquakes carefully studied (e.g. Ni and Barazangi, 1984; Molnar and Chen, 1983; Tapponnier and Molnar, 1977; Baranowski et. al 1984). Because of lack of local station net, it is almost impossible to know the source mechanisms of the smaller Tibetan earthquakes, which generated on-scale surface waves. However, we can infer roughly the source mechanism from the  $S$ -waveforms ( Langston and Helmberger, 1975 ). This rough source mechanism is sufficient for  $S$ -,  $SS$ -wave study as demonstrated by Grand and Helmberger ( 1985 ). The source depth effects on  $S$ - and  $SS$ -waveforms are corrected for by using teleseismic  $S$ -waveforms as the source time history since the ray parameter changes very slowly with distance for distances greater than 15.0 degrees. The orientation of the fault effects the amplitude ratio of  $SS$ - to  $S$ -waves, which was not used. These various approximations have been used in previous  $SS$ - $S$  studies, see for example Rial et. al ( 1984 ).

TABLE 1
---------

The crustal velocity structure has not been well determined in the Tibetan

Plateau. To constrain this portion of the model we used relatively high-frequency Love waves. But instead of applying the conventional dispersion analysis, we chose to match the Love-wave synthetics to the observations directly. The appropriateness of the model is then judged on the overall fit of the synthetics to the observed waveform in absolute travel time.

Since Love wave data are not normally used in this fashion, we start with a brief sensitivity study to test the resolving power of this approach by discussing some numerical experiments. Figures 3 and 4 summarize the results of these numerical experiments. Figure 3 shows the sensitivity of synthetics to changes in the models, source depths, and source mechanisms. Figure 4 displays the synthetics appropriate for different Moho discontinuities.

In Figure 3, the left column are the models used to generate the synthetics of fundamental Love waveforms at various depths and mechanisms. These synthetics were generated at a distance of 1000 km, assuming a the source time history of a (1, 1, 1) trapezoid. All synthetics begin at 260 seconds. The crustal thickness is 60 km for all models. The average velocities of the crust are same, 3.6 km/sec. The mantle velocities are same, 4.6 km/sec, except models g which is 4.4 km/sec and h which is 4.8 km/sec. The attenuation,  $Q_\beta$ , used is 300 for the crust, and 1000 for the mantle. Comparing the synthetics for these various sensitivities we conclude that: the mantle velocity has very little effect on both travel time and waveforms, see the synthetics of models g and h; the lowest velocity of the crust seems to dominate the travel time of Love waves, see models b, c, f and g; the velocity gradient does not have much effect on waveforms; the source depth has a profound effect on the waveforms for complicated crustal models, and less effect for simpler models; source mechanism effects travel time only weakly compared to shallow velocity structure.

Figure 4 displays some properties of regional Love waves when crossing a plateau boundary similar to the expected geometry of the Tibetan Plateau. The column on the left displays the source-receiver geometry in a simple idealized crust where all the models have the velocities given at the bottom. The distance is set

at 1000 km, and strike-slip source is assumed at a depth of 9.8 km. These synthetics were generated with generalized ray theory and finite-difference method, see Helmberger and Vidale ( 1989 ). The Love-waveforms are quite similar which lead us to conclude that the crustal thickness and dipping Moho do not have much effects for these geometries. Thus, regional Love waveforms can be used as a constraint on the velocity structure of the upper crustal layers for paths crossing the plateau with the above restrictions on geometry.

## RESULTS

The upper mantle shear velocity structures we derived are given in Table 2 and Figure 5. TIP is the model for the Tibetan Plateau, and ECH that for the eastern part of China, part of Yangtze and Sino-Korean Cratons.

### Tibetan Plateau

It is convenient to break this discussion into two sections, namely crustal and upper-mantle, where the former is constrained by regional long-period Love waves and the latter by *S*- and *SS*-waveform data.

TABLE 2
---------

### Crust

Our preferred velocity model is given in Table 2 with a 3.75 km surface layer of 2.55 km/sec ( same as that of Chen and Molnar ( 1981 ) ), follow by a 16.25 km of 3.5 km/sec, 20 km of 3.7 km/sec, and 30 km of 3.8 km/sec.

The source-station paths used in this Love wave investigation are given in Figure 6, along with two  $P_{\text{m}}$  paths discussed later. It is difficult to measure the initial arrival time of Love waves, so the first large pulse was used to denote relative timing and the synthetic has been aligned accordingly. Figure 6 indicates the number of seconds the synthetic is faster than the observed for that particular ray



path. The comparison of the data and synthetics is given in Figures 7, and 8.

In Figure 7, we display the data, whose sources are known ( Holt and Wallace, 1989 ), along with the synthetics of proposed models, where TIP indicates the synthetics appropriate for the model developed in this study, CHEN associated with model S7 of Chen and Molnar ( 1981 ), and CHUN computed from the model derived by Chun and McEvilly ( 1985 ). The data and synthetics are displayed in absolute travel time. From this figure, the waveform matches of TIP are better than the others, and the travel times at stations NDI and SHL are better. However, for the paths of event 24 to NIL, and event 13 to LAH, the travel times of TIP are 13 seconds faster than the data and are not as good as CHEN. CHUN is slow. In Figure 8, the time shift was applied for each comparison. In this figure, the depth used to generate the synthetic is given. The depths may be different from the corresponding ones given in Table 1. Because the source depth is poorly known, we just compared the data of unknown source depth with the data of known source depth to estimate the source depth. The basic assumption is that, the source depth should be roughly the same if the two data are roughly alike. A strike-slip source with a time history ( 2, 2, 2 ) trapezoid was used to generate all synthetics. From these two figures, the travel times and the waveforms fit the data reasonably well, although TIP is faster, or slower for certain paths. We consider this model to be an average velocity distribution of the crust of the Tibetan Plateau which is considerably faster than previous proposed models.

### Upper-mantle

The upper-mantle shear velocity distribution of the Tibetan Plateau beneath the crust is constrained by 11 *S*-waveforms with distances from  $15.5^{\circ}$  to  $27.2^{\circ}$ , and 16 *SS-S* waveforms with distances from  $35.3^{\circ}$  to  $59.7^{\circ}$ . Some of the *S*-wave data are from Lyon-Caen's paper ( 1986 ), and some of the *SS-S* wave data are from Wang and Yao's paper ( 1989 ). The travel times of the *S*-waves are not used, for they are rather scattered, and a large portion of their paths lie outside the Tibetan Plateau. Note that the *SS-S* waveform data is controlled by triplica-

tion positions or differential times where rays share common paths near the source and receiver and thus much less susceptible to travel time offsets caused by lateral variation ( Grand and Helmberger 1984a ). The ray paths of the *S*-wave data and the bounce points of the *SS*-wave data are given in Figure 9a. The triangles represent the stations; stars the events generating the *S*-waves; circles the bounce points of the *SS*-waves for distances greater than 45 degrees; and squares the bounce points of the *SS*-waves for distances less than 45 degrees. In order to avoid the strong lateral heterogeneity, we did not use the *SS*-wave data with bounce points near the boundary of the Tibetan Plateau.

The starting model for the upper mantle shear velocity structure of the Tibetan Plateau is TNA ( Tectonic North America, Grand and Helmberger, 1984a ), with the crustal model derived above. After comparisons of synthetics and the data for several dozens of models, following a trial-and-error procedure, we obtained model TIP, see Figure 5 and Table 2. This model has a 60 km thick lid of 4.6 km/sec, and 40 km of 4.55 km/sec below. It does not have a distinct low velocity zone, and is shield-like below.

Figure 10 shows the comparison of the observed waveforms with synthetics. Because most of the *S*-wave data do not correspond to pure paths and sample an area with large heterogeneities, it is difficult to say which part of the data gives the most definitive information about the Tibetan Plateau. However, by comparing the paths indicated in Figure 9a we see that the shallowest structure is sampled best by the western station, NIL. Almost all of the data and synthetics have three arrivals that are due to three sets of rays, one bottoming above the 405 km discontinuity ( branch AB ), one bottoming below the 405 km discontinuity and above the 670 km discontinuity ( branches BC and CD ), and another bottoming below the 670 km discontinuity ( branches DE and EF). We will generally refer to branches by single letters, which will denote the two arrivals forming the cusp designated by the letter ( Figure 11 ). With long-period data the two geometric arrivals forming a branch usually cannot be distinguished. When there is possible confusion in the branch name, we will indicate a full designation. A

good fit of the waveforms and, therefore, differential travel times of branches A, B, C, D, E and F to the data at distances of  $17.2^\circ$ ,  $20.1^\circ$ ,  $24.0^\circ$ ,  $24.6^\circ$ ,  $25.3^\circ$ , and  $26.7^\circ$  is achieved. Note that the A branch is missing from the LZH data ( $18.4^\circ$ ) indicating a shallow heterogeneity along the path (Grand and Helmberger, 1985). The differential travel time between the branches A and C of the data recorded at NIL at a distance of  $15.5^\circ$  is 3.5 seconds faster than that of the synthetics, and that of the data also recorded at NIL at a distance of  $16.4^\circ$  is 2 seconds faster than that of synthetics. Perhaps these differences were caused by the local faster structure and thinner crust thickness near the station NIL. The amplitude of the E branch for QUE data at a distance of  $21.0^\circ$  could be due to the missing A branch.

The travel times and waveforms of *S*-waves alone do not yield definitive constraints on the velocity distribution of the Tibetan Plateau, because a large part of the ray paths are outside the region. Figure 12 shows the *SS-S* wave data with synthetics of the model TIP. The fits of the waveforms and differential travel times between the first and the second arrivals (F and D branch), and the *S*-wave of the data recorded at SEO at a distance of  $54.5^\circ$  with the synthetics indicate that the shear velocity distribution beneath the 405 km discontinuity is the same as that beneath the Canadian Shield (Grand and Helmberger, 1984). The source functions used for the synthetics of *SS* waveforms are the teleseismic *S* waveforms. The advantage of using the teleseismic *S*-waveform as a source function is that the importance of the source mechanisms and source depth is almost completely eliminated. The waveforms of *S*-waves are the sum of direct *S* and *aS*-waves. The travel time difference between these two phases is controlled by the source depth and the ray parameter, or take-off angle. The amplitude ratio is determined by the source mechanism (Langston and Helmberger, 1975). The different *S*-waveforms at different distances are due to the ray parameters. The ray parameter changes very slowly with distance beyond 15 degrees, becoming nearly a constant for distances beyond 25 degrees. Thus the effects of source depth and source mechanism are almost the same on triplication *S*-waves as on teleseismic *S*-waves.

The differential travel time of the C branch and *S*-wave of the data recorded at MSH at a distance of  $35.3^\circ$  is about 5 seconds faster than that of the synthetics, and the branch A is absent. The bounce point for it is the far west point indicated in Figure 9a. The ray of the C branch in this case travels almost entirely in the upper 405 km with only a very small part of it going below the 405 km discontinuity. A large part of the time difference is due to the more than 10 degrees of horizontal travel distance in a shield-like region ( Rial et. al, 1984 ) outside of the Tibetan Plateau. Also, the lateral heterogeneity could cause some difference in the differential travel time of *SS*- and *S*-waves. The differential travel times and waveforms of *SS*- and *S*-waves of the HKC (  $35.7^\circ$  ) data, see Figure 12, are matched very nicely for the branches C and E, although the A branch is not clear. The beginning waveform of the HKC station at a distance of  $52.0^\circ$  is most likely *S*. If it is a combination of *S* and *sS*, the source depth should be about 80 km, and the amplitude of the second one would not likely be so big. If we use all of the beginning waveform as the *S*-wave, or source function, the synthetics for the *SS*-wave are very good, but we could not label the branches. The waveforms of the *SS*-waves of HKC at a distance of  $51.0^\circ$  do not agree well with that of the synthetics, but the match of the differential travel time is not bad. The arrival between the *S*- and *SS*-waves on the data HKC  $51.0^\circ$ , GZH  $51.8^\circ$ , HKC  $52.0^\circ$ , SEO  $54.5^\circ$ , and HKC  $59.7^\circ$  is the phase *ScS*.

The synthetic fits to this dataset proved particularly difficult. The reason is in the inherent complexity of the structure itself in terms of heterogeneity. Nevertheless, it appears that the derived model for the structure beneath the Tibetan Plateau fits the *S*-*SS* waveform data better than existing models, as will be discussed in more detail later.

#### Eastern China

The data coverage of the eastern portion of China is presently lacking but will become more complete when the new digital array becomes operational. The ray paths of the data used for the study of Eastern China are displayed in Figure

13. It is clear from the figure that the region sampled includes the Yangtze Craton and the southern half of the Sino-Korea Craton. Although the region is relatively complex, we will assume a uniform upper-mantle structure as a first order approximation of the area. The data set we used to constrain the upper mantle shear velocity distribution includes 5 *S*-wave data, distances from  $19.0^\circ$  to  $24.5^\circ$ , and 10 *SS*-wave data, distances from  $33.2^\circ$  to  $39.7^\circ$ . The model, ECH, we obtained, is given in Table 2 and Figure 5. The comparisons of the synthetics with the data are given in Figure 14 and Figure 15.

In Figure 14, we display synthetic and *S*-wave observation comparisons along with the theoretical responses and source function estimates. The branches are identified on the theoretical responses similar to Figure 10 discussed earlier. Although all the branches cross each other in this distance range, we can see pulses of branches on both the data and the synthetics. The travel time of the synthetics is 3 seconds faster than that observed at HKC ( $19.0^\circ$ ), 3 seconds slower than that of ANP ( $20.8^\circ$ ), 4 seconds slower than that of SHL ( $22.9^\circ$ ), 7 seconds slower than that of SEO ( $23.2^\circ$ ), and 9 seconds slower than that of ANP ( $24.5^\circ$ ) (Figure 13). The fit of the travel times is certainly reasonable for such a big laterally heterogeneous area. The synthetics are produced by convolving the theoretical responses (Earth responses) with the effective source functions which contain  $sS$ . The source function of ANP ( $20.8^\circ$ ) is the *S*-waveform observed at MAT ( $36.0^\circ$ , Figure 15). The other source functions are theoretical predictions assuming a strike-slip at SHL and SEO, and a dip-slip at ANP and HKC. The bottom two observations at SEO and ANP, showing the interference of F and D branches, are very similar to those displayed in Figure 17 of Grand and Helmburger (1984a).

Figure 15 gives the comparisons of the synthetics of *SS*-waveforms and the data. The *SS*-waveform recorded at a distance less than  $45^\circ$  gives not only information about the bounce point, but also information about a large part of the upper mantle structure along the ray path. All of the *SS*-wave data we have used are less than  $40^\circ$ , so this may cause some difficulties for the large lateral hetero-

geneity. Also it is difficult to locate the E, F branches of the model. The complexity of the waveforms of SHK (  $35.0^\circ$  ) is due to the depth of the source, 134 km. We have not matched  $sS$ - and  $sSS$ -waves, so the synthetic is incomplete. Note that 7 of the 10 seismograms used are recorded at MAT, and one third of their ray paths lie out of continental China ( Figure 13 ). Actually, for some of the  $SS$ -wave data, only one third of their paths and bounce points are in the eastern part of China, Yangtze Craton, and the south half of the Sino-Korea Craton. It can be inferred from the data and the synthetics ( Figure 14, and Figure 15 ) and the travel time residuals ( Figure 13 ) that the velocity of the Sino-Korea Craton is faster than that of the Yangtze Craton, and that the northern part of Yangtze Craton is faster than the southern part. The model we derived here is, obviously, only a very approximate model for the upper mantle shear velocity distribution for the eastern part of China. Nevertheless, these preliminary results suggests that the mantle beneath eastern China is predominantly shield at depths greater than a few hundred kilometers. The large travel time off-sets suggest strong shallow lateral variation. More data will be required to resolve the connection with the surface geology and interplate interaction.

## DISCUSSION AND CONCLUSION

In this section we will briefly compare synthetics associated with existing models ( Figure 16 ) proposed for the Tibetan Plateau with some of the key  $SS$ - $S$  observations. The  $SS$ - $S$  data is the least contaminated by lateral variation as discussed earlier and thus the most definitive. This will be followed by an indepth discussion of the upper 200 kms of the models since this is the region where models differ the most and are the most significant in terms of tectonic implications. The waveforms of  $SS$ - $S$  waves are the results of the interference of the five branches AB, BC, CD, DE and EF ( Figure 11). Since the travel time branches are nearly straight lines, we can get a shear velocity model for a homogeneous structure if we have two ideal waveforms of  $SS$ - $S$  waves at a distance near 30 and 60 degrees. We present three key data taken from Figure 12, located at roughly  $10^\circ$

intervals, namely, HKC at  $35.7^\circ$ , ANP at  $44.8^\circ$ , and SEO at  $54.5^\circ$  in Figure 17. The waveforms of SEO at  $54.5^\circ$  are particularly meaningful, because waveforms of the different branches have separated. At ANP the branches are all together. In order to see clearly the differences between the data and synthetics, we have inserted the vertical lines. The bottom four traces of each group are synthetics for proposed models for this region.

Comparing the various models presented in Figure 16 we note that TIP has a faster crust and a slower lid than the other models. Thus, the  $S_n$  and  $P_n$  arrival time prediction for TIP are distinctly slower than others. Comparing with the data at HKC (  $35.7^\circ$  ), the branches C and E of the TIP synthetics are about two seconds faster than the data, this means that either the shear velocity of the upper part, especially the crust, is faster than the observed or the crustal thickness at the bounce point is greater than the model TIP, as discussed earlier. The C branch, and the E branch of the synthetics of Lyon-Caen's models ( Ltib ) are 7.5, and 4.5 seconds slower than that of the HKC data. The synthetics for Wang's model are also slower than the HKC data by a few seconds. The branches arrive at almost same time for the ANP (  $44.8^\circ$  ) data. The synthetics of Wang and Ltib are slower. The F, D and B branches of Ltib are 3.5, 5 and 16 seconds slower than those of SEO data respectively. The B branch of Wang is 11 seconds slower than that of SEO data. Lyon-Caen's Indian model presents a comparison of Indian Shield with the Tibetan Plateau. The slow B branch of Ltib and Wang suggest that the velocities of the upper 200 km of the models are too slow.

To check our results further requires some absolute travel time constraints or better knowledge about the earthquake sources used in terms of location and mechanism. For instance, we used the ISC location and origin time for event 22 in timing NDI, see Figure 6, and found a residual of +10 seconds. This means that the model TIP is 1.5 % faster than the average velocity along this path, but if we used the USGS location and origin time for this event, the travel time residual would be +2 seconds, which means this model is very good. We have no particular reason to say the ISC location and origin time are better. We choose to use them

simply for book-keeping. Since these locations given by the agencies do not use depth phases in their analysis we decided to do an indepth study of one of these events to assess uncertainties and establish a few absolute travel time constraints. Event 36 was selected for this purpose since it also has a few  $P_w$  waves on scale. the origin time and location used are 3:2:47.2, 30.506° N, 88.583° E, and an epicentral depth of 33 km assigned by NEIS. This event is big enough to be recorded worldwide,  $m_b=5.7, M_s=6.2$ .

First, we derive the source depth by modeling the teleseismic P waveforms. The results are given in Figure 18 where the best fitting source depth is 10 km. We estimate the errors in depth to be less than 3 km, and fault plane less than 5°. Figure 18 displays the best overall fit of different runs, indicating a strike of 160°, a dip of 60°, and a rake of 250°. Stations POO and CHG are within upper mantle distances and the P waveforms recorded by them are complicated by triplications, and matched well by the synthetics. The model used in these calculation was derived by comparing TIP with a P-wave model for the Canadian Shield, namely S25 ( LeFevre and Helmberger, 1989 ) and SNA ( Grand and Helmberger, 1984a ), and using the relationship with shear velocities of rocks of basaltic composition ( Ludwig et al, 1970 ) ( Table 3 ). Some bad-looking seismograms are due to digitizing since the line-thickness of the recordings is 3-5 seconds thick, and the maximum amplitudes of some recordings do not exceed half of the line-thickness, such as MUN.

TABLE 3
---------

The results of the relocation, based on the new source depth, are given in Table 4. In this table, STAT are station names; TPK are the times we picked from vertical component of short-period WWSSN data after minute mark in second; TPKP are the times picked by station operator; TOBS1 and TOBS2 are the observed P wave travel times after the old and new origin time; TCOM1 and TCOM2 are the computed P wave travel times for the old epicenter and origin



time, and for the new epicenter and origin time. DT1 and DT2 are the residual travel times after Dziewonski and Anderson ( 1983 ) station correction, minus sign means TCOM is faster than TOBS. The standard deviation is 1.5 seconds. This error mainly comes from the contributions of the three stations UME, HLW and STU, whose deviations are greater than 4 seconds. After relocation: the location becomes  $30.658^{\circ}$  N,  $88.649^{\circ}$  E, and the origin time becomes 03:02:43.7. The new location is 18 km from the location given by NEIS. The origin time is 3.5 seconds earlier than that given by NEIS, 1.3 seconds earlier than that given by ISC. We used the modified P-wave TIP model as discussed before for the source region and JB for the receivers to calculate the TCOM. For a distance greater than  $30^{\circ}$ , the half way travel time difference between the model TIP and the model JB is only 0.5 seconds. If we used JB model for the source region, the new location would be  $30.625^{\circ}$  N ,  $88.632^{\circ}$  E, only 4 km from the location given by different source velocity models, the origin time would be 03:02:43.7, only 0.04 seconds difference. This is because the upper 400 km of JB model is slow, or the average velocity of upper 400 km of JB is about same as that of the model TIP.

TABLE 4
---------

As a check on the accuracy of our crustal model, we make synthetics of  $P_n$  waveforms and compare with the data recorded at the stations NDI and NIL due to the Tibetan earthquake we relocated above. Figure 19 displays the  $P_n$  data along with the synthetics of the model TIP. The method used to make these synthetics is reflectivity. The synthetics of NDI is shifted left 1.5 seconds, that of NIL is shifted left 0.5 seconds. We present only three seismograms here since the amplitudes of the north components of both stations are very small and the vertical component of NIL station was not available. We can see from Figure 19 that the fits are good. This means that the average velocity structure and the crustal thickness of the Tibetan Plateau can be approximated by the model TIP for the paths ( Figure 6 ), although these paths only sample the southern part of the Pla-

teau. The time shifts given above are largely caused by the dipping Moho. Thinning the crust at the receiver by 20 km reduces the  $P_n$  travel time by 2.2 seconds, see Figure 6. Thus, considering the possible crustal thickness beneath the stations, and assuming that the crustal thickness beneath NDI and NIL is 50 km, we conclude that the model TIP is about 0.7 seconds faster for the path to NDI, 1.7 seconds faster for that to NIL. This implies that the P wave velocity of the mantle for these paths is 8.23 km/sec instead of the 8.29 km/sec that we used in the above flat layered  $P_n$  calculation.

Barazangi and Ni ( 1982 ), and Ni and Barazangi ( 1983 ) used  $P_n$ - and  $S_n$ -waves crossing the Tibetan Plateau, and obtained velocities of 8.42 km/sec for  $P_n$ , and 4.73 km/sec for  $S_n$ . They concluded that these velocities were very similar to those beneath the Himalaya Mountains and the Indian shield, and suggested that the Indian continental lithosphere underthrusts the Tibetan Plateau at a shallow angle. However, our earlier experiments suggest a high velocity bias for most recording geometries if one simply assumes a flat-layered model. For instance, in Figure 4, the  $S_n$  arrives about 3.5 seconds earlier in the model d than a flat structure with a crustal thickness 70 km, model f. A mantle velocity would be 4.69 km/sec, instead of 4.6 km/sec used in Figure 4. Thus, an average  $S_n$  velocity of 0.1 km/sec greater than the average velocity beneath the Tibetan Plateau is very likely obtained if the only  $S_n$  data are used. Seismograms for two-dimensional models crossing this interesting region will be discussed in a later paper.

Our results ( TIP ) are consistent with that of the attenuation study of pure path long-period Rayleigh waves across the Tibetan Plateau by Romanowicz ( 1984 ). The conclusion of "no lid" for the Tibetan Plateau is consistent with that for the central Chang-Thang of Tibet from pure path phase velocity measurement of long period Rayleigh waves by Brandon and Romanowicz ( 1986 ). These results are similar to those obtained from modeling multi-bounce S-waves by Grand and Helmberger ( 1985 ), who constructed a 2D cross-section from Tibet to Europe. Resolution from their study begins at the edge of Tibet and indicates

that the structure beneath the Tarim basin is similar to our results for Tibet, namely, a shield-like model with a slow upper 200 km. We do not presently have a detailed shear velocity models available for the eastern part of China, except that it appears similar to other shields. Thus, from this study, and the studies by Grand and Helmberger ( 1985 ), and Rial, Grand and Helmberger ( 1984 ) we suggest that the upper mantle of the Eurasian plate is shield-like below 200 km.

Although these results are preliminary in nature it would appear that the deformations of the European plate is confined mainly to the upper 200 km. This type of velocity distribution thus becomes an important piece of evidence to be used in deducing the tectonics of the area.

It is generally assumed that major underthrusting is occurring along the Himalayan arc as deduced from source mechanism studies, see Ni and Barazangi ( 1984 ) and others. The dynamic processes that lead to the formation and maintenance of a mean elevation of 5 kms over some 2 million square kms behind the Himalayan arc appears more controversial. Essentially two hypothesis have been put forward, namely underthrusting and crustal shortening. Underthrusting in the Pacific Northwest results in complex crustal structures with a large low velocity zone associated with the subducted upper crustal section, see Langston ( 1977 ). We did not find much evidence for such structures in this study. Crustal shortening has been suggested by Molnar and his associates. They argue that the temperature at the base of the crust is 250 to 300° higher than beneath platforms, see Chen and Molnar ( 1981 ). Increased radiogenic material per horizontal area is thought to contribute to this heating. If we compare the mantle shear velocity at the top of our model with those of pure shield models we obtain a reduction of 0.1 - 0.2 km/sec, essentially 4.7 - 4.8 to 4.6 km/sec. The temperature difference for this velocity difference is 300-600°, assuming that the upper mantle is composed of olivine ( 40 % ), clinopyroxene and garnet as suggested by Duffy and Anderson ( 1989 ). We have  $(d\beta/dT)_p = -3.3 \times 10^{-4} \text{ km}/(\text{sec} \cdot ^\circ\text{C})$  for upper mantle materials at 1000°K ( Duffy, personal communication; Suzuki et. al, 1983 ). This temperature estimation are somewhat higher than the above estimates, see Molnar ( 1989 ),

reflecting the contrast in velocity models, see Figure 16, where the Lyon-Caen's model has a higher lid velocity than TIP. Our results suggests that the crustal structure is playing a particularly important role in controlling the tectonics of the Tibetan Plateau and in surrounding regions. Thus the higher resolution of this complex structure is essential and will be addressed in future efforts as the new digital observations from the Soviet Union and China become available.

### ACKNOWLEDGEMENTS

Dr. Don L. Anderson reviewed the manuscript. This research was supported, by the National Science Foundation grant EAR-89-04767, and by the Advanced Research Projects Agency of the Department of Defense and was monitored by the Air Force Geophysics Laboratory under the contract F19628-89-K-0028. Contribution number 4733 from the Division of Geological and Planetary Sciences, California Institute of Technology, Pasadena, California, 91125.

## REFERENCES

- Baranowski, H., H. Armbruster, Seeber, L. and P. Molnar, 1984. Focal depths and fault plane solutions of earthquakes and active tectonics of the Himalaya, *J. Geophys. Res.*, **89**, 6919-6928.
- Barazangi, M., and J. Ni, 1982. Velocities and propagation characteristics of *Pn* and *Sn* beneath the Himalayan arc and Tibetan plateau: possible evidence for underthrusting of Indian continental lithosphere beneath Tibet, *Geology*, **10**, 179-185.
- Brandon C. and B. Romanowicz, 1986. A "no - lid" zone in the central Chang - Thang platform of Tibet: Evidence from pure path phase velocity measurements of long period Rayleigh waves, *J. Geophys. Res.*, **B6**, 6547-6564.
- Chapman, C. H., 1978. A new method for computing synthetic seismograms, *Geophys. J. R. astr. Soc.*, **57**, 649-670.
- Chen, Wang-Ping, and P. Molnar, 1981. Constraints on the seismic wave velocity structure beneath the Tibetan Plateau and their tectonic implications, *J. Geophys. Res.*, **86**, 5937-5962.
- Chun Kin-yip and T. V. McEvilly, 1985. New seismological evidences of Tibetan lithosphere structure, *Acta Geophysica Sinica*, **28**, Supp. I., 135-147 ( in Chinese, English Abstract ).
- Duffy, T. S., and D. L. Anderson, 1989. Seismic velocities in mantle minerals and the mineralogy of the upper mantle, *J. Geophys. Res.*, **94**, 1895-1912.
- Dziewonski, A. M., and D. L. Anderson, 1983. Travel times and station corrections for P waves at teleseismic distances, *J. Geophys. Res.*, **88**, 3295-3314.
- Feng, C., 1982. A surface wave study of crustal and upper mantle structures of Eurasia, *Ph.D thesis*, University of Southern California.
- Grand, S. P., and D. V. Helmberger, 1984a. Upper mantle shear structure of North America, *Geophys. J. R. astr. Soc.*, **76**, 399-438.
- Grand, S. P., and D. V. Helmberger, 1984b. Upper mantle shear structure beneath the northwest Atlantic Ocean, *J. Geophys. Res.*, **89**, 11465-11475.
- Grand, S. P., and D. V. Helmberger, 1985. Upper mantle shear structure beneath Asia from multi-bounce *S* waves, *Phys. Earth Planet. Inter.*, **41**, 154-169.
- Harkrider, D. G., 1964. Surface waves in multilayered elastic media, I. Rayleigh and Love waves from buried sources in a multilayered elastic half-space, *Bull. Seism. Soc. Am.*, **54**, 627-679.
- Harkrider, D. G., 1970. Surface waves in multilayered elastic media, II. Higher mode spectra and spectral ratios from point sources in plane layered Earth models, *Bull. Seism. Soc. Am.*, **54**, 1937-1987.

- Helmberger, D. V. and J. E. Vidale, 1988. Modeling strong motions produced by earthquakes with two-dimensional numerical codes, *Bull. Seism. Soc. Am.*, **78**, 109-121.
- Hirn, A., J.-C. Lepine, G. Jobert, M. Sapin, G. Wittlinger, Z. X. Xu, E. Y. Gao, X. J. Wang, J. W. Teng, S. B. Xiong, M. R. Pandey, and J. M. Tater, 1984. Crustal structure and variability of the Himalayan border of Tibet, *Nature*, **307**, 23-25.
- Holt, W. E. and T. C. Wallace, 1989. Crustal Thickness and upper mantle velocities in the Tibetan Plateau region from the inversion of regional  $P_n$  waveforms: Evidence for a thick upper mantle lid beneath southern Tibet, submitted to *J. Geophys. Res.*
- Langston, C. A., 1977. Corvallis, Oregon, crustal and upper mantle receiver structure from teleseismic P and S waves, *Bull. Seis. Soc. Am.*, **67**, 713-724.
- Langston, C. A., and D. V. Helmberger, 1975. A procedure for modeling shallow dislocation sources, *Geophys. J. R. astr. Soc.*, **42**, 117-130.
- LeFevre, L. V. and D. V. Helmberger, 1989. Upper mantle P velocity of the Canadian Shield, *J. Geophys. Res.*, **B12**, 17749-17765.
- Ludwig, W. J., J. E. Nafe, and C. L. Drake, 1970, Seismic refraction, in *The Sea*, edited by A. E. Maxwell, Vol. 4, Part I, 53-84, Wiley-Interscience.
- Lyon-Caen, H., 1986. Comparison of the upper mantle shear wave velocity structure of the Indian Shield and the Tibetan Plateau and tectonic implications, *Geophys. J. R. astr. Soc.*, **88**, 727-749.
- Molnar, P. and W.-P. Chen, 1983. Focal depths and fault plane solutions of earthquakes under the Tibetan Plateau, *J. Geophys. Res.*, **88**, 1180-1196.
- Molnar, P., 1989. The geology evolution of the Tibetan Plateau, *American Scientist*, **77**, 350-360.
- Minster, J. F., T. J. Jordan, Molnar, P., and E. Haines, 1974. Numerical modeling of instantaneous plate tectonics, *Geophys. J. R. astr. Soc.*, **38**, 541-576.
- Ni, J., and M. Barazangi, 1983. High frequency seismic wave propagation beneath the Indian Shield, Himalayan arc, Tibetan Plateau and surrounding regions: High uppermost mantle velocities and efficient  $S_n$  propagation beneath Tibet, *Geophys. J. R. astr. Soc.*, **72**, 665-681.
- Ni, J., and M. Barazangi, 1984. Seismotectonics of the Himalayan collision zone: geometry of the underthrusting Indian plate beneath the Himalaya, *J. Geophys. Res.*, **89**, 1147-1163.
- Rial, J. A., S. Grand, and D. V. Helmberger, 1984. A note on lateral variation in upper mantle shear-wave velocity across the Alpine front, *Geophys. J. R. astr. Soc.*, **77**, 639-654.
- Romanowicz, B. A., 1982. Constraints on the structure of the Tibet Plateau from

- pure path phase velocities of Love and Rayleigh waves, *J. Geophys. Res.*, **87**, 6865-6883.
- Romanowicz, B. A., 1984. Pure path attenuation measurements of long-period Rayleigh waves across the Tibet Plateau, *Phys. Earth Planet. Inter.*, **36**, 116-123.
- Shedlock, K. M., and S. W. Roecker, 1987. Elastic wave velocity structure of the crust and upper mantle beneath the North China basin, *J. Geophys. Res.*, **92**, 9327-9350.
- Singh, D. D., 1977. Crust and upper mantle velocity structure beneath north and central India from the phase and group velocity of Rayleigh and Love waves, *Tectonophysics*, **139**, 187-203.
- Suzuki, I., O. L. Anderson, and Sumino, Y., 1983, Elastic Properties of a Single-Crystal Forsterite  $Mg_2SiO_4$ , up to 1200 K, *Phys. Chem. Min.*, **10**, 38-46.
- Tapponnier, P., and P. Molnar, 1977. Active faulting and tectonics of China, *J. Geophys. Res.*, **82**, 2905-2930.
- Teng, Ji-Wen, 1987. Explosion study of the structure and seismic velocity distribution of the crust and upper mantle under the Xizang ( Tibet ) Plateau, *Geophys. J. R. astr. Soc.*, **89**, 405-414.
- Wang, Kai, and Zhen-Xing Yao, 1989. Preliminary study of upper mantle shear velocity structure of China, *Chinese J. of Geophysics*, **32**, 49-60. ( English edition published by Allerton Press Inc. New York).
- Wang, Shu - Yun, and Zhong - Huai Xu, 1985. Seismic tectonic stress fields of eastern continental China, *Acta Seismological Sinica*, **7**, 17-31 ( in Chinese, Figure Captions in English ).
- Wier, Stuart, 1982. Surface wave dispersion and earth structure in south-eastern China, *Geophys. J. R. astr. Soc.*, **69**, 33-47.
- Yang, Zunyi, Yuqi Cheng, and Hongzhen Wang, 1986. *The Geology of China, Oxford Monographs on Geology and Geophysics*, **3**, Clarendon Press, Oxford.
- Zhang, Zh. M., J. G. Liou, and R. G. Coleman, 1984. An outline of the plate tectonics of China, *Geol. Soc. Am. Bull.*, **5**, 295-312.

Table 1. Earthquakes and stations used in this study.

	Date	Origin Time	Location (°N °E)	Depth (km)	Mag Mb Ms	Study area	Station	$\Delta$	Phase
1	06 14 65	13:17:02.4	32.09 87.72	36	5.2	TP	SHL	7.5	Love
							LAH	11.4	Love
2	06 16 65	23:49:08.2	32.04 87.46	69	4.8	TP	NDI	9.5	Love
3	06 17 65	20:14:50.1	32.12 87.76	15	5.1	TP	LAH	11.4	Love
4	06 18 65	01:18:39.0	32.01 87.59	43	5.1	TP	NDI	9.6	Love
5	02 05 66	15:12:32.9	26.22 103.21	32	5.6	EC	SEO	23.1	S
6	02 07 66	23:06:37.4	30.25 69.89	28	5.6	TP	ANP	45.7	SS
7	03 14 66	04:42:50.7	32.47 97.46	33	4.8	TP	SHL	8.4	Love
							NDI	17.8	Love
8	03 17 66	05:44:47.9	31.60 82.76	11	4.7	TP	SHL	10.0	Love
9	03 29 66	06:12:00.8	37.52 114.99	33	5.3	EC	SHL	23.0	S
10	09 28 66	14:00:21.0	27.53 100.08	12	5.7	TP	MSH	35.3	SS
11	03 14 67	06:58:04.4	28.41 94.29	12	5.8	EC	HKC	19.0	S
							ANP	24.5	S
							SHK	33.2	SS
							MAT	37.7	SS
12	08 15 67	09:21:03.3	31.05 93.56	10	5.5	TP	SHL	5.7	Love <sup>1</sup>
13	08 30 67	11:08:50.0	31.57 100.31	8	4.9	TP	NDI	20.2	Love <sup>1</sup>
							LAH	22.9	Love
14	09 15 67	10:32:44.2	27.42 91.86	19	5.8	EC	SHK	35.5	SS
15	12 22 68	09:06:35.0	36.25 101.83	21	5.5	TP	KBL	26.7	S
16	10 17 69	01:25:11.5	23.09 94.70	124	6.1	EC	SHK	35.0	SS
							MAT	39.7	SS
17	06 05 70	04:53:07.4	42.48 78.71	24	5.9 6.8	TP	HKC	35.7	SS
18	07 30 70	00:52:20.3	37.85 55.94	22	5.7	TP	HKC	52.0	SS
19	04 03 71	04:49:03.1	32.16 94.99	27	5.6 6.4	EC	MAT	35.7	SS
20	05 31 71	05:13:58.6	25.22 96.51	22	5.2 6.1	EC	MAT	37.3	SS
21	07 22 72	16:41:02.1	31.38 91.41	17	5.4 5.8	TP	NIL	15.5	S
							QUE	21.0	S
22	08 30 72	15:14:7.5	36.65 96.35	17	5.5 5.5	TP	NDI	17.9	Love
23	08 30 72	18:47:40.3	36.56 96.35	16	5.5 5.3	TP	QUE	25.3	S
24	02 07 73	16:06:25.8	31.50 100.33	8	5.9	TP	NDI	20.2	Love <sup>1</sup>
							NIL	22.9	Love
25	03 18 75	18:44:16.3	35.12 86.54	31	5.1 5.8	TP	QUE	17.2	S
26	05 05 75	05:18:46.3	33.13 92.84	8	5.6 6.1	TP	NIL	16.4	S
27	10 03 75	17:31:35.6	30.44 66.41	24	5.5 6.4	TP	ANP	48.6	SS
28	04 08 76	02:40:23.9	40.31 63.72	10	6.2 6.4	TP	ANP	50.0	SS
							HKC	46.0	SS
29	05 31 76	05:08:30.0	24.37 98.62	25	5.5 6.2	EC	ANP	20.8	S
							MAT	36.0	SS
30	05 31 76	18:35:05.0	24.29 98.68	20	5.1 5.5	EC	MAT	35.9	SS
31	07 03 78	08:46:32.0	32.75 94.08	8	4.7 4.9	TP	NDI	15.1	Love
32	03 15 79	12:52:26.0	23.18 101.09	6	5.5 6.2	EC	MAT	34.6	SS
33	05 20 79	22:59:11.6	29.93 80.27	16	5.7 5.7	TP	XAN	24.6	S
34	01 12 80	15:31:40.0	33.58 57.26	14	5.3 5.8	TP	HKC	51.0	SS
35	02 13 80	22:09:30.8	36.47 76.86	74	6.0 5.4	TP	GVA	27.2	S
							ANP	39.7	SS
36	02 22 80	03:02:43.7	30.66 88.65	10	6.0 5.4	TP	NDI	10.1	P <sub>s</sub> <sup>2</sup>
							NIL	13.4	P <sub>s</sub>
37	07 29 80	12:23:07.7	29.34 81.21	3	5.7 5.5	TP	LZH	20.1	S
							XAN	24.0	S
38	01 23 82	17:37:29.2	31.68 82.28	25	6.0 6.5	TP	LZH	18.4	S
39	06 15 82	23:24:28.8	31.85 99.92	7		TP	NDI	20.2	Love <sup>1</sup>
40	04 18 83	10:58:49.1	27.78 62.07	44	6.4 6.3	TP	SEO	54.5	SS
							HKC	59.7	SS
41	12 16 83	13:15:57.3	39.34 72.96	35	5.7 5.9	TP	BAG	47.2	SS
42	02 01 84	14:22:09.2	34.57 70.48	44	5.9 5.9	TP	ANP	44.8	SS
43	10 26 84	20:22:21.8	39.15 71.35	7	5.9 6.2	TP	HKC	40.1	SS
							ANP	44.2	SS
44	10 29 85	13:13:40.0	36.75 54.81	13	6.0 6.0	TP	GZH	51.8	SS

<sup>1</sup>Holt and Wallace, 1989; <sup>2</sup>this study. TP Tibetan Plateau; EC Eastern China.



**Table 2**  
Velocity models for Tibetan Plateau ( TIP )  
and Eastern China ( ECH )

Depth (km)	TIP (km/sec)	ECH (km/sec)	Depth (km)	TIP (km/sec)	ECH (km/sec)	Depth (km)	TIP (km/sec)	ECH (km/sec)
0	2.550	3.450	150	4.550	4.440	290	4.705	4.668
3.75	3.500	3.450	160	4.550	4.467	300	4.708	4.675
10	3.500	3.700	170	4.590	4.484	310	4.712	4.682
20	3.700	3.800	180	4.625	4.501	320	4.715	4.695
30	3.700	3.850	190	4.658	4.518	330	4.718	4.710
35	3.700	4.650	200	4.668	4.535	340	4.721	4.720
40	3.800	4.650	210	4.675	4.552	350	4.725	4.730
70	4.600	4.600	220	4.680	4.569	360	4.730	4.740
80	4.600	4.550	230	4.685	4.586	370	4.740	4.750
90	4.600	4.500	240	4.690	4.603	380	4.750	4.760
100	4.600	4.450	250	4.690	4.620	390	4.760	4.770
110	4.600	4.400	260	4.693	4.637	400	4.770	4.770
130	4.550	4.400	270	4.697	4.654	405	5.014	5.014
140	4.550	4.420	280	4.701	4.660	425	5.050	5.050

**Table 3** Compressional Velocities of TIP

Depth (km)	Thick (km)	Vel (km/sec)	Depth (km)	Thick (km)	Vel (km/sec)
0.00	0.00	4.530	280.0	10.0	8.470
3.75	3.75	4.530	290.0	10.0	8.480
20.0	16.25	6.160	300.0	10.0	8.486
40.0	20.0	6.550	310.0	10.0	8.510
70.0	30.0	6.740	320.0	10.0	8.540
130.0	60.0	8.290	330.0	10.0	8.560
170.0	20.0	8.200	340.0	10.0	8.570
180.0	10.0	8.270	350.0	10.0	8.594
190.0	10.0	8.340	360.0	10.0	8.623
200.0	10.0	8.400	370.0	10.0	8.653
210.0	10.0	8.420	380.0	10.0	8.691
220.0	10.0	8.430	390.0	10.0	8.730
230.0	10.0	8.440	400.0	10.0	8.770
240.0	10.0	8.450	405.0	5.0	8.810
260.0	20.0	8.460			9.280
270.0	10.0	8.462			

**Table 4.** Relocation of February 22, 1980 Tibet earthquake. The location 30.506° N, 88.583° E, and the origin time 03:02:47.2; After relocation: the location 30.658° N, 88.649° E, and the origin time 03:02:43.7.

STAT	TPK	TPKP	TOBS1	TOBS2	TCOM1	TCOM2	DT1	DT2
AAE	51.3	50.0	544.1	547.6	544.8	545.5	-3.1	-0.3
ADE	57.8	59.3	730.6	734.1	733.4	733.8	-2.9	0.2
AQU	51.3	51.3	604.1	607.6	607.9	607.7	-4.7	-1.0
BAG	17.4	16.1	390.2	393.7	392.3	392.2	-2.7	0.9
BUL	36.1	36.0	708.9	712.4	712.3	713.0	-2.8	-0.0
CHG	14.8	14.9	207.6	211.1	212.3	213.4	-4.0	-1.5
COL	27.9	28.3	700.7	704.2	705.5	704.6	-5.1	-0.6
COP	37.1	37.8	589.9	593.4	594.1	593.5	-5.1	-1.0
CTA	26.1	26.0	698.8	702.3	702.7	702.9	-3.9	-0.6
DAV	36.4	34	469.2	472.7	471.3	471.5	-3.5	-0.1
ESK	34.7	34.8	647.5	651.0	652.1	651.5	-4.9	-0.9
GDH	36.6	36.3	709.4	712.9	713.5	712.7	-4.0	0.3
GRM	28.6		761.4	764.9	764.0	764.7	-3.5	-0.6
HKC	2.8	5	315.6	319.1	319.0	318.8	-4.9	-1.2
HLW	37.9	34	530.7	534.2	529.3	529.4	1.5	4.8
IST	29.4	25	522.2	525.7	526.4	526.2	-4.7	-1.0
JER	6.2		499.0	502.5	500.3	500.4	-2.2	1.3
KBL	40.8	41.1	233.6	237.1	237.9	238.0	-4.2	-0.7
KEV	54.9	55.0	547.7	551.2	551.4	551.2	-4.0	0.4
KTG	46.8	46.2	659.6	663.1	662.0	663.1	-3.6	0.7
LOR	24.3	25.1	637.1	640.6	642.3	640.6	-4.7	-0.8
MAT	32.0	31.3	464.8	468.3	468.8	467.9	-3.6	0.9
MUN	41.9	40	654.7	658.2	658.0	658.7	-2.5	0.3
NAI	43.9	44	596.7	600.2	599.0	599.8	-3.4	-0.6
NDI	11.6	11.5	144.4	147.9	146.6	147.6	-1.4	1.0
NIL	55.2		188.0	191.5	190.9	191.0	-2.8	0.5
NUR	48.8	49.5	541.6	545.1	546.0	545.3	-4.4	-0.2
POO	54.7	54.3	247.5	251.0	250.0	251.8	-2.2	-0.4
PMG	50.5	50	663.3	666.8	666.4	666.5	-3.3	0.1
QUE	2.8		255.6	259.1	259.5	260.1	-3.7	-0.8
RAB	57.4	57.5	670.2	673.7	672.3	672.3	-2.6	0.9
SHL	12.3	12	85.1	88.6	87.6	88.9	-1.3	0.8
SNG	17.6	19	330.4	333.9	333.1	334.1	-2.9	-0.4
STU	3.5	2.0	616.3	619.8	616.5	616.1	0.2	4.2
TOL	16.3	15.0	689.1	692.6	692.0	691.8	-3.5	0.3
TRI	43.0	42.9	595.8	599.3	600.9	600.5	-4.5	-0.7
UME	2.2	6.5	555.0	558.5	564.2	563.4	-8.9	-4.6

## FIGURE CAPTIONS

Figure 1. Sketch map of plate tectonics of China, and the directions of the motions of the plates surrounding China. China occupies the Eurasian plate, part of the Indian plate, and a small part of the Philippine Sea plate ( Zhang et. al 1984 ).

Figure 2. Isopach map showing crustal thickness ( in kilometers, Zhang et. al 1984) in China. In eastern China, a distinct north-northeast-trending belt that contains a marked difference in crustal thickness is parallel to a subduction zone to the east of the Asian continent. The crustal thickness in western China, the Tibetan Plateau is more than 50 km.

Figure 3. Fundamental Love wave synthetics for a variety of models, source mechanisms, and depths. The column on the left are the models used to generate the synthetics on their right. The crustal thickness is 60 km, and the average velocity of the crust is 3.6 km/sec. The velocity of the mantle is 4.6 km/sec, except for models g., 4.4 km/sec, and h., 4.8 km/sec. The distance is 1000 km, and the source function is a trapezoid ( 1, 1, 1 ).

Figure 4. A comparison of Love wave synthetics for different models. The column on the right displays the synthetics derived from the models on the left. The models are of a two-layer crust over half space mantle. The shear velocities of the upper layer is 3.6 km/sec, that of the lower layer is 3.8 km/sec, and that of the mantle is 4.6 km/sec. Except for model d), the models have a 31.8km thick upper crust. The star is the source, and the triangle is the receiver. A strike-slip source, with a Gaussian time history, half width 1.26 seconds, is used. Source depth is 9.8 km, distance is 1000 km.

Figure 5. Shear velocity models TIP ( Tibetan Plateau ) and ECH ( southeastern part of China ) derived in this study compared to profiles of the Canadian shield ( SNA ) and the tectonic western North America ( TNA ).

Figure 6. The ray paths of Love wave data used to derive the velocity distribution of the crust of the Tibetan Plateau, where the stars are sources, and the trian-

gles are stations. The numbers are the differential maximum amplitude travel times of the data compared to the synthetics. The + sign means the model is faster in seconds. The number beside the source is event number of Table 1. The iso-bath relief contour lines with altitude of 1000 meters, 2000 meters, 3000 meters and 4000 meters are given to define the physical boundary of the Tibetan Plateau. The dark star, event 36, is the location of the  $P_n$  wave source.

Figure 7. Synthetic comparison of different models with the data from known source parameters. In each group, the first trace is data with station name and event number in Table 1, along with the distance. The second, third and fourth traces are the synthetics of models TIP, CHEN, CHUN respectively.

Figure 8. The Love wave data for paths shown in Figure 6 compared with the synthetics. Upper traces are the data, the lower ones are synthetics when the amplitude are normalized, and shifted by the amounts indicated by  $T_{obs} - T_{syn}$ . On the left of each comparison are the station names and the event number given in Table 1 followed by the distance, source depth and  $T_{obs} - T_{syn}$ .

Figure 9. ( a ): The ray paths, dotted lines, of  $S$  wave data, and the bounce points of the  $SS$  wave data used to study the upper mantle shear velocity structure of the Tibetan Plateau. Circles represent the source-receiver distances greater than  $45^\circ$ , squares less than  $45^\circ$ , Stars are sources, and triangles are stations. The solid lines from thin to thick are contour lines with 1000 meters, thinnest, 2000 meters, 3000 meters and 4000 meters, thickest, above sea level. The number beside the source is event number in Table 1. ( b ): Schematic illustration of rays producing  $S$  waveforms ( left ), and  $SS$  waveforms ( right ).

Figure 10. The comparisons of the waveforms of the  $S$ -waves for the paths of the Tibetan Plateau with the synthetics using the model TIP. " A ", " B ", " C ", " D ", " E " and " F " are the branch names of the corresponding arrivals ( Figure 11 ). On the left of each datum-synthetic comparison, are station names, distances and event number.

Figure 11. Triplication curves of the model TIP and Lyon-Caen's model, and

Lyon-Caen's travel time data of *S* waves for the Tibetan Plateau paths. The different symbols indicate the properties of the path ( Lyon-Caen, 1986, Figure 8 ).

Figure 12. *SS*- and *S*-wave data for the paths with midpoints in the Tibetan Plateau and the synthetics of the model TIP. The *S* waves are aligned with synthetic *S*-waves. When the observed *S*-waveforms are used as the source function. On the left of each data-synthetic comparison, are station names, distances and event number.

Figure 13. The ray paths of the *S* and *SS*-wave data used to derive the upper mantle shear structure of the southeastern part of China. The stars are sources, and the triangles are stations. Circles indicate the midpoints of the *SS* data. Numbers near stars are event numbers, same as in Table 1. Numbers with " + " or " - " sign on the rays of *S* waves are the differential travel times of the data relative to the synthetics using the model ECH. The symbol + means that the model is faster than the data.

Figure 14. *S* data for the paths of southeastern China and the synthetics using the model ECH. Numbers below the distances are event numbers as displayed in Table 1. They are lined up with maximum amplitudes.

Figure 15. *SS* and *S* data for the paths with midpoints in southeastern China, and the synthetics using the model ECH. The *S* waves are aligned with synthetic *S* waves.

Figure 16. Comparison of the existing models for the Tibetan Plateau.

Figure 17. Comparison of the data and synthetics of models TIP, Ltib, Lind, and Wang's model. Ltib is Lyon-Caen's model for the Tibetan Plateau, Lind is Lyon-Caen's model for the Indian shield. Letters on top of the data are the branch names ( Figure 10 ).

Figure 18. Source mechanisms, and synthetic comparison with the long-period *P* wave WWSSN data of February 22, 1980 Tibetan earthquake. The origin time is 3:2:43.7, epicenter locates at  $30.658^{\circ}$  N  $88.649^{\circ}$  E, source depth is 10

km. The strike, dip and rake are  $160^\circ$ ,  $60^\circ$  and  $250^\circ$  respectively. The moment is  $8.0 \times 10^{24} \text{ dyn} \cdot \text{cm}$  and the source function is a trapezoid ( 1, 1, 1 ). The darker traces are the data, and the lighter ones are synthetics. On the left of each data-synthetic comparison, are the component of the data used ( "Z", vertical component ), station name, the peak amplitude of the data, and the peak amplitude of the synthetics in centimeters using the moment shown in the head line. The ( + ) symbol indicates the compressional, and little circles indicate dilational. If the polarity of the short-period data is different from that of its corresponding long-period data, we use that of the short-period.

Figure 19. Synthetic comparison with  $P_{nl}$  waveform data. The darker traces are the data, and the lighter ones are the synthetics. The beginning time of the corresponding data and synthetics are 140 and 190 seconds. The data and synthetics are lined up with absolute time, with NDI synthetics shift left 1.5 seconds, NIL synthetics shift left 0.5 seconds. The numbers beside the station names are event numbers given in Table 1.

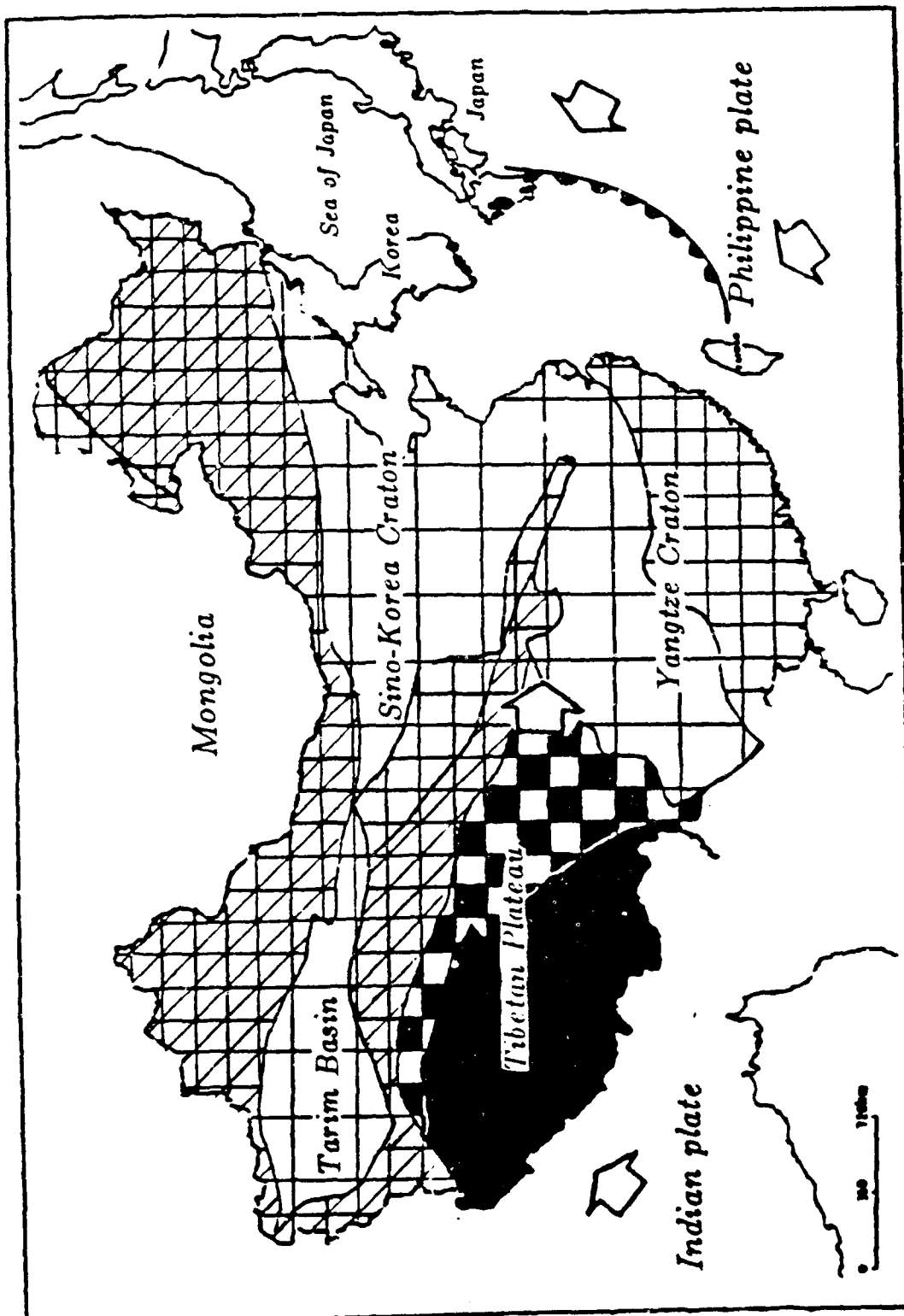


Figure 1



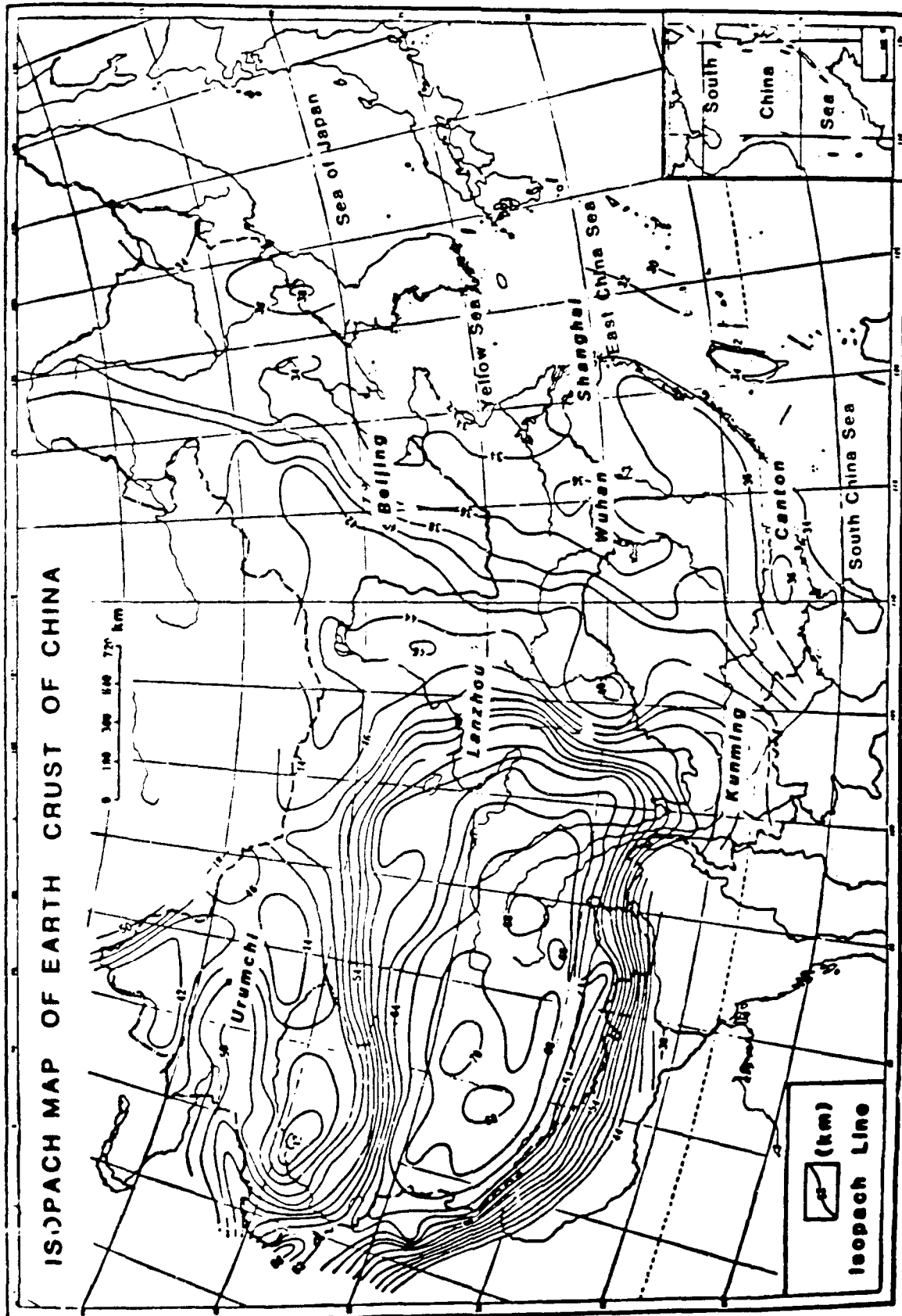


Figure 2

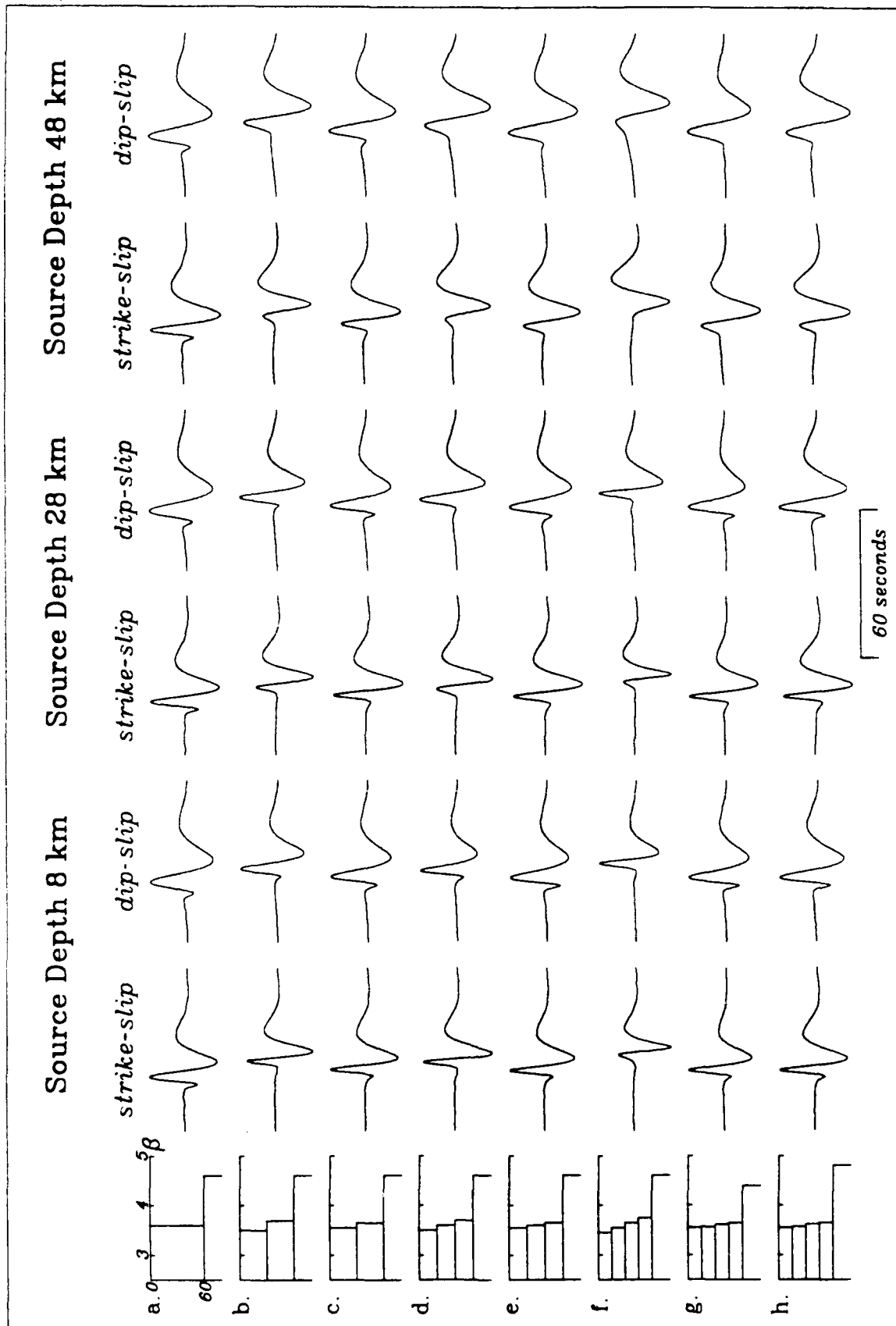
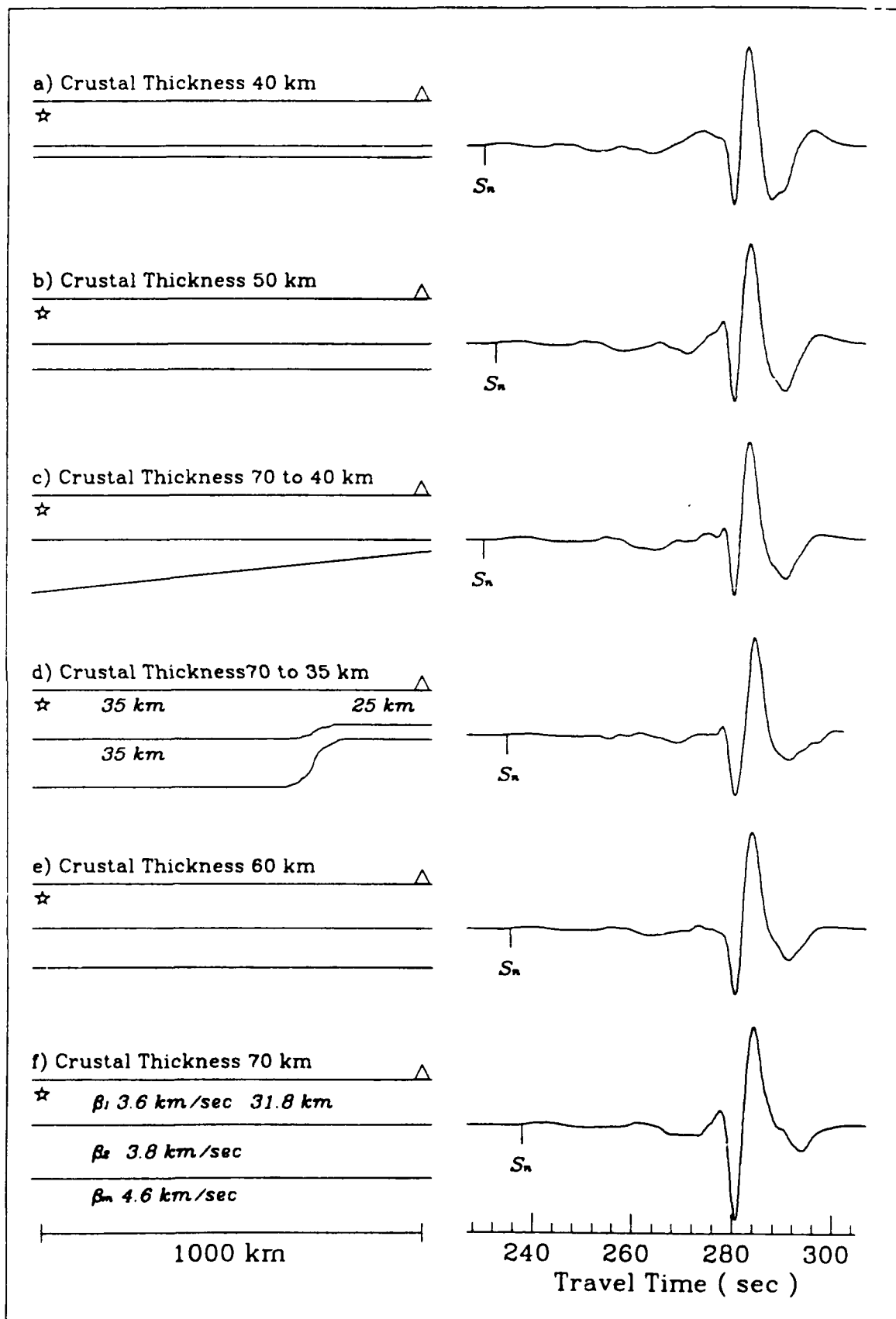
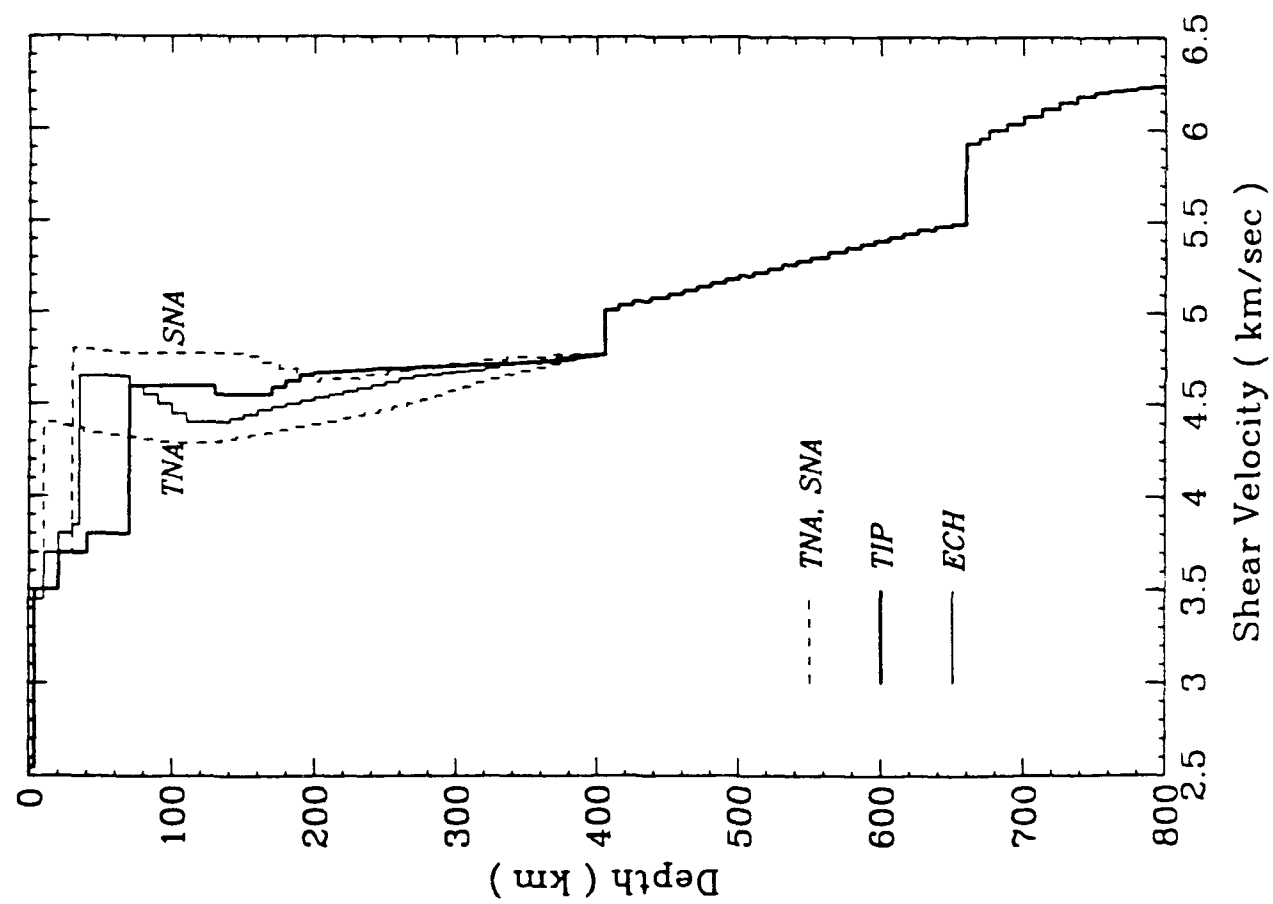


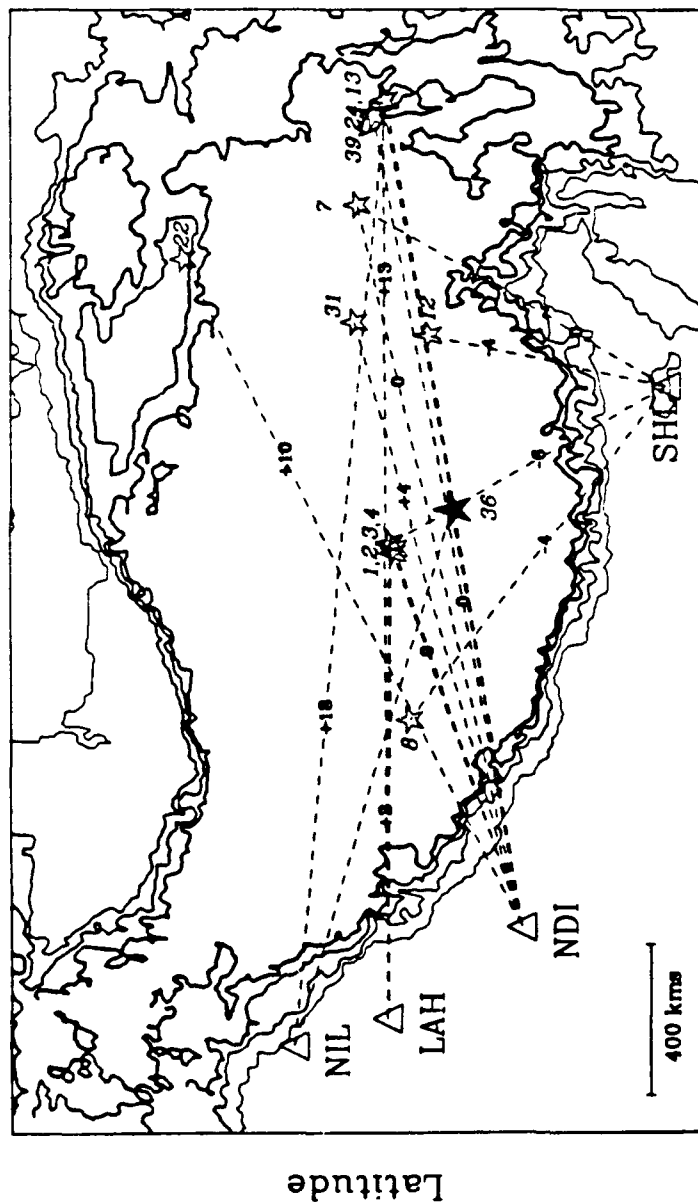
Figure 3



**Figure 4**  
35



**Figure 5**



Longitude

Figure 6

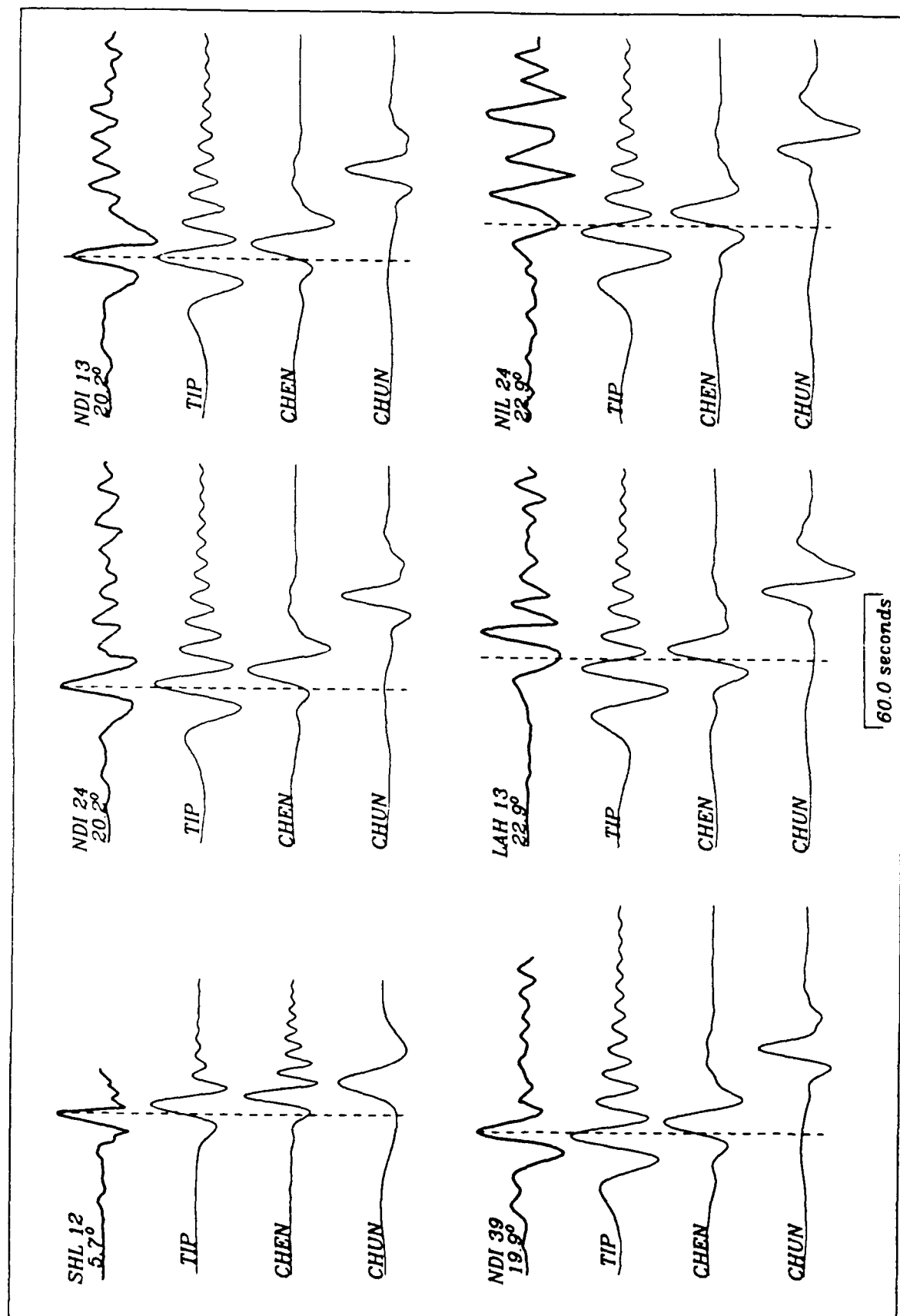
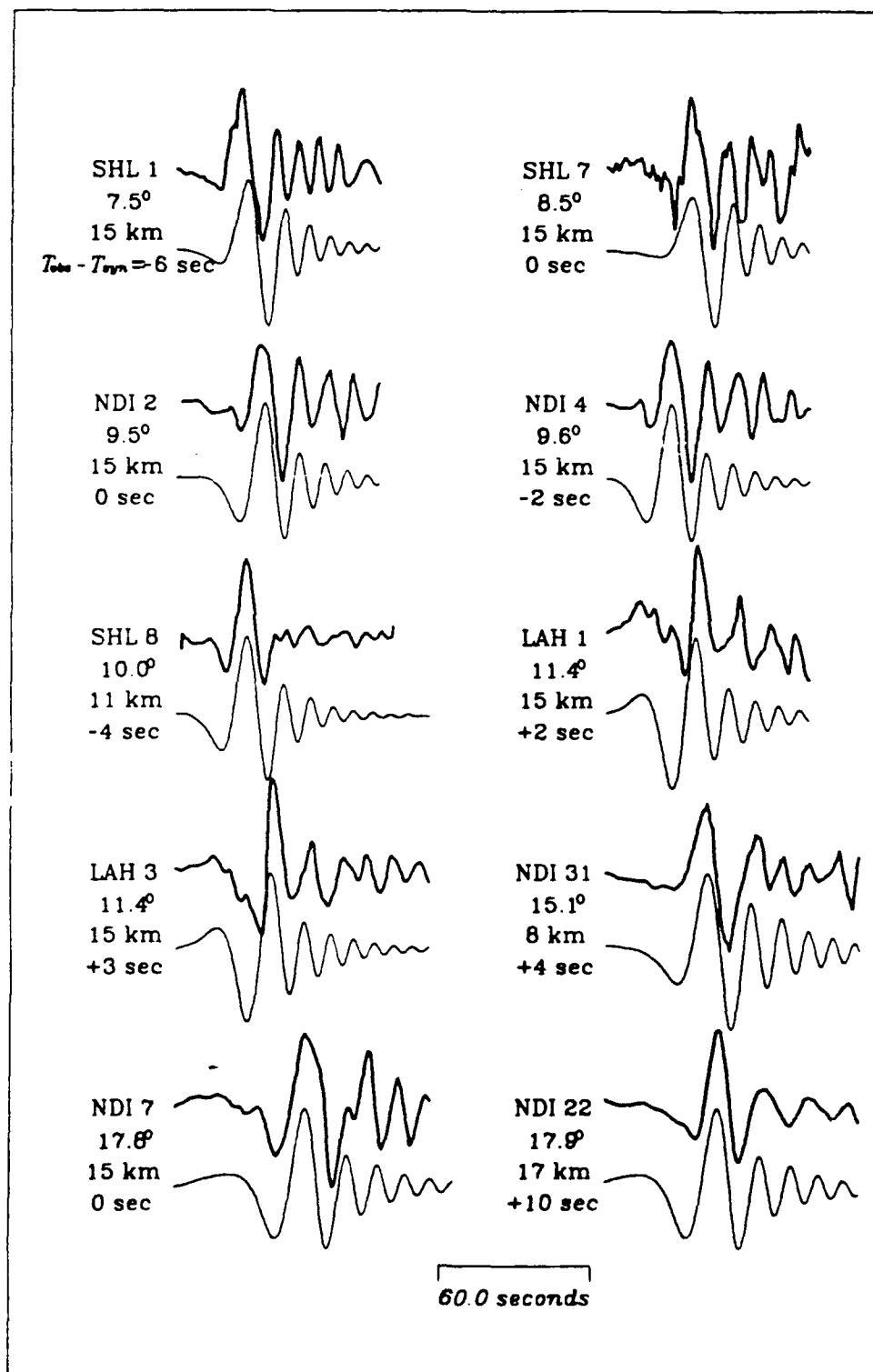


Figure 7



**Figure 8**

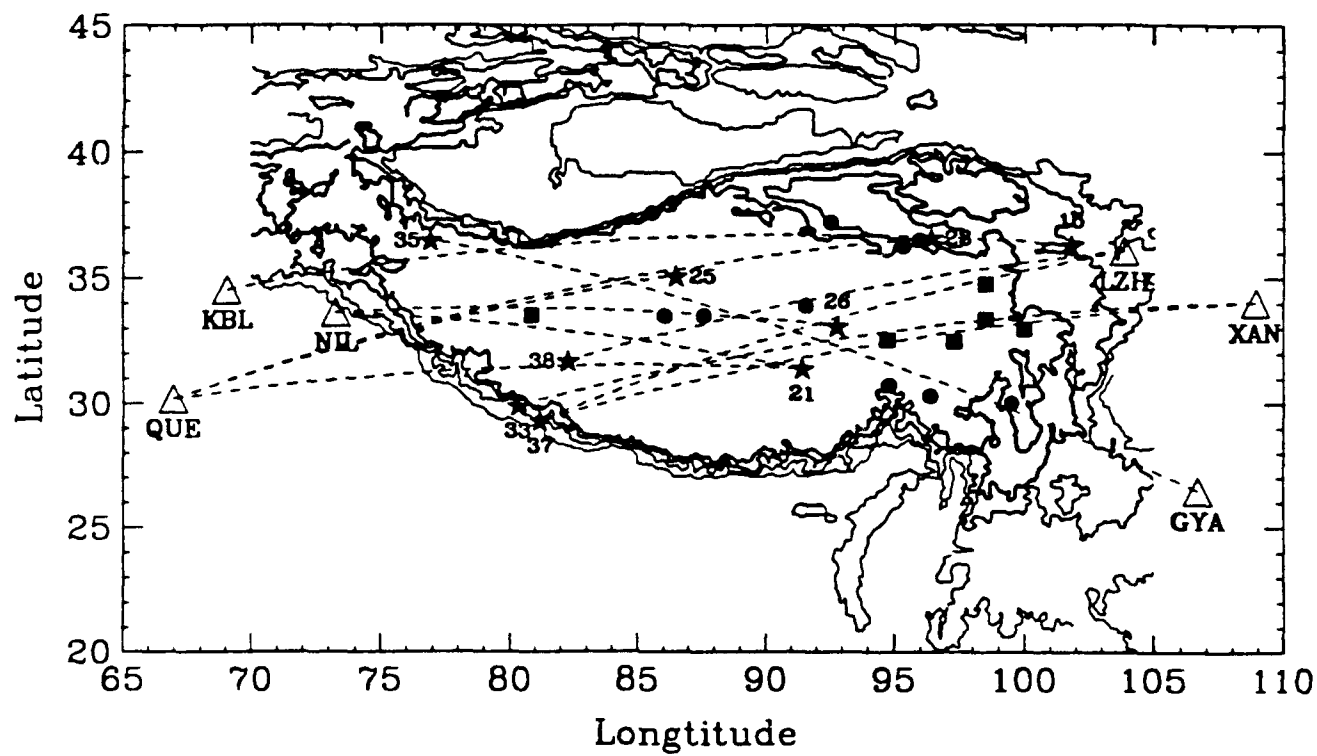


Figure 9a

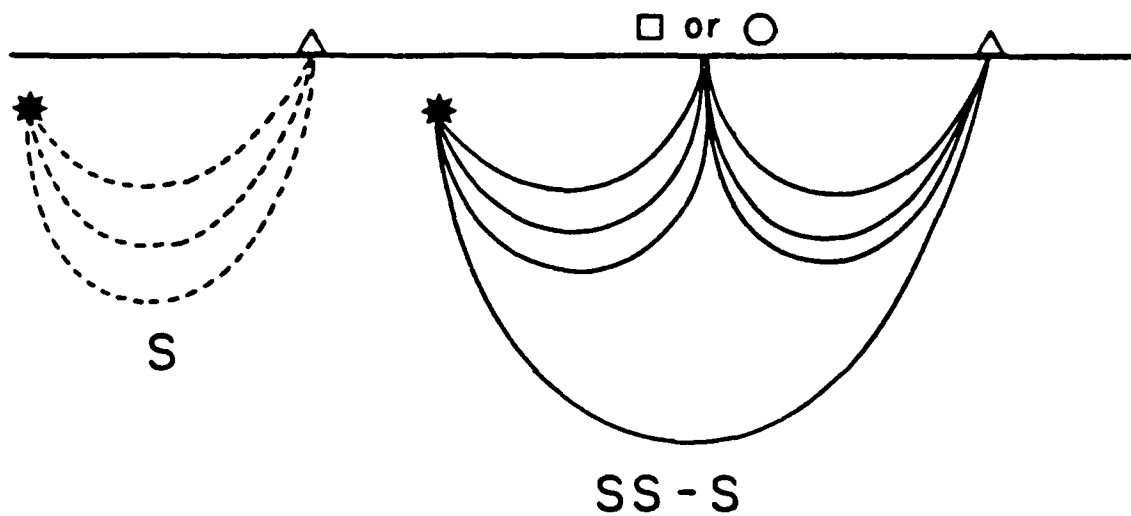


Figure 9b



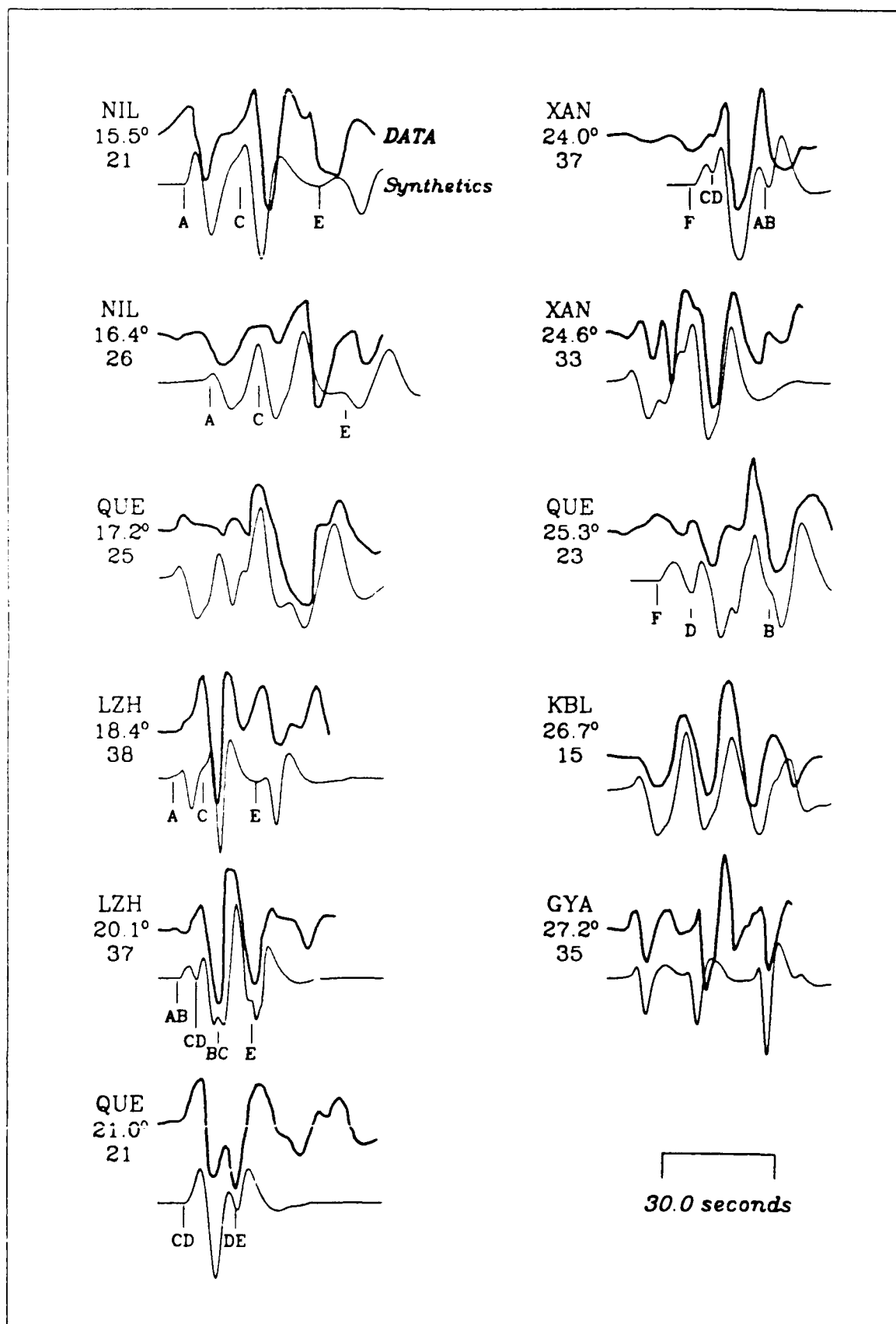


Figure 10

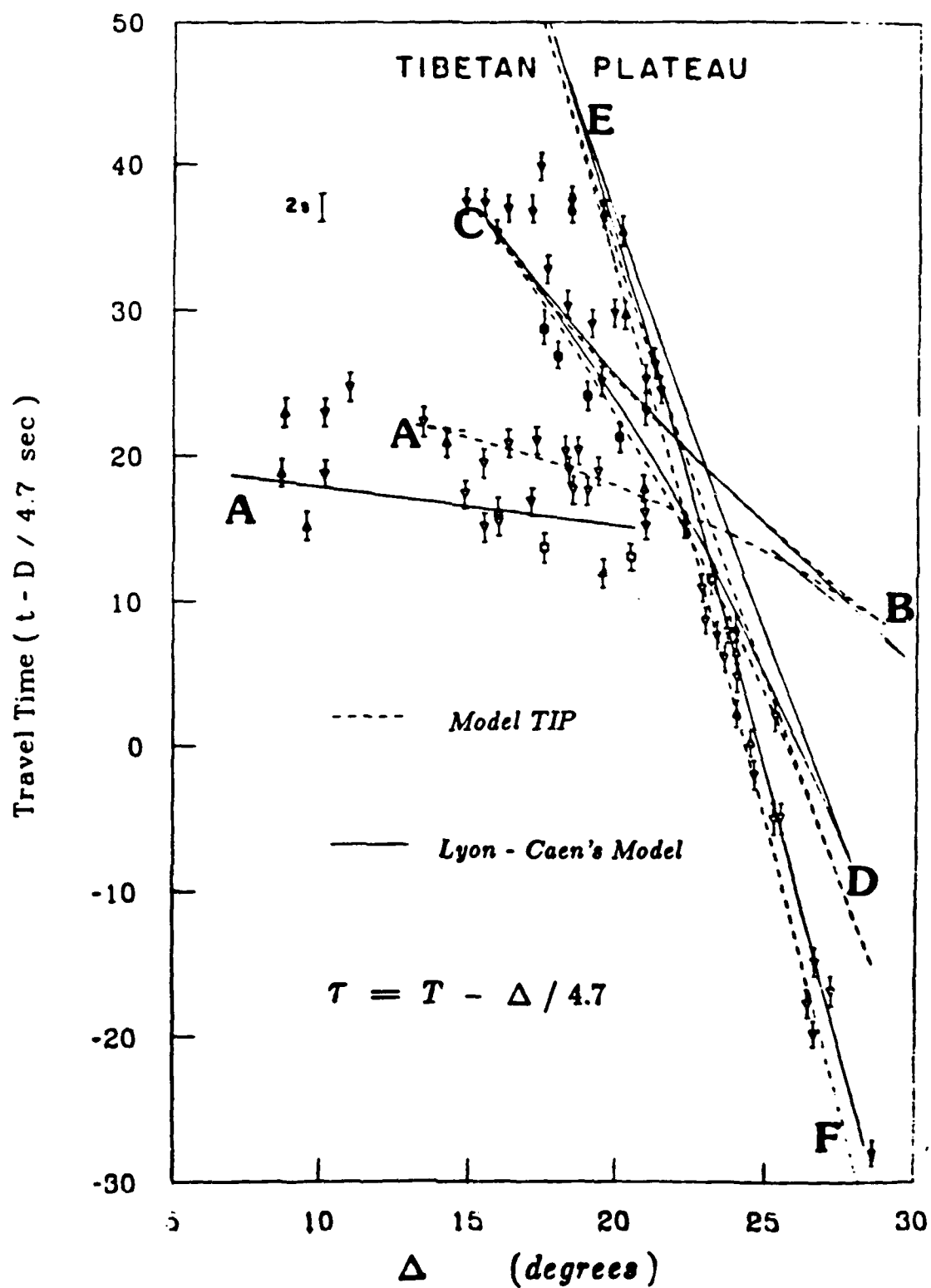
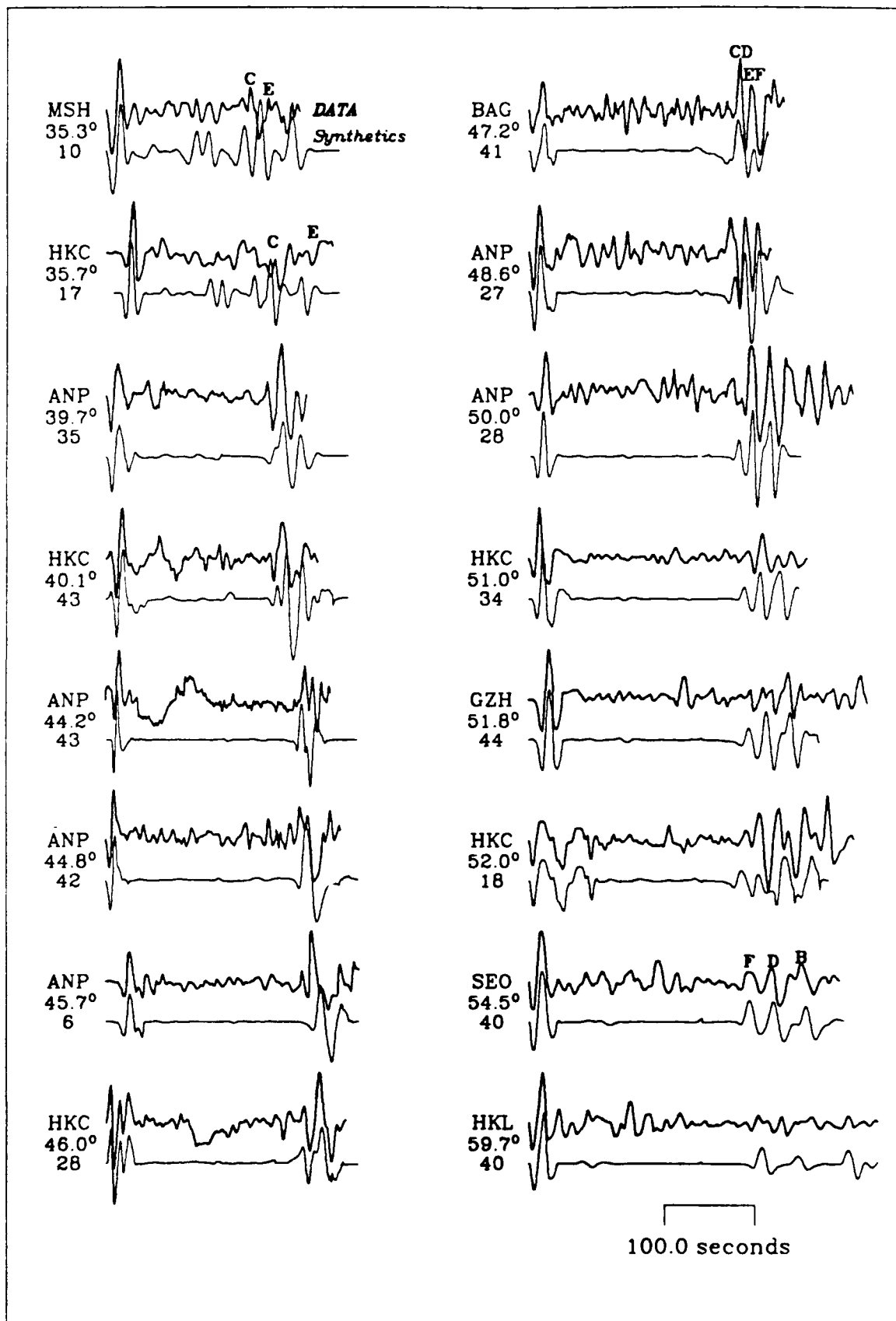
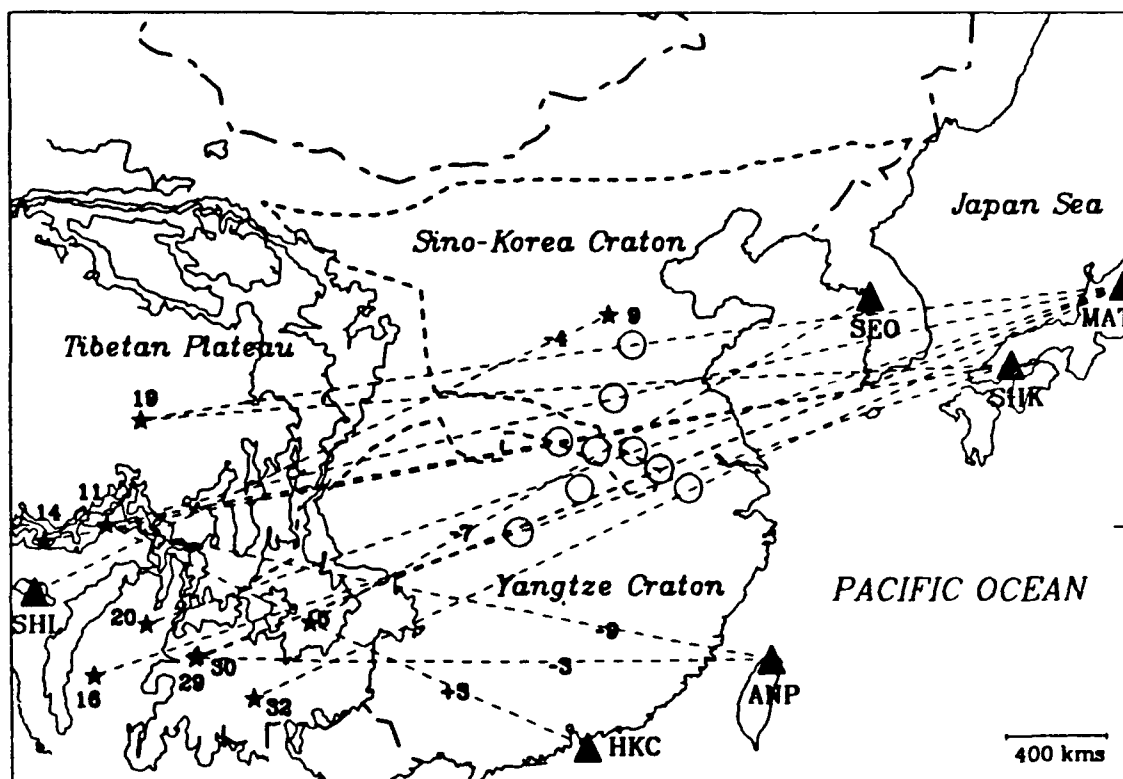


Figure 11



**Figure 12**



**Figure 13**

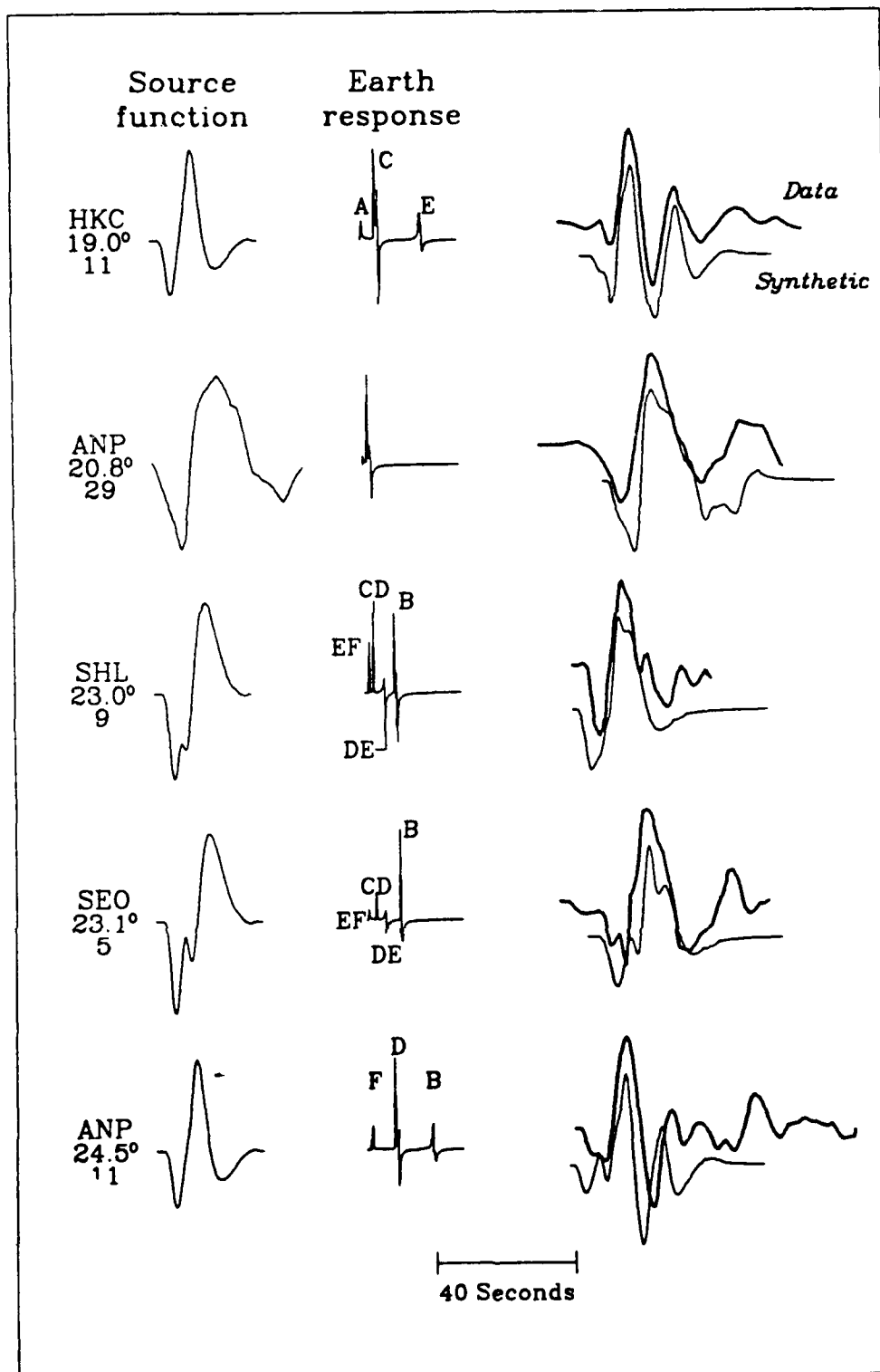


**Figure 14**

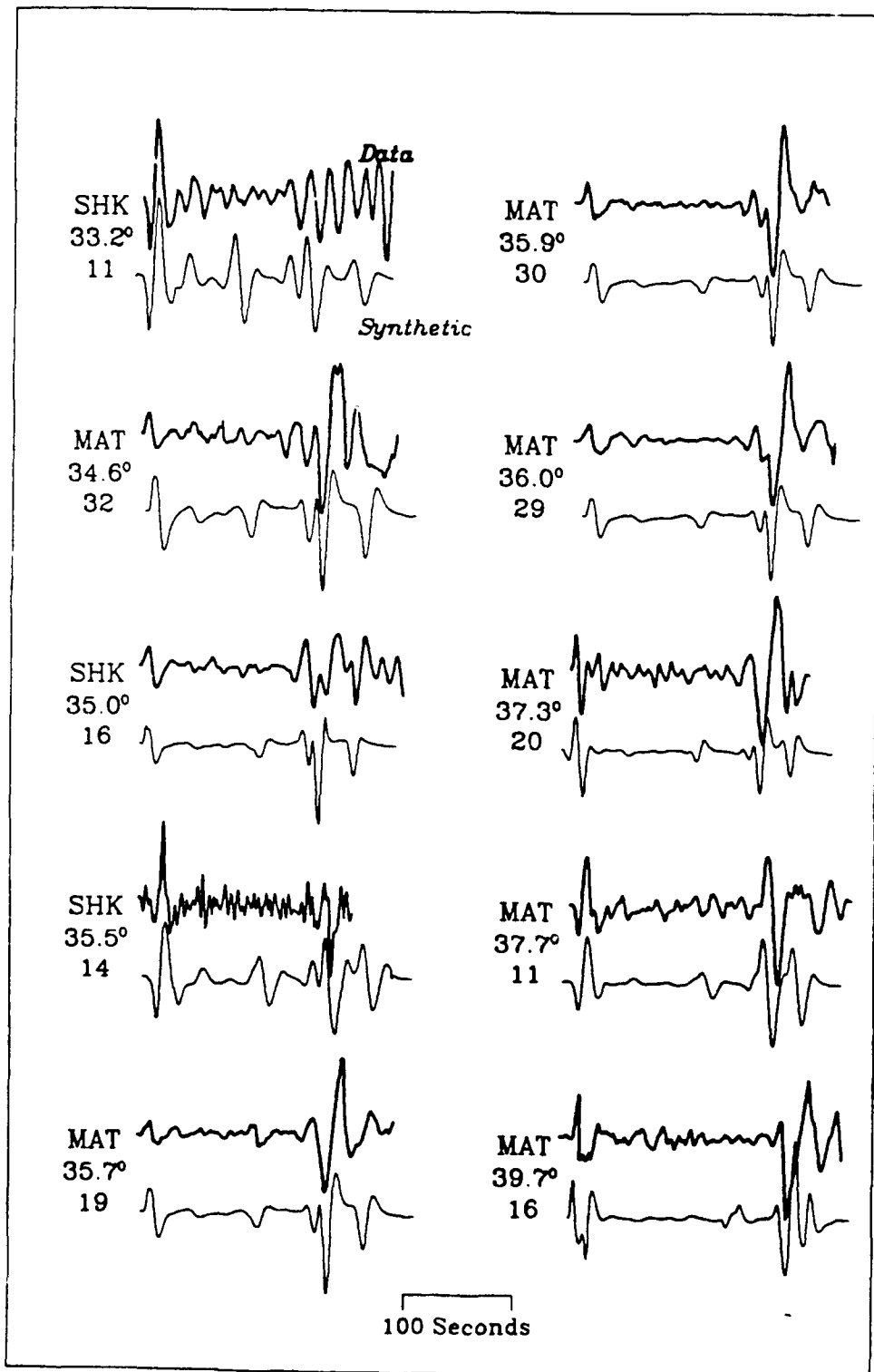


**Figure 15**

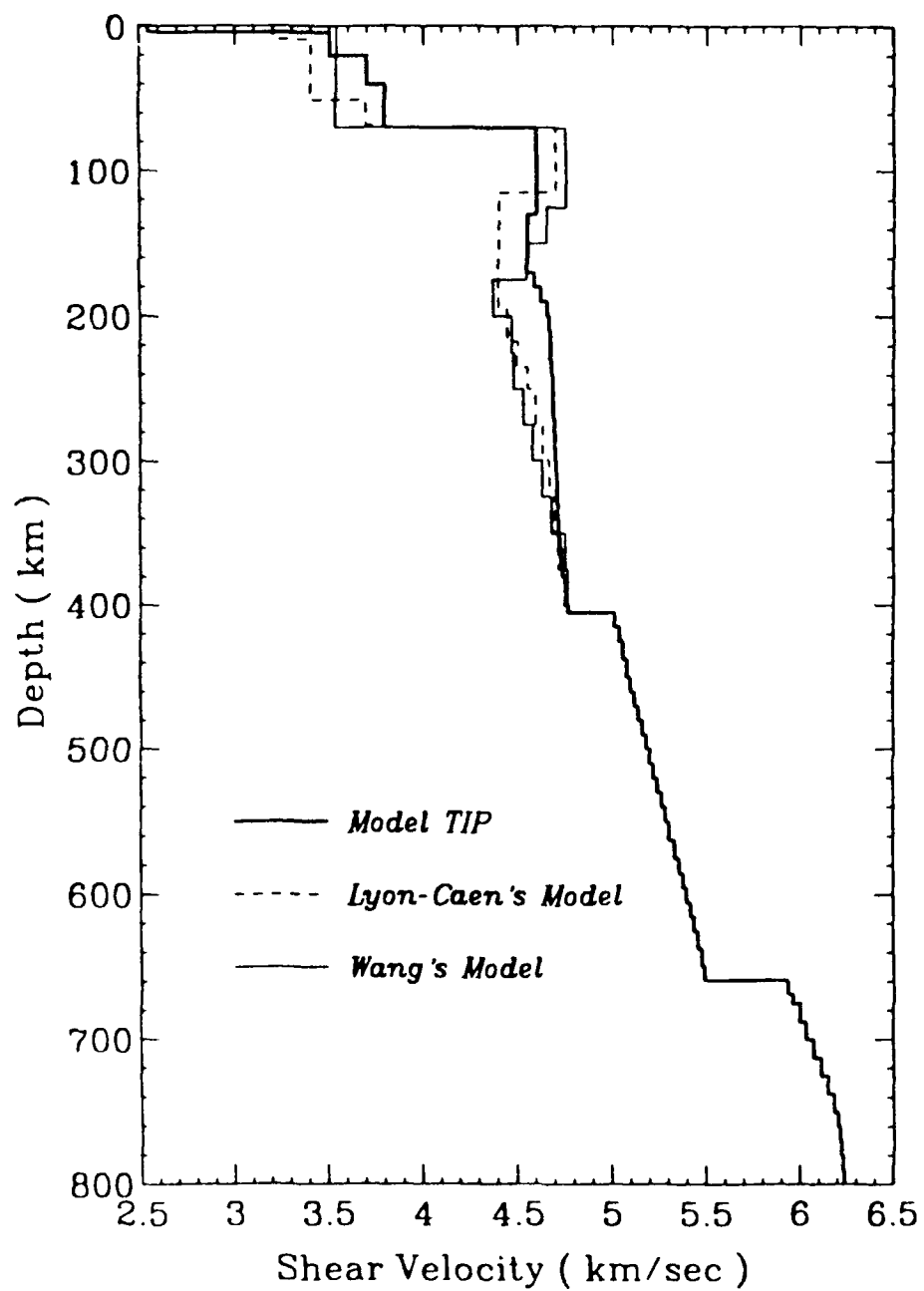


**Figure 16**

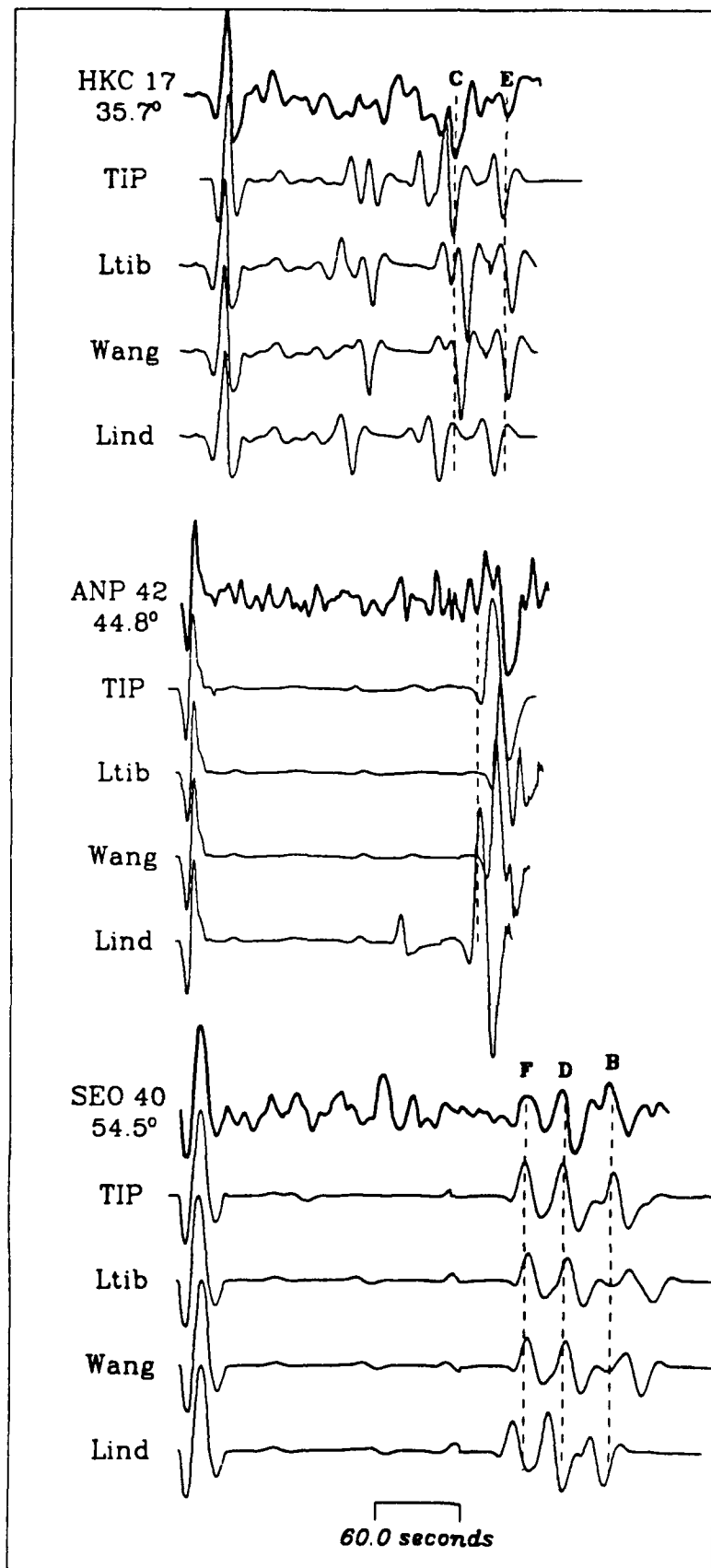


**Figure 17**



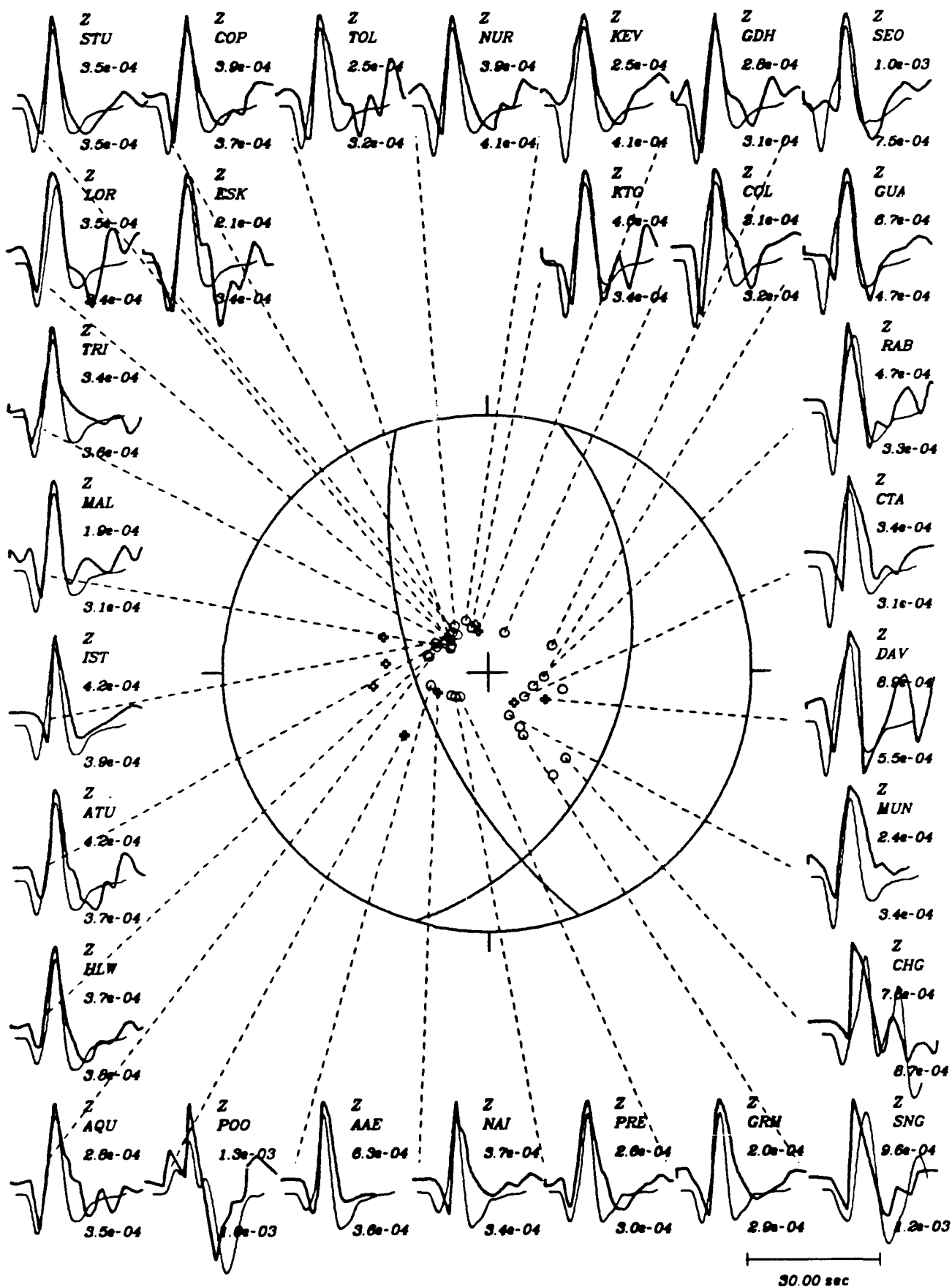
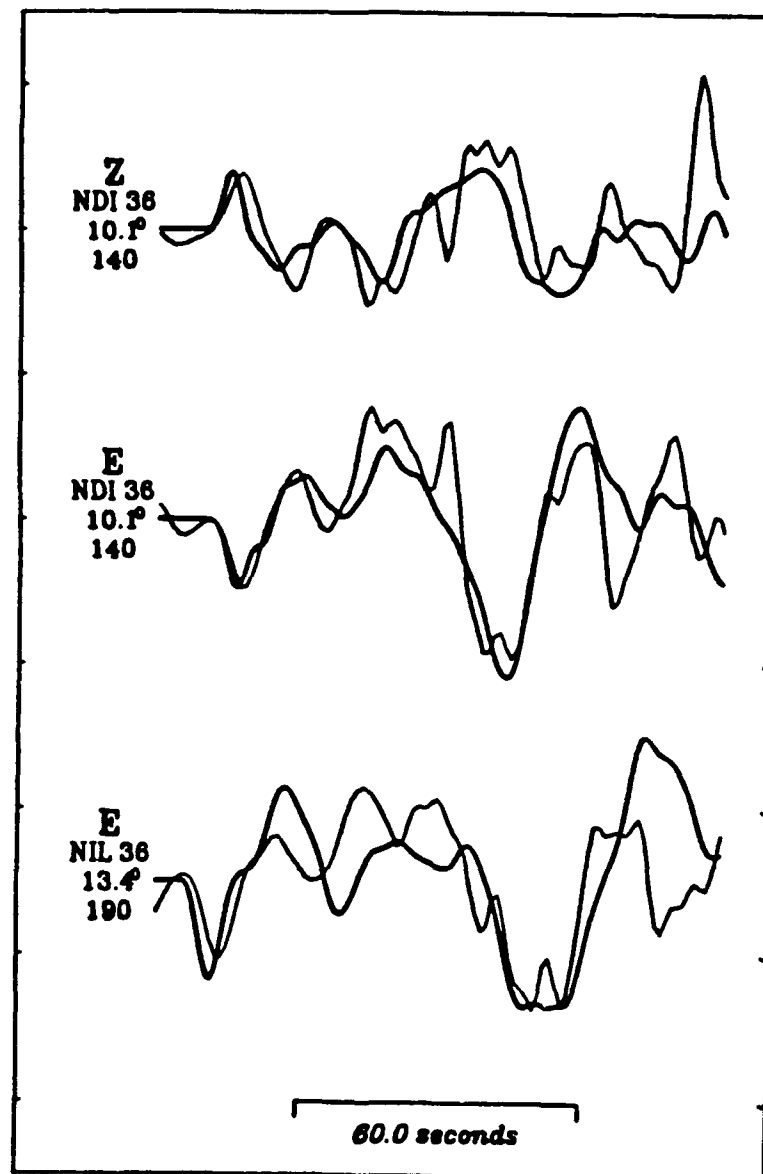


Figure 18



**Figure 19**

## **SECTION 2**

**Broadband Modeling Along a Regional Shield Path,  
Harvard Recording of the Saguenay Earthquake**

**Broadband Modeling Along a Regional Shield Path,  
Harvard Recording of the Saguenay Earthquake**

***Lian - She Zhao and Donald V. Helmberger***

**Seismological Laboratory, 252 - 21**

**California Institute of Technology**

**Pasadena, California 91125**

Broadband Modeling Along a Regional Shield Path,  
Harvard Recording of the Saguenay Earthquake

*Lian - She Zhao and Donald V. Helmberger*

Seismological Laboratory, 252 - 21

California Institute of Technology

Pasadena, California 91125

Abstract

The Saguenay earthquake, November 25, 1988, is one of the first large shield type events recorded by a broadband - high dynamic range instrument, the Streckeisen system, installed at Harvard station ( HRV ). The event is sufficiently large to be well recorded teleseismically and thus the source characteristics can be determined by independent means and considered known. This allows a detailed study of the propagational effects along this path, at an epicentral distance of 625 km, where the strengths of the surface waves can be compared with the crustal body phases. Broadband modeling using standard analytical techniques and flat layered models works amazingly well over the period range of 0.5 to 20 seconds. A detailed strategy for modeling broadband regional phases is given in terms of a decomposition of the vertical and radial seismograms into three segments:  $P_{nl}$  ( containing  $P_n$ ,  $pP_n$ ,  $aP_n$ ,  $P_mP$ ,  $P$  coupled  $PL$  waves ) ;  $S_{nl}$  ( containing  $S_n$ ,  $aS_n$ ,  $S_mS$ , etc. ) ; and the fundamental Rayleigh waves. Information about the upper crust is obtained from the fundamental Rayleigh waves while crustal thickness and velocity gradients in the mantle are obtained from  $P_{nl}$  and  $S_{nl}$ . This particular crustal model has a thickness of 35 km with a sharp mocho and a substantial gradient in the top 20 km of the mantle, 0.01 km/sec per km for both P and S velocities. The mantle velocities,  $\alpha=8.2$  and  $\beta=4.55$  km/sec are slower

than expected for a shield environment. Attenuation is not required for waveform modeling or for absolute amplitude estimation.

Keywords: Broadband modeling, Generalized Ray Method ( GRM ), Mode Summation Method ( MSM ), Reflectivity

## I. Introduction

In recent years, short-period seismology has concentrated on small events and local crustal structure while long-period seismology has concentrated more on inverting source mechanisms of larger earthquakes and deep earth structure. Long period seismograms at regional distances have not received much attention in either source studies or in studies of the Earth's shallow structure. One reason is that only small events,  $4 < m < 5$ , remain on scale on the standard long-period WWSSN at these distances. The source properties of these events are generally poorly understood, since they can not be easily studied teleseismically. Thus, these events are not so useful in Earth structure investigations. Larger events produce visible  $P_n$  and  $PL$  waves and these waveforms have been used in earthquake studies ( e. g. Helmberger and Engen, 1980; Wallace and Helmberger 1982 ), but the surface waves of the events go off-scale. Most digital systems have, unfortunately, not performed well at regional distances for assorted reasons.

With the installation of the Streckeisen seismometer and high dynamic range digitizer, the broadband nature of regional phases can now be appreciated ( see Figure 1 ). The HRV recording of the Saguenay earthquake, at an epicentral distance of 625 km, is one of the first such unclipped recordings of a sizable earthquake occurring in a predominantly shield region. This event is the largest earthquake to occur in over 50 years in Eastern North America and was recorded both locally and teleseismically ( e. g. North et al., 1989; and Somerville et al.,

1989 ). These studies provide seismic source parameters for the event ( strike  $-323^\circ$ , dip  $-65^\circ$ , rake  $-78^\circ$ , moment  $-5.0 \times 10^{24}$  dyne-cm, depth  $-28$  km ), as well as some constraints on the time history.

Figure 2 gives the three component long-period WWSSN recordings obtained by convolving the broadband data displayed in Figure 1 with the WWSSN instrument response. The peak to peak amplitude of the Rayleigh wave is about 1.1 meters. If the gain of the instrument is taken as the average WWSSN ( 2250 ), the Rayleigh wave goes off-scale on conventional records. The first 40 seconds of these records is controlled by the ( $P-SV$ ) system. This wavetrain begins with  $P_n$  and evolves into  $PL$  and has been called  $P_n$  ( Helmberger and Engen, 1980 ). The later arriving phases begin with  $S_n$ ,  $s_n$ , etc and go off-scale somewhere near the direct  $S$  arrival. The beginning portion of this group which arrives before the fundamental Rayleigh wave will likewise be called  $S_n$  for convenience.

Figure 3 displays a comparison of the broadband data and synthetics constructed from a flat-layered model. A brief comparison of these waveforms indicates that quantitative methods based on layered models work quite well, at least in a shield environment. This paper addresses some techniques and strategies which were used in deriving the above model along with numerous sensitivity studies. What can be learned from regional broadband seismograms is our main concern in this study.

## II. Numerical Methods

There are many different techniques available for generating synthetics for a flat-layered model ( see Aki and Richards, 1980 for example ). The reflectivity method and various modifications essentially perform a double integration and produce accurate results if the integration windows are properly placed with

respect to the range of ray parameter and frequency. This technique lends itself to vectorization and looks more attractive than the other methods with the availability of vector computers. Comparison of synthetics generated with this approach and with generalized rays ( Helmberger, 1983 ), has been discussed by Apsel and Luco ( 1983 ) for simple models where it is possible to sum enough rays to construct the entire wavefield. The advantage of rays is that insight can be gained into the timing of individual pulses. However, in strong waveguides the number of significant multiples become large and the method becomes impractical. Fortunately, the normal mode method or mode summation method ( Harkrider, 1964 ) works well for modeling surface waves at about this time window, as we discuss next.

In this study, the earthquake will be represented by a simple point source dislocation, which can be computed by constructing a linear combination of responses for pure strike-slip, dip-slip and 45° dip-slip sources, as discussed by Helmberger and Harkrider ( 1978 ). Synthetics of these three types of source descriptions are displayed in Figures 4 and 5, where the generalized ray results are compared with those of reflectivity and the normal mode method. The model used is the same as that considered by Apsel and Luco ( 1983 ), in their study of the various methods of generating synthetics. The bottom traces display  $P_n$ ,  $P_m P$  and direct  $P$ , followed by  $pP_n$ ,  $pP_m P$  and  $aP_n$ , etc. A similar set of  $S$  phases occurs near the surface waves, which appears to be included in the mode solution and produce synthetics in good agreement with the ray solution. It is difficult to prove theoretically that the direct  $S$ -arrivals and multiple reflected  $S$  phases are handled properly in the modal approach because of the neglect of head waves. Although the amplitudes predicted by reflectivity and rays differ somewhat, the waveforms predicted by them are almost identical. The differences in amplitudes are caused by an assortment of analytical approximation in each individual



method, however, in this particular application it appears to produce accurate enough results for our purposes. The locked mode approach ( Harvey, 1981 ) could be used to construct the entire solution but this involves considerably more computing effort. We will use all these methods in this study, exploiting the particular advantages of each as appropriate.

### III. Modeling Strategy

Given a stack of 10 layers with 30 parameters, we would predict a synthetic match comparable to that displayed in Figure 3 by letting each parameter vary over 10 values. In this section we discuss a strategy of finding a good fitting model without wandering through this large parameter space. Two basic elements are necessary for this strategy to work, namely, broadband signals and the bag of seismological tools just discussed.

The strategy has four stages. First, we model a long-period version of the data assuming a single crustal layer. We find that the long-period  $P_n$  and  $S_n$  depend only on the upper-mantle velocities and the average properties of the crust. Five parameters are sufficient for initial modeling, that is two velocities in the mantle, two average velocities in the crust, and crustal thickness. These parameters are easily found by mostly timing and identifying particular phases,  $P_n$ ,  $S_n$ , etc. The next stage, we add some layers to the crust with the above constraint to model the fundamental Rayleigh wave.

In the third stage we model the broadband waveforms by adding some upper-mantle structure, which controls the short-period signals riding on top of  $P_n$  and  $S_n$ , etc. This is achieved by assuming the single layered crustal model and working with rays.

In the fourth stage, we compute complete synthetics using reflectivity for the layered stack and make some final adjustments by trial-and-error. A possible

fine-tuning operation, or fifth stage, would involve a formal waveform inversion. We will not perform such an inversion here but we will show a number of parameter sensitivity studies of the models near our preferred model.

#### a) Long Period Modeling

The data used in this section contain the WWSSN long-period response, and will be referred to as conventional long-period data. The beginning portion of these records are displayed at the top of the Figure 6, essentially the  $P_n$  and  $S_n$  wavetrains. Since a layer-over-half space model has proved effective in modeling the  $P_n$  portion of these records it is natural to examine the  $S_n$  portion assuming the same models and summing generalized rays. Possible models are give in Table 1 with corresponding synthetics displayed in Figure 6. The  $S_n$  phase arriving just after 140 seconds, as labeled in Figure 3, appears to be phase-shifted relative to  $P_n$ . This is the case, as is seen by examining the receiver functions describing the vertical (  $SZ$  ) and radial components (  $SR$  ) of motion for an incoming  $SV$  signal:

$$R_{SZ} = \frac{\eta_\alpha \eta_\beta}{\beta^2 R(p)}$$

$$R_{SR} = \frac{2\eta_\beta (\eta_\beta^2 - p^2)^{1/2}}{\beta^2 R(p)}$$

where

$$\eta_\alpha = \left( \frac{1}{\alpha^2} p^2 \right)^{1/2}$$

$$\eta_\beta = \left( \frac{1}{\beta^2} p^2 \right)^{1/2}$$

$$R(p) = (\eta_\beta^2 - p^2)^2 + 4p^2 \eta_\alpha \eta_\beta$$

and where  $\alpha$  is compressional velocity,  $\beta$  shear velocity,  $p$  ray parameter ( Helmberger, 1983 ). For  $p=1/\beta_n$ , the parameter appropriate for the  $S_n$  head wave, we obtain

$$R_{SZ} = -0.28i \text{ and } R_{SR} = -0.013 .$$

Thus, we expect  $S_n$  and  $aS_n$  to be much stronger on the vertical component than

on the radial component. Since these receiver functions are very sensitive to the station site conditions we would expect to see considerable variation in observed phase shifting from station to station.

TABLE 1
---------

Models 2 and 5 predict better fits to radial components, whereas models 6 and 7 do better on the vertical components. Since  $S_{\text{v}}$  is the strongest on the vertical component we chose model 7 as a preferred starting model, noting that phase shifts will be expected when we add more layers to the crust.

The best fitting model of the complete long-period seismograms, LPM, is given in Table 3 and contains five layers in the crust yielding the average crustal velocities found in Table 1, Model 7. The synthetic comparison of LPM is given in Figure 7. These synthetics were computed by summing 10 modes and assuming a one-second triangle source function. These synthetics are aligned in absolute time except the tangential component which is shifted 4.5 second to the left, implying a slightly faster  $SH$  velocity than  $SV$  velocity. Several dozen models were investigated but this particular model explains the timing of most of the phases the best. Note that  $S_{\text{h}}$  ( $SH$ ) is nearly nodal at HRV and, therefore, any source complexity or errors in mechanism produce strong changes in the synthetics. For this reason we have concentrated our efforts in fitting the more stable ( $P-SV$ ) system where the source can be assumed known.

#### b) Broadband Modeling

The source function was assumed known in the previous section but as we move to shorter periods we must be more concerned about source complexity as

mentioned in the introduction. We will discuss time history sensitivity later, but in this section we have assumed an asperity type model consisting of three different trapezoids in which the  $\delta t$ s are ( 0.4, 0.05, 0.25 ), ( 0.2, 0.15, 0.15 ), and ( 0.08, 0.31, 0.23 ), after Somerville et. al ( 1989 ). The broadband synthetics displayed in Figure 8 are appropriate for the long-period model, LPM. The overall fit is promising but lacks the shorter-period signals arriving on top of  $S_n$  and  $aS_n$ . To model these we return to summing generalized rays. Figure 9 gives the comparison of synthetics of the preferred model short-period model, SPM, ( Table 3, Figure 11 ), to the waveform data. The model was derived by adding some shallow mantle structure.

TABLE 2
---------

The shear velocity gradient at the top of the mantle has a strong effect on the  $S_n$  and  $aS_n$  behavior as displayed in Figure 10. The models used in constructing these synthetics are given in Table 2. The blank boxes in Table 2 indicate that the layers have the same parameters as Model 209. Each model is different from Model 209 in one parameter, namely the shear velocity or thickness. The numbers on the left of Figure 10 are model names. We tried dozens of models with a crustal thickness of 40 km, and concluded that the crust should be thinner to match the gradients and appearances of waveforms of  $S_n$ . If we use a faster crust, Model 218, see Table 2, we can see the earlier arrivals of  $aP_nP$  group ( letter *a* on the radial component of the synthetics of model 218, Figure 10 ) and  $aP_nSP_nP$  group ( letter *b* ), and the  $aS_nSS_nS$  group ( letter *c* ) phase, and the  $S_n$  waveforms predictions are too early. Model 213, and 215 are similar to Model 209 except that the thicknesses of the second layer are 20 km and 5 km respectively.

Model 213 predicts smaller amplitudes of  $S_n$  and  $sS_n$  phases, and discordant waveforms of  $sS_n SS_n S$  group phases. Model 215 predicts a nice fit on the radial component of the  $S_{nL}$  wave, but the vertical component fit is not so good. The thickness of the second layer can also be estimated from the  $S_{nL}$  data. The shear velocity of third layer can be inferred from comparing the synthetics of models 209, and 211. Comparing the synthetics of the models 209 and 212, we can see that Model 209 is better. We also have tried other velocities for this layer, but 4.55 km/sec appears to be the best. Model 209 is the shear velocity model of the SPM, short period model, while the compressional velocities are obtained by modeling the broadband  $P_n$  data described below.

A similar sensitivity study of the  $P_{nL}$  waveform was applied and used to adjust the  $P$ -velocity gradient while holding the shear velocity structure fixed. The best fitting short period model, SPM, found in this fashion is given in Table 3. Note that the lower portion of this model can not be resolved by this data and therefore we have simply adopted a model extended at constant compressional and shear velocities. The appearance of  $S_n$  synthetic waveforms of Mode summation Method suggests that this constant velocity layer may not have a shear velocity as high as 4.775 km/sec in a layer of thickness of at least 90 km.

### c) Fine-Tuning

In order to fit the surface waves better, we combine the long-period model and the short period model and arrive at the best model, MPM, see Figure 11, and Table 3. At this step, we fix the gradient at the top of the mantle and make some adjustments in the five-layered crustal model discussed earlier. The normal mode method was applied here since the fundamental Rayleigh waveform is the sensitive to the crustal velocity gradient.

TABLE 3

Figure 12 displays the long-period data along with the synthetics of three models, LPM, MPM, and SPM. The second, third and fourth traces of each group are the synthetics of model MPM, SPM and LPM respectively. Models LPM and MPM predict a reasonable fit to the fundamental Rayleigh waveforms, and models SPM and MPM predict a good fit to the early portion of  $S_{\text{SH}}$  waveforms.

As a final check, we used the reflectivity method to construct synthetics for the model MPM. The synthetic comparisons are given in Figure 13. The first 100 seconds of the synthetics fit the data well. In this calculation, we used a slowness window of 0.0-0.4 and a frequency band 0.004-4 Hz, assuming an exponential decay factor of 50 (  $Q_p$  8600, and  $Q_s$  6200 ).

#### IV. Source Effects

Thus far, we have assumed that the earthquake source parameters were well determined by other studies, namely that the strike, dip and rake angles are roughly  $323^\circ$ ,  $65^\circ$  and  $78^\circ$  respectively. The source depth was estimated by regional  $P_{\text{SH}}$  and teleseismic depth phases to be near 28 km ( Somerville et al., 1989; North et al., 1989 ). The source time history is not so well known nor are the rupture properties. The latter become important for regional phases, especially at short periods.

In this section, we will discuss what can be inferred from these single station regional broadband records if we know the velocity structure of the path. Assuming that our velocity model is correct; we now perturb the above source parameters and test the sensitivity of the broadband waveforms. Because of the amplitude difference between the weak  $P_{\text{SH}}$  waves relative to the surface waves, we

have displayed these sensitivity results in two sections, namely  $P_{nl}$  and  $S_{nl}$  together and a separate scale for the larger  $S_{nl}$  and surface waves.

In Figure 14 we display the sensitivity of the strike, dip and rake angles, while holding the other two parameters fixed at the original values. Varying the strike appears to change the overall amplitude and the ratio without affecting the ratio of  $P_{nl}$  to  $S_{nl}$ . The ratio of  $P_n$  to  $PL$  drops somewhat for strikes less than  $323^\circ$  and does not match the observation as well. A similar feature occurs when the dip angle falls below  $55^\circ$ . The original dip looks the best. Varying the rake produces the most interesting results where we see a change in the  $aS_n$  waveshape, becoming sharper for pure thrust angles. The radial synthetics for the  $\lambda=88^\circ$  looks the best, as determined by overlay, whereas the vertical fits  $\lambda=78^\circ$  are slightly better in terms of  $P_{nl} - S_{nl}$  amplitude ratio.

Figure 15 displays the long-period WWSSN data along with the synthetics of different source mechanisms. The source mechanisms do not have much effect on the surface waveforms, but do effect the amplitudes. A smaller rake or a smaller dip appears to fit the Love waveform data better than the original orientation. Note that  $S$  (  $SH$  ) is near a node and, thus, is susceptible to nonplanar fault effects. Since this event is known to contain at least two strong asperities it is possible that they have slightly different orientations and this could cause the above distortant behavior. One of the reasons for concentrating on the  $P-SV$  system is the insensitivity to source descriptions relative to the unknown details needed to study  $SH$  as mentioned earlier.

Figure 16 shows the source depth effects on the  $P_{nl}$  and  $S_{nl}$  waveforms. The absolute travel time of  $P_n$  decreases with the depth as expected, as well as the time separation between  $P_n$  and  $aP_n$ . The  $S_{nl}$  wavetrain does not seem to change shape as much as one might have expected. The source depth should be not difficult to determine if the waveforms of the  $P_{nl}$  and  $S_{nl}$  waves are used for a well

calibrated path. The synthetics for a depth of 28 km fit the data the best, which should be of no surprise. Clearly, the depth constraint is the most important of all the assumptions about source properties with respect to modeling. We could have easily adjusted the crustal thickness or velocities to compensate  $\pm P_n$  times, etc.

Source time history sensitivity is displayed in Figure 17 where various possible time histories are given on the right. These time histories originate from different data sets from this event, and are all idealizations of complicated phenomena. The simplest ones were derived from modeling teleseismic short and long-period P-waves as discussed earlier, namely ( b ) and ( c ). Case ( b ) was used in the long-period modeling where one usually uses a relatively coarse time sampling and thus a simple triangle is sufficient. The more detailed information about source complexity comes from the strong motion data. Far-field approximations of the time histories depend on direction with two possible sources ( a ) and ( e ) proposed by Somerville and Helmberger ( 1990 ) with case ( e ) preferred. Case ( d ) was used in the broadband modeling discussed earlier which is an analytical approximation to case ( a ) ( Somerville et al. 1989 ). Case ( f ), ( g ) and ( h ) are still more approximations. An overlay comparison of source function ( e ) with the data appears to be the best although there is not very much difference between the synthetics.

The point of this section was not necessarily to help constrain this particular earthquake but to display the source resolving power once these Green's functions are established. This model and associated Green's functions can be used to study other events roughly along this path such as older historic events recorded at Weston, etc.

## V. Discussions and Conclusions

Our velocity structure along the path from Quebec to Harvard is distinctly



slower than proposed in other studies. For example, the shear velocity of the lid of the model, 4.6-4.7 km/sec, is slower than that of either the ATL model, 4.75 km/sec (Grand and Helmberger, 1984a), or the SNA model, 4.8 km/sec (Grand and Helmberger, 1984b). In a tomographic inversion study for shear velocity beneath the North American Plate, Grand (1987) concluded that the upper 140 km of the crust and mantle of this region was very fast although he did find a major velocity boundary along this path at greater depths. It seems that the data we used do not agree with this fast structure. This may be due to velocity anisotropy. SNA model is a  $SH$  velocity model, the model we derived is a  $SV$  model. The travel times of  $S_n$  and  $\alpha S_n$  waves of the synthetics of model MPM match those of the  $SH$  data, see Figure 3 although  $S_n$  ( $SH$ ) is nodal. The maximum group velocity of Love waves of model MPM is 0.8 percent slower than that of the data, suggesting crustal anisotropy, although small. Another explanation may arise from epicentral distance uncertainty, since the velocities are sensitive to the distance and origin time. For example, if the epicentral distance were 640 km instead of 625 km, the model would be 2 percent slower than the SNA model (Figure 18 and Table 4). Note that waveform fits are comparable to those found earlier. Errors in distances up to 15 km or more are possible, if the location is determined by teleseismic means. For instance, the distance between the location given by USGS and that given by HRV is 12 km for this event. However, in this particular case, the location, based on close-in aftershock data recorded by the Geological Survey of Canada (North et al., 1989) is probably accurate to 5 km. Finally, perhaps this path to Harvard, which runs along an old suture zone, is indeed slow and this slowness is caused by a regional anomaly (Sykes, 1978).

TABLE 4
---------

In summary, we presented a strategy for modeling broadband records at regional distances. The basic procedure consists of breaking the seismograms into segments where the waveforms of each segment prove sensitive to a particular portion of the waveguide. Three divisions appear to be the most useful, namely, a ) the  $P_{nl}$  segment containing  $P_n$ ,  $pP_n$ ,  $aP_n$ ,  $P_mP$ , its multiples and  $P$ -coupled  $PL$ ; b ) the  $S_{nl}$  segment containing  $S_n$ ,  $aS_n$ ,  $S_mS$ , its multiples and  $S$ -coupled  $PL$ ; c ) the fundamental Rayleigh wave segment.

(a)  $P_{nl}$  wavetrain

The long-period component of the  $P_{nl}$  wavetrain is controlled by the crustal thickness, the average crustal velocities, and the compressional velocity of the mantle. Its shorter period contributions are influenced by the sharpness of the Moho transition, the fine structure at the top of the mantle, compressional velocity gradients, etc.

( b )  $S_{nl}$  wavetrain

This segment is probably the most difficult to appreciate. It has been studied less, and produces the strongest short-period arrivals, usually called the  $L$ , phase. The beginning portion of this wavetrain consists of  $S_n$ , and  $aS_n$ , as identified in this study, and can be used to study the shear velocity properties of the top of the mantle. Further into this wavetrain, one finds stronger arrivals associated with multiple-bounce  $S_mS$  and probably  $S$ -coupled  $PL$  from the uppermost surface layer. These phases are included in the synthetics of both methods, the normal mode method and reflectivity, but have not been subdivided into individual ray groups for special study. The longer period  $S$ -coupled  $PL$  waves trapped in the crustal layer over a mantle waveguide have been studied

extensively, and are responsible for contaminating teleseismic *SV* body waves to the extent that they are rarely used in source studies. The laterally varying surface waveguide consisting of the upper few kilometers of the Earth is likely to produce similar types of semi-trapped shorter period *P* waves. Such waves are easily identified in local records ( Dreger and Helmberger, 1990 ), but have not been investigated at these ranges.

### ( c ) Fundamental Rayleigh wavetrain

The fundamental Rayleigh waves are controlled by the shear velocity structure of the crust at these ranges and are not particularly sensitive to the mantle parameters. This statement is generally true for the fundamental Love waves as well ( Zhao et al., 1989 ). Normal surface wave modes are easily generated for possible models and fitting this portion of the record proved relatively easy.

In conclusion, this study demonstrates that broadband regional phases can be modeled. This study, thus, has several implications with respect to source discrimination and with respect to exploration of the lithosphere. Earlier studies have established the ease of modeling the beginning portion of a long period record in terms of  $P_n$ ,  $pP_n$ , and  $aP_n$ ; i. e. a layer over halfspace. Apparently, the  $S_n$ ,  $pS_n$ , and  $aS_n$  window is also easily modeled on the vertical component. The phases can be seen at low magnitudes where teleseismic signals are no longer recorded above the noise. For example, the Saguenay earthquake produced only a few high quality teleseismic waveforms. Thus,  $S_n$  and  $P_n$  on standard long period WWSSN records can probably be used to study events down to magnitude 4.5 since  $P_n$ 's have proved useful down to magnitude 5 and  $S_n$ 's are considerably stronger. In addition, the strongest short period signals are related in timing with the long period arrivals. One can use the latter as a guide in constructing broadband models ( many layers ) and scattering models for still shorter periods.

Presently, it has proven quite difficult to discriminate small explosions

from small earthquakes as well as the  $m_b/M_s$  ratio does at larger magnitudes ( see Taylor et al., 1989 ). One excellent method of establishing the identification of an event is by depth and, therefore, by depth phases. Calibrating crustal models and the development of regional Green's functions addresses this problem.

Exploration of the continental lithosphere in interesting regions has proven difficult. Molnar ( 1989 ) and his colleagues have spent a great deal of effort studying the collision zone between the Indian and Asian plates. The absolute velocities of P and S at the top of the mantle is one of the key factors in establishing temperatures there. Furthermore, velocity gradients can probably establish whether heating is taking place from the top-down or vice versa ( Zhao et al. 1989 ). Thus, broadband modeling of regional data from southern platforms of the Soviet Union and transition zones of western China can provide some key information and will be presented in future reports.

#### Acknowledgments

We would like to thank David G. Harkrider, Mrinal Sen, Laura Jones, Bradley Woods, Larry Burdick and Hiroo Kanamori for their help with the computer codes and their reviews. We would like to thank Adam Dziewonski for setting-up this excellent recording system. We would, also, like to thank Paul Spudich, George Choy and several official reviewers for their comments. This research was supported by the Advanced Research Projects Agency of the Department of Defense and was monitored by the Air Force Geophysics Laboratory under the contract F19628-89K-0028. Contribution No. 4839, Division of Geological and Planetary Sciences, California Institute of Technology, Pasadena, California.

## REFERENCES

- Aki, K. and P. G. Richards, 1980. *Quantitative Seismology, Theory and Methods*, W. H. Freeman and Company, San Francisco.
- Apsel, R. J. and J. E. Luco, 1983. On the green's functions for a layered halfspace, *Bull. Seism. Soc. Am.*, **73**, 931-952.
- Dreger, D. and D. V. Helmberger, 1990. Broad-band modeling of local earthquakes, submitted to *Bull. Seism. Soc. Am.* .
- Grand, S. P., 1987. Tomographic inversion for shear velocity beneath the North American plate, *J. Geophys. Res.*, **92**, 14065-14090.
- Grand, S. P., and D. V. Helmberger, 1984a. Upper mantle shear structure beneath the northwest Atlantic Ocean, *J. Geophys. Res.*, **89**, 11465-11475.
- Grand, S. P., and D. V. Helmberger, 1984b. Upper mantle shear structure of North America, *Geophys. J. R. astr. Soc.*, **76**, 399-438.
- Harkrider, D. G., 1964. Surface waves in multilayered elastic media, I. Rayleigh and Love waves from buried sources in a multilayered elastic half-space, *Bull. Seism. Soc. Am.*, **54**, 627-679.
- Harvey, D., 1981. Seismogram synthesis using normal mode superposition: The locked mode approximation, *Geophys. J. R. Astr. Soc.*, **66**, 37-61.
- Helmberger, D. V., 1983. Theory and application of synthetic seismograms, in *Proceedings of the International School of Physics << Enrico Fermi >>, Course LXXXV, Earthquakes: Observation, Theory and Interpretation*, edited by Kanamori, H. and E. Boschi, North-Holland Publishing Company.
- Helmberger, D. V. and G. R. Engen, 1980. Modeling the long - period body waves from shallow earthquakes at regional distances, *Bull. Seism. Soc. Am.* , **70**, 1699-1714.
- Helmberger, D. V. and D. G. Harkrider, 1978. Modeling earthquakes with generalized ray theory, in *Proceedings of IUTAM Symposium: Modern Problems in Elastic Wave Propagation*, edited by J. Miklowitz, and J. Achenback, New York, N. Y.

- Molnar, P., 1989. The geologic evolution of the Tibetan Plateau, *American Scientist*, **77**, 350-360.
- North, R. G., R. J. Wetmiller, Adams, J., F. M. Anglin, Hasegawa, H. S., M. Lamontagne, R. Du Berger, Seeber, L. and J. Armbruster, 1989. Preliminary results from the November 25, 1988 Saguenay ( Quebec ) earthquake, *Seism. Res. Let.* , **60**, 89-93.
- Somerville, P. G., and D. V. Helmberger, 1990. The effect of crustal structure on the attenuation of strong ground motion in eastern north America. Submitted to Fourth U. S. National Conference of Earthquake Engineering at Palm Springs, May 1990.
- Somerville, P. G., J. P. McLaren, Saikia, C. K. and D. V. Helmberger, 1989. The November 25, 1988 Saguenay, Quebec earthquake, submitted to *Bull. Seism. Soc. Am.* .
- Sykes, L. R., 1978. Intraplate seismicity, reactivation of preexisting zones of weakness, alkaline magmatism, and other tectonism postdating continental fragmentation, *Rev. Geophys. Space Phys.*, **16**, 621-688.
- Taylor, S. R., M. K. Denny, E. S. Vergino, and R. E. Glaser, 1989. Regional discrimination between NTS explosions and western U. S. earthquakes, *Bull. Seism. Soc. Am.*, **79**, 1142-1172.
- Wallace, T. C. and D. V. Helmberger, 1982. Determining source parameters of moderate-size earthquakes from regional waveforms, *Phys. Earth Planet. Inter.*, **30**, 185-196.
- Zhao L. - S., D. V. Helmberger, and Harkrider, D. G., 1989, Shear-velocity structure of the crust and upper mantle beneath Tibetan and Southeastern China, submitted to *Geophys. J. R. astr. Soc.* .

Table 1 models for Pnl waves

Model	1	2	3	4	5	6	7
$\alpha$	6.50	6.40	6.40	6.30	6.40	6.40	6.40
$\beta$	3.70	3.65	3.70	3.70	3.65	3.70	3.70
Thick	40.0	40.0	40.0	40.0	35.0	40.0	40.0
$\alpha$	8.10	8.20	8.20	8.20	8.20	8.20	8.20
$\beta$	4.70	4.70	4.70	4.70	4.70	4.65	4.68
Thick							

$\alpha$  is compressional velocity,  $\beta$  is shear velocity.

**Table 2. Models for sensitivity study of Pnl - Snl, figure 10 209**

MODEL	209	211	212	213	214	215	216	218
$\alpha$	6.23							6.4
$\beta$	3.6							3.7
thickness ( km )	35.0							35.0
$\alpha$	8.06			8.06		8.06		
$\beta$	4.6			4.6		4.6		
thickness ( km )	10.0			20.0		5.0		
$\alpha$	8.2	8.2			8.2		8.2	
$\beta$	4.7	4.65			4.7		4.7	
thickness ( km )	10.0	10.0			20.0		5.0	
$\alpha$	7.97		7.8					
$\beta$	4.55		4.45					
thickness ( km )								



**Table 3. Model comparison, SPM, LPM, and MPM**

LPM			SPM			MPM		
$\alpha$	$\beta$	Th	$\alpha$	$\beta$	Th	$\alpha$	$\beta$	Th
5.97	3.44	8.0	6.30	3.60	35.0	6.04	3.49	8.0
6.18	3.57	8.0				6.24	3.61	8.0
6.36	3.68	8.0				6.30	3.70	8.0
6.52	3.77	8.0				6.52	3.77	8.0
6.57	3.80	8.0				6.58	3.80	3.0
			7.90	4.60	10.0	7.90	4.60	10.0
8.20	4.68	40.0	8.10	4.70	10.0	8.10	4.70	10.0
8.36	4.775	65.0	8.20	4.55	90.0	8.20	4.55	90.0
8.27	4.723	35.0	8.27	4.723	35.0	8.27	4.723	35.0
8.13	4.64	45.0	8.13	4.64	45.0	8.13	4.64	45.0

**Table 4. Model comparison**

625 km			640 km		
$\alpha$	$\beta$	Th	$\alpha$	$\beta$	Th
6.04	3.49	8.0	6.26	3.56	8.0
6.24	3.61	8.0	6.45	3.67	8.0
6.30	3.70	8.0	6.59	3.75	8.0
6.52	3.77	8.0	6.71	3.82	8.0
6.58	3.80	3.0	6.71	3.82	3.0
7.90	4.60	10.0	8.10	4.70	10.0
8.10	4.70	10.0	8.35	4.80	10.0
8.20	4.55	90.0	8.40	4.65	90.0

## FIGURE CAPTIONS

Figure 1: The Broadband displacement data recorded by Harvard station ( HRV ) of the 25 November 1988 Saguenay earthquake. The first trace is vertical component, where upward is positive; second trace is radial component, positive southward; and the third trace is tangential component, positive eastward. The numbers on the right are the maximum amplitudes in *mm*. The instrument response is flat in velocity between 0.0027 Hz to 7 Hz. Integrating within this band produces the displacement records displayed.

Figure 2: The broadband data convoluted with the WWSSN long - period instrument response. These would be the real long period record with a gain of 2250. The three components are the vertical, radial and tangential. The letters on the left indicate the positive directions.

Figure 3: This figure displays the first hundred seconds of the broadband waveform data along with the synthetics generated by a flat-layered model found in this study. The main phases such as  $P_n$ ,  $sP_n$ , and PL,  $S_n$ , and  $sS_n$  are labeled.

Figure 4: Comparison of the radial components of the synthetics generated by Generalized Ray Method ( GRM ), " rays" in this figure, reflectivity, refl, and Mode Summation Method ( MSM ), modes. The numbers on the left are the distances of the three nearest traces. The left column is for the strike slip source; the middle for dip slip source; and the right for 45° dip slip source. The source function is a 0.2 0.2 0.2 trapezoid. The moment is  $10^{25}$  *dyne·cm*. The source depth is 8.0 km. The numbers on the right margin of each column are the amplitudes for the corresponding traces in centimeters. The parameters of the model are:  $\alpha=6.2\text{km/sec}$ ,  $\beta=3.5\text{km/sec}$ , with a 32 km thick crust; mantle velocities are  $\alpha=8.2\text{km/sec}$ ,  $\beta=4.5\text{km/sec}$ . Mode synthetics include 12 modes. The parameters used for reflectivity synthetics are: decay factor 50, slowness window ( 0.0-0.5 ), frequency band ( 0.0025-5 ) Hz,  $Q_\alpha(80000)$  and  $Q_\beta(40000)$ .

Figure 5: Comparison of the vertical components of the synthetics generated by GRM method, reflectivity and MSM methods. The left is for strike slip source; the middle for dip slip source; and the right for 45° dip slip source.

Figure 6: Comparison of the long period  $P_{nl}$  and  $S_{nl}$  data and the synthetics generated for different models. The upper group of traces are vertical components, the lower are radial components. The models used are given in Table 1. The numbers on the left are the model numbers. The source function is a triangle (1,0,1).

Figure 7: Comparison of the synthetics of the long period model, LPM, and the long period data. Ten modes were used in constructing synthetics for model MPM. The tangential component of the synthetics has been shifted to the left by 4.5 seconds. The upper traces are the observed waveforms. The observations and synthetics are on the same scale.

Figure 8: Comparison of the broadband data and the synthetics of the long period model, LPM. Eight modes were used to make these synthetics. The tangential component of the synthetics has been shifted to the left by 1.5 seconds.

Figure 9: Comparison of the broadband data and the synthetics of the final short period model, SPM. The synthetics were generated with the GRM.

Figure 10: Sensitivity study of the waveforms of  $S_{nl}$  and  $P_{nl}$  waves to model parameters. The numbers on the left are model numbers indicated in Table 2. The letters *a*, *b* and *c* on the bottom radial component of the synthetics indicate  $sP_m P$ ,  $sP_m SP_m P$ , and  $sS_m SS_m S$  groups of phases respectively.

Figure 11: The upper 150 km of the models: long period model, LPM; short period model, SPM and final model, MPM. The bottom portion of SPM is the same as that of MPM.

Figure 12: Comparison of the synthetics of the different models with the long period data. The top traces are observed; the second is the synthetics of the final model, MPM; the third is that of the short period model, SPM; and the

fourth is that of the long period model, LPM. A 1.5 second time shift to the left was applied to all the tangential components of the synthetics.

Figure 13: Comparison of the whole broadband data with the synthetics of model MPM. The synthetics were generated using the reflectivity method. The tangential component of the synthetic was shifted 1.5 seconds to the left.

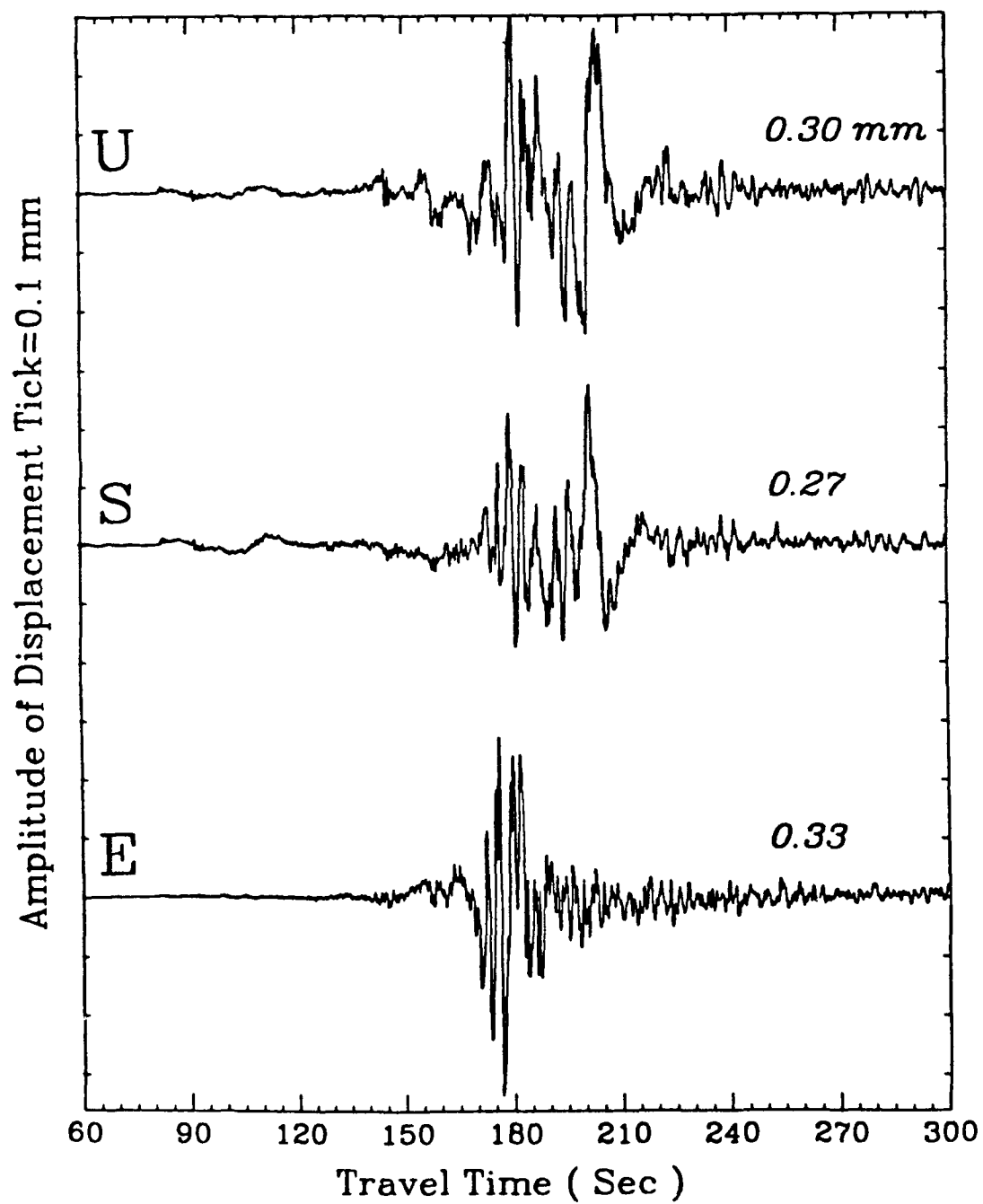
Figure 14: Sensitivity analysis of waveform changes do to variations in strike with  $\delta=65^\circ$ ,  $\lambda=78^\circ$  fixed, left column; in dip with  $\theta=323^\circ$ ,  $\lambda=78^\circ$  fixed, middle column; and in rake with  $\theta=323^\circ$ ,  $\delta=65^\circ$  fixed, right column. The Green's functions used here are the same as those in Figure 3 and 13.

Figure 15: Sensitivity study of surface waveform data and amplitude to variations in strike, dip and rake. The MSM technique was used to generate these synthetics. The vertical components are given on the left and the tangential components on the right holding the other parameters fixed as in Figure 14.

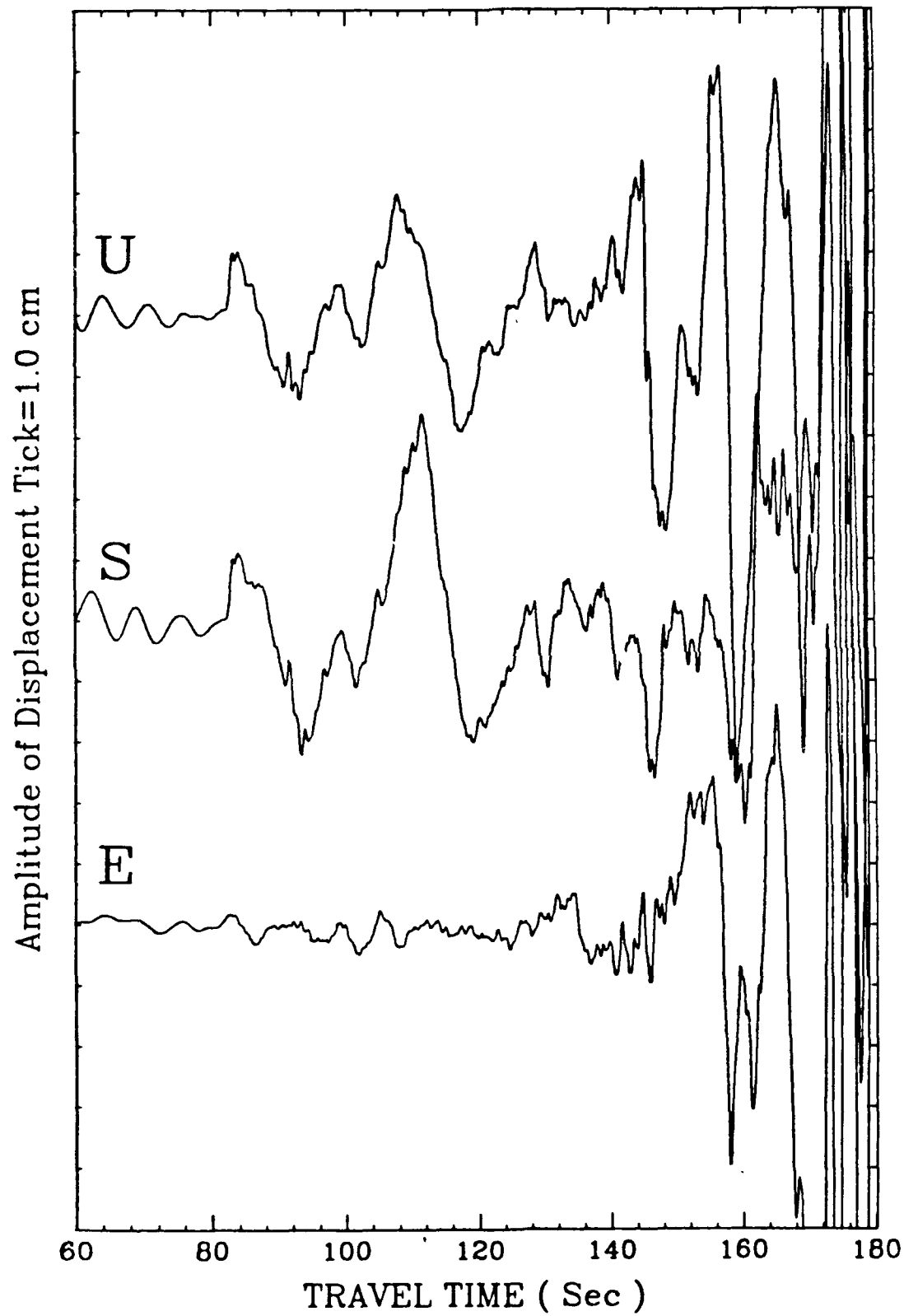
Figure 16: Source depth sensitivity analysis where the upper four traces display the vertical components, and the lower traces display the radial components. The first trace of each set is the broadband data followed by synthetics for various depths.

Figure 17: Sensitivity analysis of the waveform effects do to variations in source history. The left column are the vertical components of the data and synthetics. The middle two are radial and tangential components. The column on the right indicates the various source histories used with the corresponding synthetics on the left. These are reflectivity synthetics.

Figure 18: Comparison of the synthetics generated from model MPM, and the model for 640 km ( Table 4 ) with the broadband data displayed as the middle trace of each set.



**Figure 1**



**Figure 2**  
79

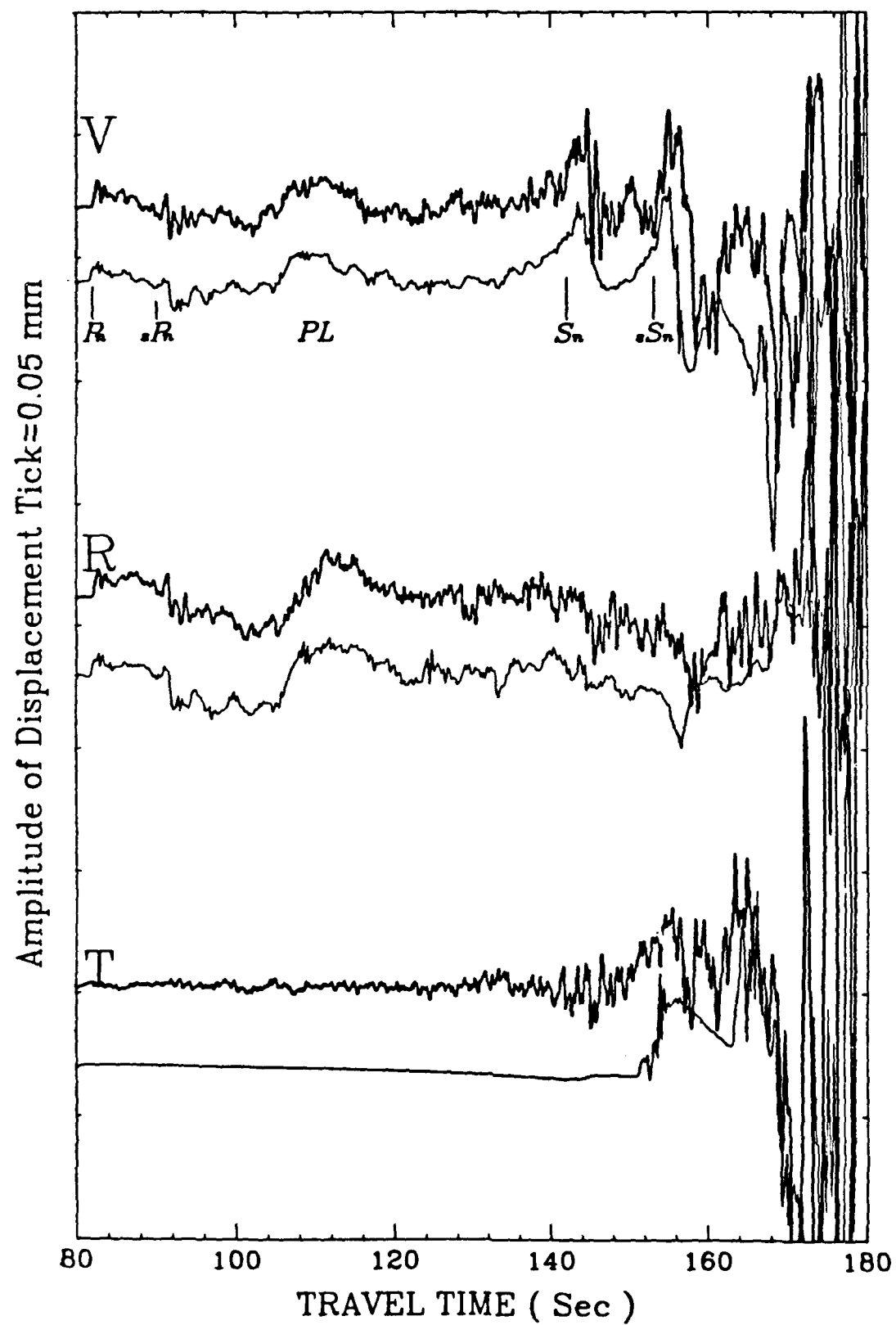


**Figure 3**



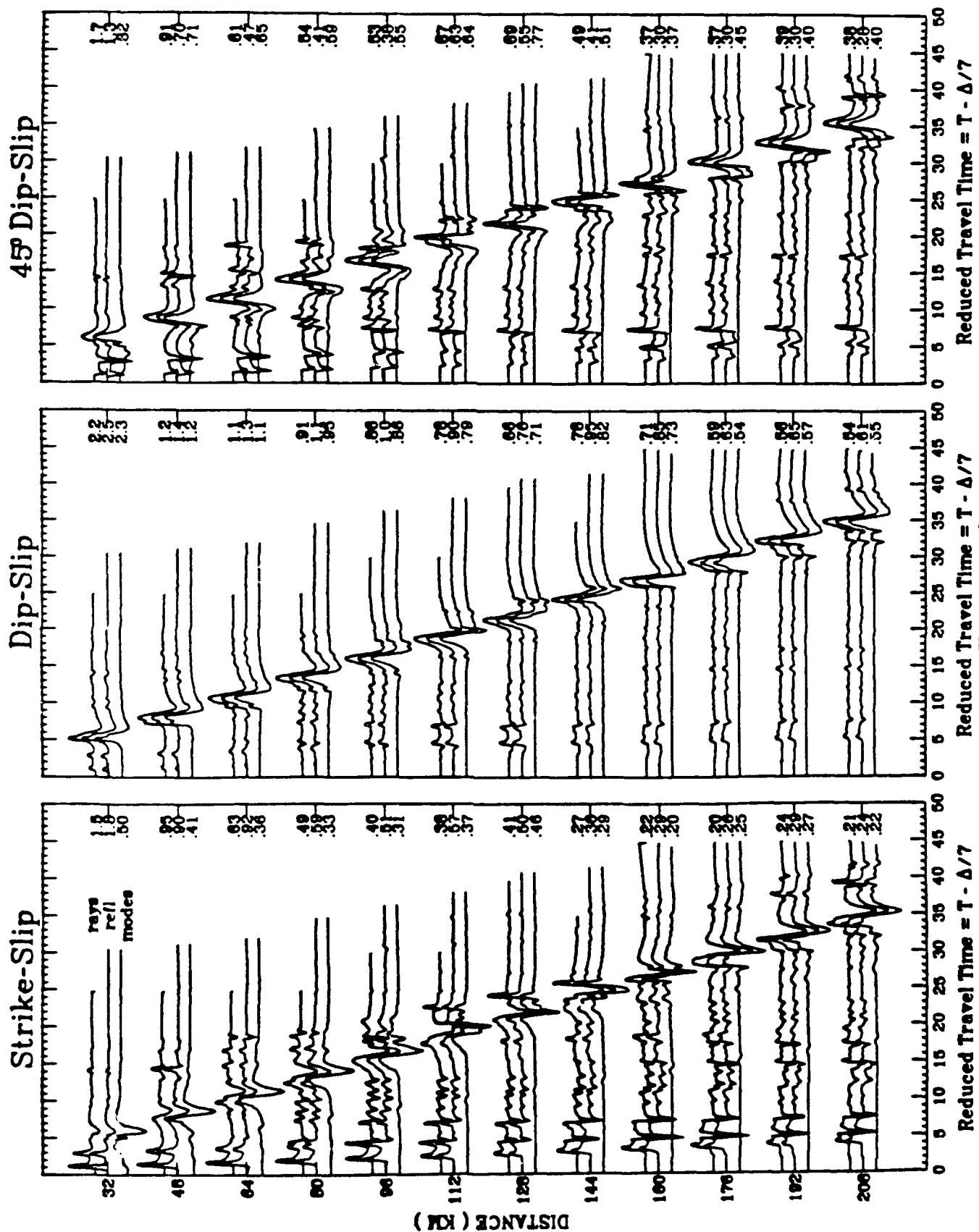


**Figure 4**

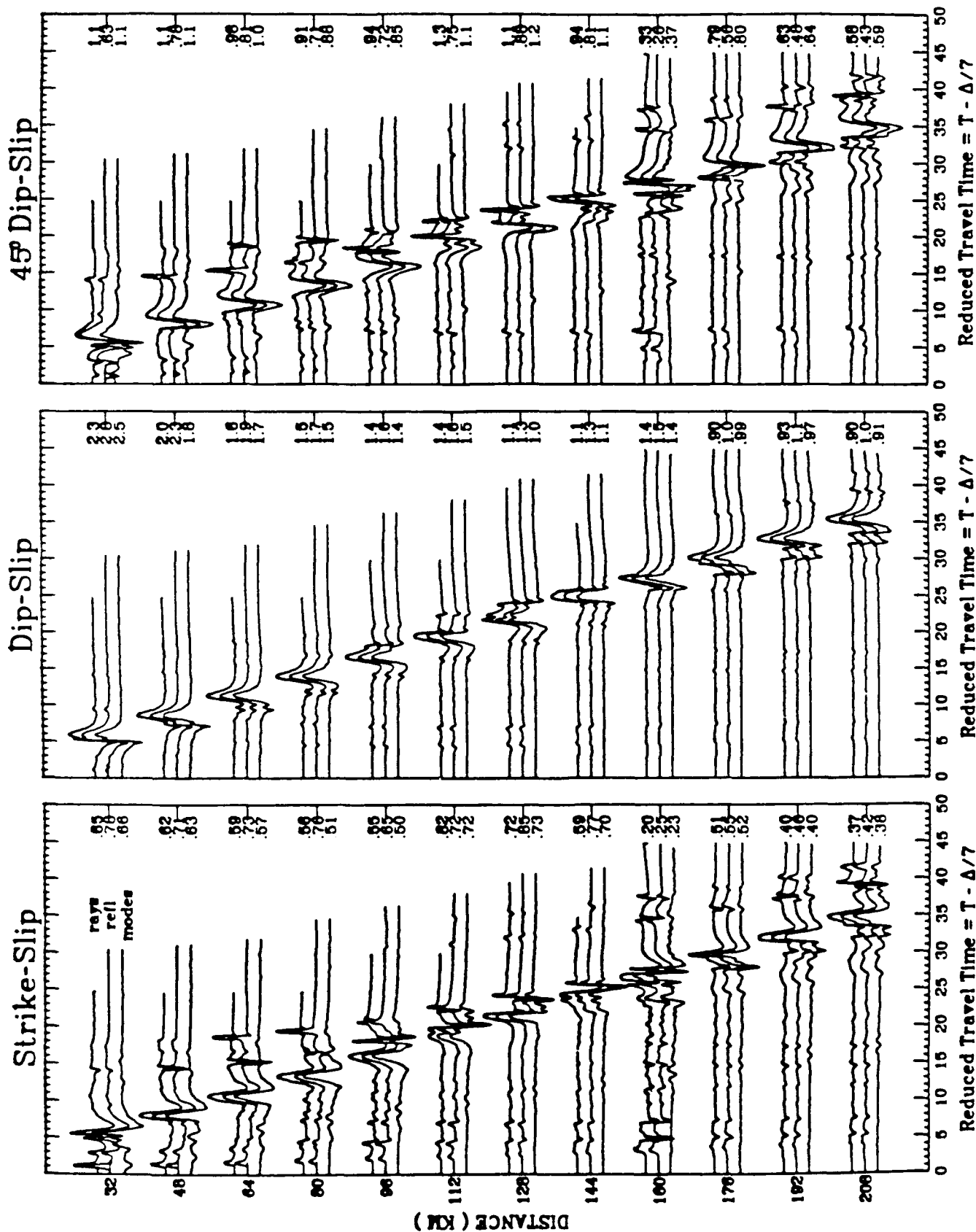


Figure 5

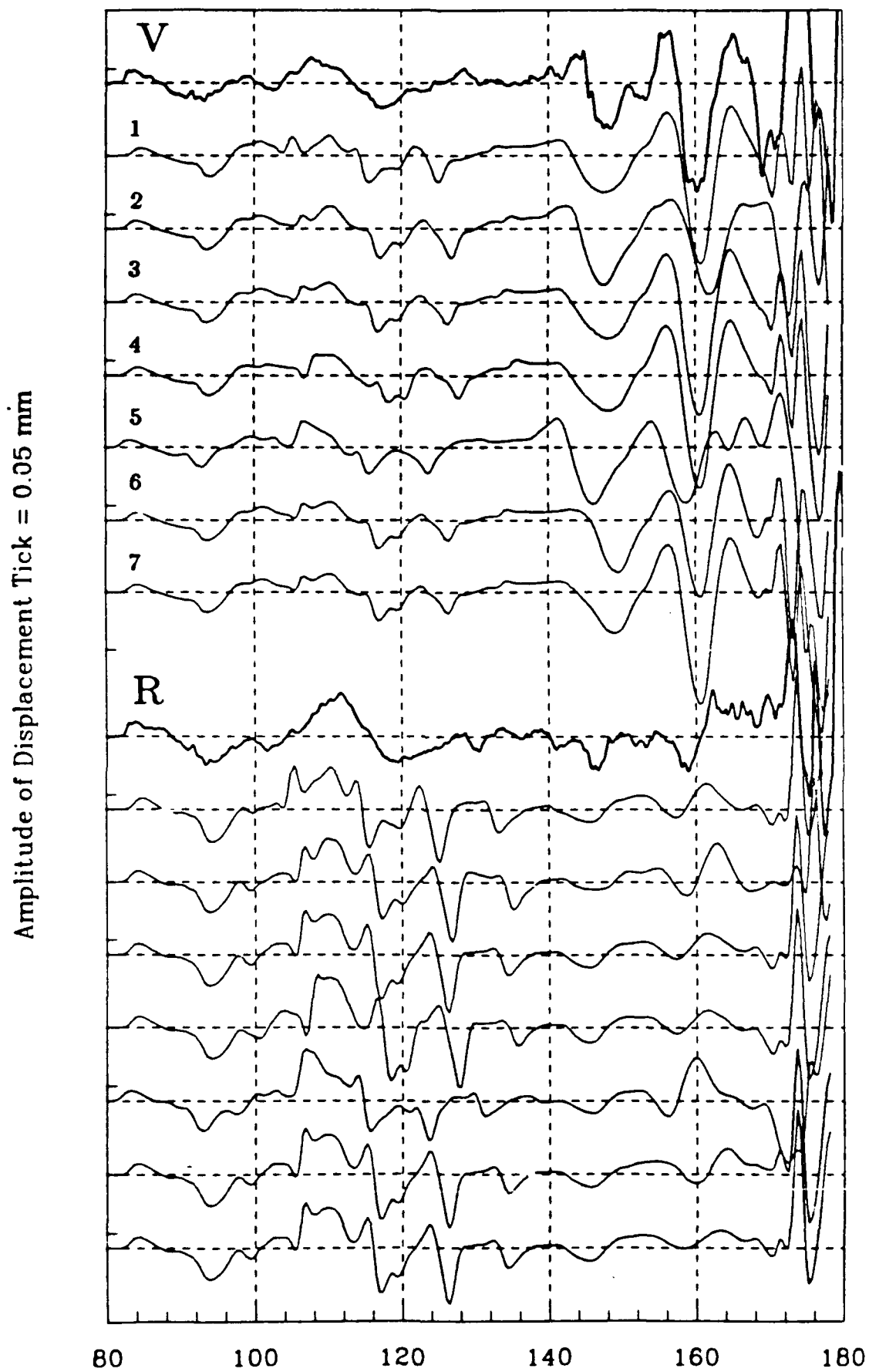


Figure 6

AMPLITUDE Tick = 0.25 mm

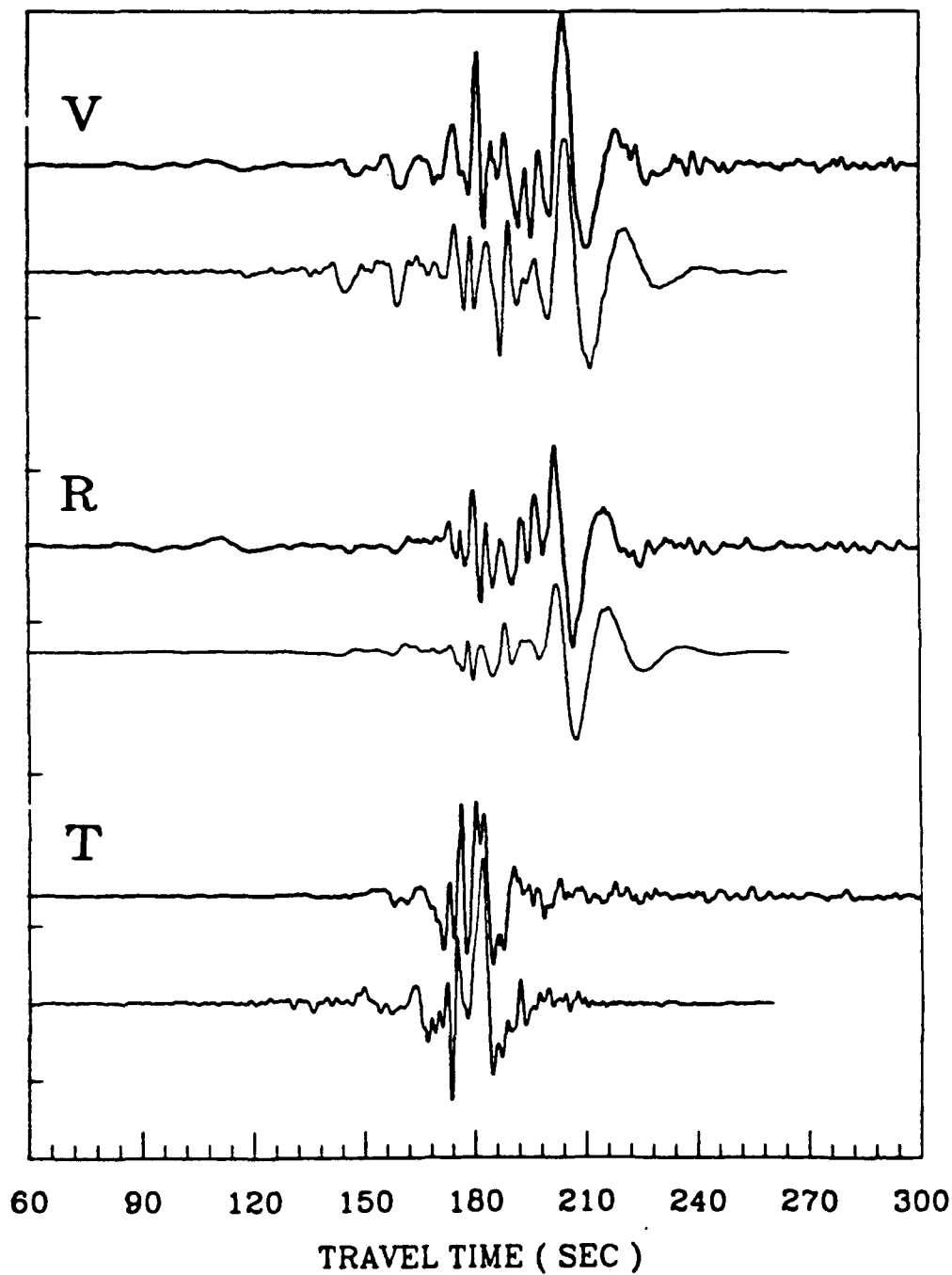


Figure 7

AMPLITUDE Tick = 0.3 mm.

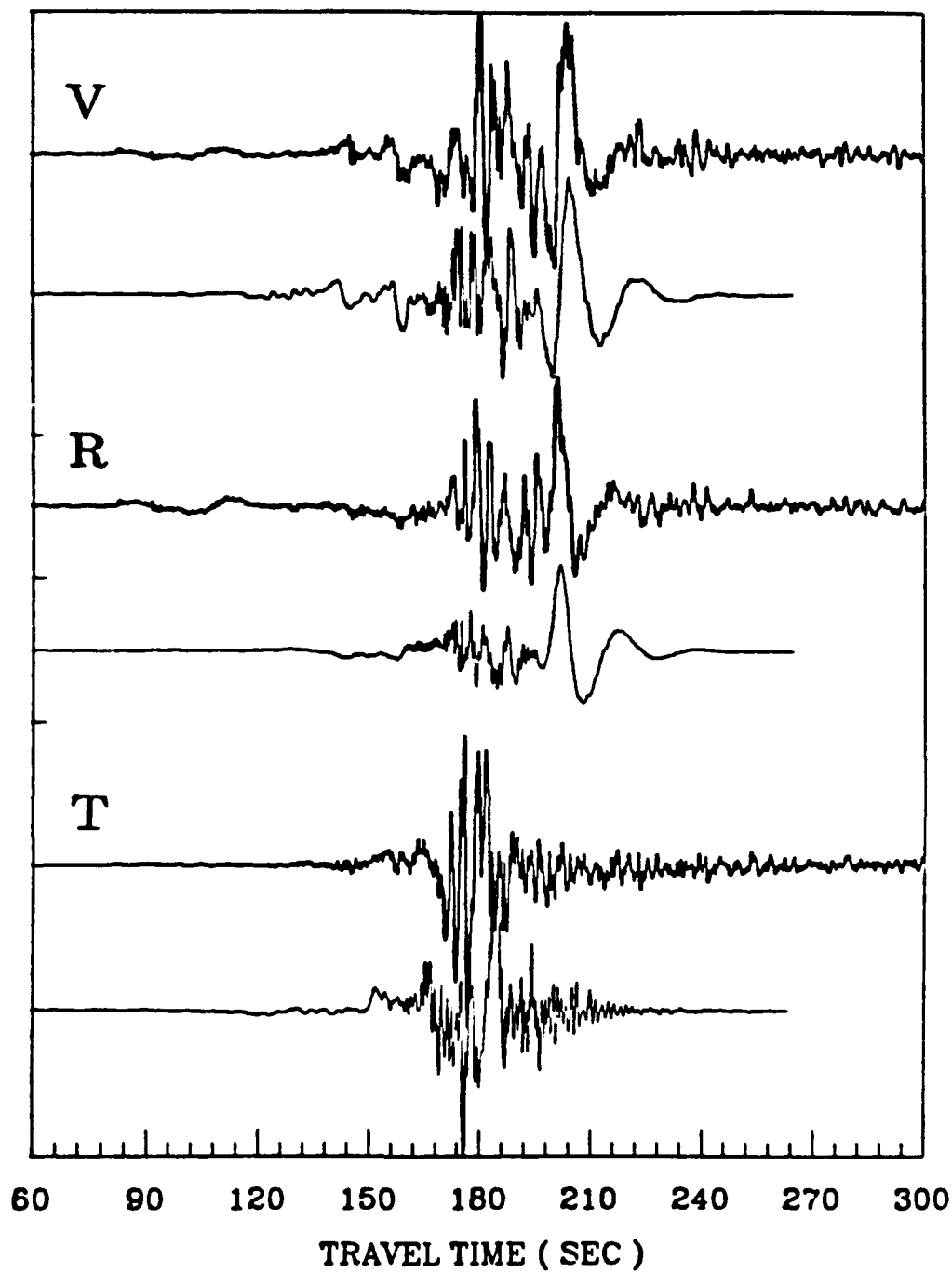


Figure 8

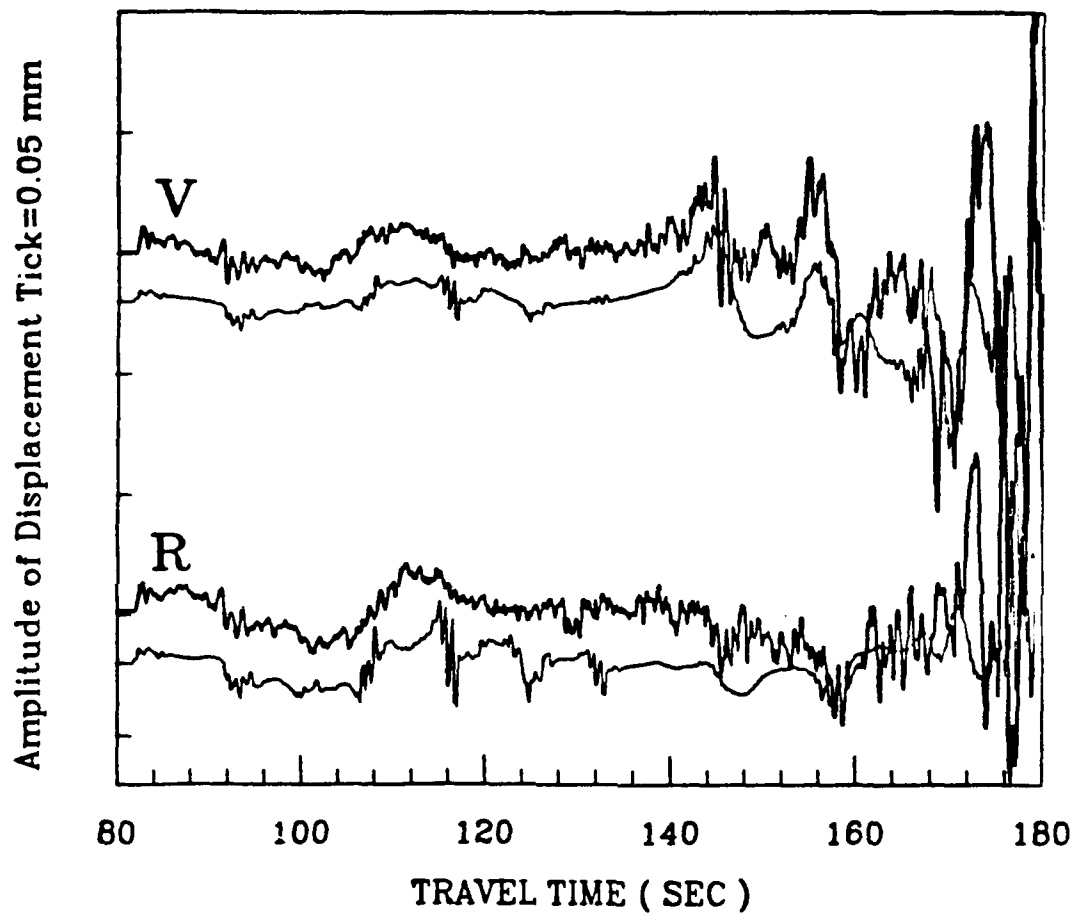


Figure 9

AMPLITUDE OF DISPLACEMENT Tick = 0.1 mm

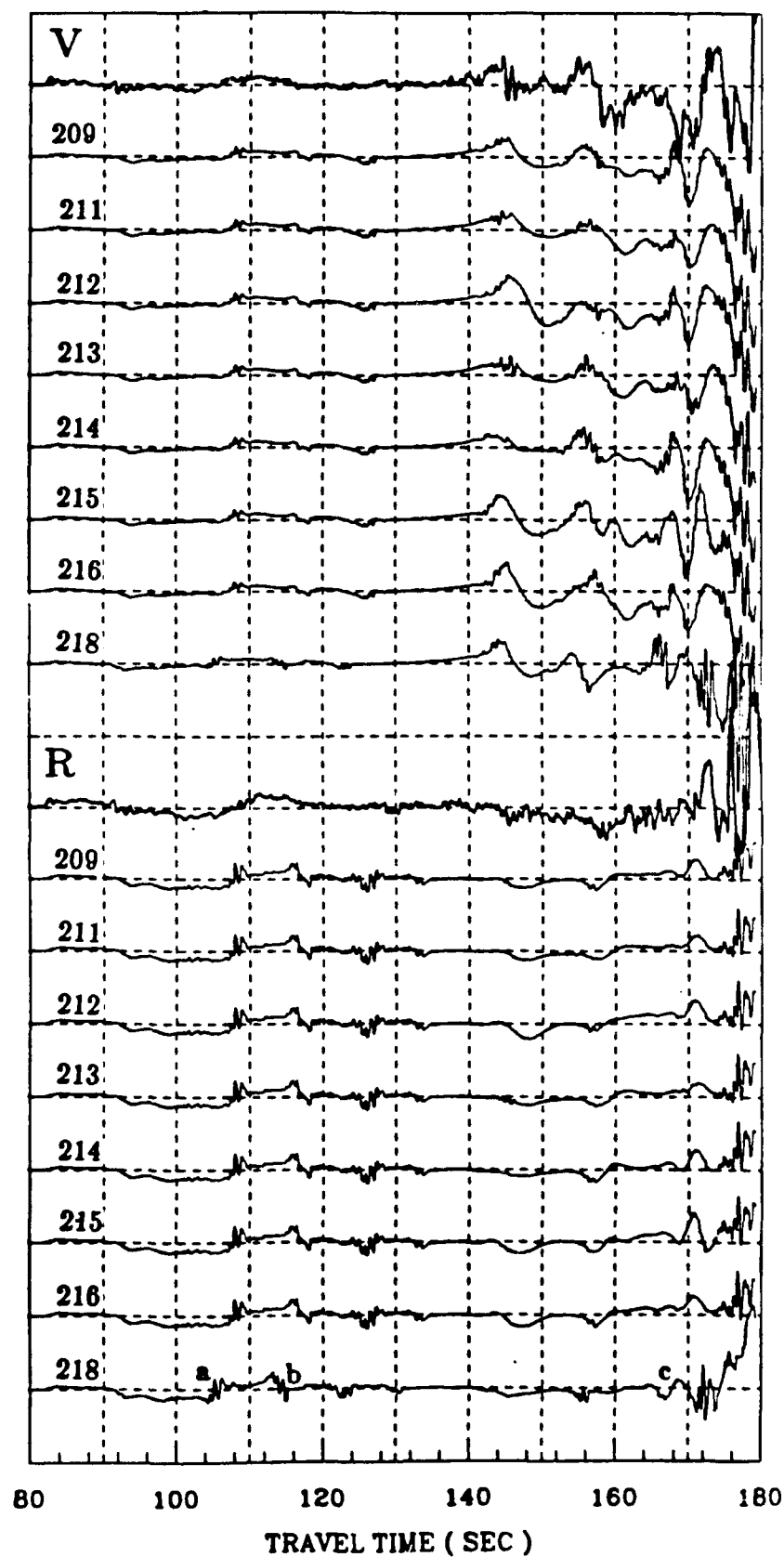
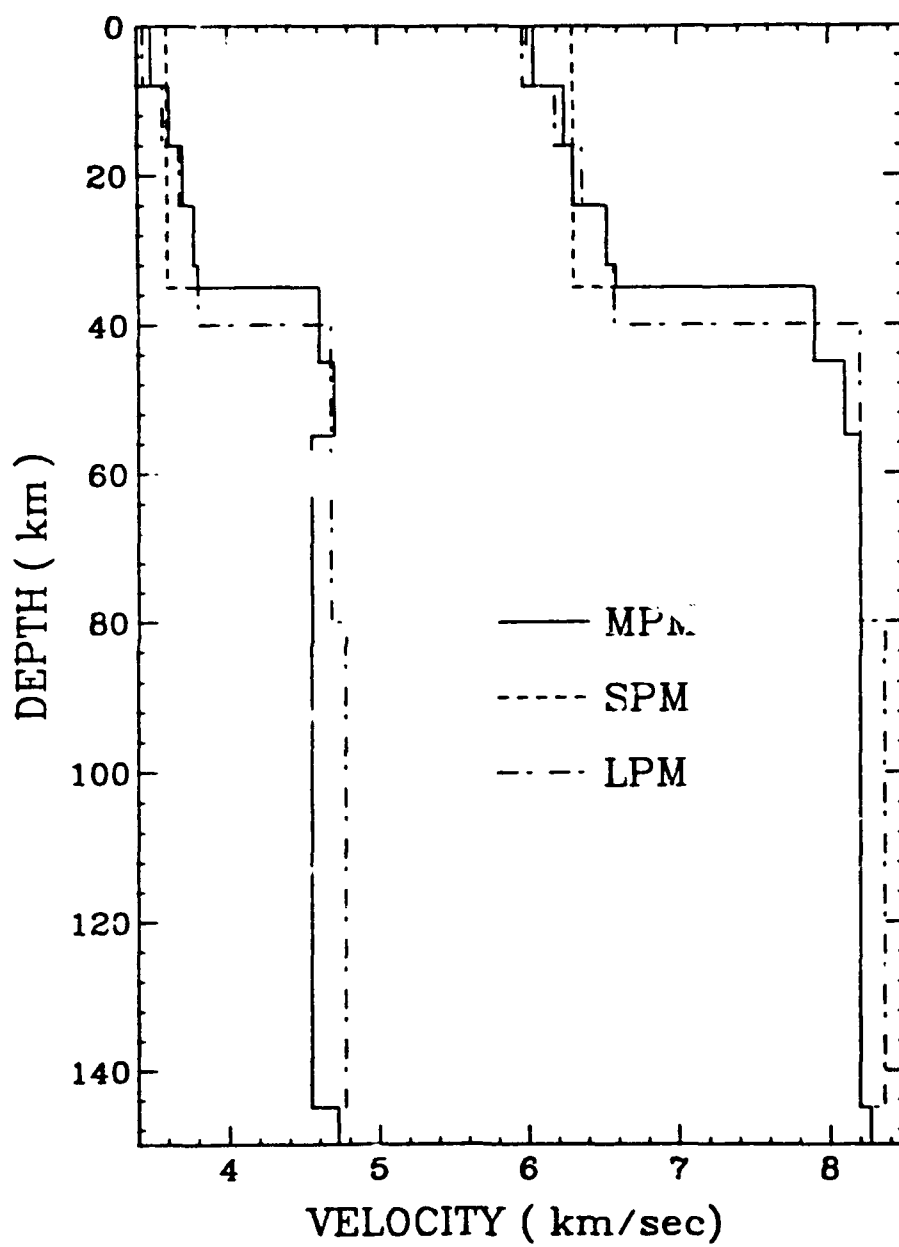
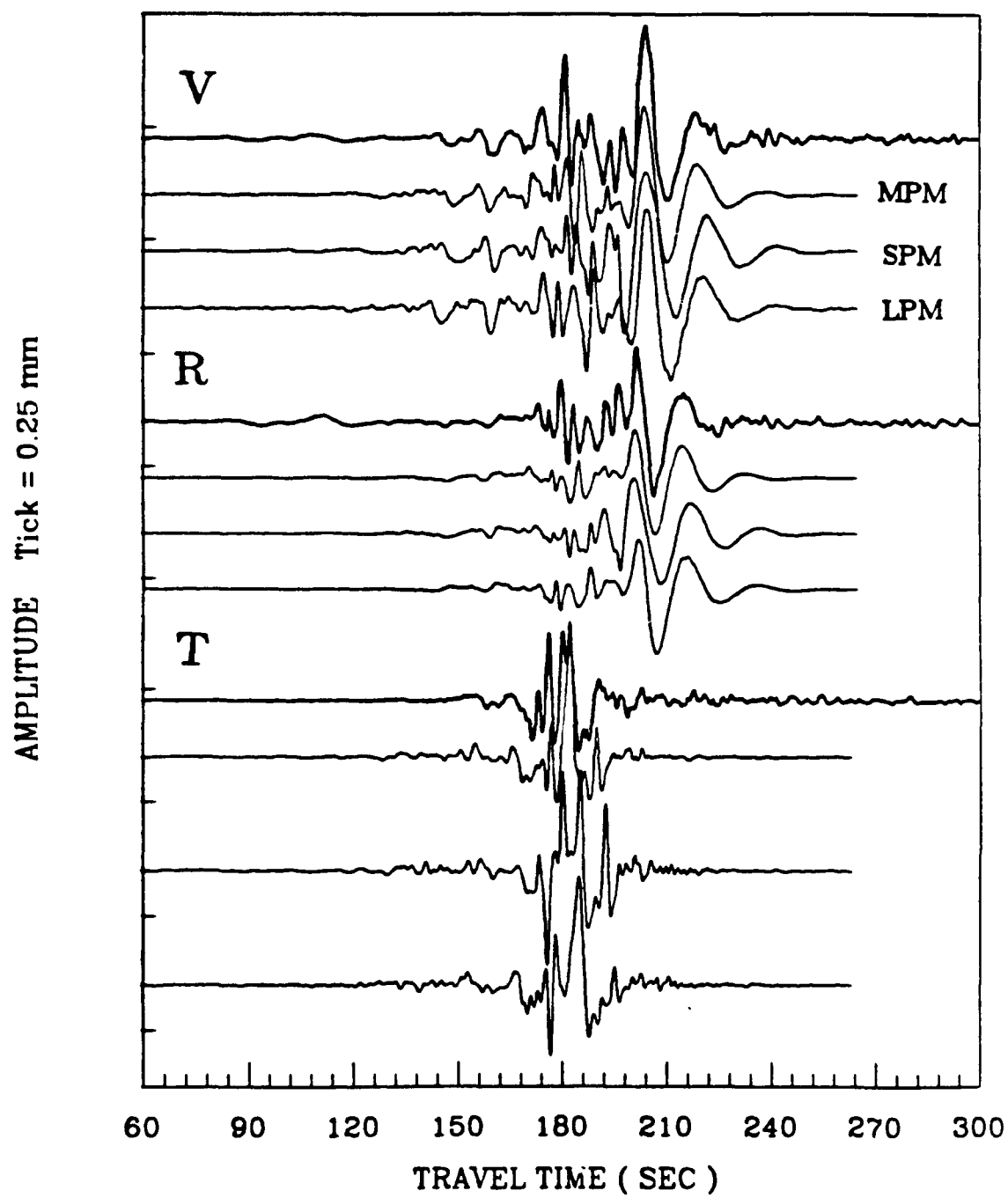


Figure 10



**Figure 11**





**Figure 12**

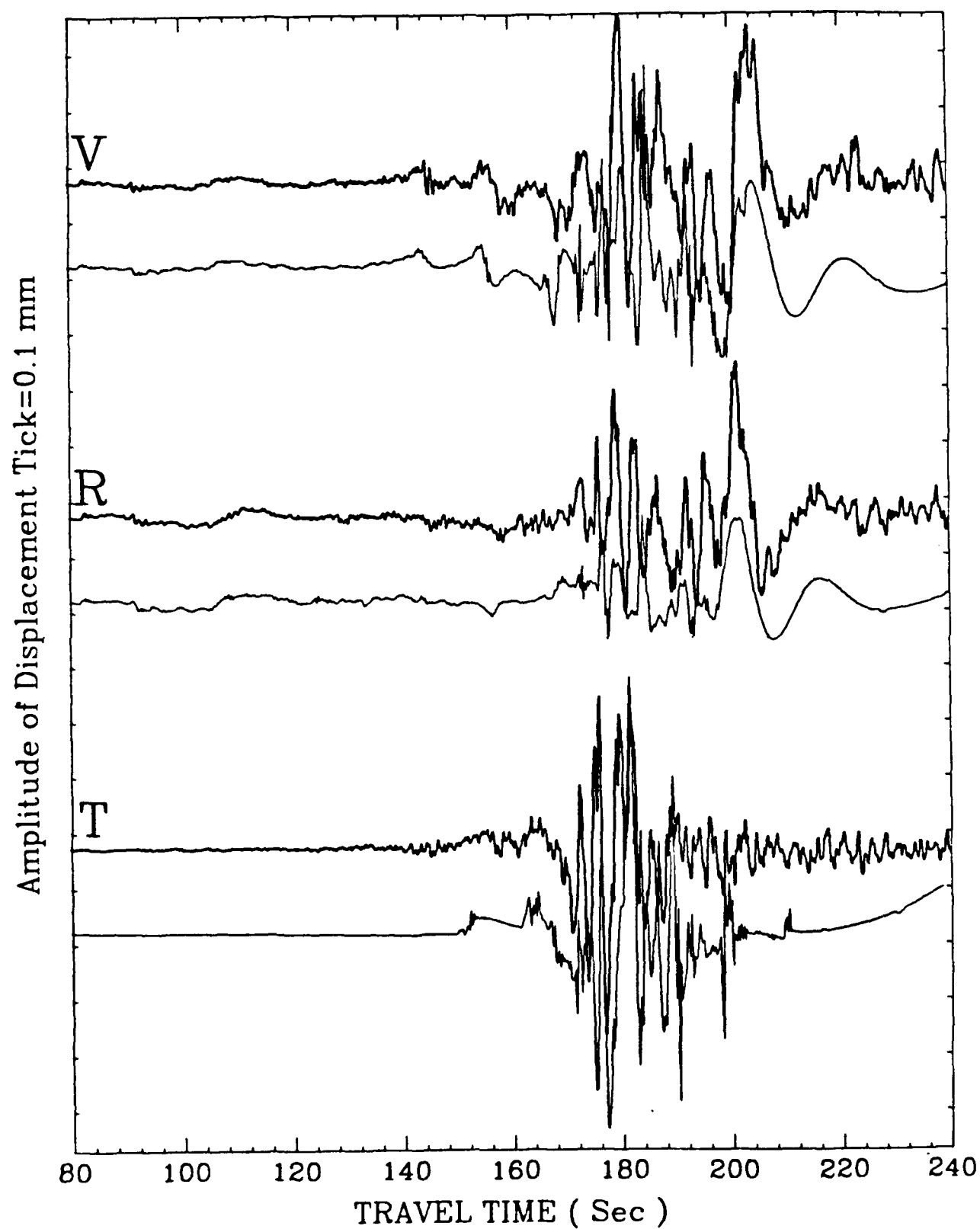


**Figure 13**

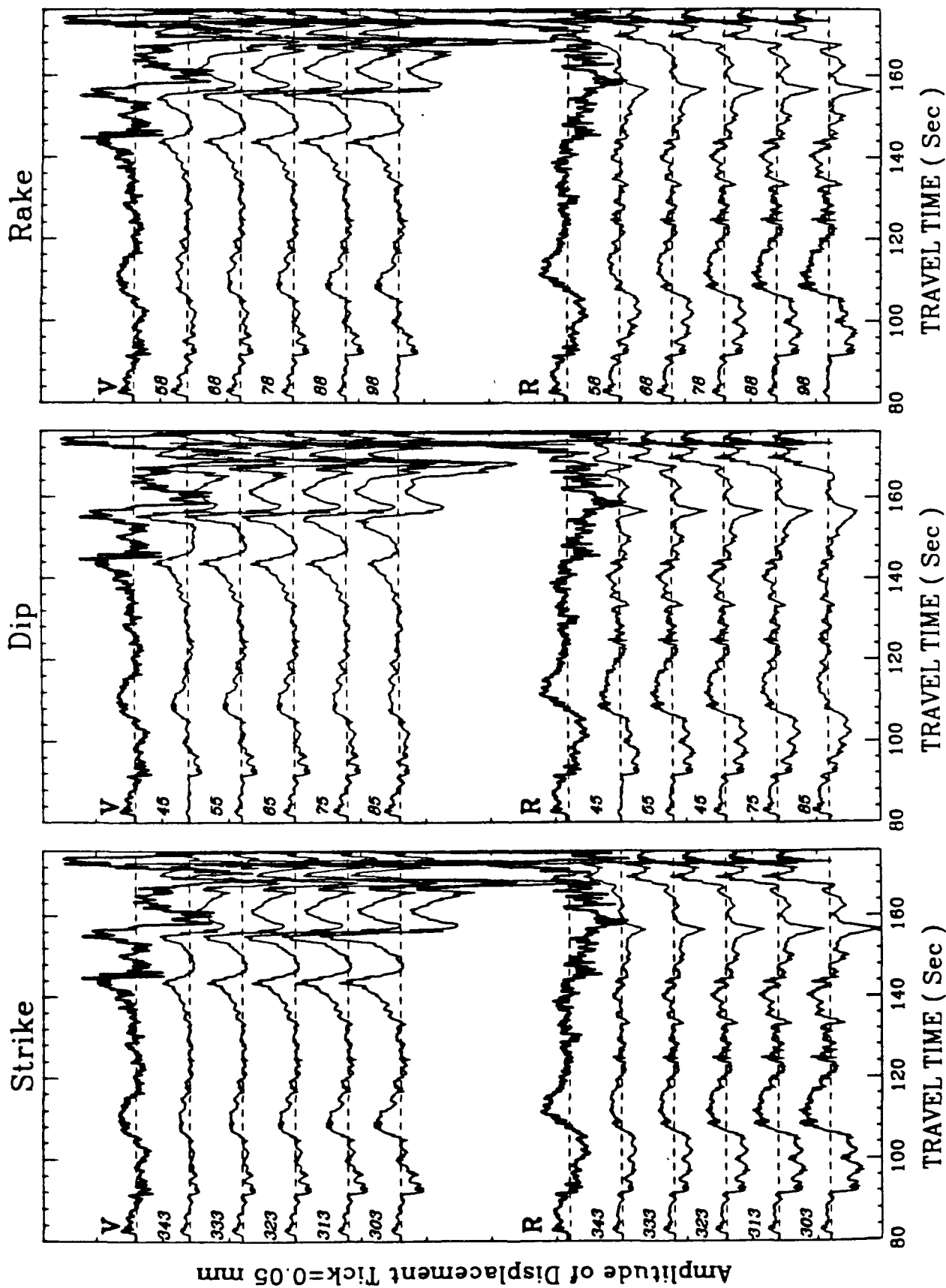
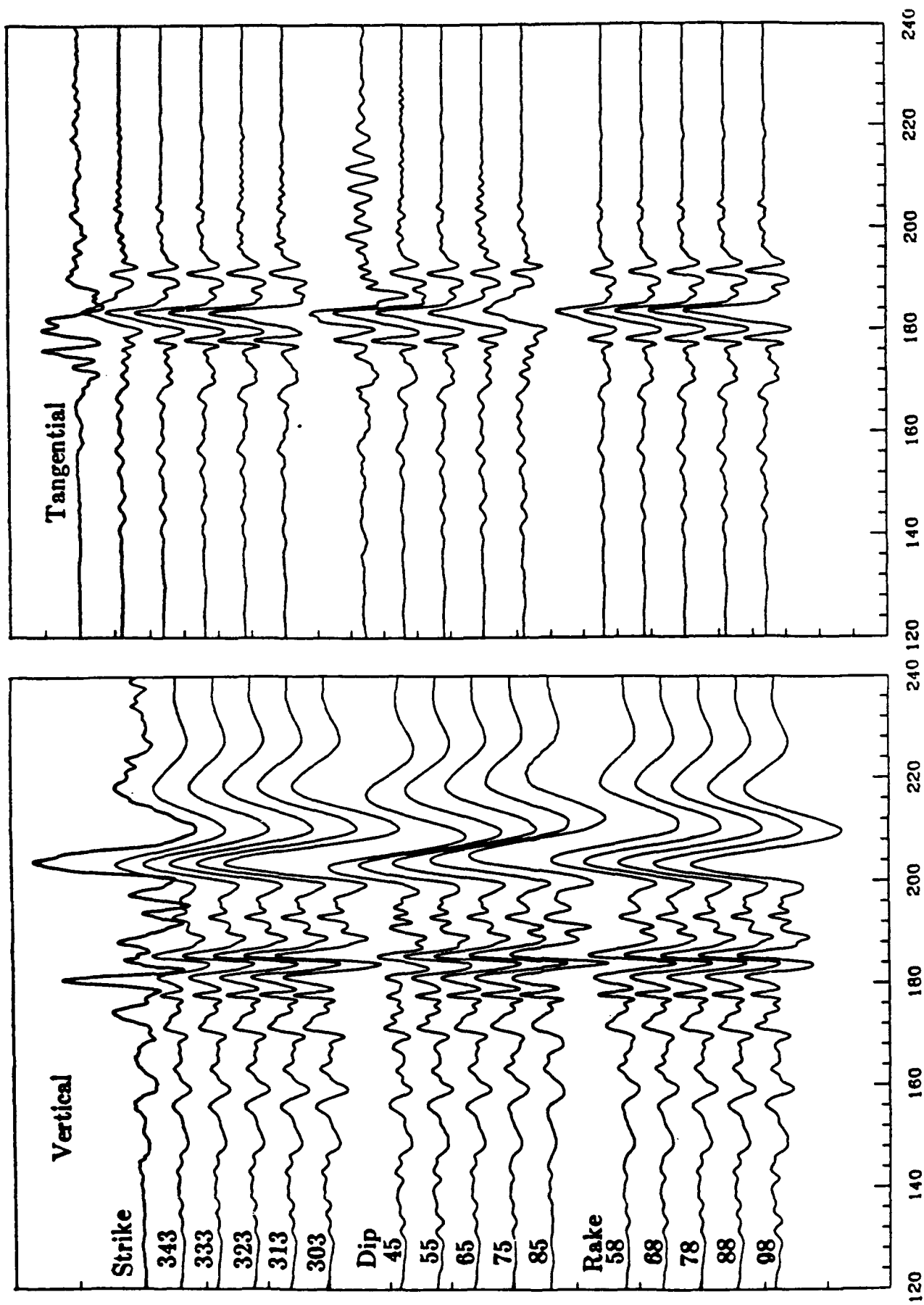


Figure 14



**Figure 15**

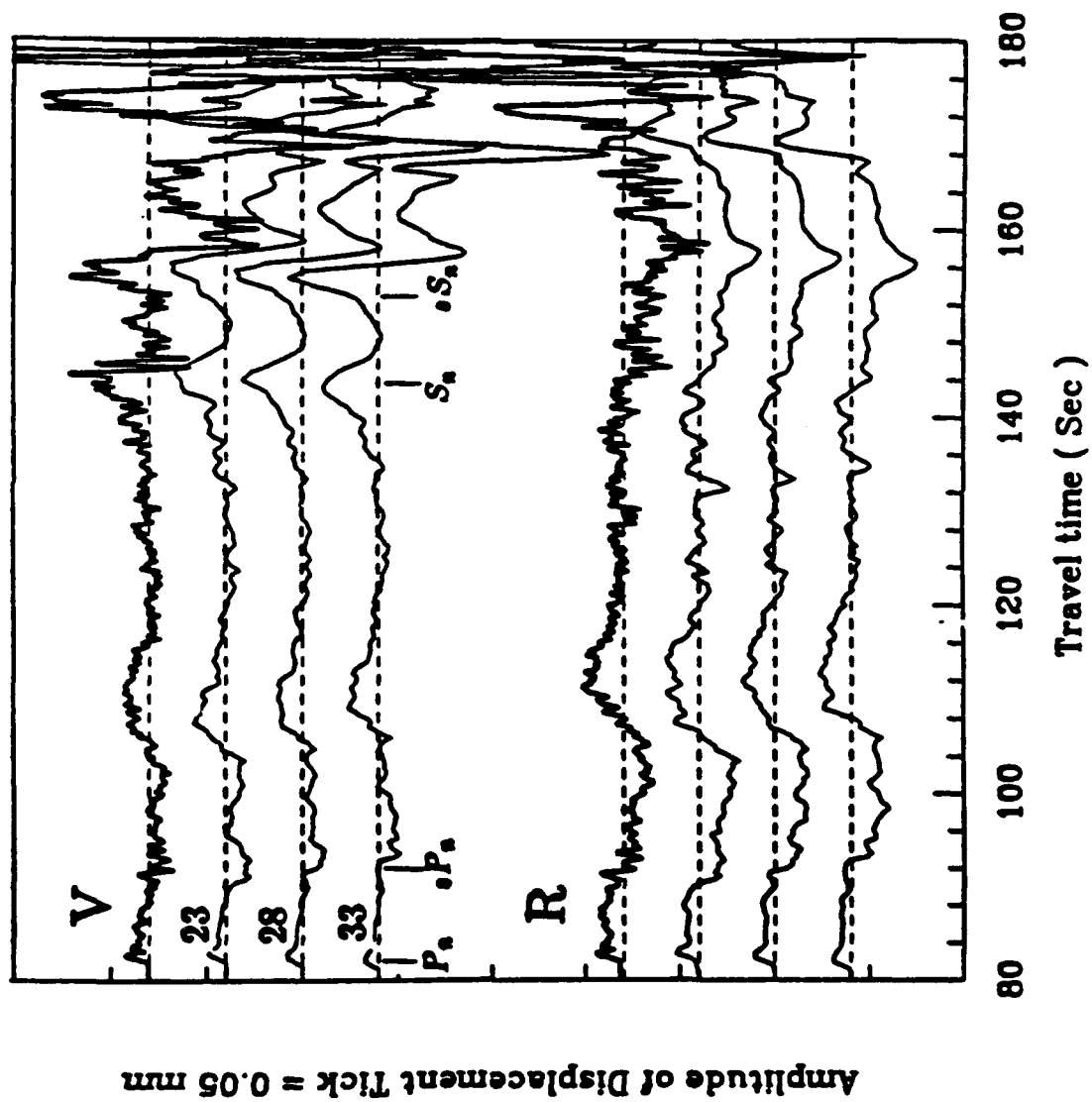


Figure 16



**Figure 17**

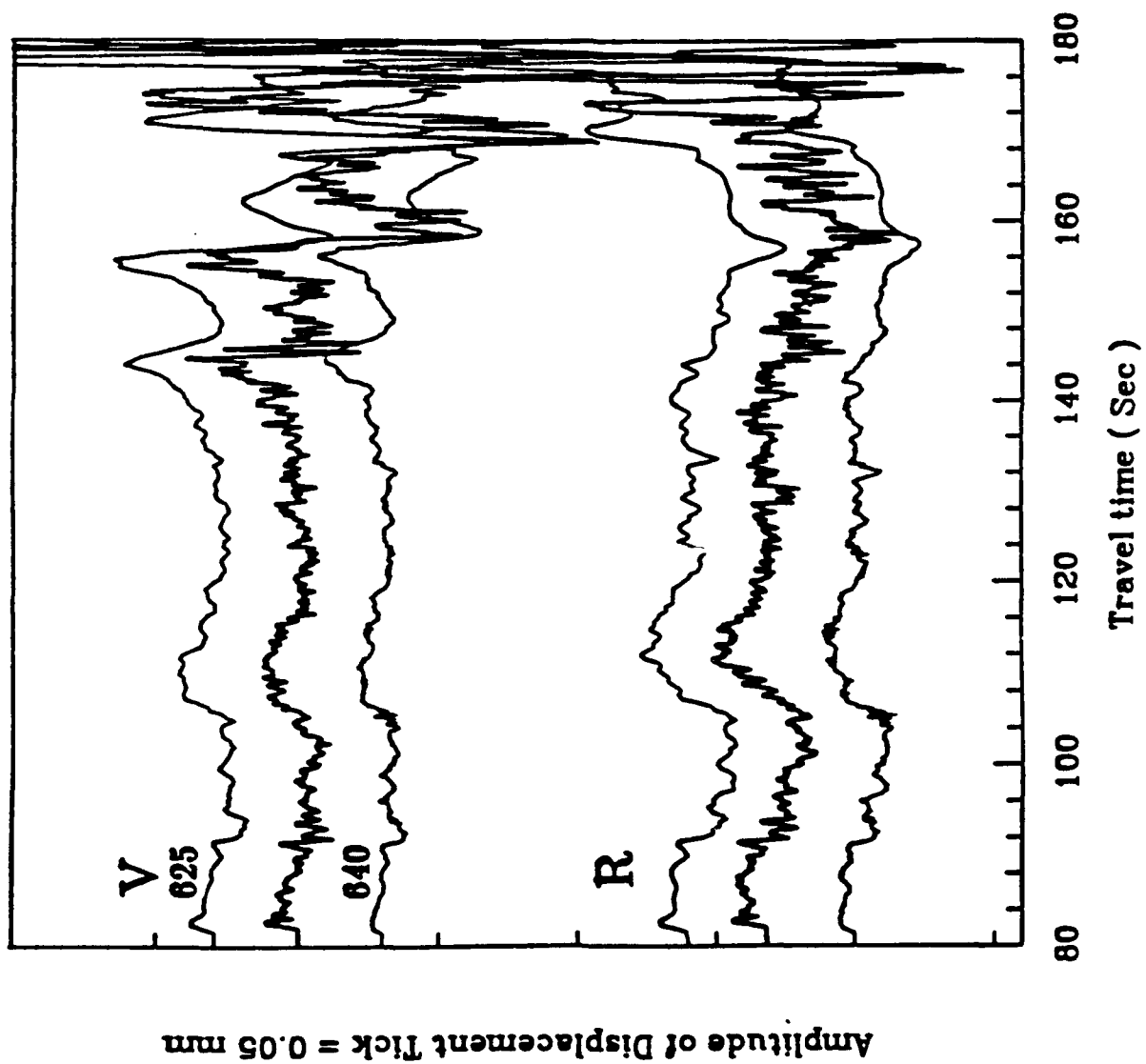


Figure 18





## **SECTION 3**

### **Broad-band Modeling of Local Earthquakes**

# Broad-band Modeling of Local Earthquakes

by Douglas S. Dreger & Donald. V. Helmberger

## Abstract

Three component broad-band waveforms of two small earthquakes near Upland, California recorded on the Pasadena broad-band, high dynamic range instrument, were forward modeled to obtain useful Green's functions. The sensitivity of the synthetic seismograms to differing layered structure, boundary sharpness, and two-dimensional structures was also investigated. We assumed that the sources of these events were both simple and known, as determined from the Caltech-USGS array first-motions. A trapezoidal time function was chosen such that the width of the direct S-wave was well modeled. The waveforms were forward modeled using Generalized Rays, Reflectivity, and Finite-Difference techniques. In addition, estimates of moment, fault dimension, and stress drop were computed.

The results of the modeling exercise indicate that a simple layer over a half-space model is a adequate approximation of the upper crust along this profile. In particular, the waveforms are controlled by a relatively slow, surficial layer. The sensitivity analyses indicate that the details of boundary sharpness, and deep crustal structure are not very important at frequencies less than 1 Hz, and at ranges less than 50 km. The thickness of the surface layer was constrained to be greater than 3 km and less than 5 km thick. The boundary sharpness sensitivity study indicated that the contact between the surficial material, and underlying material can be smoothed to 2 km without adversely affecting the synthetic waveform shapes. A number of two-dimensional finite-difference calculations were performed, and it was found that a ridge structure beneath the recorder, acted as a lowpass filter, and the lower frequency phases were largely unaffected. Other two-dimensional models with ridges between the source to receiver clearly did not fit the data however, the extended duration of these synthetic waveforms may be important in modeling more complicated waveforms observed in data from events south of this study. Synthetic seismograms computed for the best fitting model were used to estimate a long period moment of  $6 \times 10^{22}$  dyne-cm ( $M_L = 4.6$ ) and  $1 \times 10^{22}$  dyne-cm ( $M_L = 3.7$ ) with identical triangular source time durations of 0.3 seconds. Assuming the same fault dimension of 0.4 km from standard scaling, stress drop estimates of 410 and 70 bars are obtained. Generally, we found that it is possible to model local waveforms to frequencies of 1 Hz., without a complete understanding of fine structural detail. Resulting Green's functions can be useful in studying historic events, and in simulation of large events from a given source region.

## Introduction

With the installation of the broad-band, high dynamic range Streckeisen instrument at Pasadena, California, it has become possible to compare the waveforms of different sized events. In many cases, events in the range of  $M_L = 3.0$  to about  $M_L = 5.0$ , for a particular source region have similar waveforms.

Figure 1 shows the location of the Pasadena station relative to two of these earthquakes, and the two small Upland events which will be discussed in detail in this paper. These events are reasonably well located, since they occur within the dense USGS - Caltech array. In addition, focal mechanisms from first motions are easily obtained, and appear quite accurate for events of this magnitude scale. Larger events sometimes show complexity because of the presence of asperities, on distributed fault zones. Furthermore, the frequency of occurrence of earthquakes in this size range is much higher than for the occasional larger earthquakes, giving a greater availability of data. In short, we can assume the source is known (point source), and analyze these seismograms in terms of propagational effects and study the crustal structure. Once the crustal structure, or Green's functions are obtained, they can be used to study the sources of sparsely recorded historic earthquakes, or to scale up the source and estimate strong ground motion for larger earthquakes.

On traditional instruments, such as the short-period Wood-Anderson (WASP) and the long-period Wood-Anderson (WALP), there is a rather narrow range of earthquake magnitudes which would provide useful waveforms to model at a given receiver distance. Figure 2 shows an example of two small local earthquakes, that occurred near Chino, California in February, 1989 (figure 1). These tangential component records were recorded on the very broad-band channel of the Pasadena high dynamic range Streckeisen instrument, and then convolved with the instrument response of a WASP instrument. This figure shows that these two events, although different in size by more than one order of magnitude, have nearly identical records. This example demonstrates the deterministic nature of the records, indicating that they could probably be modeled by a deterministic approach. Furthermore, note the maximum amplitudes shown on this figure. The larger of the events could be used if recorded on a traditional instrument, however digitization would be difficult. The small event could not be used.

The purpose of this paper is to demonstrate the methodology of obtaining useful Green's functions, as well as, to show that quite a lot can be learned about earthquake sources, and propagation effects using broad-band waveforms at just

one site. This paper is a two part study. First, a crustal model is determined and the modeling approach is discussed. Secondly, the sensitivity of the synthetic seismograms with respect to two-dimensional model perturbations is examined.

### Data and Processing

The Caltech Streckeisen instrument is both broad-band, and high dynamic range. The instrument response is flat in velocity between 0.0027 Hz and 7 Hz. Integrating within this band produces displacement seismograms. These displacement seismograms can then be convolved with the response of any instrument to obtain the equivalent instrument seismograms. In this study the displacement seismograms, as well as, the WASP and WALP instruments seismograms are used in the forward modeling approach.

Two small earthquakes ( $M_L = 4.6$  and  $3.7$ ) were recorded by this instrument on June 26, 1988 and July 6, 1988, respectively. Both of these earthquakes occurred in the Upland, California area (figure 1), and the hypocenters located by the Southern California Network are within 1 km of each other. These events occurred at distances of about 43 km and the azimuth to the Pasadena station is  $272^\circ$ . Figure 3 displays the three component displacement data and the same convolved with the WASP instrument. It is evident that these two earthquakes have very similar waveforms, however the similarity is not as great as for the earthquakes presented in figure 2. Since the events occurred in nearly the same location, the differences in the waveforms are probably due to source complexities. The most significant difference in the waveforms for the two events is in the relative amplitudes of the various S-wave phases on the tangential components. The identification of these phases, and an understanding of the differences of their waveforms is a priority in forward modeling these events to obtain useful Green's functions.

### Methodology

The approach taken in this study was to identify the phases in the waveforms via forward modeling using Generalized Ray Theory (GRT). GRT is especially useful for this purpose because it allows one to build the waveform with

individual rays. Before the modeling process can begin, some of the parameters must be constrained by other means, or assumptions. The source parameters (location, focal mechanism) are constrained from first motion studies utilizing the entire Caltech-USGS network data, as mentioned earlier. The mechanisms for the two events are  $\phi=125^\circ$ ,  $\delta=85^\circ$ ,  $\lambda=130^\circ$ , and  $\phi=305^\circ$ ,  $\delta=85^\circ$ ,  $\lambda=150^\circ$  (L. Jones, personal communication). We assumed a point source for both events, and a trapezoidal source time function. A 0.15 sec. rise-time, 0.15 sec. duration, and 0.15 sec fall-time was determined by modeling the width of the direct S-wave. The same source time function was used for both the main shock and the aftershock. All of the synthetic seismograms which will be presented in this paper were constructed with the focal mechanism of the mainshock. Initial modeling of the records indicated that differences in the synthetic waveforms were not significant for the two different mechanisms. With the source parameters constrained, the velocity model was perturbed until good fits to the data were obtained.

### Modeling Results

Forward modeling the tangential component seismograms with GRT revealed that a near surface layer, with a relatively low S-wave velocity was required. The seismograms for both events possess a large amplitude phase which arrives after the initial direct S-wave. This phase is identified as a near receiver multiple within the near surface layer. Figure 4 shows how the synthetics are developed with the addition of rays, aiding the identification of the multiple phases ( $S_1$  and  $S_2$ ). The phases  $S_0$ ,  $S_1$ ,  $S_2$  are all observed in the data, especially on the tangential records. Note the ramp like feature beginning at the P-wave traveltime and continuing to the arrival of the direct S-wave ( $S_0$ ). This phase arises with the addition of near-field terms in the calculations, and is evident on the tangential displacement records (figure 3). Note that both the WASP and WALP (figure 5) instruments filter out the near-field phase on the tangential records. Finally, the longer period phase arriving after  $S_1$  is the Love wave. Five phases have been identified on the tangential component seismograms using GRT. It is rather surprising that such a simple model can give rise to such complexity. Figures 5, 6, and 7 compares the tangential, radial, and vertical synthetic seismo-

grams to the Upland data, respectively. The amplitude given in these figures is the maximum amplitude in cm. In each figure the amplitude of the displacement synthetic was scaled to the amplitude of the data by multiplying by a moment. The same moment was used for the WASP and WALP synthetics. It is evident that there is good agreement in absolute amplitudes in the band-widths of these instruments. The synthetics were computed using a reflectivity code vectorized and programmed by Mallick and Sen, and the model LOHS1 (table 1). The fits of the synthetics to the tangential data are exceptional, with good fits to the radial and vertical components for the first 20 seconds of waveform data. The later arriving signals are difficult to model but show a strong depth dependence. We plan to address this subject later. This practical code however does not take the near-field problem into account, and as a result the near-field phase discussed earlier is not included in these synthetic seismograms. It is important to note that although the model used contains deeper structure, the waveform is really controlled by a layer over a half-space, composed of the velocities of the top two layers of the model LOHS1.

The relative amplitudes of  $S_0$  and  $S_1$  are modeled by differing source depths. Recall, that we began by constraining the source depth via first motions. It was found during the modeling process that the relative amplitudes of the  $S_0$  and  $S_1$  phases are most sensitive to the depth of the source below the layer. The mainshock is best modeled with a source depth of 6 km, while the aftershock is best modeled with a source depth of 8 to 9 km. In addition, there is evidence that rupture initiated at depth and propagated upward (Mori and Hartzell, 1990). Introducing the source shallower than the layer changes the character of the synthetic waveforms considerably. In short, there is strong evidence which favors a source shallower than that obtained from first motions or there was a distributed source, with a significant moment release at shallower depth.

### **Sensitivity Analysis**

The result of a simple structure controlling the waveforms is surprising. Figure 1 indicates that there is considerable geologic complexity along this profile. Ignoring details of faulting, and folding, the profile still retains a ridge-basin-ridge

structure. Specifically, the energy released during the earthquakes propagated through the San Jose Hills, San Gabriel basin, and the eastern margin of the Verdugo mountains. The second part of this paper investigated the question of the sensitivity of the synthetic seismograms to perturbations of the layer over a half-space structure. Gradients, deep crustal structure, layer thickness, and two dimensional velocity models were tested. Three component synthetic seismograms for flat layered models, were computed by a reflectivity method. Synthetic seismograms for the two-dimensional studies were computed with a finite-difference approach (Helmberger & Vidale, 1988).

Figure 8 shows the results of perturbing the layer over a half-space structure by introducing velocity gradients. All of the perturbed models produce synthetics resembling the layer over a half-space result. This is especially true for the last two presented. Here, a gradient is introduced to smear out the sharpness of the contact between the two layers. Some of the effects to take note of are the removal of the second multiple ( $S_2$ ), and the broadening of the Love wave. The second model has a linear gradient from the surface to the half-space. The shape of the Love wave is severely altered, as are the radial and vertical component synthetics. The general result here is that it is possible to smear out the contact between the two layers and still obtain synthetics which are good fits to the data, however it is important that there is a well defined surface layer. It was found that 1 to 2 km of smearing at the layer contact could be tolerated in the synthetics at these frequencies.

Figure 9 shows the results of including varying deep crustal structure, and the effect of the velocity/thickness tradeoff for the shallowest layer. LOHS1 is the preferred model, discussed earlier. Table 1 gives the details of all of the models used in the construction of these synthetics. First, in comparing the synthetics associated with the LOHS1, SoCal, and LOHS2 models one can see that there is some variation. The SoCal model is an average model of southern California which is used to routinely invert for source location and focal mechanism from first motion data. The synthetics produced by this model do not fit the data well, and one of the primary reasons is the thickness and velocity of the surface layer.

This layer is 5 km thick, with a velocity of  $3.18 \text{ km s}^{-1}$ . The greatest effect on the tangential components is that the Love wave is not as developed. LOHS2 has the same deep crustal model as LOHS1, however, it has a thinner and slower surface layer. The effects are that the Love wave and the  $S_2$  multiple are more developed. Generally, the thickness of this layer must be less than 5 km, and greater than or equal to 3 km.

Model L1 is a modified version of a crustal model for Pasadena determined by C. Langston (1989), where the velocity and thickness of the surface layer was changed to that of the one-layered model discussed earlier. L1 contains a low velocity zone at depth. Model L2 is the same model as L1 except the low velocity zone was removed, and replaced with a increasing gradient. It is apparent that the synthetic seismograms do not change very much. The important result here is that the details of deep crustal structure are not particularly important in the waveforms of local earthquakes (less than 44 km), except at higher frequencies (greater than 1 Hz.).

Figure 10 shows the results of the two dimensional finite difference calculations. We begin with the previously discussed layer over a half-space synthetics displayed in figure 10a. This figure shows that the reflectivity and finite-difference methods correlate, and is used to identify the occurrence of artifacts in the finite-difference synthetics. The finite difference calculation clearly reproduces the result of the reflectivity calculations, however there are two artifacts present. These artifacts arise from reflections from the grid boundaries, however they occur later in time than the Love wave, and do not cause any substantial distortion of the synthetic waveforms. Figures 10b and 10c show the effect of a ridge structure introduced beneath the Pasadena station. The effect is basically a low-pass filter. When an intermediate velocity is introduced into the ridge (figure 10c) much of the characteristics of the layer over a half-space is retained, although there is a reduction of the higher frequency energy. The WASP instrument synthetics would be affected. Since the ridge structure attenuates the upward propagating higher frequency energy, initial downward propagating energy, reflected back to the receiver would be more important in the WASP synthetics. This figure



demonstrates that a ridge structure beneath Pasadena does not have a large affect at lower frequencies. Figures 10d, and 10e show the effect of the addition of a ridge between the source and the receiver. The effect is to completely change the character of the waveform, especially the Love waves. Surface waves propagate to the ridge, propagate through the ridge as body waves, and then develop surface waves on the other side of the ridge (Vidale & Helmberger, 1988). The secondary surface waves are typically higher frequency than those for the flat model. In fact, the character of the waveform resembles those for shallow sources, within the surface layer. The synthetics for this type structure do not fit the Upland data. Figures 10f, 10g, and 10h explore the possibility of a shallow basin within the surface layer. Figure 10f has a basin with a  $1.8 \text{ kms}^{-1}$  shear wave velocity and a  $2.0 \text{ gcm}^{-3}$  density. Figures 10g and 10h differ in that the velocity of the basin is linear gradient where  $V = 1.8 + 0.4Z$ . The geometry of the shallow basin for figures 10f and 10g was interpolated from the depth to basement results of Yerkes, (1967). In these calculations the layer at 4 km depth was retained because of its importance in producing the  $S_1$  and  $S_2$  multiple phases as well as the Love wave. The result of these calculations is that there is an amplification of 134 % to 273 % of the maximum amplitude, and an extension of the duration of the synthetic seismograms, compared to the layer over a half-space synthetics (figure 10a). Both of these effects are the result of focusing of reverberating energy in the basin which dives out at the shallow basin boundary. The diving energy however encounters the deeper layer responsible for  $S_1$  and  $S_2$  at near critical angle, and is reflected back up to the receiver. The differences in the synthetic waveforms for figures 10f and 10g are the result of the effect of the gradient on the development of a local Love wave within the basin. The lack of the gradient allows the Love wave to develop, extending the duration of the waveform. As discussed earlier this trapped energy reaches the basin boundary and leaks out as body waves, and is reflected back by the deeper layer responsible for  $S_1$  and  $S_2$ . Note that shallow sources are more effective at generating surface waves and thus, to generate stronger coda via this type of scattering. This may be the explanation of the coda arriving in the observed data, for example see figure 7. It appears that case (10c) closely resembles the actual situation at the recording station, where the main effect is to remove the highest frequencies for the flat layer calculation.

Figure 11 shows the finite difference results calculated from the structure of figure 10c for the radial and vertical components. These synthetics are compared with the reflectivity calculations for the layer over a half-space. The synthetic waveforms do not change dramatically for this two dimensional structure, and the Rayleigh wave seems to be the most affected phase, with a slight phase shift. To identify scattered ridge phases array measurements would be required. The results of both the SH and P-SV two-dimensional studies indicate that these structures do not control the shape of the synthetic waveforms, except at higher frequencies, and in the phase of the Rayleigh wave.

### Discussion and Conclusions

We envision the usefulness of these Green's functions in several ways. Firstly, they can be used to study less well recorded historic events where the only seismological waveform data available is a pair of long period horizontal torsion recording (WALP), as is the case at Pasadena. This is particularly valuable for studying growth structures in basins under compression, where mechanisms are likely to show considerable variation. Secondly, they can be used to calibrate the empirical Green's function approach in the simulation of large events from small ones, Hartzell (1979) and Mori and Hartzell (1990). The latter paper uses a small aftershock of the same  $M_L=4.6$  Upland event considered above to study the plane of faulting of the main event and it is interesting to compare results.

The fundamental assumption in the empirical Green's function approach is that the waveform distortions caused by the path and site conditions are shared by the mainshock and the aftershock. If the mechanisms are identical, one can use the aftershock P-waveforms to generate the main event P-waveforms by considering finite rupturing on the two possible focal planes, namely ( $\phi=125^\circ$ ,  $\delta=85^\circ$ ,  $\lambda=130^\circ$ , and  $\phi=221^\circ$ ,  $\delta=40^\circ$ ,  $\lambda=8^\circ$ ). They found that southwest trending plane gave the best results indicating left-lateral motion which is consistent with the overall motion in the Transverse Ranges frontal fault zone.

Mori and Hartzell obtained a moment estimate of  $4.2 \times 10^{22}$  dyne-cm for the main event from the P-wave amplitude following an expression given by Boat-

wright (1980). Their inversion gave a source area of one  $km^2$  and a stress drop of 38 bars.

We obtained a larger moment,  $6 \times 10^{22} + 2 \times 10^{22}$  dyne-cm by modeling the amplitudes of the displacement data convolved with a Press-Ewing instrument response. A considerably large stress drop, based on the far-field time duration,  $\tau$ , was estimated, by assuming that:

$$\tau = \frac{a}{\beta} \left[ \frac{16}{7\pi} + \left( \frac{1}{.8} + \sin\delta \right) \right]$$

where  $a$  is the fault dimension (circular fault),  $\beta$  is the shear velocity and  $\delta$  is the angle between the normal to the fault plane and the ray path, see Cohn et. al. (1982) for details. The trapezoidal far-field time function discussed earlier, can be represented by a triangular time function (Helmberger and Malone, 1975). Where  $\tau = 0.5\delta T_1 + \delta T_2 + 0.5\delta T_3$ . For a  $\tau$  of 0.3 seconds, this expression yields an estimate of fault dimension  $a$ , of 0.4 km. Assuming,  $\delta\sigma = \frac{7M_0}{16a^3}$  (Kanamori and Anderson, 1975), a stress drop of 410 bars is obtained. This estimate of stress drop is considerably larger than Mori and Hartzell's estimate, however different models of fault rupture were used. Recall that the same source time function were used for both the mainshock and the aftershock. The moment of the mainshock was found to be about 6 times larger than that of the aftershock, and therefore the stress drop of the mainshock should be large relative to the aftershock. Mori and Hartzell report that rupture on the southwest trending fault plane (their preferred fault plane) propagated upward and to the southwest (toward Pasadena). Considering unilateral rupture toward Pasadena would increase our estimate of fault dimension, and would result in a lower estimate of stress drop. In any case, clearly a combination of numerical and empirical approaches would be the most powerful, where the longer period properties, namely moment, effective time history and orientation are modeled numerically, and shorter period effects namely rupture properties are modeled empirically.

In conclusion, it is possible to interpret local broad-band records with relatively simple models. The broad-band records facilitate the identification of different phases particularly phases with different frequency contents (i.e. near-field, post-critical, and surface-wave phases). The results of the forward modeling indicate that the waveforms of the two Upland, California earthquakes are controlled by the relatively slow material at the surface for which a single-layer structure is an adequate approximation. The forward modeling approach used here is also useful in studying source complexities. This is facilitated by studying two, or more, earthquakes in a given area. The differences in the waveforms can be understood in terms of differing focal mechanism, source-time function, or in dislocation complexities. In the case of the  $M_L=4.6$  Upland, California earthquake it was found that a significant portion of the energy was released at a shallower depth, roughly 3 km shallower than the array location. This is not surprising in that a strong trade-off in depth vs. origin time exists. Thus, it appears that one of the first impacts of the addition of local broad-band waveform data will be on depth control.

The sensitivity analysis indicates that the layer must be between 3 to 5 km thick, and that the boundary of the layer can be smeared out in velocity over 1 to 2 km. Deeper crustal structure is not important at this distance, however two dimensional near receiver structures attenuate the higher frequencies ( $> 1$  Hz.). None of the closed basin models, nor the shallow basin models satisfied the data, however, the extended duration produced by shallow basins may account for the extended duration of S-wave packets for earthquakes observed to the south. Fortunately, the relative insensitivity of the synthetics to details of boundary sharpness, layer thickness, and to some degree two dimensional near receiver structure, shows that useful Green's functions can be found without knowing the fine structural details.

### Acknowledgements

The authors would like to acknowledge Mrinal Sen and Richard Stead for their help with the computer codes. We would like to thank Brad Woods, and David Wald for their reviews, and especially Hiroo Kanamori for his review and

efforts in setting-up the Streckeisen instrument. This research was supported by the Advanced Research Projects Agency of the Department of Defense and was monitored by the Air Force Geophysics Laboratory under the contract F19628-89-K-0028. Contribution No. 4838, Division of Geological and Planetary Sciences, California Institute of Technology, Pasadena, California.

## References

- Boatwright J., (1980), A Spectral Theory for Circular Seismic Sources; Simple Estimates of Source Dimension, Dynamic Stress Drops, and Radiated Energy, *Bull. Seism. Soc. Am.*, V. 70 , p 1 - 28.
- Cohn, S. N., Hong, T., Helmberger, D. V., (1982), The Oroville Earthquakes: A Study of Source Characteristics and Site Effects, *J. Geophys. Res.*, V. 87 , n. B6, p 4585 - 4594.
- Hartzell, S., (1978), Earthquake Aftershocks as Green's Functions, *Geophys. Res. Lett.*, V. 5 , p 1 - 5.
- Helmberger, D. V., and Vidale, J. E., (1988), Modeling Strong Motions Produced by Earthquakes with Two-Dimensional Numerical Codes, *Bull. Seism. Soc. Am.*, V. 78 , No. 1, p 109 - 121.
- Helmberger, D. V., and Malone, S. D., (1975), Modeling Local Earthquakes as Shear Dislocations in a Layered Half Space, *J. Geophys. Res.*, V. 80 , No. 35, p 4881 - 4888.
- Kanamori, H. and Anderson, D. L., (1975), Theoretical Basis of some Empirical Relations in Seismology, *Bull. Seism. Soc. Am.*, V. 65 , p 1073 - 1095.
- Langston, C., (1989), Scattering Under Pasadena, California, *J. Geophys. Res.*, V. 94 , p 1935 - 1952.
- Mori, J. and Hartzell, S., (1990), Source Inversion of the 1988 Upland Earthquake: Determination of a Fault Plane for a Small Event *Submitted to Bull. Seism. Soc. Am.*
- Vidale, J. E., D. V. Helmberger, (1988), Elastic Finite-Difference Modeling of the 1971 San Fernando, California Earthquake, *Bull. Seism. Soc. Am.*, V. 78 , No. 1, p 122 - 141.
- Yerkes, R. F., McCulloh, T. H., Schoellhamer, J. E., and Vedder, J. G., (1965), Geology of the Los Angeles Basin California - an Introduction, *U.S.G.S. Prof. Paper 420-A*, pp 57.

Table No. 1

## One Dimensional Velocity Models

LOHS1				SoCal				LOHS2			
$V_s$	$V_r$	$\rho$	Z	$V_s$	$V_r$	$\rho$	Z	$V_s$	$V_r$	$\rho$	Z
4.5	2.6	2.4	0.0	5.5	3.18	2.4	0.0	4.7	2.4	2.4	0.0
5.9	3.5	2.67	4.0	6.3	3.64	2.67	5.5	5.5	3.5	2.67	3.3
6.6	3.8	2.8	16.0	6.7	3.87	2.8	16.0	6.0	3.6	2.7	10.3
8.0	4.1	3.1	26.0	7.8	4.5	3.0	37.0	6.6	3.81	2.8	22.3
8.2	4.2	3.3	30.0					7.4	4.27	2.95	26.3
								8.0	4.4	3.0	30.3
L1				L2							
$V_s$	$V_r$	$\rho$	Z	$V_s$	$V_r$	$\rho$	Z				
4.5	2.6	2.4	0.0	4.5	2.6	2.4	0.0				
5.9	3.5	2.67	4.0	5.9	3.5	2.67	4.0				
6.5	3.75	2.7	10.0	6.5	3.75	2.7	10.0				
5.6	3.23	2.7	15.0	6.55	3.78	2.8	15.0				
6.6	3.81	2.8	21.0	6.6	3.81	2.8	21.0				
7.2	4.16	2.9	23.0	7.2	4.16	2.9	23.0				
7.4	4.27	2.95	25.0	7.4	4.27	2.95	25.0				
7.6	4.39	3.0	27.0	7.6	4.39	3.0	27.0				
8.0	4.62	3.2	32.0	8.0	4.62	3.2	32.0				
8.3	4.8	3.35	38.0	8.3	4.8	3.35	38.0				

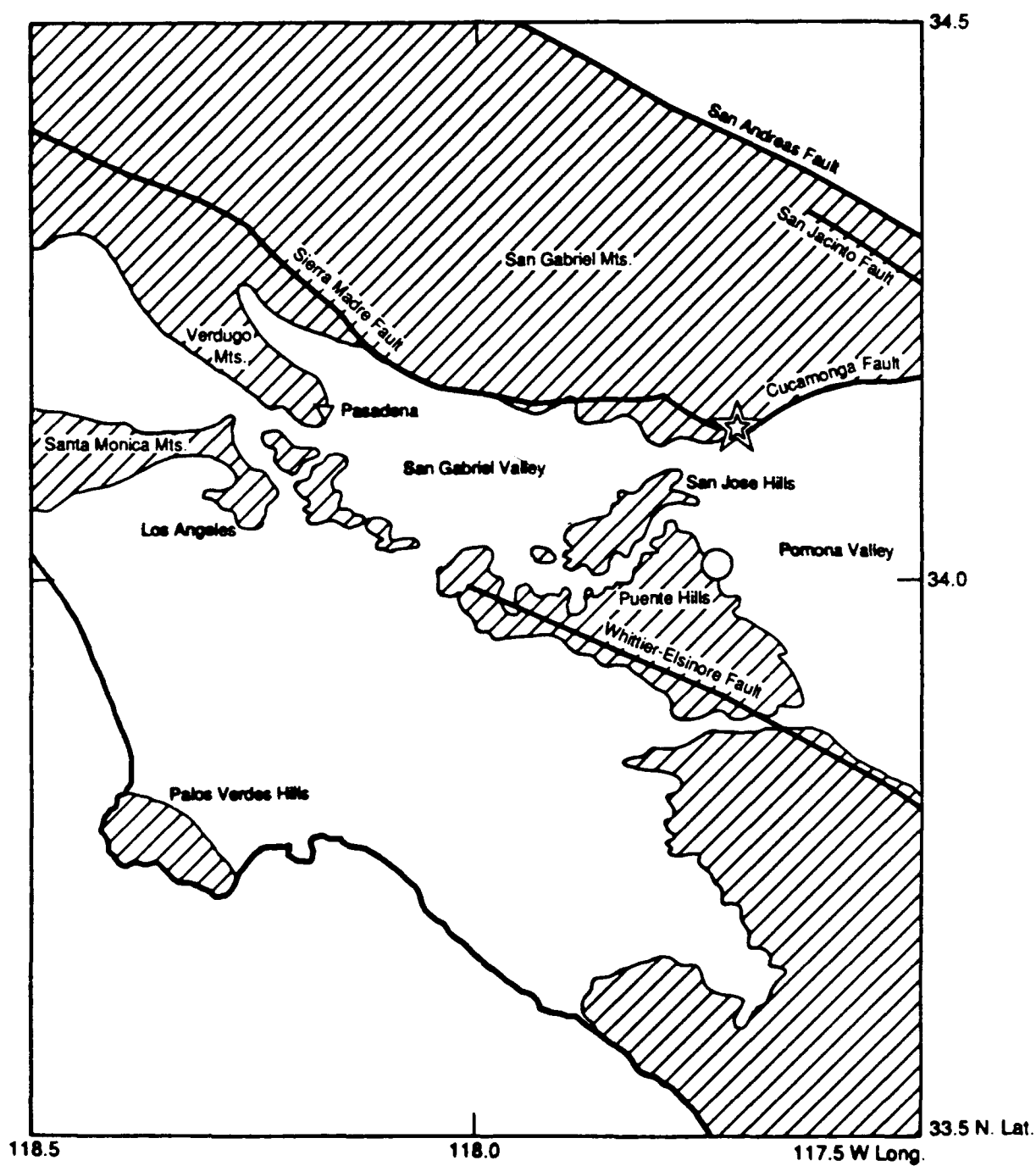
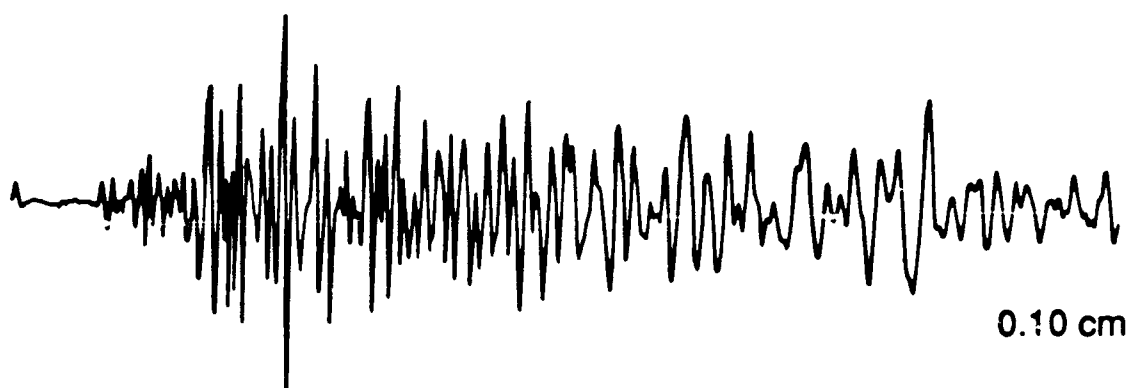


Figure 1

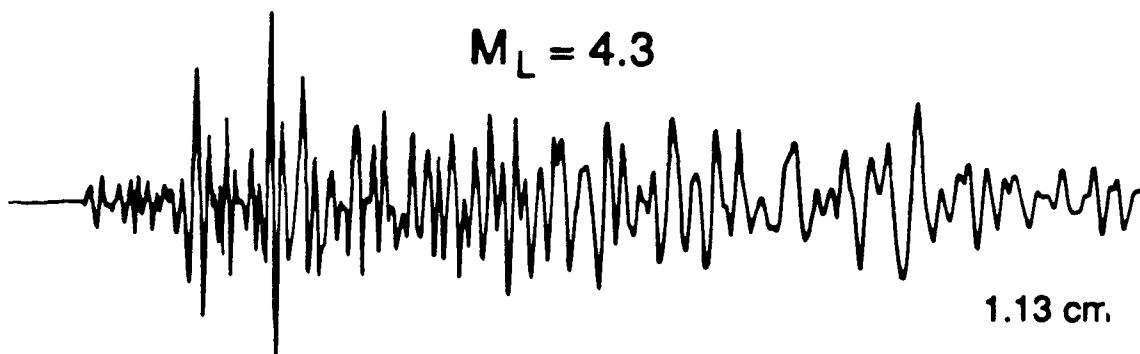


$M_L = 3.2$



0.10 cm

$M_L = 4.3$



1.13 cm.

0 10 sec

**Figure 2**

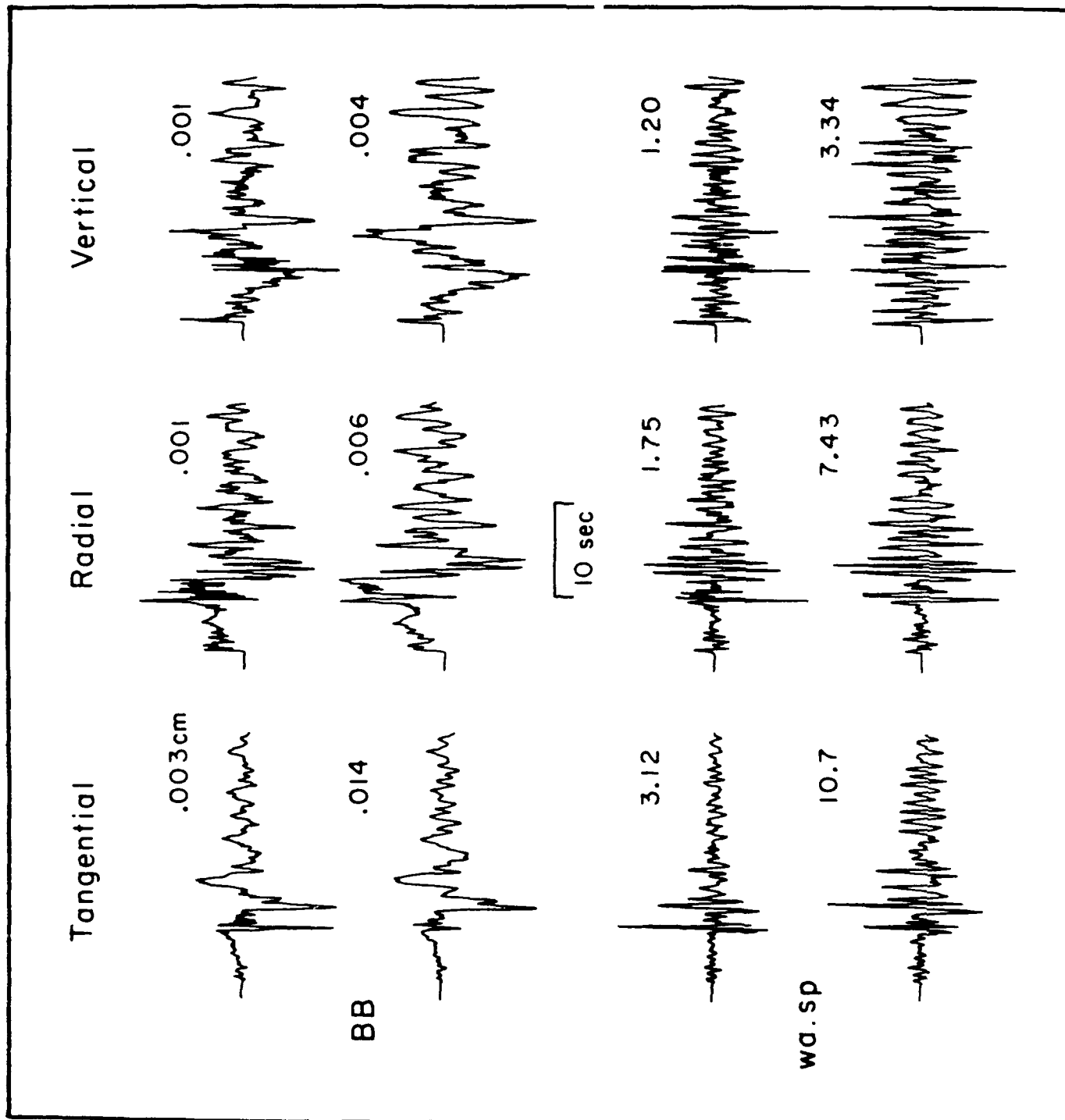
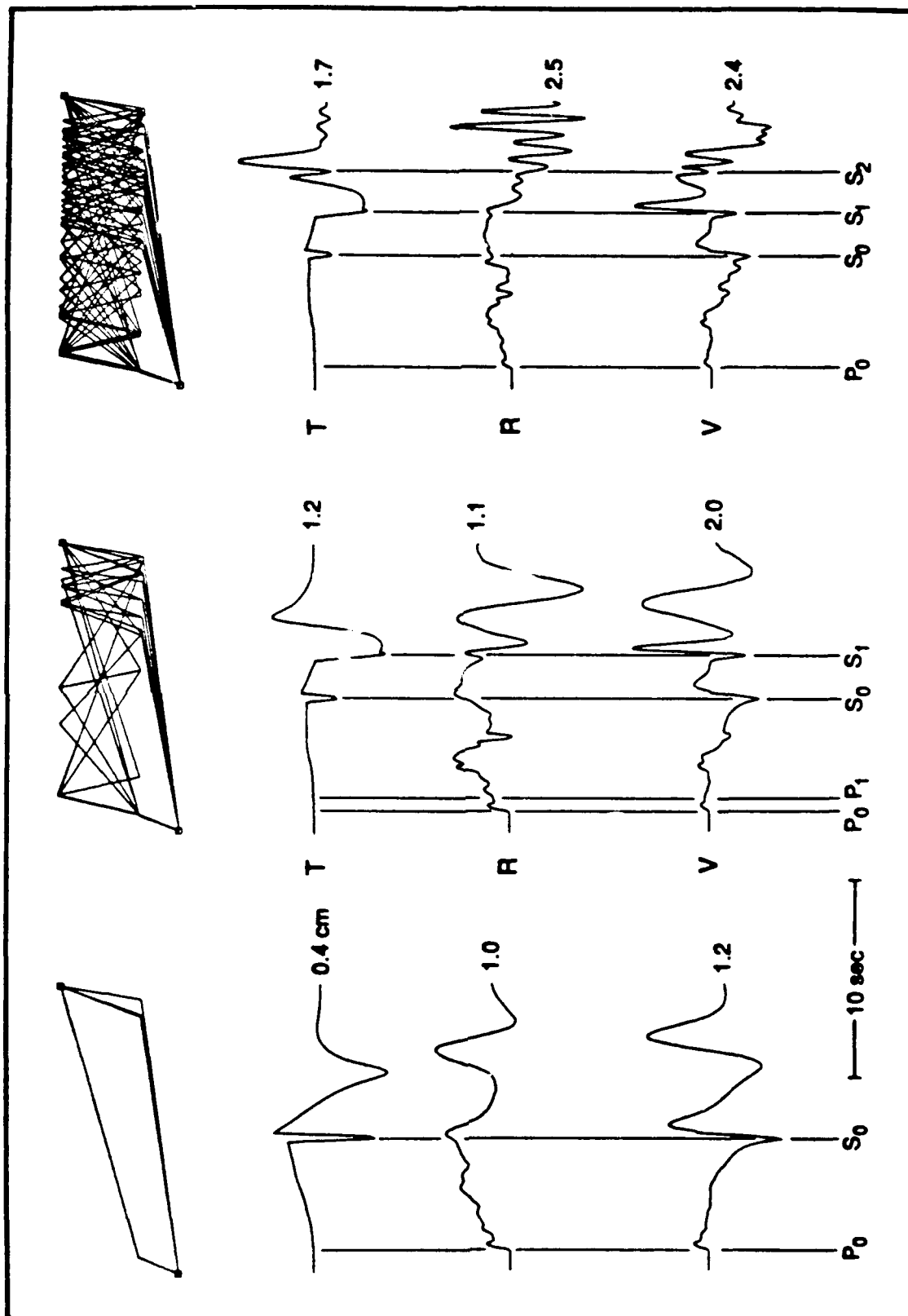


Figure 3



**Figure 4**

# TANGENTIAL

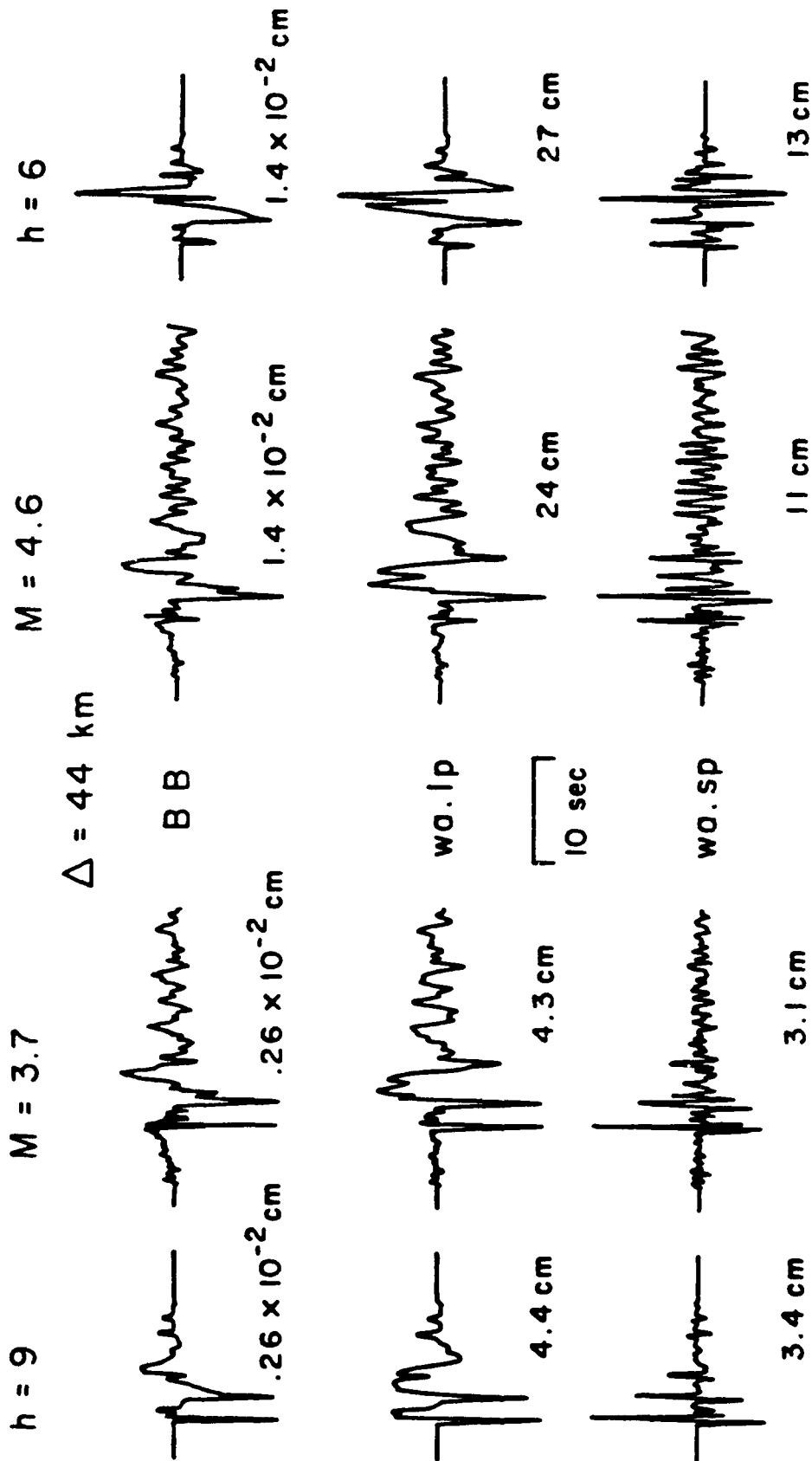
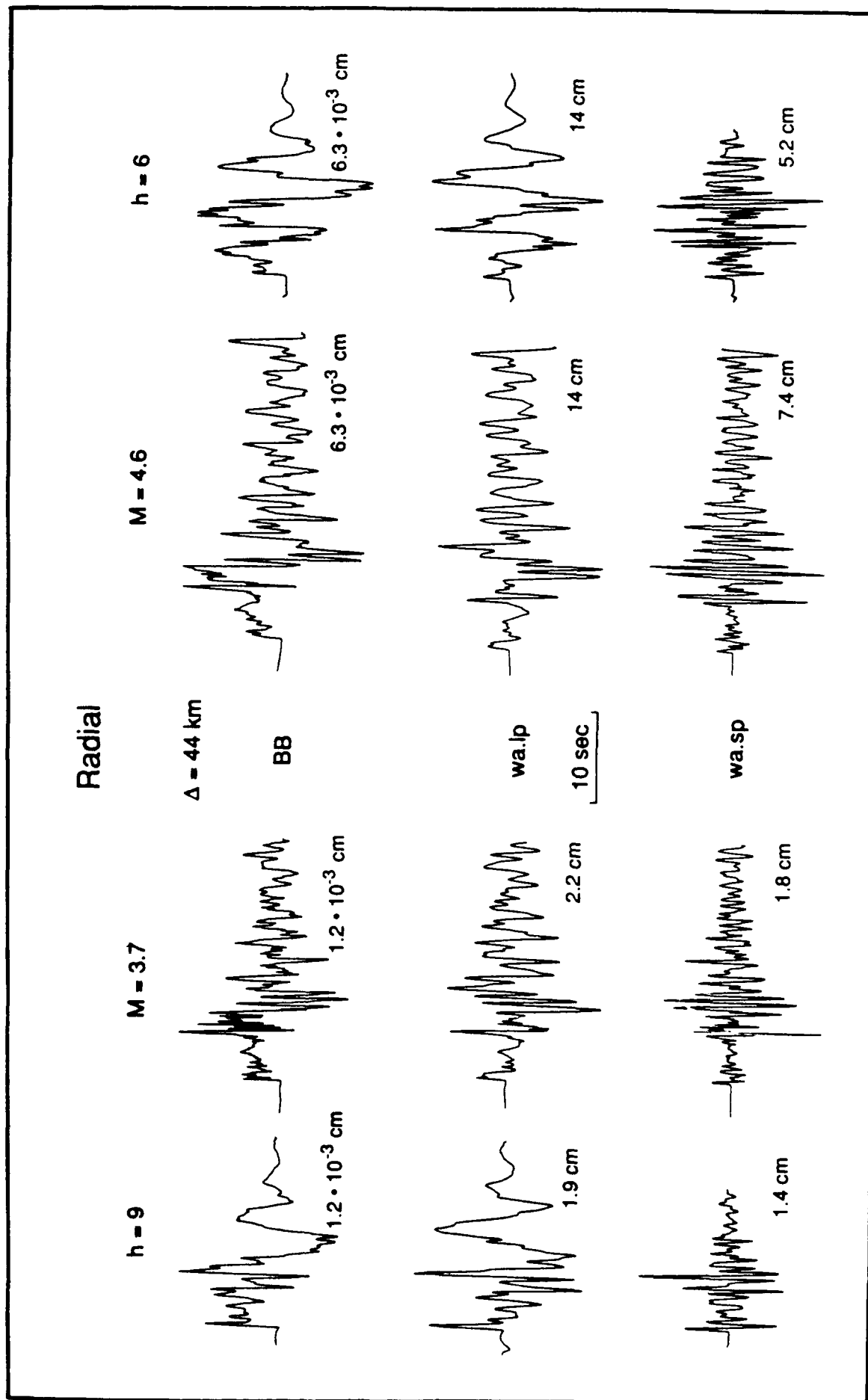


Figure 5



**Figure 6**

# Vertical

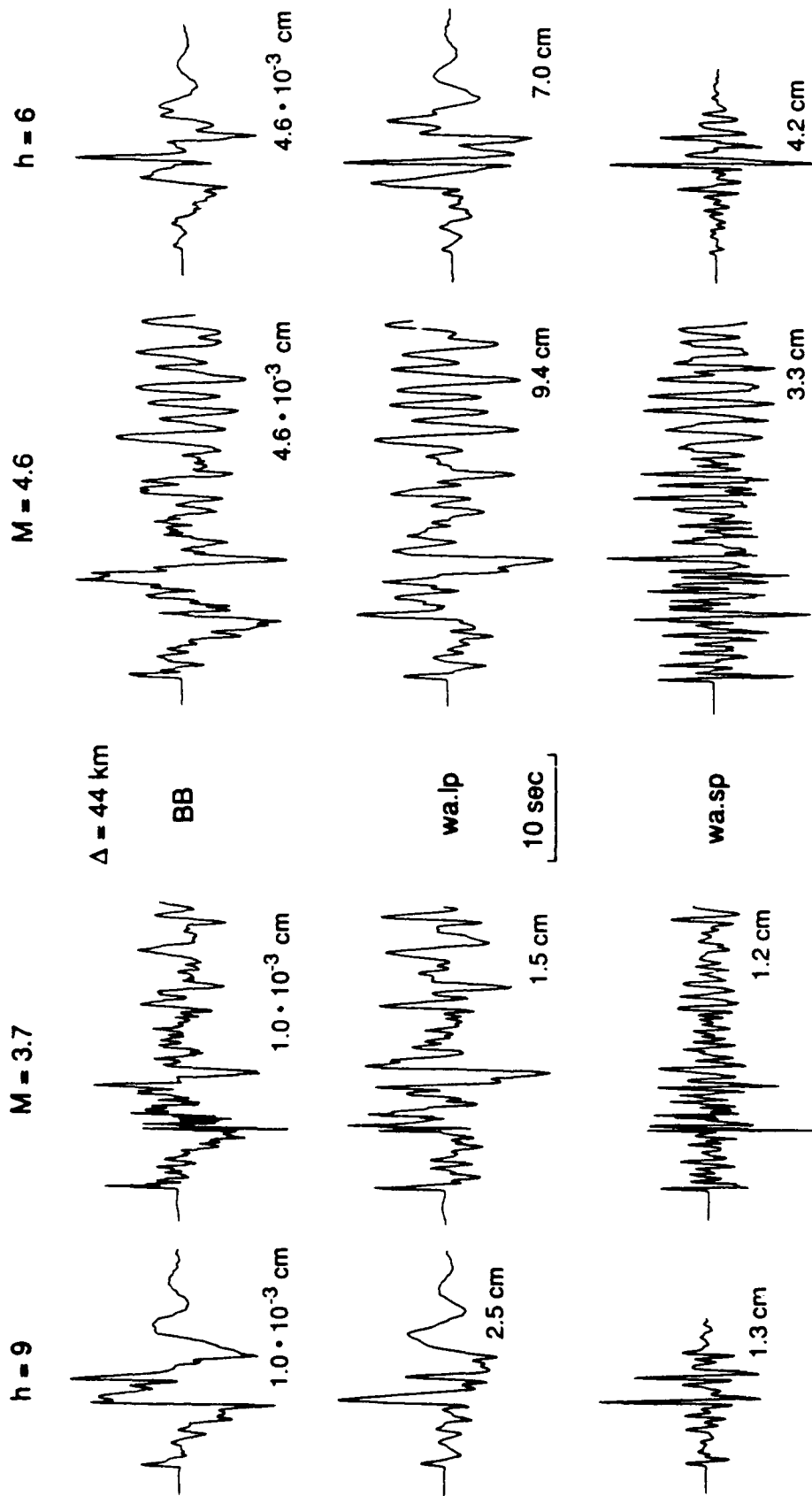


Figure 7

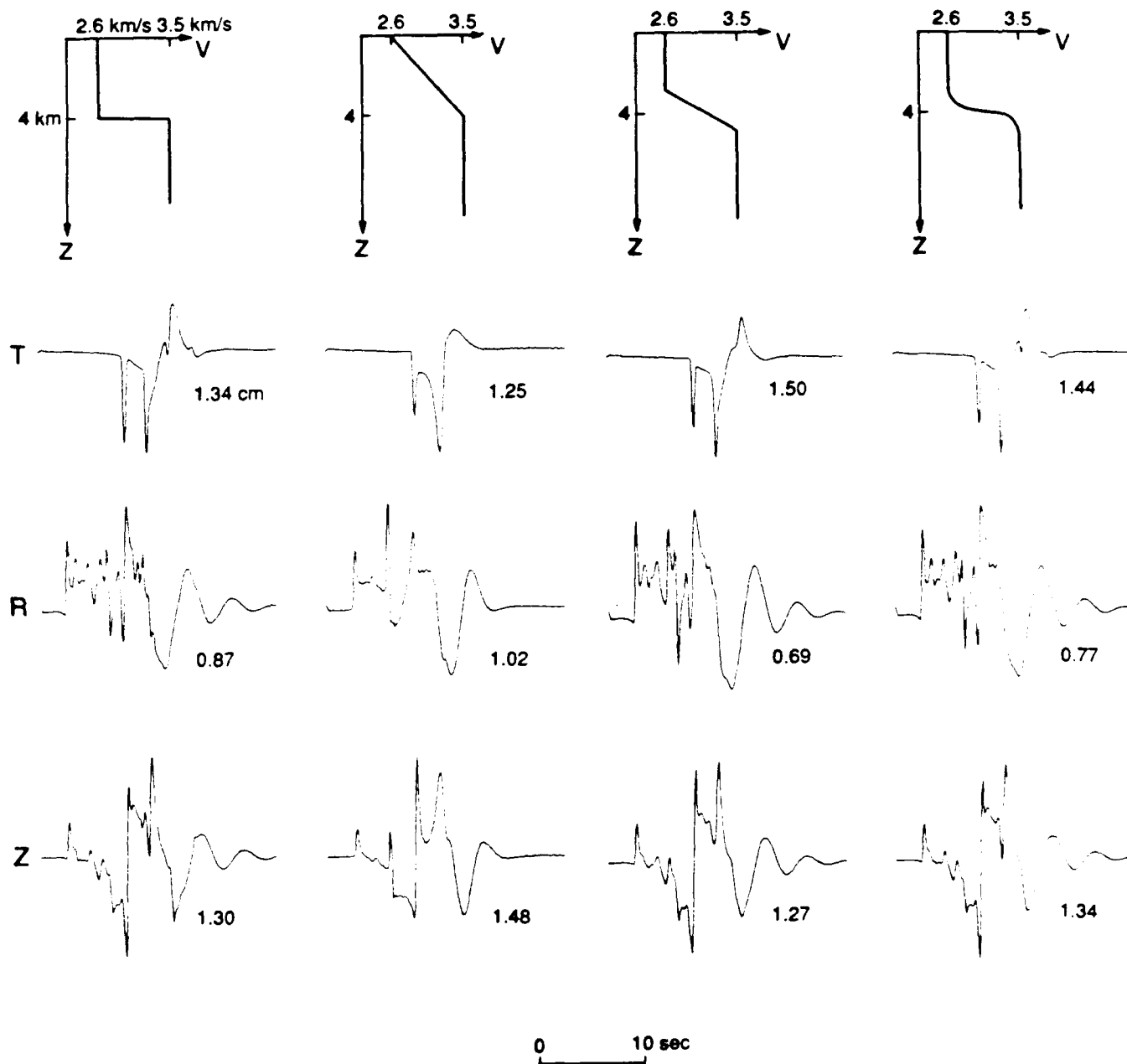


Figure 8

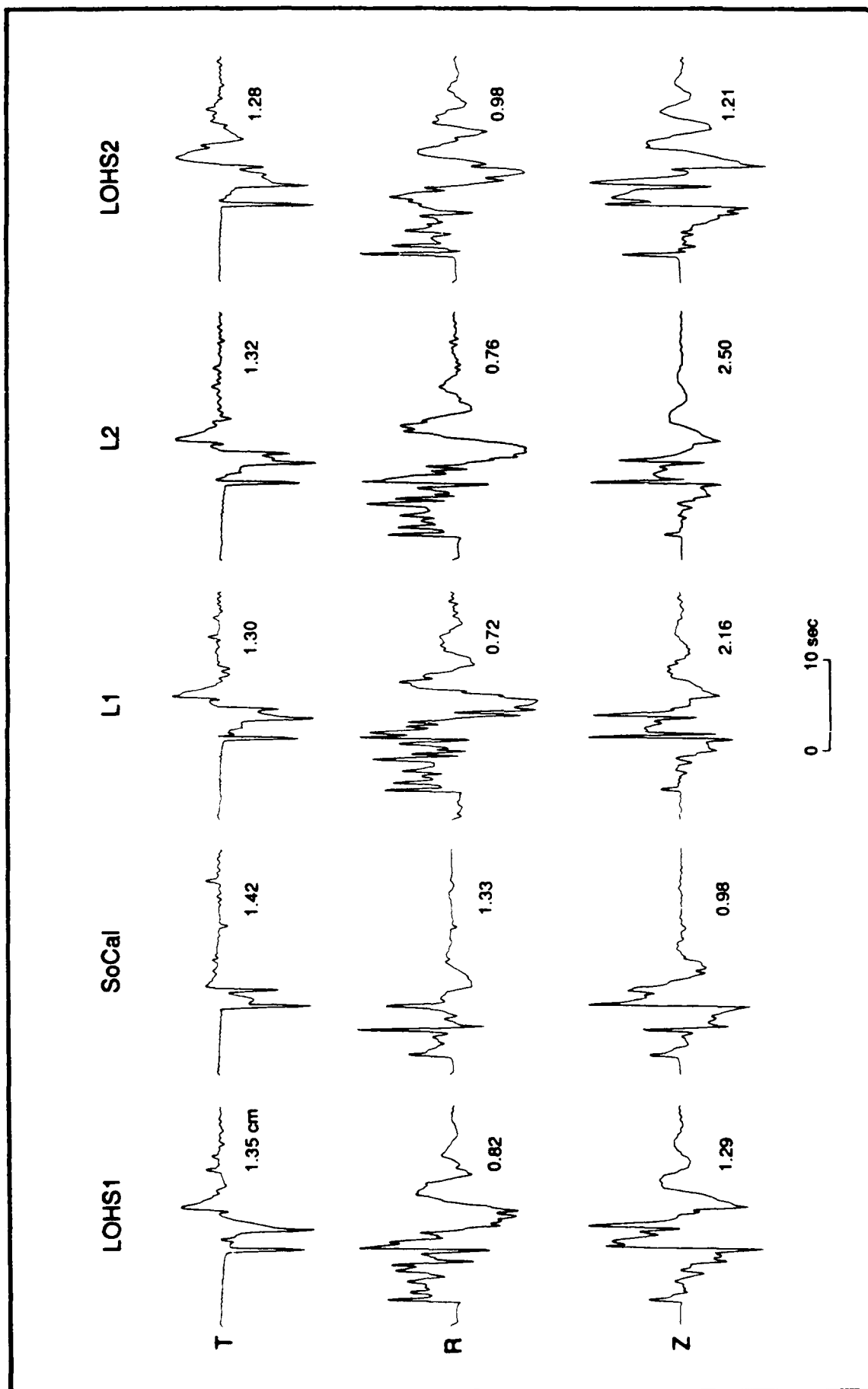


Figure 9  
120



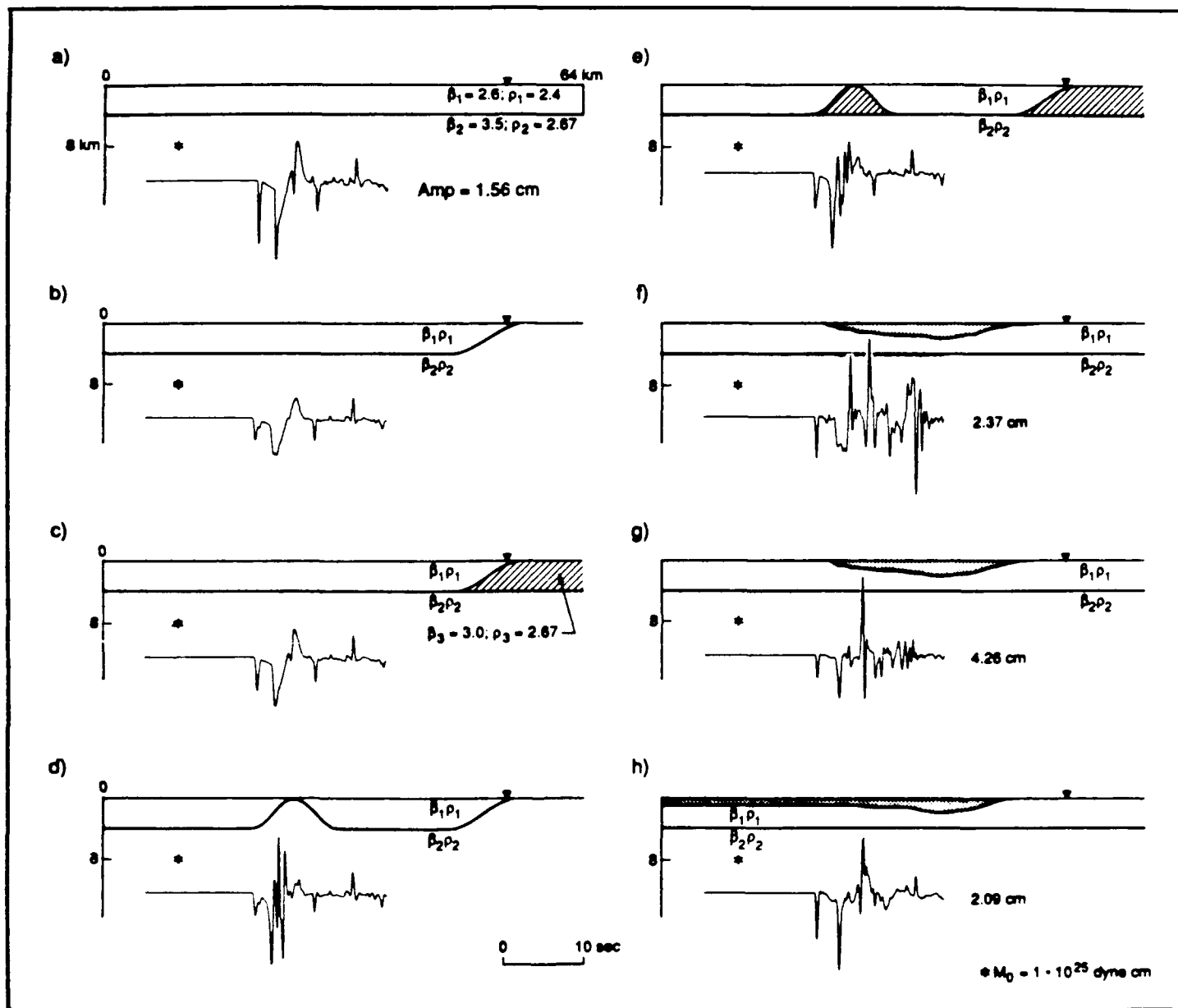
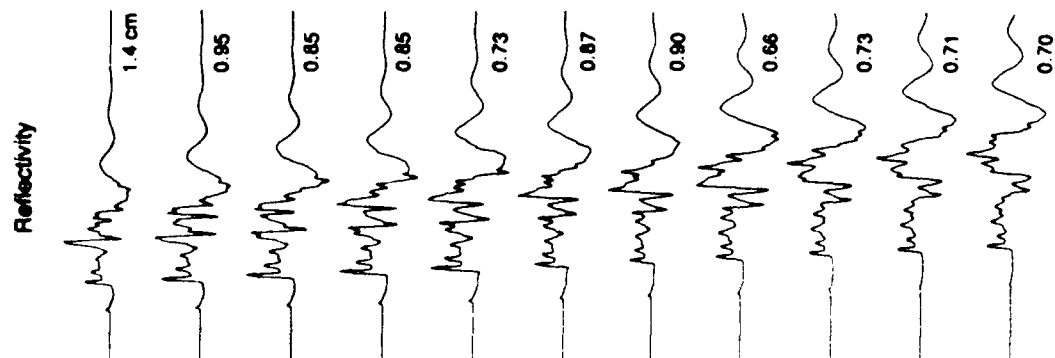
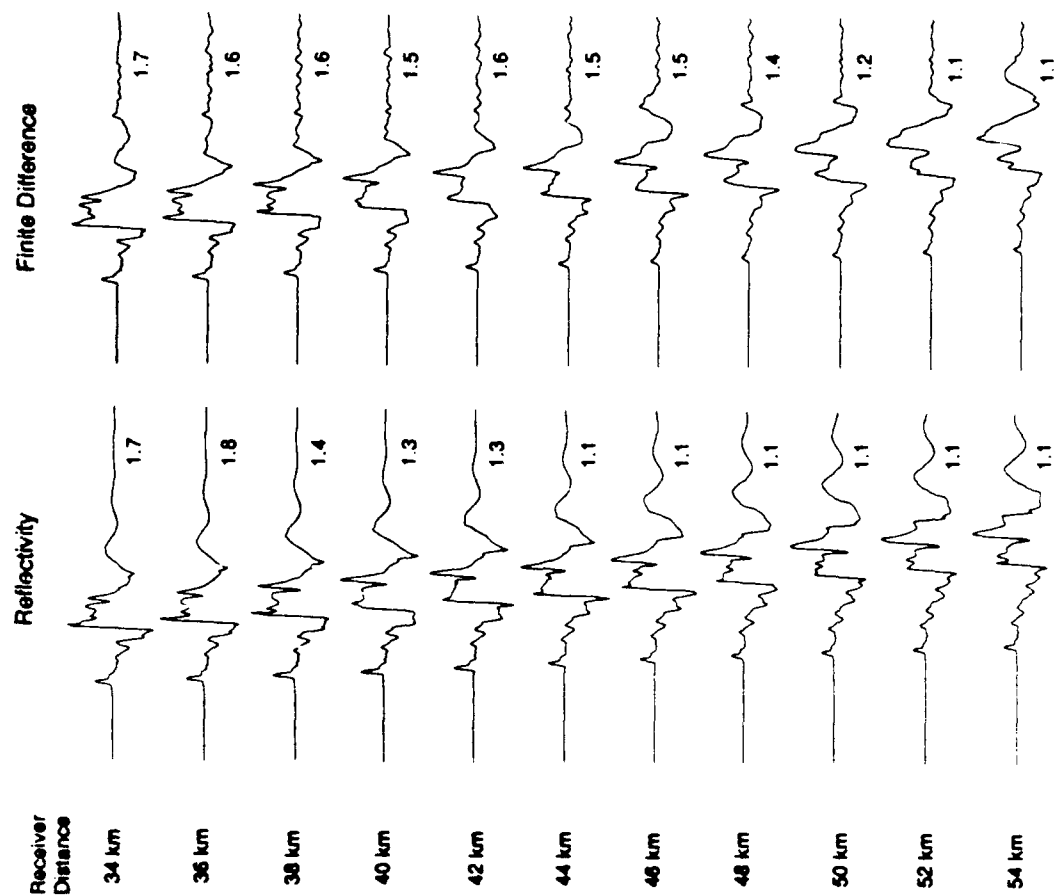


Figure 10

# Radial



# Vertical



0 10 sec

Figure 11

## Figure Captions

Figure 1. Map showing the locations; the triangle is the Pasadena station, the circle is the Chino events, and the stars denote the Upland events. Hatched regions represent areas of shallow or surficial basement rocks after Yerkes (1965).

Figure 2. Tangential components of the February 16, 1988 ( $M_L=3.2$ ) and February 18, 1988 ( $M_L=4.3$ ) Chino earthquakes. The integrated broad-band recordings have been convolved with a short-period Wood-Anderson instrument response. Each seismogram is scaled to maximum amplitude.

Figure 3. Three component, displacement, and short-period Wood-Anderson data for the June 26, 1988 ( $M_L=4.6$ ) and July 6, 1988 ( $M_L=3.7$ ) Upland events. Each seismogram is scaled to maximum amplitude.

Figure 4. The addition of rays to construct a synthetic waveform, assuming a moment of  $1.0 \times 10^{25}$  dyne-cm. Note the ramp like near field term on the tangential component. Each seismogram is scaled to maximum amplitude.

Figure 5. Comparison of tangential component synthetic seismograms with data (synthetics were computed with generalized rays). Moments are  $1.7 \times 10^{22}$ , and  $7.9 \times 10^{22}$  dyne-cm for the aftershock and mainshock, respectively. Each seismogram is scaled to maximum amplitude.

Figure 6. Comparison of radial component synthetic seismograms with data (synthetics were computed with reflectivity). Moments are  $1.5 \times 10^{22}$ , and  $8.2 \times 10^{22}$  dyne-cm for the aftershock and the mainshock, respectively. Each seismogram is scaled to maximum amplitude.

Figure 7. Comparison of vertical component synthetic seismograms with data (synthetics were computed with reflectivity). Moments are  $7.7 \times 10^{21}$ , and  $1.9 \times 10^{22}$  dyne-cm for the aftershock and the mainshock, respectively. Each seismogram is scaled to maximum amplitude.

Figure 8. Boundary sharpness sensitivity assuming a moment of  $1.0 \times 10^{25}$  dyne-cm. Each seismogram is scaled to maximum amplitude.

Figure 9. Flat layered model sensitivity assuming a moment of  $1.0 \times 10^{25}$  dyne-cm. Each seismogram is scaled to maximum amplitude.

Figure 10. SH finite difference calculations showing ridge structures and realistic basins after Yerkes, 1965. Dotted region in 10f represents  $\rho=2.0 \text{ g cm}^{-3}$  and  $\beta=1.8 \text{ km s}^{-1}$ . For figures 10g and 10h the dotted region represents a linear gradient in velocity with the form  $v = 1.8 + 0.4z$ . Moment used is  $1.0 \times 10^{25}$  dyne-cm. Each seismogram is scaled to the maximum amplitude of 10a, except 10fgh, where their maximum amplitudes are given.

Figure 11. Radial and vertical component synthetics showing the difference between a flat layer over a half-space and the model in figure 10c. Moment used is  $1.0 \times 10^{25}$  dyne-cm. Each seismogram is scaled to maximum amplitude.

## **SECTION 4**

### **Wave Fields From An Off-Center Explosion In An Embedded Solid Sphere**

# WAVE FIELDS FROM AN OFF-CENTER EXPLOSION IN AN EMBEDDED SOLID SPHERE

BY LIAN-SHE ZHAO AND DAVID G. HARKRIDER

## ABSTRACT

This study investigates the effects of explosions in asymmetric source regions on the excitation of seismic body waves. We give an analytic formulation for determining the wave fields from an off-center explosion in an embedded solid sphere in an elastic whole-space. As expected, this geometry generates shear as well as compressional body waves. The calculated wave fields show that the *SV* and *SH* wave generation is determined by the asymmetry of the source region. The results are compared with the known analytic solutions of an explosion in an elastic whole-space and at the center of an elastic sphere embedded in the whole-space. The radiation patterns at different periods for different parameters of the media suggest that the asymmetry of the source region has significant effects on shorter period, but has only minor effects on long periods. The long period *P* to *S* wave maximum amplitude results are in agreement with that for explosions in axisymmetric cavities.

## INTRODUCTION

Shear waves are almost always observed from underground explosions. One can visualize many ways to convert explosion *P* waves into *SV* waves. An obvious mechanism is the free-surface or other near by boundaries. But the presence of *SH* waves is especially perplexing. The *SH* waves are generally considered to be due to tectonic release from volume relaxation of the local prestress surrounding

the shot point or as a triggered earthquake on nearby fault planes (Press and Archambeau, 1962). Other mechanisms for SH wave excitation have also been investigated; such as, the conversion of source P waves from explosions in long narrow valleys and the generation of S waves by explosions in anisotropic media and axisymmetric cavities (Glenn et al, 1985, 1986, and Rial and Moran, 1986). We show in this paper that a significant amount of shear waves can be generated by an asymmetric source region. We give the formulation for the wave fields of an off-center explosive source in an elastic homogeneous sphere embedded in an elastic homogeneous whole-space with different elastic constants and densities. We expand the wave fields for the problem into spherical harmonics and use the welded interface boundary conditions at the spherical contact to find the coefficients of the expansion. Initially, the spherical coordinate system is oriented with the source on the vertical axis, ie.  $\theta=0$ , so that only SV waves are generated. Once the displacement field is obtained, the coordinate system is rotated for a more general source location and expressions are then given to convert the wave fields into P, SV, and SH wave potentials and their respective displacement fields.

## THEORY

The geometry and the coordinate system are given in Figure 1. The displacement resulting from an explosive source located at  $(r_0, \theta_0, \phi_0)$  in spherical coordinate system, in a homogeneous, isotropic, unbounded elastic medium may be expressed in the form (Ben-Menahem and Singh 1981, p384):

$$\mathbf{u}_0 = i k_a g(\omega) A_0 \nabla h_0^{(2)}(k_a R)$$

for the receiver located at  $(r, \theta, \phi)$ , where  $g(\omega)$  is the spectrum of explosive source function;  $\nabla$  is gradient;  $h_0^{(2)}(k_a R)$  is spherical Hankel function of second kind;  $k_a = \omega/\alpha$ ;  $\alpha$  is the compressional velocity;  $\alpha^2 = (\lambda + 2\mu)/\rho$  in terms of the density  $\rho$  and the lame' constants;  $R$  is distance between source and receiver; and

$$A_0 = \frac{M_0}{4\pi(\lambda + 2\mu)}$$

where  $M_0$  is seismic moment.

We now express the spherical Hankel function  $h_0^{(2)}(k_a R)$  in terms of  $r_0$ ,  $r$  and the angle  $\delta$  between the position vectors of the source and receiver as

$$h_0^{(2)}(k_a R) = \sum_{l=0}^{\infty} (2l+1) j_l(k_a r_0) h_l^{(2)}(k_a r) P_l(\cos\theta)$$

where  $r \geq r_0$ ,  $j_l(k_a r)$  is spherical Bessel function; and  $P_l(\cos\theta)$  is the Legendra function. The replacement of  $\delta$  by  $\theta$  is equivalent to assuming that the source is located on the  $z$  axis, that is,  $\theta_0 = 0$ . With this substitution, the displacement expression becomes

$$u_0 = i k_a^2 g(\omega) A_0 \sum_{l=0}^{\infty} (2l+1) j_l(k_a r_0) L_{0l}^-(k_a r)$$

for  $r \geq r_0$  and where  $L_{0l}^-(k_a r)$  is defined below.

If we bound the source medium by a sphere of radius  $r=a$ , we can assume the displacement field inside and outside as

$$u_1 = u_0 - \sum_{l=0}^{\infty} (2l+1) [a_l N_{0l}^+(k_{\beta_1} r) + b_l L_{0l}^+(k_{\alpha_1} r)] \quad (1a)$$

for  $r > r_0$ ,  $r \leq a$  and

$$u_2 = \sum_{l=0}^{\infty} (2l+1) [c_l N_{0l}^-(k_{\beta_2} r) + d_l L_{0l}^-(k_{\alpha_2} r)] \quad (1b)$$

for  $r \geq a$ , where  $k_{\beta} = \omega/\beta$ ;  $\beta$  is the shear velocity; and  $\beta^2 = \mu/\rho$ . The boundary conditions to be satisfied at  $r=a$  are

$$u_1 = u_2 \quad (2a)$$

$$e_r \cdot \Xi(u_1) = e_r \cdot \Xi(u_2) \quad (2b)$$

, where  $\Xi$  is the stress dyadic. The displacement and stress dyadic can be



conveniently expressed in terms of the Hansen vectors, which are the eigenvector solutions of the force-free Navier equation (Ben-Menahem and Singh 1981, Chapter 2). The Hansen vectors in terms of spherical harmonics are

$$\mathbf{L}_{ml}^{\pm}(\xi) = \frac{d}{d\xi} f \tilde{r}^{\pm}(\xi) \mathbf{P}_{ml}(\theta, \phi) + \frac{1}{\xi} f \tilde{r}^{\pm}(\xi) [l(l+1)]^{\frac{1}{2}} \mathbf{B}_{ml}(\theta, \phi)$$

$$\mathbf{N}_{ml}^{\pm}(\eta) = \frac{1}{\eta} f \tilde{r}^{\pm}(\eta) l(l+1) \mathbf{P}_{ml}(\theta, \phi) + \left( \frac{d}{d\eta} + \frac{1}{\eta} \right) f \tilde{r}^{\pm}(\eta) [l(l+1)]^{\frac{1}{2}} \mathbf{B}_{ml}(\theta, \phi)$$

where

$$\mathbf{P}_{ml}(\theta, \phi) = \mathbf{e}_r P_l^m(\cos\theta) e^{im\phi} = \mathbf{e}_r Y_{ml}(\theta, \phi)$$

$$\sqrt{l(l+1)} \mathbf{B}_{ml} = (\mathbf{e}_\theta \frac{\partial}{\partial \theta} + \mathbf{e}_\phi \frac{\partial}{\sin\theta \partial \phi}) P_l^m(\cos\theta) e^{im\phi}$$

and where  $\xi = k_\alpha r$ ,  $\eta = k_\beta r$ ,  $f \tilde{r}^+(z) = j_l(z)$ , and  $f \tilde{r}^-(z) = h_l^{(2)}(z)$ .

The corresponding stresses are given by

$$\mathbf{e}_r \cdot \Xi(\mathbf{L}) = 2\mu k_\alpha [F_{l,3}(\xi) \mathbf{P}_{ml} + F_{l,1}(\xi) [l(l+1)]^{\frac{1}{2}} \mathbf{B}_{ml}]$$

$$\mathbf{e}_r \cdot \Xi(\mathbf{N}) = \mu k_\beta [2l(l+1) F_{l,1}(\eta) \mathbf{P}_{ml} + F_{l,2}(\eta) [l(l+1)]^{\frac{1}{2}} \mathbf{B}_{ml}]$$

The functions  $F_{l,i}$  are given by

$$F_{l,1}(z) = \frac{1}{z} \left( \frac{d}{dz} - \frac{1}{z} \right) f \tilde{r}^{\pm}(z) = \frac{(l-1)}{z^2} f \tilde{r}^{\pm}(z) - \frac{1}{z} f \tilde{r}_{+1}^{\pm}(z)$$

$$F_{l,2}(z) = \left[ \frac{2}{z^2} (l^2 - 1) - 1 \right] f \tilde{r}^{\pm}(z) + \frac{2}{z} f \tilde{r}_{+1}^{\pm}(z) = \frac{d^2 f \tilde{r}^{\pm}}{dz^2} + \frac{(l-1)(l+2)}{z^2} f \tilde{r}^{\pm}(z)$$

$$F_{l,3}(z) = \left[ \frac{1}{z^2} l(l-1) - \frac{1}{2} \left( \frac{\alpha}{\beta} \right)^2 \right] f \tilde{r}^{\pm}(z) + \frac{2}{z} f \tilde{r}_{+1}^{\pm}(z) = \frac{d^2 f \tilde{r}^{\pm}}{dz^2} - \frac{\lambda}{2\mu} f \tilde{r}^{\pm}(z)$$

Substituting the above into equation (1), we have for the  $l$ th components of the displacements

$$\begin{aligned}
 u_{1l} = & i k_{\alpha_1}^2 g(\omega) A_0 (2l+1) j(k_{\alpha_1} r_0) [f_{l,1}'(\xi_1) P_l e_r + \frac{1}{\xi_1} f_{l,1}(\xi_1) \frac{d}{d\theta} P_l e_\theta] \\
 & -(2l+1) a_l \frac{N^2}{\eta_1} f_{l,1}^+(\eta_1) P_l e_r - (2l+1) a_l \left( \frac{d}{d\eta} + \frac{1}{\eta_1} \right) f_{l,1}^+(\eta_1) \frac{d}{d\theta} P_l e_\theta \\
 & -(2l+1) b_l f_{l,1}'(\xi_1) P_l e_r - (2l+1) b_l f_{l,1}(\xi_1) \frac{1}{\xi_1} \frac{d}{d\theta} P_l e_\theta \\
 u_{2l} = & (2l+1) c_l \frac{N^2}{\eta_2} f_{l,2}^-(\eta_2) P_l e_r + (2l+1) c_l \left( \frac{d}{d\eta} + \frac{1}{\eta_2} \right) f_{l,2}^-(\eta_2) \frac{d}{d\theta} P_l e_\theta \\
 & + (2l+1) d_l f_{l,2}'(\xi_2) P_l e_r + (2l+1) d_l f_{l,2}(\xi_2) \frac{1}{\xi_2} \frac{d}{d\theta} P_l e_\theta
 \end{aligned}$$

and the  $l$ th components of the spherical surface tractions

$$\begin{aligned}
 e_r \cdot \Xi(u_{1l}) = & i k_{\alpha_1}^2 g(\omega) A_0 (2l+1) j_l(k_{\alpha_1} r_0) [F_{l,3}(\xi_1) P_l(\cos\theta) e_r + F_{l,1}(\xi_1) \frac{d}{d\theta} P_l(\cos\theta) e_\theta] \\
 & -(2l+1) a_l \mu_1 k_{\beta_1} [2N^2 F_{l,1}^+(\eta_1) P_l(\cos\theta) e_r + F_{l,2}^+(\eta_1) \frac{d}{d\theta} P_l(\cos\theta) e_\theta] \\
 & -2(2l+1) b_l \mu_1 k_{\alpha_1} [F_{l,3}(\xi_1) P_l(\cos\theta) e_r + F_{l,1}(\xi_1) \frac{d}{d\theta} P_l(\cos\theta) e_\theta] \\
 e_r \cdot \Xi(u_{2l}) = & (2l+1) c_l \mu_2 k_{\beta_2} [2N^2 F_{l,1}^-(\eta_2) P_l(\cos\theta) e_r + F_{l,2}^-(\eta_2) \frac{d}{d\theta} P_l(\cos\theta) e_\theta] \\
 & +2(2l+1) d_l \mu_2 k_{\alpha_2} [F_{l,3}(\xi_2) P_l(\cos\theta) e_r + F_{l,1}(\xi_2) \frac{d}{d\theta} P_l(\cos\theta) e_\theta]
 \end{aligned}$$

where  $N^2 = l(l+1)$  and the prime  $(')$ , denotes differentiation by the functions argument, and where  $\xi_1 = k_{\alpha_1} a$ ,  $\eta = k_{\beta_1} a$ ,  $\xi_2 = k_{\alpha_2} a$ , and  $\eta = k_{\beta_2} a$

Using equation (2), and comparing the coefficients of  $P_l(\cos\theta)\mathbf{e}_r \cdot \mathbf{u}_l$ ,  $\frac{d}{d\theta}P_l(\cos\theta)\mathbf{e}_\theta \cdot \mathbf{u}_l$ ,  $P_l(\cos\theta)\mathbf{e}_r \cdot \Xi(\mathbf{u}_l) \cdot \mathbf{e}_r$ , and  $\frac{d}{d\theta}P_l(\cos\theta)\mathbf{e}_r \cdot \Xi(\mathbf{u}_l) \cdot \mathbf{e}_\theta$ , we have

$$\mathbf{Y}\mathbf{C}=\mathbf{D} \quad (3)$$

where

$$\mathbf{D}=ik_{\alpha}^2g(\omega)A_0j_l(k_{\alpha}r_0)[f_l^{-'}(\xi_1),\frac{1}{\xi_1}f_l^{-}(\xi_1),2\mu_1k_{\alpha}F_{l,3}^{-}(\xi_1),2\mu k_{\alpha}F_{l,1}(\xi_1)]^T \quad (4)$$

$$\mathbf{C}=(a_l,b_l,c_l,d_l)^T \quad (5)$$

$$\mathbf{Y}=\begin{bmatrix} \frac{N^2}{\eta_1}f_l^{+}(\eta_1) & f_l^{+'}(\xi_1) & \frac{N^2}{\eta_2}f_l^{-}(\eta_2) & f_l^{-'}(\xi_2) \\ (\frac{d}{d\eta}+\frac{1}{\eta_1})f_l^{+}(\eta_1) & \frac{1}{\xi_1}f_l^{+}(\xi_1) & (\frac{d}{d\eta}+\frac{1}{\eta_2})f_l^{-}(\eta_2) & \frac{1}{\xi_2}f_l^{-}(\xi_2) \\ 2\mu_1k_{\beta_1}N^2F_{l,1}^{+}(\eta_1) & 2\mu_1k_{\alpha_1}F_{l,3}^{+}(\xi_1) & 2\mu_2k_{\beta_2}N^2F_{l,1}^{-}(\eta_2) & 2\mu_2k_{\alpha_2}F_{l,3}^{-}(\xi_2) \\ \mu_1k_{\beta_1}F_{l,2}^{+}(\eta_1) & 2\mu_1k_{\alpha_1}F_{l,1}^{+}(\xi_1) & \mu_2k_{\beta_2}F_{l,2}^{-}(\eta_2) & 2\mu_2k_{\alpha_2}F_{l,1}^{-}(\xi_2) \end{bmatrix} \quad (6)$$

We can now determine the coefficients (5) of the expansion (1) by equation (3).

For inclusion of this and rotated versions of this source into a vertically inhomogeneous half-space, it is frequently convenient to express the source in terms of P and S waves by use of the Helmholtz resolution,

$$\mathbf{u}=\nabla\Phi+\nabla\times\Psi \quad (7)$$

where  $\Phi$  is P the potential and  $\Psi$  is the S wave potential. For the external medium, they can be expressed as

$$\Phi=\frac{1}{k_{\alpha}}\sum_{l=0}^{l=\infty}(2l+1)d_lh_l^{(2)}(k_{\alpha}r)P_l(\cos\theta) \quad (8)$$

$$\Psi=-\frac{1}{k_{\beta}}\sum_{l=0}^{l=\infty}(2l+1)c_lh_l^{(2)}(k_{\beta}r)\frac{d}{d\theta}P_l(\cos\theta)\mathbf{e}_{\theta} \quad (9)$$

Generally, if the source is located at  $(r_0,\theta_0,\phi_0)$ ,  $\theta$  and  $\phi$  in equation (8) and (9) should be changed to  $\delta$  and  $\gamma$ , with  $\cos\delta=\cos\theta\cos\theta_0+\sin\theta\sin\theta_0\cos(\phi-\phi_0)$ . The unit

vectors at the source are now  $\mathbf{e}_r = \mathbf{e}_{r_0} \times \mathbf{e}_r / \sin \delta$ , and  $\mathbf{e}_{r_0}$ . The range of  $\delta$  is 0 to  $360^\circ$ , and  $\delta$  is defined as the angle measured clockwise from the position vector of the source to the position vector of the receiver. The potentials can be written as (Appendix A):

$$\Phi = -\frac{1}{k_\alpha^2} \sum_{n=0}^{\infty} \sum_{m=0}^n [A_{nm} \cos m \phi + B_{nm} \sin m \phi] P_n^m(\cos \theta) h_n^{(2)}(k_\alpha r) \quad (10)$$

$$\Psi_j = -\frac{2}{k_\beta^2} \sum_{n=0}^{\infty} \sum_{m=0}^n [C_{nm}^{(j)} \cos m \phi + D_{nm}^{(j)} \sin m \phi] P_n^m(\cos \theta) h_n^{(2)}(k_\beta r) \quad (11)$$

where  $\Psi_j$  ( $j=1,2,3$ ) are the Cartesian components of the S wave potential  $\Psi$ , and

$$A_{nm} = -(2n+1) \frac{(n-m)!}{(n+m)!} k_\alpha d_n \epsilon_m P_n^m(\cos \theta_0) \cos m \phi_0$$

$$B_{nm} = -(2n+1) \frac{(n-m)!}{(n+m)!} k_\alpha d_n \epsilon_m P_n^m(\cos \theta_0) \sin m \phi_0$$

$$C_{nm}^{(1)} = -\frac{k_\beta}{2} (2n+1) \frac{(n-m)!}{(n+m)!} \epsilon_m c_n \left[ \frac{d}{d\theta_0} P_n^m(\cos \theta_0) \sin \phi_0 \cos m \phi_0 \right. \\ \left. - m P_n^m(\cos \theta_0) \cot \theta_0 \cos \phi_0 \sin m \phi_0 \right]$$

$$D_{nm}^{(1)} = -\frac{k_\beta}{2} (2n+1) \frac{(n-m)!}{(n+m)!} \epsilon_m c_n \left[ \frac{d}{d\theta_0} P_n^m(\cos \theta_0) \sin \phi_0 \sin m \phi_0 \right. \\ \left. + m P_n^m(\cos \theta_0) \cot \theta_0 \cos \phi_0 \cos m \phi_0 \right]$$

$$C_{nm}^{(2)} = \frac{k_\beta}{2} (2n+1) \frac{(n-m)!}{(n+m)!} \epsilon_m c_n \left[ \frac{d}{d\theta_0} P_n^m(\cos \theta_0) \cos \phi_0 \cos m \phi_0 \right. \\ \left. + m P_n^m(\cos \theta_0) \cot \theta_0 \sin \phi_0 \sin m \phi_0 \right]$$

$$D_{nm}^{(2)} = \frac{k_\beta}{2} (2n+1) \frac{(n-m)!}{(n+m)!} \epsilon_m c_n \left[ \frac{d}{d\theta_0} P_n^m(\cos \theta_0) \cos \phi_0 \sin m \phi_0 \right. \\ \left. - m P_n^m(\cos \theta_0) \cot \theta_0 \sin \phi_0 \cos m \phi_0 \right]$$

$$C_{nm}^{(3)} = -\frac{k_\beta}{2} (2n+1) \frac{(n-m)!}{(n+m)!} \epsilon_m c_n P_n^m(\cos \theta_0) \sin m \phi_0$$

$$D_{nm}^{(3)} = \frac{k\beta}{2}(2n+1)\frac{(n-m)!}{(n+m)!}\epsilon_m c_n P_n^m(\cos\theta_0)\cos m\phi_0$$

where  $\epsilon_m = 1$  if  $m = 0$ ,  $\epsilon_m = 2$  if  $m \neq 0$ .  $\Psi_3$  is the SH wave potential.

From the equations (11), we can see that SH waves will be generated if  $C_{nm}^{(3)}$  and  $D_{nm}^{(3)}$  are not zero in Cartesian coordinate system. Harkrider et al. (1991) gives a detailed derivation of the surface waves in layered media due to a transparent source expressed in the general form (10) and (11).

When the explosion source is on the  $z$  axis, as in equation (9), there are only  $SV$  waves because of symmetry. As one moves the source off the  $z$  axis, the  $C_{nm}^{(3)}$  and  $D_{nm}^{(3)}$  are no longer zero and we have SH waves as one would expect.

Even though equations (10) and (11) are convenient for calculating surface waves, they are awkward for evaluating the whole space wave fields. We introduce an alternative approach. If the source is located at  $(r_0, 0, 0)$ , the displacement fields and the potentials are given by equations (1), (8) and (9). If the source is located at  $(r_0, \theta_0, \phi_0)$ , as discussed above, the coordinate system, with  $\mathbf{e}_{r_0}$  as north pole, has unit base vectors  $(\mathbf{e}_r, \mathbf{e}_\delta, \mathbf{e}_\gamma)$ , and coordinates  $(r, \delta, \gamma)$ , where the definitions of  $\delta$  and  $\mathbf{e}_\gamma$  are given above. In this coordinate system, the displacement fields and  $S$  potential can be written as:

$$\mathbf{u} = (u_P^r + u_{SV}^r)\mathbf{e}_r + (u_P^\delta + u_{SV}^\delta)\mathbf{e}_\delta, \quad (12)$$

and

$$\Psi = \psi \mathbf{e}_\gamma. \quad (13)$$

where

$$\mathbf{e}_\gamma = \mathbf{e}_{r_0} \times \mathbf{e}_r / \sin\delta$$

and

$$\mathbf{e}_\delta = \mathbf{e}_\gamma \times \mathbf{e}_r$$

$$= \frac{1}{\sin \delta} (\mathbf{e}_r (\mathbf{e}_r \cdot \mathbf{e}_{r_0}) - \mathbf{e}_{r_0}).$$

Thus, the displacement fields in the coordinate system  $(r, \theta, \phi)$  can be written as:

$$\mathbf{u} = u^r \mathbf{e}_r + u^\theta \mathbf{e}_\theta + u^\phi \mathbf{e}_\phi, \quad (14)$$

with

$$u^r = u_P^r + u_{SV}^r,$$

$$u^\theta = -(u_P^\theta + u_{SV}^\theta) (\sin \theta_0 \cos \theta \cos(\phi - \phi_0) - \cos \theta_0 \sin \theta) / \sin \delta,$$

and

$$u^\phi = (u_P^\phi + u_{SV}^\phi) \sin \theta_0 \sin(\phi - \phi_0) / \sin \delta.$$

And the  $S$  potential can be written as:

$$\Psi = \psi^r \mathbf{e}_r + \psi^\theta \mathbf{e}_\theta + \psi^\phi \mathbf{e}_\phi \quad (15)$$

with

$$\psi^r = 0,$$

$$\psi^\theta = -\psi \sin \theta_0 \sin(\phi - \phi_0) / \sin \delta,$$

and

$$\psi^\phi = -\psi (\sin \theta_0 \cos \theta \cos(\phi - \phi_0) - \cos \theta_0 \sin \theta) / \sin \delta.$$

When  $\delta = 0$  or  $180^\circ$ , equations (14) and (15) no longer hold. This is when the source and receiver are on a line through the sphere origin and then we should use equations (8) and (9).

Before going on to numerical examples, there is one further point to discuss. The observed seismic moment is

$$M_{obs} = \frac{\rho_2 \alpha_2^2}{\rho_1 \alpha_1^2 + \frac{4}{3}(\rho_2 \beta_2^2 - \rho_1 \beta_1^2)} M_0 \quad (16)$$

Where  $M_0$  is the input moment. This equation can be obtained by using the equation (B4) of Appendix B and letting  $\omega$  go to zero. Since nuclear explosion sources are frequently characterized by  $A_0$  or the more familiar notation,  $\Psi(\infty)$ , which is the asymptotic value of the reduced displacement potential for large time, and

$$M_0 = 4\pi\rho\alpha^2\Psi(\infty),$$

we can write equation (16) as

$$\Psi(\infty)_{obs} = \frac{1}{1 + \frac{4}{3} \frac{\beta_1^2}{\alpha_1^2} \left( \frac{\mu_2}{\mu_1} - 1 \right)} \Psi(\infty) \quad (17)$$

where the elastic rigidity  $\mu = \rho\beta^2$ . Thus the difference between observed and shot point  $\Psi(\infty)$  is independent of density contrast and in source media with similar Poisson ratios is only a function of the rigidity ratio of the material in which the  $\Psi(\infty)$  is measured and the shot point material. The smaller the source region rigidity, the smaller the observed  $\Psi(\infty)$  while large source rigidities cause amplification. Since the minimum realistic ratio of P to S wave ratios is  $\sqrt{2}$ , which corresponds to a Poisson ratio of zero, the maximum possible amplification is a factor of 3.

## RESULTS

In this section, we present some numerical results. For all of the synthetics, we assume that the moment time history is a step function, ie.

$$g(\omega) = 1/i\omega,$$

and

$$M_0 = 4\pi\rho_1\alpha_1^2 \times 10^{20} \text{ dyne-cm},$$

where  $\rho$  is in  $g/cm^3$ , and the velocities,  $\alpha$  and  $\beta$ , are in  $km/sec$ , and distances in  $km$ . Thus  $\Psi(\infty)$  is kept the same for the different spherical source media models. The distances are in  $km$  and the displacement is in  $cm$ . The spectral band-width

is from 102.4 seconds in period to 10 Hz. As our standard model, we assume the elastic parameters and dimensions given in Table 1. The receiver is located 10 km from the center of the elastic sphere unless otherwise indicated. The material model for the whole-space outside of the sphere is reasonable for sedimentary regions, see for example Zhao et al. (1991). When investigating the effect of different elastic properties of the sphere, Nafe's velocity-density relation (Ludwig et al. 1970) is used to obtain densities and S wave velocities for a given P velocity. We used 20 terms to sum up the wave fields, see Equation (1). The error induced from truncation of order  $m$ , is approximately the order  $m^6(r_0/r)^m$ .

Figure 2 gives a comparison of displacement fields calculated by our infinite series formulation, ie. inversion of equation (5), and by the numerical evaluation of two analytic closed form solutions. The upper pair of synthetics show the whole space results, while the lower pair show the results for a source located at the center of the solid sphere in a whole-space. The formulation for the wave field outside of the solid sphere due to a centered explosion is given in Appendix B. The solutions, both closed and series, are calculated in the frequency domain, and then transformed to the time domain, so that each pair of time histories show almost identical precursor artifacts, which are caused by the numerical transforms. The agreement within pairs is excellent.

In the following figures, we will refer to P and S wave arrivals as radial and azimuthal. These are  $u_P^r$ ,  $u_P^\theta$ ,  $u_S^r$ , and  $u_S^\theta$  respectively in the notation of the previous section. The P waves are the contribution to the displacement field from the P potential, begin at the P wave arrival time, and physically correspond to P or compressional waves arriving at the receiver which have undergone multiple reflections and conversions between P and S in the spherical source region. An analogous statement applies to the S waves with P replaced by S and compressional by shear. At a range,  $r$ , of 10 km for the standard model, the near-field P



arrival  $u_p^f$ , which is the displacement component perpendicular to the propagation direction, and the near-field S arrival  $u_s^f$ , which is the component in the radial or propagation direction, are about 10% of the far-field arrivals  $u_p^f$  and  $u_s^f$ . For a dynamic point source, one would expect far-field displacements to fall off as  $1/r$  and the near-field to attenuate as  $1/r^2$ . This was investigated by generating wave fields at ranges from 5 to 40 km in 5 km intervals for the standard model. The wave form of each of these displacement components was found to be independent of range and by 10 km, the displacements fields indeed attenuated as predicted.

In most of the following examples,  $\theta$  is set to  $90^\circ$ , i.e. the source and receiver are both in the horizontal plane. This was done to check our numerical algorithms for the transformations given in equation (14), which are used to obtain SV and SH displacements from the initial SV only shear displacement field.

Figure 3 shows displacements at a receiver located at  $(r, \theta, \phi) = (10, 90^\circ, 90^\circ)$ , with the source at  $(0.45, 90^\circ, 180^\circ)$ . At these coordinates, the source and receiver position vectors are  $90^\circ$  to each other with respect to the sphere origin. We see that, strong shear waves, as evidenced by the azimuthal component of  $S$  waves, are generated at receiver azimuths  $90^\circ$  from the symmetry axis of the source and the center of the sphere. Also the time difference between the two biggest arrivals in both the  $P$  and  $S$  waveforms, is about 2.5 seconds, which is the time needed for an  $S$  phase to travel through the sphere. This interval can be detected between many arrivals. Thus the bigger arrivals in the seismograms, except for direct  $P$  and  $S$  generated at the sphere boundary can be interpreted as phases, which have traveled through the sphere at least once as  $S$ . The  $S$  wave displacement is about a factor of 10 greater than the  $P$  wave displacement. This is somewhat misleading, since as we shall see in later examples, this is the azimuth of minimum  $P$  displacement and of maximum long period  $S$ .

The change in displacement fields as a function of source asymmetry is

displayed in Figure 4 . The model and the geometry are the same as that used for Figure 3, except that the source radius,  $r_0$  is varied from 0 to 0.45 km, the location in Figure 3, in 0.05 km increments. From this figure, we see that only  $P$  waves are generated when the source is at the center of the sphere,  $r_0$  equal to 0. At this azimuth, as  $r_0$  increases, the  $P$  wave maximum amplitude is reduced by about a factor of 10, while the  $S$  wave amplitude is increased to almost 50% greater than the  $P$  waves due to the centered source. The bottom traces,  $r_0=0.45$  km , are the same as those in Figure 3 except on a common scale.

Figure 5 illustrates the effects on the wave fields as the the velocity-density structure of the spherical source region is varied. The exterior medium properties are same for all cases and are given in Table 1. The first row of traces are the same as those in Figure 3. For the bottom row, the sphere and surrounding space have identical properties and thus these traces are the results for an explosion in a whole space. The source-receiver geometry is the same as Figure 3. We see that, the greater the elastic contrast between the spherical source region and exterior medium, the greater the  $S$  waves generated. This is evidenced by the relative excitation between  $P$  and  $S$  on any given row. In making amplitude comparisons between differing source media in the figure, one must remember that the moment increases as one moves down the row with increasing velocities and density while  $\Psi(\infty)$  remains unchanged.

Figure 6 shows the wave field variations as the angle,  $\delta$ , between the source and receiver position vectors changes. When  $\delta=0$ , the source, the receiver, and the center of the sphere are in a line. At this angle, no  $P$  or  $S$   $\delta$  components are generated. The near-field  $S$   $r$  components are  $P$  to  $S$  conversions at the boundary which are focused back on the axis. The elastic sphere acts as a contact lens magnifying the the wave fields, like the Earth does at the antipode of an earthquake (Rial, 1980). When  $\delta$  increases, the  $P$  amplitude decreases, and  $S$  amplitude

increases.

The bottom traces are again those of Figure 3. Comparing the bottom row with the top row and then with the top row of Figure 4, we see that the maximum *S* wave amplitude is almost 3 times the maximum *P* wave amplitude for this the maximum degree of asymmetry investigated and is more than 50% greater than the *P* wave amplitude for the center explosion. Thus from Figures 4,5 and 6, we see that the degree of asymmetry of the source region and the contrast between the media determine the intensity of the *S* wave fields.

In Figure 7, we show the results for different sizes of the elastic sphere. The source radius is kept at the same fraction of the sphere's radius as in previous cases, ie.  $r_0$  is  $0.9a$ . The fourth row in the figure is the same as the last row in Figure 6 since the radii and source-receiver angles are the same, ie. 0.5 km and  $90^\circ$ . Most of the observed effects can be explained by noting that increasing the radius under these conditions is similar to decreasing the velocity. Thus we expect time differences between arrivals to increase and a decrease in frequency content as the radius increases.

Figure 8 displays the radial components of the *P* waves on the symmetry axis for different source radii with  $\delta=0$ , ie. source and receiver on the same side of sphere center and  $180^\circ$ , ie. opposite sides. The distance used is 10 km from the source while in previous figures the receiver was 10 km from the sphere center. If the source is located at the center of the solid sphere, the wave fields for  $\delta=0$ , and  $180^\circ$  are of course identical. The numerical evaluation of the analytical solution was shown in Figure 2. As the source is moved toward the boundary of the sphere, the early arrivals separate and diminish in amplitude for  $\delta=0$ . For  $\delta=180^\circ$ , they converge and grow in amplitude as the source passes through an effective focus in the sphere and then decrease in amplitude as the source is moved closer

to the boundary.

In Figure 9, we keep the dimensions and source-receiver angles the same as Figure 8 but vary the sphere elastic properties using the same relationship between velocities and densities as before. The source radius is 0.45. The first row is the radial  $P$  wave field for velocities and density, which are the same as the previous figure. They can be considered an additional row to the previous figure with the source radius increased from 0.4 to 0.45 km. All traces on this figure are on a common scale in order to demonstrate the increase in amplitude of the early arrivals at  $\delta=0^\circ$  and the reduction in amplitude of the later arriving  $S$  coupled internal reflections at both receiver positions as the velocities and density of the sphere are increased to that of the whole-space. The whole-space result is only slightly larger than the  $\delta=0^\circ$  trace on the bottom and of course smaller than the  $\delta=180^\circ$  bottom trace. The effect of decreasing the impedance contrast and of reducing the travel time for reflections in the sphere reduces the partitioning of direct  $P$  into later arrivals. The increase in moment while keeping  $\Psi(\infty)$  constant as we go down the rows seems to have only a minor effect on the direct  $P$  amplitude. It is notable that the largest amplitude of direct  $P$  is in the middle rows where the elastic contrast is intermediate and in the receiver direction where the path is longest in the sphere, ie.  $\delta=180^\circ$ . This is due to the source being near the focus which changes position relative to source point as we change velocities. This is similar to the previous figure where we moved the source relative to the fixed focus.

With the exception of Figure 6, we have investigated the time histories at either the long period maxima for the  $S$  waves, ie  $\delta=90^\circ$  or at the  $P$  wave maxima, ie.  $\delta=0^\circ$  or  $180$ . Even in Figure 6,  $\delta$  ranged only from 0 to  $90^\circ$ . In the next three figures, we show the radiation pattern for  $P$  and  $S$  at periods of 1 and 20 seconds as a function of source radius, elastic parameters and radius of the sphere.

The periods were chosen for their obvious significance to seismic magnitudes. The asymmetry of the source region is seen to have significant effects on short period radiation patterns, but to have only minor effects on the long period.

Figures 10, 11 and 12 show radiation patterns for different configurations. "P" and "S" in these figures denote the radial component of  $P$  waves and the  $\delta$  component of  $S$  waves respectively. The distance used for these calculations is 1000 km to void the near-field contributions. The source is on the horizontal line for all these figures. The direction of  $\delta$  is indicated on the diagram of the sphere at the top of Figure 10 with a star marking the source. The sphere center is shown as a "+" in all the radiation patterns. The dashed circles with the same centers as the  $P$  radiation patterns are the  $P$  wave radiation pattern for the source located at the center for the particular model and demonstrate the amplitude effect due to source asymmetry. The dashed line part of the  $S$  wave radiation pattern indicates negative amplitude compared to the solid line. The number at the right hand side of the  $S$  wave radiation pattern is the multiplier of the  $S$  wave pattern used to plot on the figure, ie. the larger the number the smaller the actual pattern compared to other  $S$  wave patterns on the figure and the  $P$  wave pattern next to it.

Figure 10, using the standard model, shows the radiation patterns for different source locations,  $r_0$ . Figure 12 uses the same elastic model but different radii of the solid sphere. In Figure 11, the sphere's elastic parameters are varied in the inverse order to Figure 9. Similar effects are seen in all three numerical experiments. As the source radius is increased, the elastic parameters of the sphere are decreased, or the sphere radius is increased, the radiation patterns become more asymmetric. In other words, the  $P$  wave radiation becomes less spherical and the 20 second  $S$  wave pattern, which is essentially the radiation pattern for a point force pointed away from the source, becomes larger. From these figures, we also

see that the intensity of the  $P$  waves radiated by an off-center explosion is greater than that by the corresponding center explosion with the same  $\Psi(\infty)$  except in Figure 12 where increasing the source and sphere radius beyond the dimensions of the standard model, the opposite is true. Also by comparison within each row, we can see that  $S$  wave generation is much smaller and that the  $P$  wave fields are closer to the center explosion excitation for longer periods than for shorter periods.

An interesting feature is the shape of the radiation patterns at short periods. For the  $P$  wave in Figures 10 and 11, we see that the radiation pattern is similar to a dipole. The radiation patterns are reminiscent of those of far-field  $P$  and  $S$  waves scattered from localized inhomogeneities when plane  $P$  waves are incident (Aki and Richards, 1981, pg. 732). This should not be surprising since in our case the incident wave is a spherical  $P$  wave interior to the scatterer. In comparing the Aki and Richards figure with ours, one must remember that our  $P$  wave radiation patterns include the transmitted spherical wave perturbed by the scattering or asymmetric contribution where theirs is only the scattered wave.

Another interesting feature in all three figures is that the maximum long period 20 second  $P$  wave amplitudes are at least twice ( $\approx 1.8$ ) as large as the corresponding maximum  $S$  wave amplitudes for all cases calculated. This is in agreement with the empirical formula for explosions in axisymmetric cavities of Rial and Moran (1986). But because their sources were in the symmetry center of the cavity, the resulting  $S$  wave radiation was more like a dipole than a point force at low frequencies.

In Figure 13, we investigate the error introduced if we estimate the moment by using a finite time length which may include only the initial few pulses. The synthetics in Figure 13 are calculated for our standard velocity and density model keeping only  $1/r$  terms, ie. the far-field approximation. The distance used is 10 km from the center. The top trace is the response of a centered

explosion; the lower one is the response of an off-center explosion. The source is 0.45 km from the center of the sphere and the angle,  $\delta$ , between the source and receiver is  $45^\circ$ . From the long period  $P$  wave radiation patterns, we know that the angle is irrelevant as long as we are interested in moment. The moment is calculated from the area using the zero frequency spectra and corrected from observed to actual moment by equation (16). From the figure, the longer the time interval we use, the better the estimate we get. The first few pulses hold more than 80 percent of the moment in these two examples. Even though the first pulse holds about 90 percent of the moment, in a real situation it would be difficult to separate the effect of local reverberation. In this case, if we take a long enough window, the reverberations finally die down and we get a good estimate.

Figure 14 shows  $M_{obs}/M_0$  as a function, equation (16), of the sphere compressional velocity,  $\alpha_1$ , for different values of the whole-space compression velocities,  $\alpha_2$ , assuming Nafe's velocity-density relation. For exterior velocities greater than those of the sphere, the observed moment  $M_{obs}$  is greater than the input  $M_0$ . And for velocities less, the opposite is true.

## CONCLUSIONS

In this study, we gave the analytical formulae for the wave fields from an off-center explosion in an embedded sphere. Numerical calculations were compared with the known analytic solutions. We also calculated  $P$  and  $S$  wave fields for different  $r_0$ , the source distance to the center (Figure 4), for different sphere materials (Figure 5), for different azimuths,  $\delta$  (Figure 6), and for different sphere radii (Figure 7). The degree of media contrast and the asymmetry of the source determined the size of  $S$  wave generation. For the most extreme case investigated, we found that the maximum  $S$  wave amplitude in the time domain is almost 3 times the maximum  $P$  wave amplitude and is more than 50% greater than the  $P$

wave amplitude for the center explosion. Before extrapolating these time-domain results to more realistic environments, one must remember that this is a very high frequency source with a contribution to the far-field displacement, which is essentially flat in frequency.

In the frequency domain the asymmetry of the source region has significant effects on the radiation patterns of short period, but has only minor effects on that of long period. We also found that the the maximum long period *P* wave amplitude was at least a factor of two greater than the *S* wave maximum amplitude for our models. We also investigated the amount of moment error caused by using a finite time window. With care one can obtain meaningful estimates using only a short duration which contains relatively few pulses. Since the moment relation, which is obtained in the limit of zero frequency, is independent of the source location in the sphere and does not involve the geometry or dimensions of the sphere, we infer that it probably holds for embedded homogeneous source regions of any shape.

### ACKNOWLEDGMENTS

This research was supported by the Defense Advanced Research Projects Agency (DOD), Nuclear Monitoring Research Office and was monitored by Air Force Geophysics Laboratory under Contract F19628-89-K-0028. Contribution No. 4993, Division of Geological and Planetary Sciences, California Institute of Technology, Pasadena, California.

SEISMOLOGICAL LABORATORY  
CALIFORNIA INSTITUTE OF TECHNOLOGY  
PASADENA, CALIFORNIA 91125



## REFERENCES

- Aki, K. and P. G. Richards (1980). *Quantitative Seismology: Theory and Methods*, W. H. Freeman, San Francisco, California.
- Ben-Menahem, A. and S. J. Singh (1981). *Seismic Waves and Sources*, Springer-Verlag, New York.
- Glenn, L. A., A. J. C. Ladd, B. Moran, and K. A. Wilson (1985). Elastic radiation from explosively-loaded ellipsoidal cavities in an unbounded medium, *Geophys. J. R. astr. Soc.* , Vol. 86, 231-242.
- Glenn, L. A., B. Moran, A. J. C. Ladd, K. A. Wilson and J. A. Rial (1986). Elastic radiation from explosively-loaded axisymmetric cavities, *Geophys. J. R. astr. Soc.* , Vol. 86, 119-136.
- Harkrider, D. G., J. L. Stevens and C. B. Archambeau (1991). Theoretical Rayleigh and Love waves from an explosion in prestressed source regions. Submitted to *Bull. Seis. Soc. Am.*.
- Ludwig, W. J., J. E. Nafe and C. L. Drake (1970), Seismic refraction, in *The Sea*, edited by A. E. Maxwell, Vol. 4, Part I, 53-84, Wiley-Interscience.
- Press, F. and C. B. Archambeau (1962). Release of tectonic strain by underground nuclear explosions. *J. Geophys. Res.*, **67**, 337-343.
- Rial, J. A. and V. F. Cormier (1980). Seismic waves at the epicenter's antipode, *J. Geophys. Res.*, Vol. 85, No. B5, 2661-2668.
- Rial, J. A. and B. Moran (1986). Radiation patterns for explosively-loaded axisymmetric cavities in an elastic medium: analytic approximations and numerical results, *Geophys. J. R. astr. Soc.* , Vol. 86, 855-862.
- Zhao L. - S., D. V. Helmberger, and D. G. Harkrider (1991), Shear-velocity structure of the crust and upper mantle beneath Tibetan and Southeastern China, submitted to *Geophys. J. Int.*

## APPENDIX A

In this appendix, we give the derivation of equations (10) and (11) from equations (7), (8) and (9). The addition theorem for zonal harmonics is

$$P_l(\cos\delta) = \sum_{m=0}^l \epsilon_m \frac{(l-m)!}{(l+m)!} P_l^m(\cos\theta) P_l^m(\cos\theta_0) (\cos m\phi \cos m\phi_0 + \sin m\phi \sin m\phi_0) \quad (A1)$$

Substituting (A1) into equation (8), we obtain equation (10).

Defining

$$\phi_n = \frac{d}{d\delta} P_n(\cos\delta) e_\gamma \quad (A2)$$

,we have

$$\phi_n = -P_n'(\cos\delta) e_{r_0} \times e_r \quad (A3)$$

Thus

$$\phi_{n1} = -P_n'(\cos\delta) (\sin\theta_0 \sin\phi_0 \cos\theta - \sin\theta \sin\phi \cos\theta_0)$$

$$\phi_{n2} = -P_n'(\cos\delta) (\cos\theta_0 \sin\theta \cos\phi - \sin\theta_0 \cos\phi_0 \cos\theta)$$

$$\phi_{n3} = -P_n'(\cos\delta) (\sin\theta_0 \sin\theta \sin(\phi - \phi_0))$$

where

$$P_n'(\cos\delta) = \frac{dP_n(\cos\delta)}{d\cos\delta}$$

Obviously,

$$\frac{\partial P_n(\cos\delta)}{\partial \phi_0} = P_n'(\cos\delta) \sin\theta \sin\theta_0 \sin(\phi - \phi_0) = -\phi_{n3}, \quad (A4)$$

$$\phi_{n1} = \sin\phi_0 \frac{\partial P_n(\cos\delta)}{\partial \theta_0} - \cot\theta_0 \cos\phi_0 \cdot \phi_{n3}, \quad (A5)$$

and

$$\phi_{n2} = -\cos\phi_0 \frac{\partial P_n(\cos\delta)}{\partial \theta_0} - \cot\theta_0 \sin\phi_0 \cdot \phi_{n3}. \quad (A6)$$

From equations (A1) - (A6), it is not difficult to get equation (11).

## APPENDIX B

In this appendix, we give the analytic solution for the source at the center of the cavity.

From equation (1), we have

$$u_1 = A L_{0,0}(k_{a_1} r) - b L_{0,0}^+(k_{a_1} r) \quad (B1)$$

$$u_2 = d L_{0,0}(k_{a_2} r) \quad (B2)$$

where  $A$  is  $ik_{a_1}^2 g(\omega) A_0$ . Other terms in (1) are zero. From the boundary condition at  $r=a$ , we have

$$\begin{pmatrix} b \\ d \end{pmatrix} = \frac{A}{\Delta} \begin{bmatrix} F_{0,3}^-(\xi_2) & -h_0^{(2)\gamma}(\xi_2) \\ -\gamma F_{0,3}^+(\xi_1) & j_0'(\xi_1) \end{bmatrix} \begin{pmatrix} h_0^{(2)\gamma}(\xi_1) \\ \gamma F_{0,3}^-(\xi_1) \end{pmatrix} \quad (B3)$$

where  $\xi_i = k_{a_i} a$ ,  $\gamma = \frac{\mu_1 k_{a_1}}{\mu_2 k_{a_2}}$ ,

and

$$\Delta = F_{0,3}^-(\xi_2) j_0'(\xi_1) - \gamma h_0^{(2)\gamma}(\xi_2) F_{0,3}^+(\xi_1).$$

According to the relations of Bessel functions, we have

$$\begin{aligned} \Delta = & h_0^{(2)\gamma}(\xi_2) j_0(\xi_1) \left[ \left( \cot \xi_1 - \frac{1}{\xi_1} \right) \left( i + \frac{1}{\xi_2} \right) \left( \frac{2}{\xi_2} - \frac{2\gamma}{\xi_1} \right) - \right. \\ & \left. \frac{1}{2} \left( \frac{\alpha_2}{\beta_2} \right)^2 \left( \cot \xi_1 - \frac{1}{\xi_1} \right) - \frac{1}{2} \left( \frac{\alpha_1}{\beta_1} \right)^2 \gamma \left( i + \frac{1}{\xi_2} \right) \right]. \end{aligned}$$

From equations (B2) and (B3),  $u_2$  can be written as

$$u_2 = \frac{A_0}{2a^2 \Delta} g(\omega) \frac{\mu_1 k_{a_1}}{\mu_2 k_{a_2}} \left( \frac{\alpha_1}{\beta_1} \right)^2 h_0^{(2)\gamma}(k_{a_2} r) e_r. \quad (B4)$$

**Table 1. Model**

$\alpha$ ( <i>km/sec</i> )	$\beta$ ( <i>km/sec</i> )	$\rho$ ( <i>g/cm</i> <sup>3</sup> )	radius <i>km</i>
1.80	0.41	1.84	0.5
4.55	2.57	2.45	$\infty$

## FIGURE CAPTIONS

Figure 1. The geometry and the coordinate system used in this study. star is source, and triangle is receiver.

Figure 2. Comparisons of numerical results with two known analytical solutions. The upper is for the wavefields of whole space, while the lower is for the wave fields from a centered source in an embedded sphere. " Num. " denotes numerical and " Ana. " denotes analytic.

Figure 3. A example of wavefields from an off-centered source in a embedded sphere with a radius of 0.5 km. " P " is for the  $P$  waves, " S " is for the  $S$  waves. " Rad " is for the  $e_r$  component, " Az " is for the  $e_\phi$  component. The numbers are the peak amplitudes.

Figure 4. Wave fields for different source distances to the center of the embedded sphere with a radius of 0.5 km. The  $10^{-2}$  on the second and third traces of the first line, apply to all the traces in the second and third columns.  $r_0$  is the distance from the source to the center. The vertical scale is same for all seismograms.

Figure 5. Wave fields for different materials in the embedded sphere.  $\alpha$  is compressional velocity, and  $\beta$  is shear velocity. Nafe's velocity-density relation is assumed for the shear velocity and density  $\rho$ .

Figure 6. Wave fields as a function of  $\delta$  for the standard model.  $\delta$  ranges from 0 to  $90^\circ$ .

Figure 7. Wave fields for different radii, 0.2 - 0.9 km, of the embedded sphere.

Figure 8. Radial components of  $P$  waves at  $\delta=0$  and  $180^\circ$  for the different source locations. In the cartoon of the sphere at the top, the star indicates the source.

Figure 9. Radial components of  $P$  waves at  $\delta=0$  and  $180^\circ$  for different  $P$  and  $S$

velocities and density in the sphere.

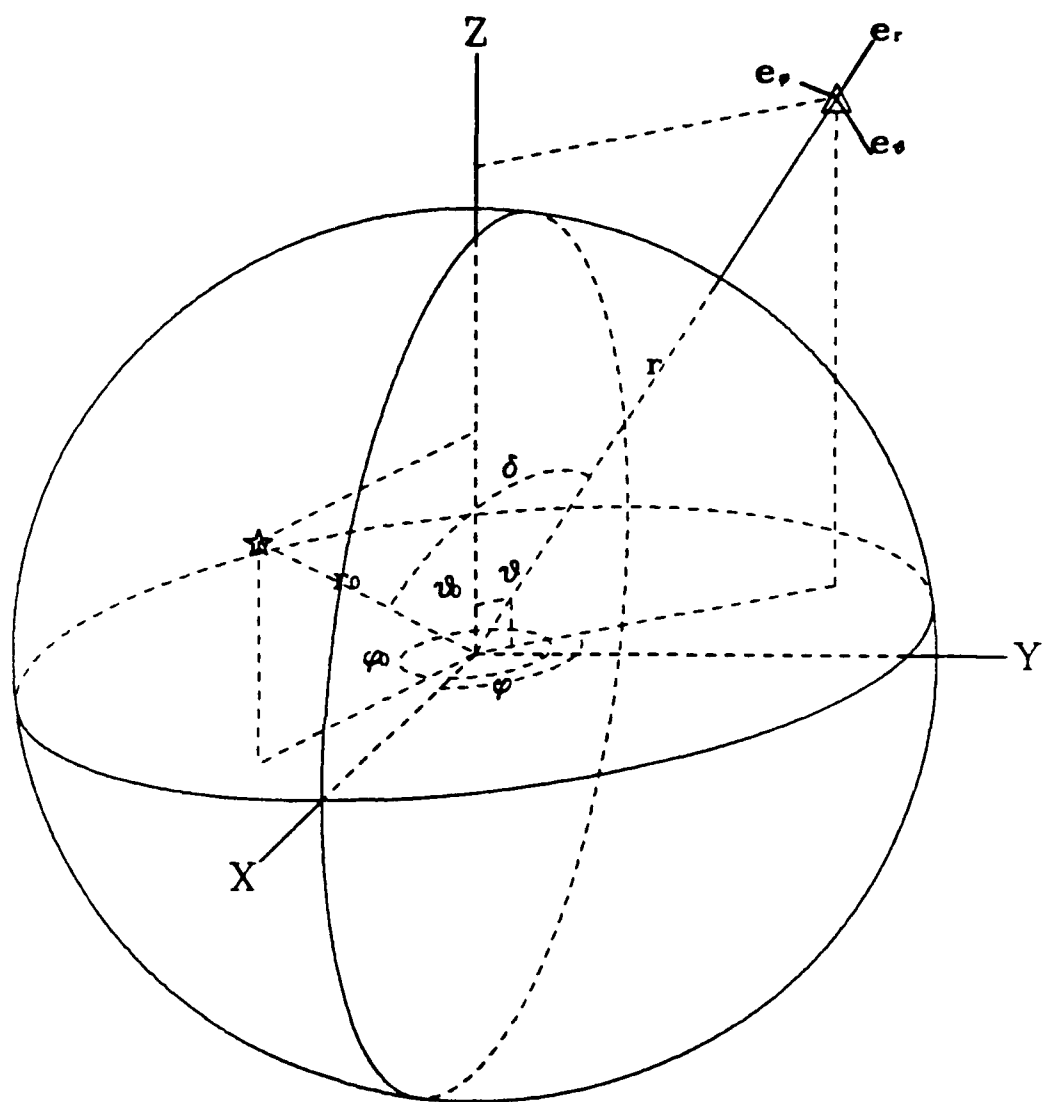
Figure 10. Spectral radiation patterns at periods of 1 and 20 seconds for different source locations. "P" is for the radial component of  $P$  waves, "S" is for the  $\delta$  component of  $S$  waves. On the cartoon of the sphere at the top, the direction of  $\delta$  is indicated. The star indicates the source. "+" is the center. Dash circles with the same centers as the  $P$  radiation patterns are the  $P$  wave radiation patterns for a source located at the center. The numbers on the right of the  $S$  wave radiation patterns are the multiplicative factors used to adjust the size of  $S$  wave radiation patterns for comparison with the corresponding  $P$  wave radiation patterns in the figure.

Figure 11. Spectral radiation patterns for different elastic media of the embedded sphere.

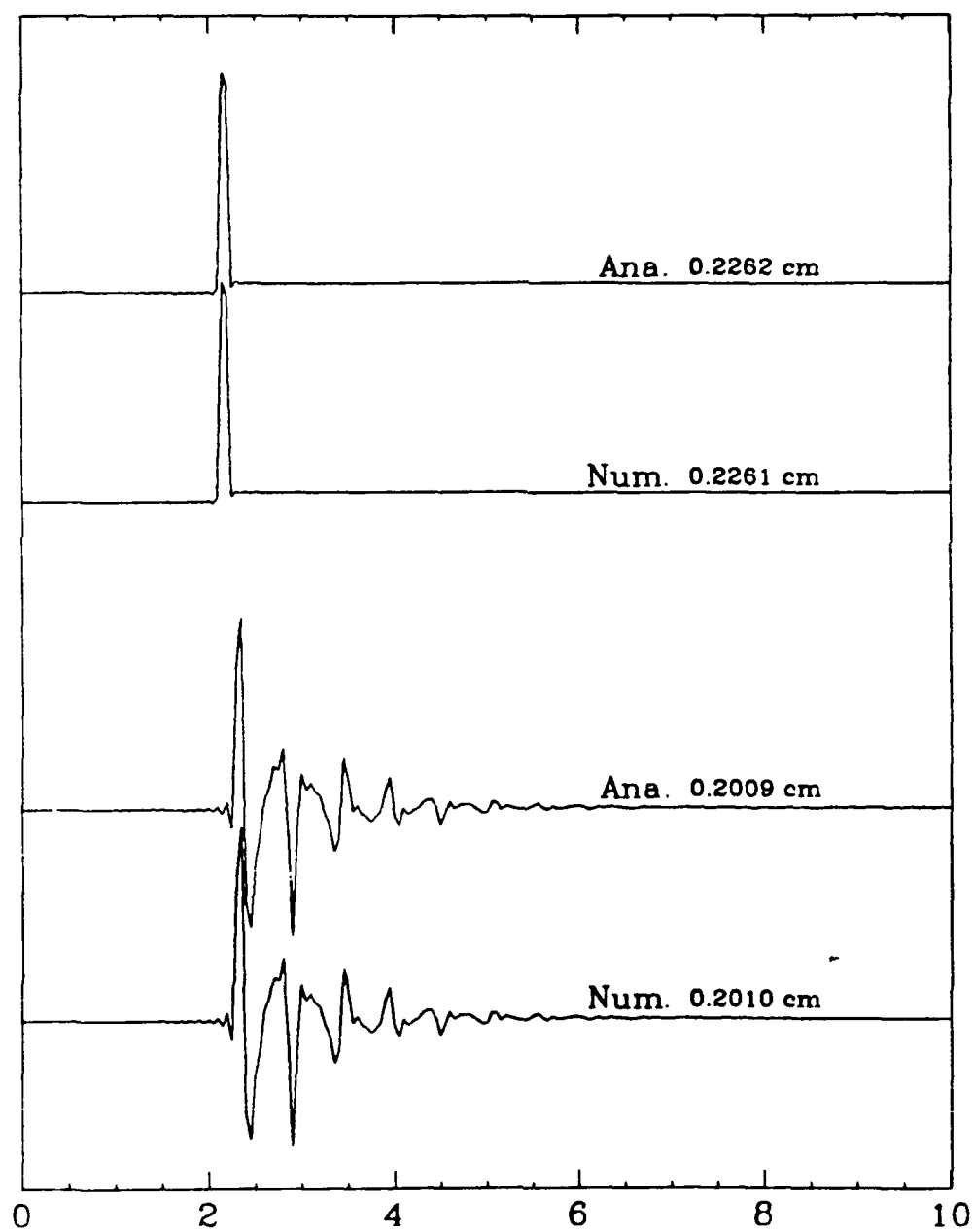
Figure 12. Spectral radiation patterns for different radii of the elastic sphere.

Figure 13. Moment estimates as a function of record length. The numbers are the percentage of estimated moment to input moment obtained using the time length from the beginning to the dash line mark on the record below the number. The upper trace is the seismogram of a centered explosion. The lower one is the seismogram of an off-center explosion. Detailed parameters are given in the text.

Figure 14. Ratio of the observed moment to the input source moment,  $M_{obs}/M_0$ , as a function of the compressional velocities  $\alpha_1$  of the embedded sphere for different whole-space velocities,  $\alpha_2$ , assuming Nafe's velocity-density relation.



**Figure 1**



**Figure 2**



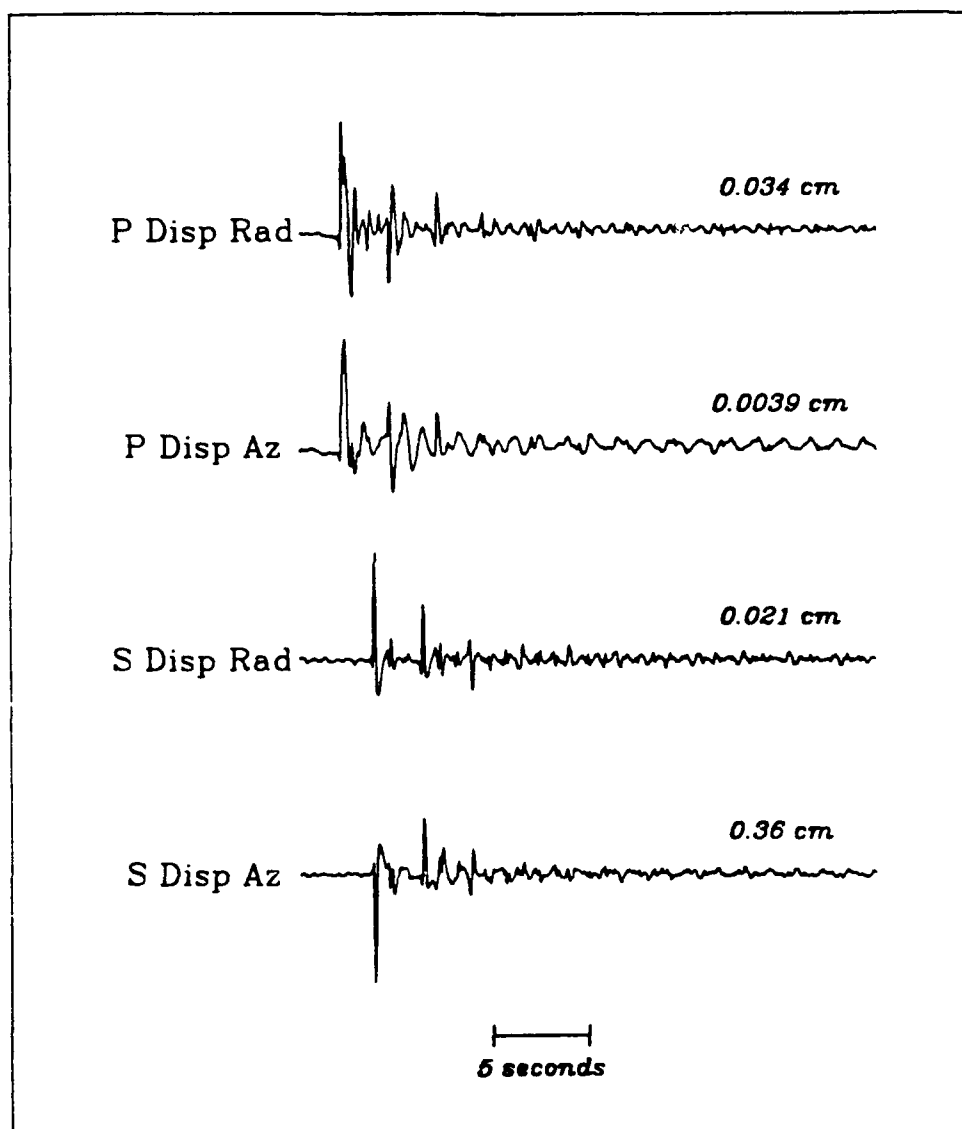


**Figure 3**

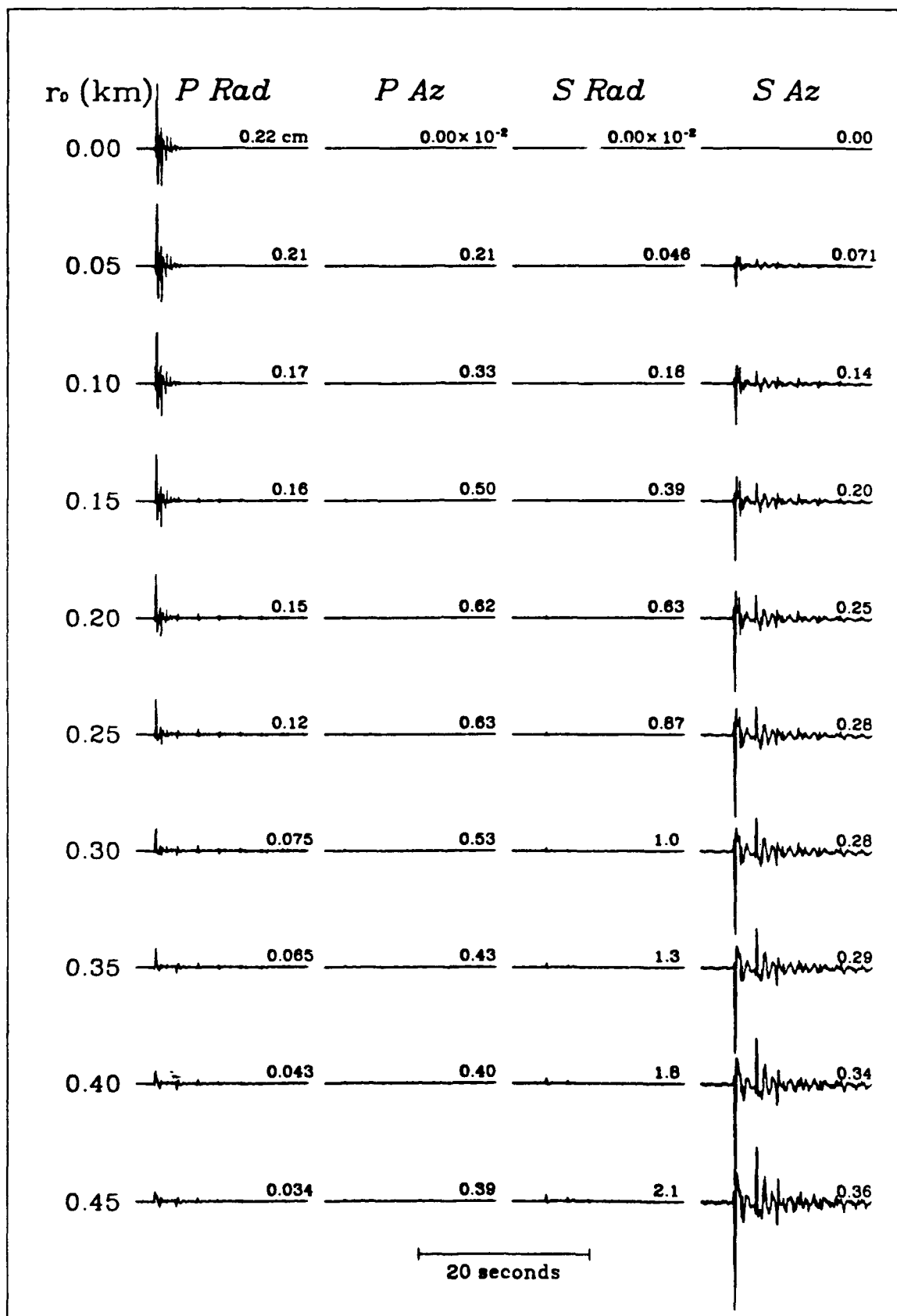


**Figure 4**

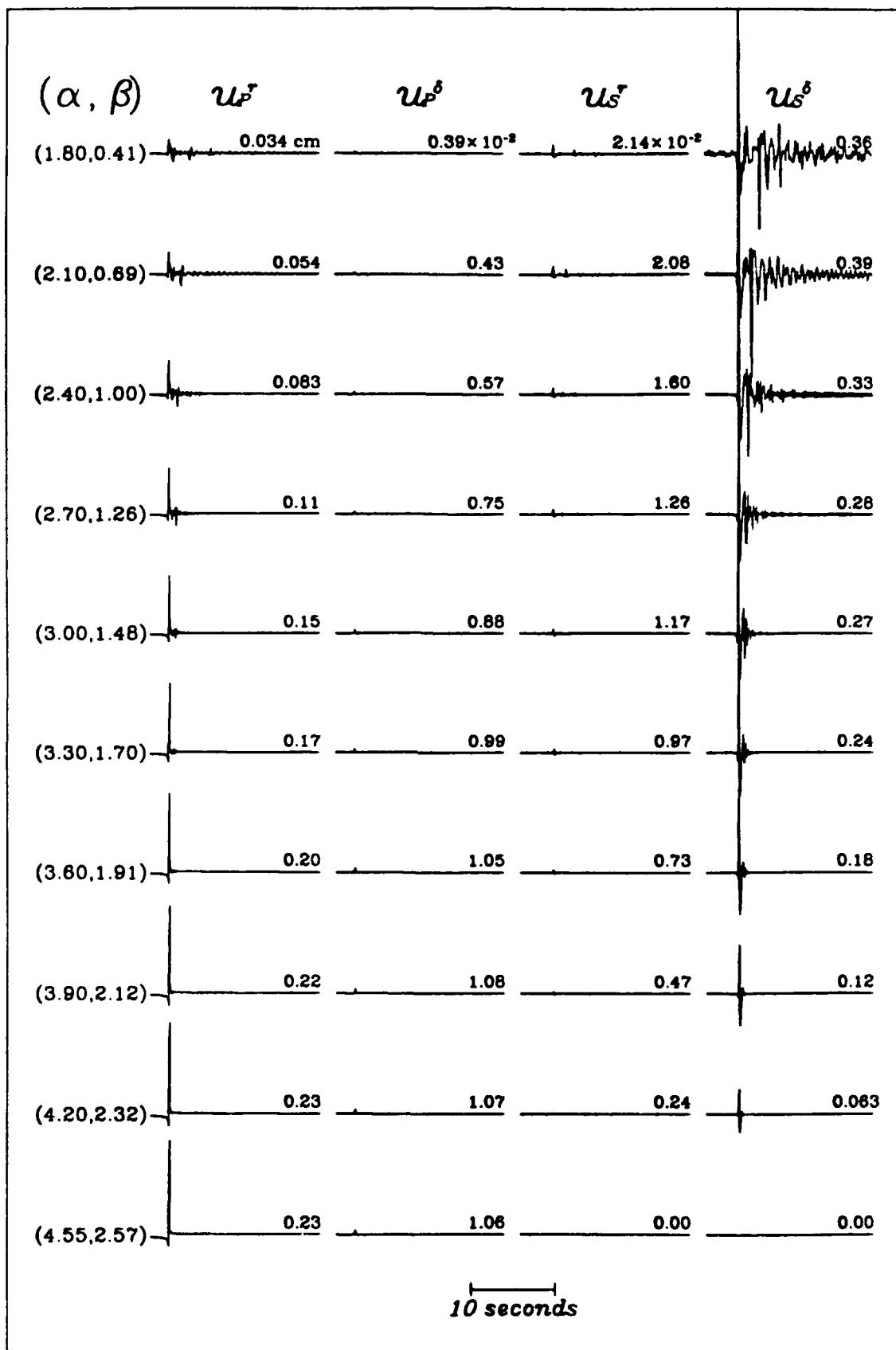


**Figure 5**

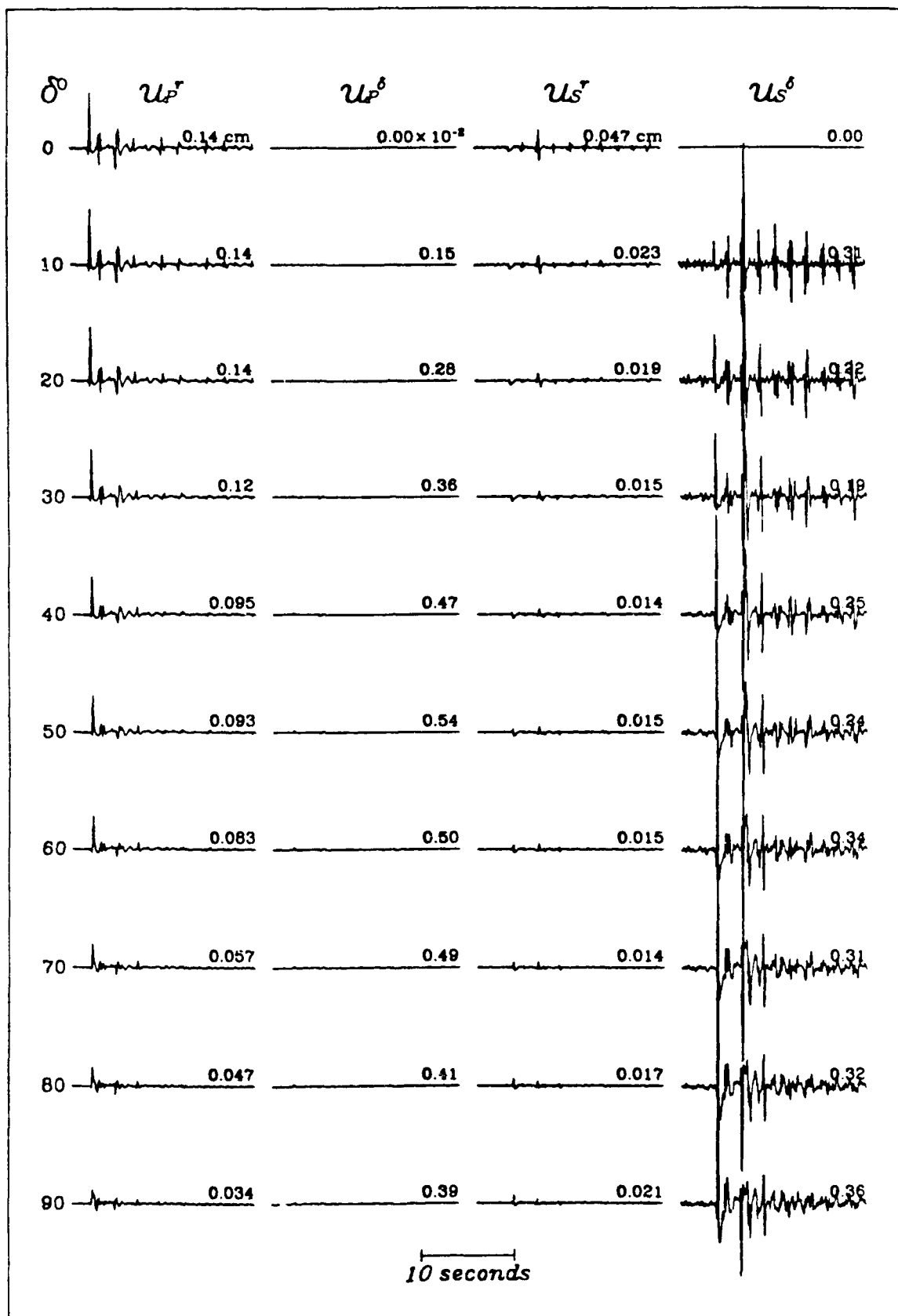
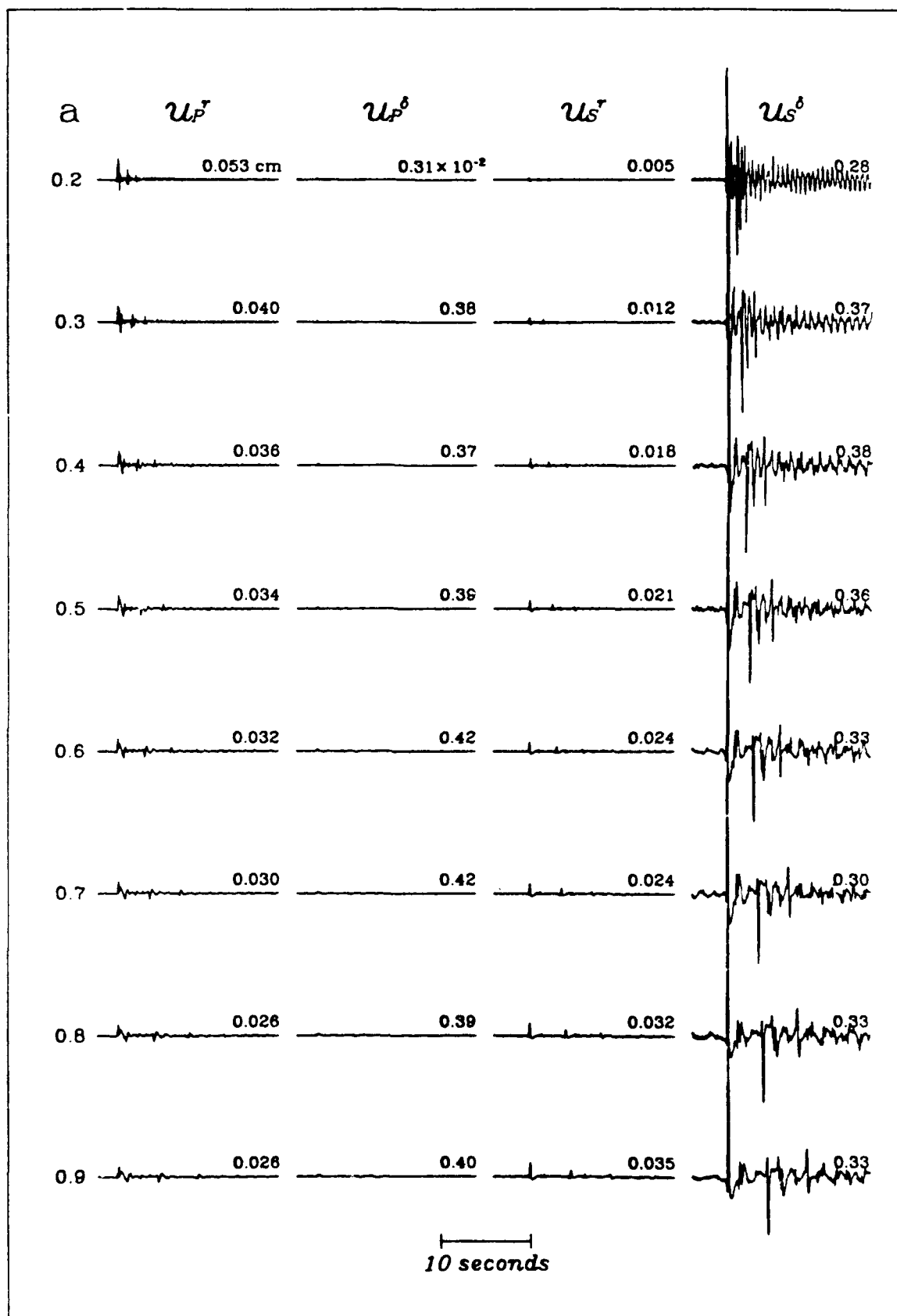
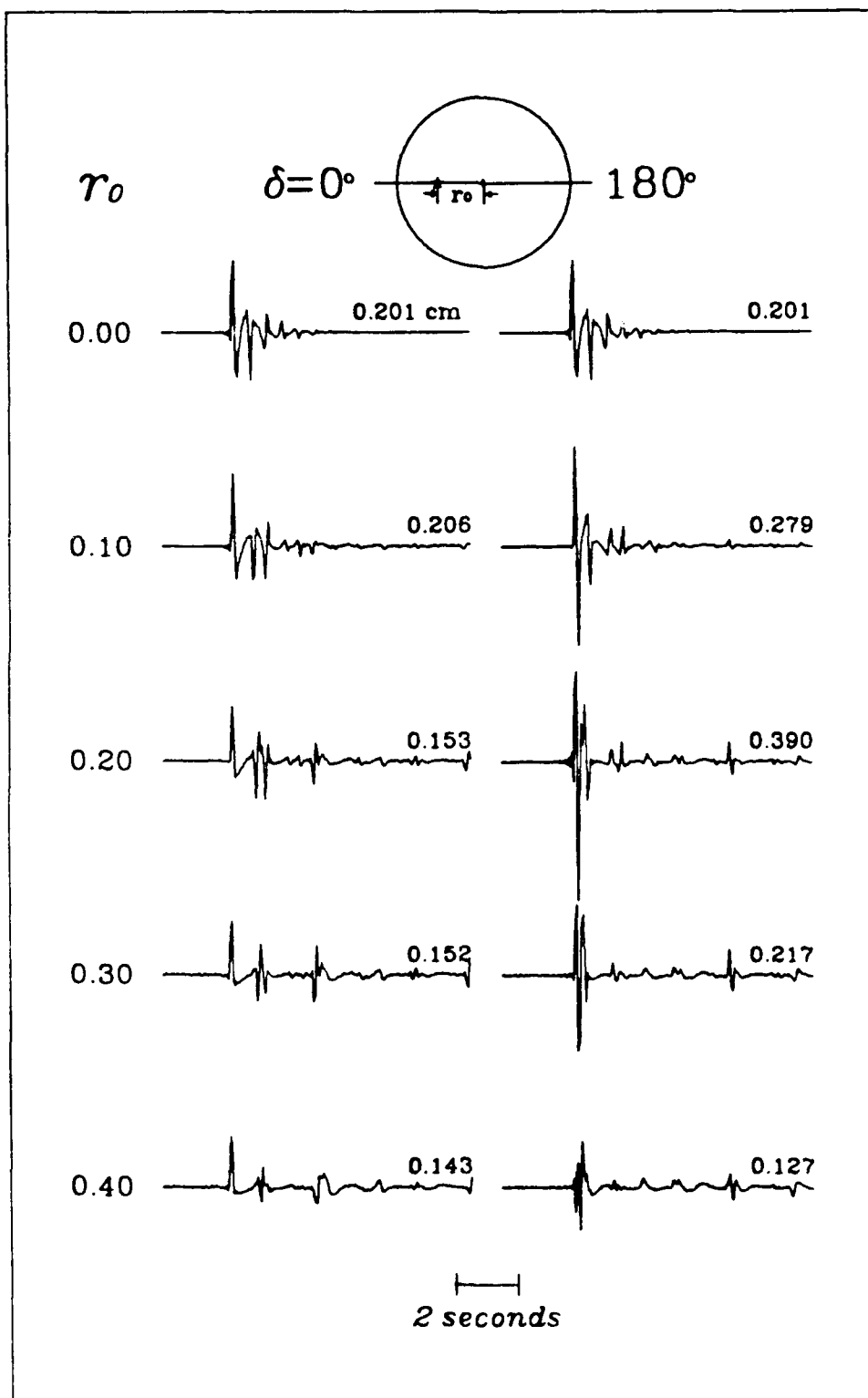


Figure 6



**Figure 7**



**Figure 8**

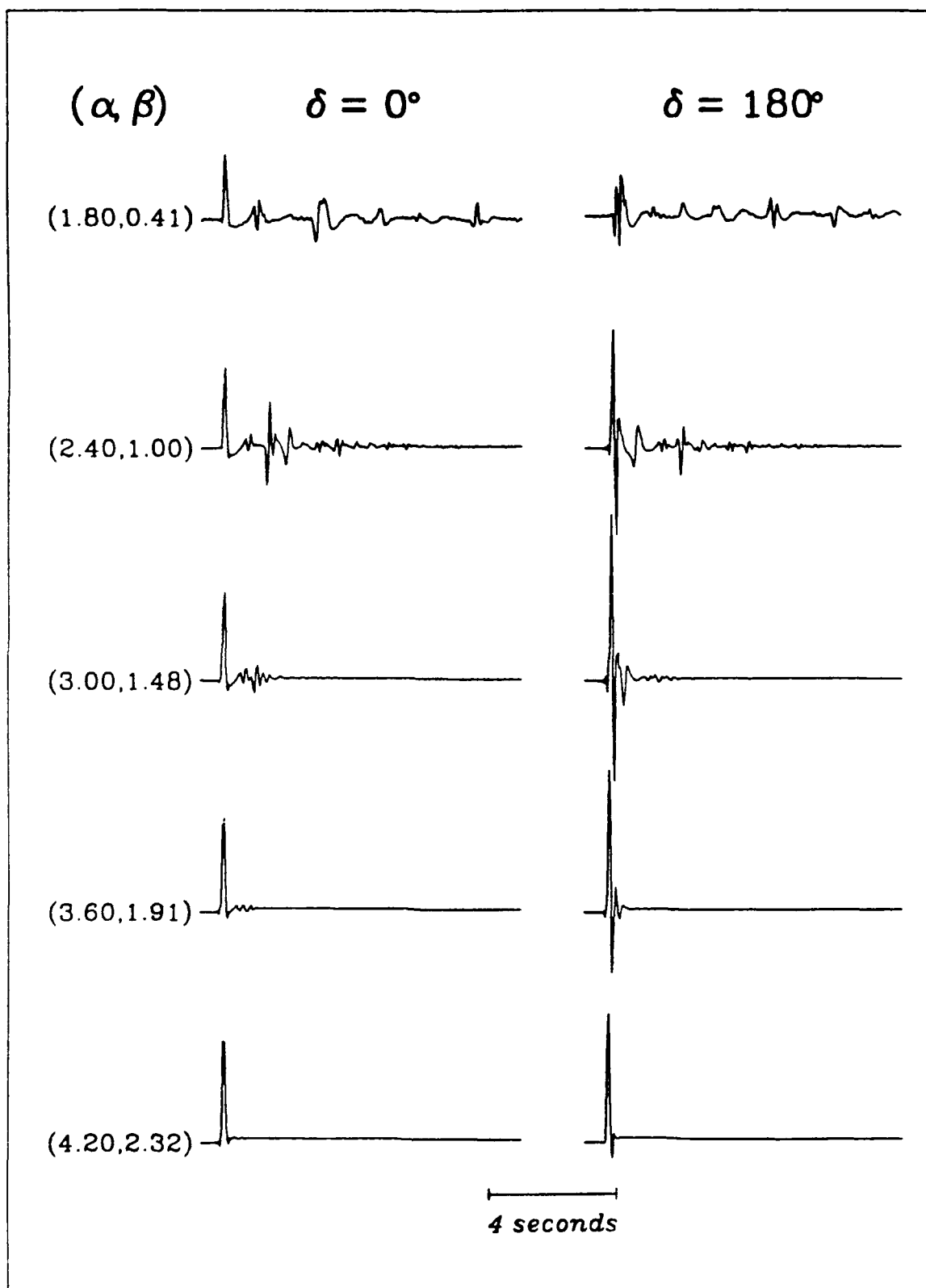


**Figure 9**

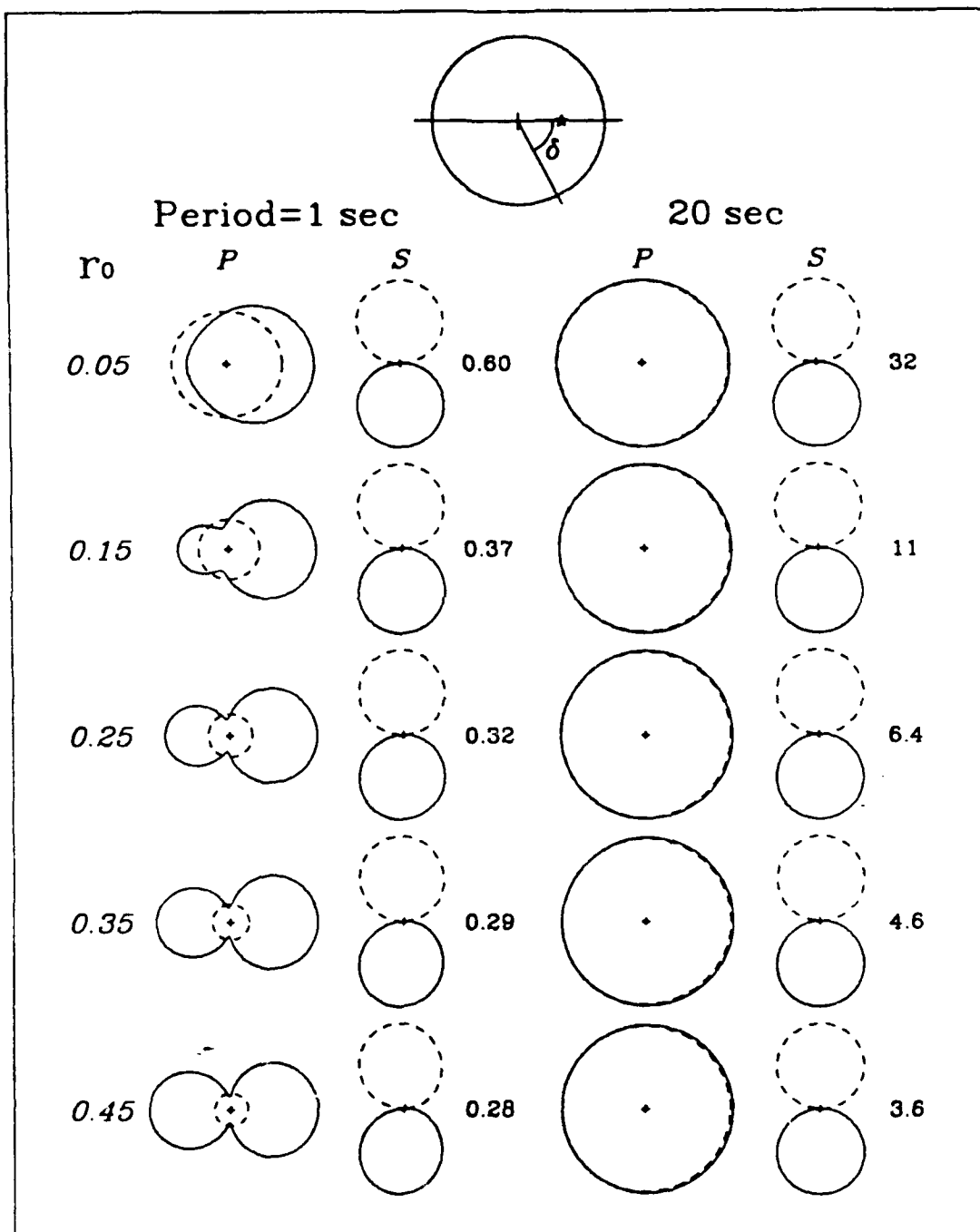


**Figure 10**



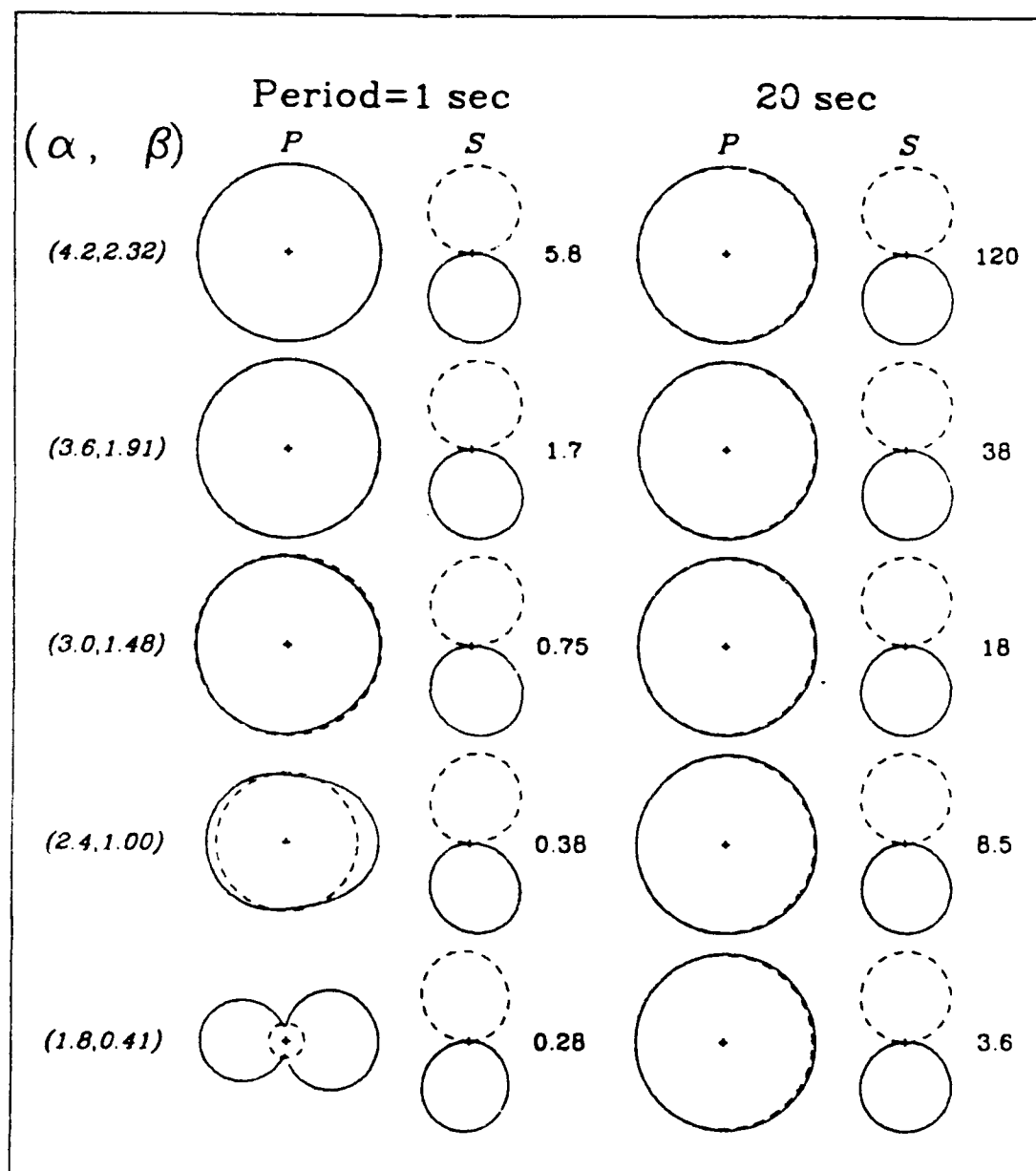


**Figure 11**

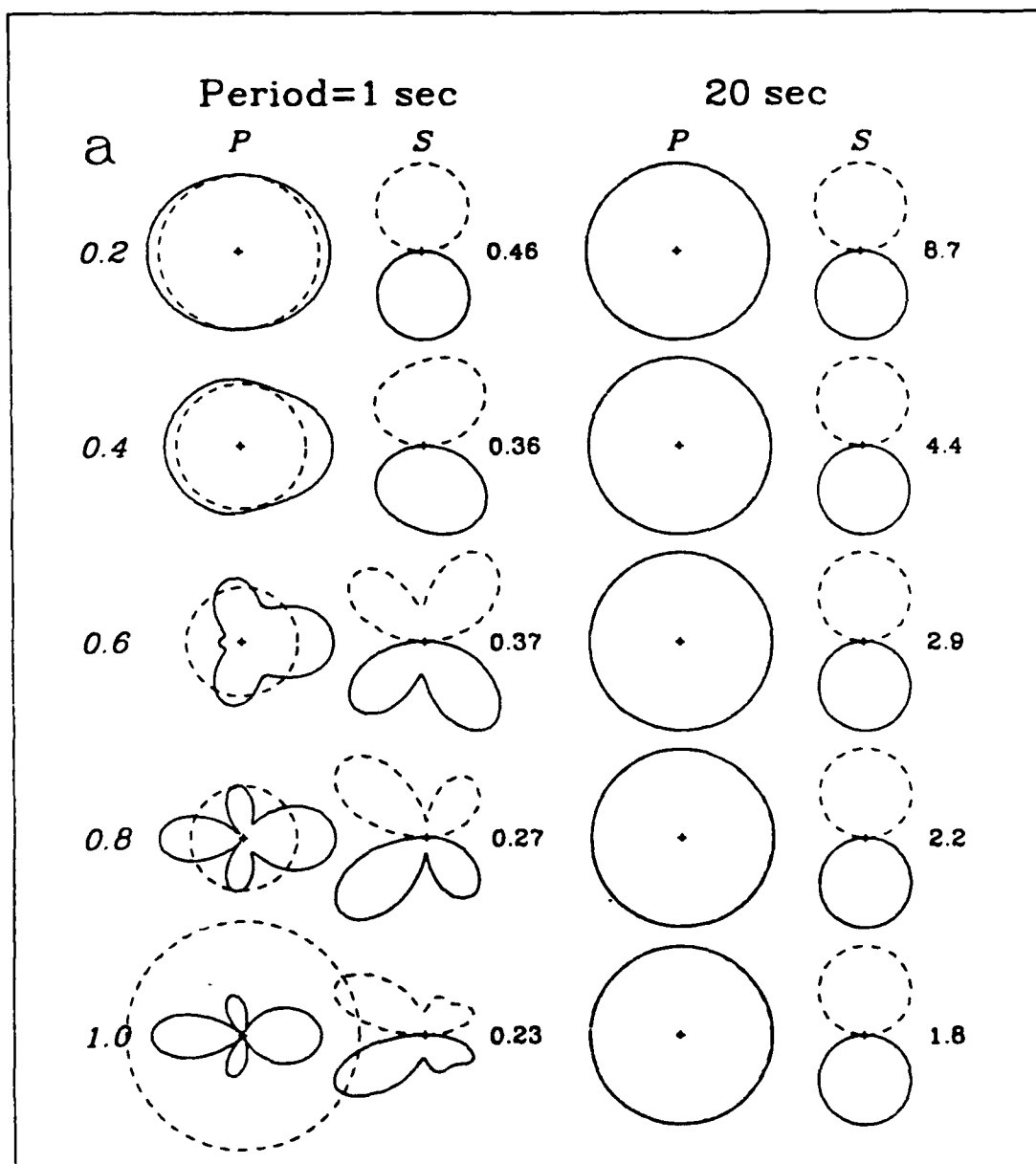


**Figure 12**

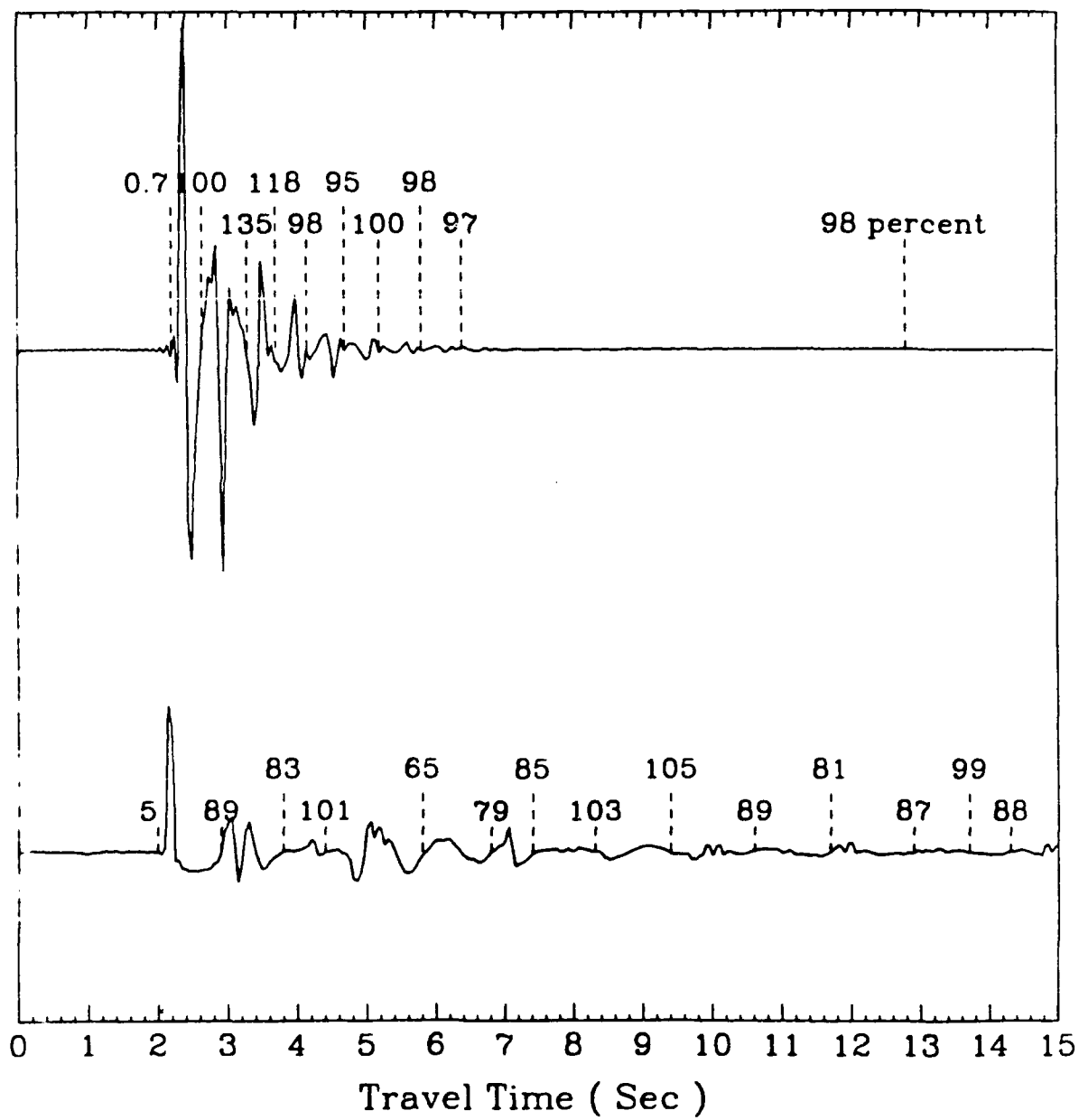


**Figure 13**

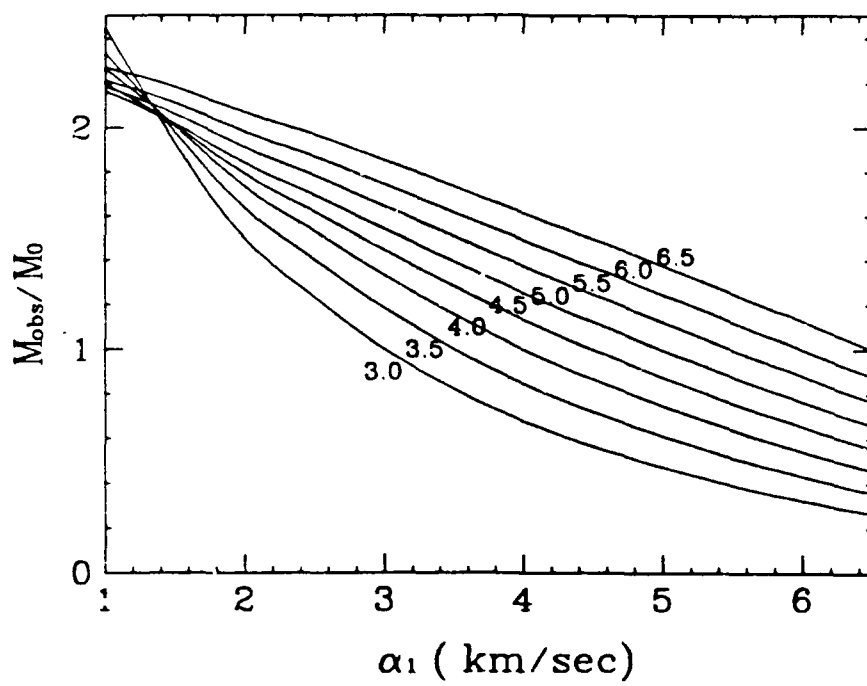


**Figure 14**

Prof. Thomas Ahrens  
Seismological Lab, 252-21  
Division of Geological & Planetary Sciences  
California Institute of Technology  
Pasadena, CA 91125

Prof. Charles B. Archambeau  
CIRES  
University of Colorado  
Boulder, CO 80309

Dr. Thomas C. Bache, Jr.  
Science Applications Int'l Corp.  
10260 Campus Point Drive  
San Diego, CA 92121 (2 copies)

Prof. Muawia Barazangi  
Institute for the Study of the Continent  
Cornell University  
Ithaca, NY 14853

Dr. Jeff Barker  
Department of Geological Sciences  
State University of New York  
at Binghamton  
Vestal, NY 13901

Dr. Douglas R. Baumgardt  
ENSCO, Inc  
5400 Port Royal Road  
Springfield, VA 22151-2388

Prof. Jonathan Berger  
IGPP, A-025  
Scripps Institution of Oceanography  
University of California, San Diego  
La Jolla, CA 92093

Dr. Gilbert A. Bollinger  
Department of Geological Sciences  
Virginia Polytechnical Institute  
21044 Derring Hall  
Blacksburg, VA 24061

Dr. Lawrence J. Burdick  
Woodward-Clyde Consultants  
566 El Dorado Street  
Pasadena, CA 91109-3245

Dr. Jerry Carter  
Center for Seismic Studies  
1300 North 17th St., Suite 1450  
Arlington, VA 22209-2308

Dr. Karl Coyner  
New England Research, Inc.  
76 Olcott Drive  
White River Junction, VT 05001

Prof. Vernon F. Cormier  
Department of Geology & Geophysics  
U-45, Room 207  
The University of Connecticut  
Storrs, CT 06268

Professor Anton W. Dainty  
Earth Resources Laboratory  
Massachusetts Institute of Technology  
42 Carleton Street  
Cambridge, MA 02142

Prof. Steven Day  
Department of Geological Sciences  
San Diego State University  
San Diego, CA 92182

Dr. Zoltan A. Der  
ENSCO, Inc.  
5400 Port Royal Road  
Springfield, VA 22151-2388

Prof. Lewis M. Duncan  
Dept. of Physics & Astronautics  
Clemson University  
Clemson, SC 29634-1901

Prof. John Ferguson  
Center for Lithospheric Studies  
The University of Texas at Dallas  
P.O. Box 830688  
Richardson, TX 75083-0688

Dr. Mark D. Fisk  
Mission Research Corporation  
735 State Street  
P. O. Drawer 719  
Santa Barbara, CA 93102

Prof. Stanley Flatte  
Applied Sciences Building  
University of California  
Santa Cruz, CA 95064

Dr. Alexander Florence  
SRI International  
333 Ravenswood Avenue  
Menlo Park, CA 94025-3493

Dr. Holy K. Given  
IGPP, A-025  
Scripps Institute of Oceanography  
University of California, San Diego  
La Jolla, CA 92093

Prof. Henry L. Gray  
Vice Provost and Dean  
Department of Statistical Sciences  
Southern Methodist University  
Dallas, TX 75275

Dr. Indra Gupta  
Teledyne Geotech  
314 Montgomery Street  
Alexandria, VA 22314

Prof. David G. Harkrider  
Seismological Laboratory  
Division of Geological & Planetary Sciences  
California Institute of Technology  
Pasadena, CA 91125

Prof. Danny Harvey  
CIRES  
University of Colorado  
Boulder, CO 80309

Prof. Donald V. Helmberger  
Seismological Laboratory  
Division of Geological & Planetary Sciences  
California Institute of Technology  
Pasadena, CA 91125

Prof. Eugene Herrin  
Institute for the Study of Earth and Man  
Geophysical Laboratory  
Southern Methodist University  
Dallas, TX 75275

Prof. Bryan Isacks  
Cornell University  
Department of Geological Sciences  
SNEE Hall  
Ithaca, NY 14850

Dr. Rong-Song Jih  
Teledyne Geotech  
314 Montgomery Street  
Alexandria, VA 22314

Prof. Lane R. Johnson  
Seismographic Station  
University of California  
Berkeley, CA 94720

Dr. Richard LaCoss  
MIT-Lincoln Laboratory  
M-200B  
P. O. Box 73  
Lexington, MA 02173-0073 (3 copies)

Prof Fred K. Lamb  
University of Illinois at Urbana-Champaign  
Department of Physics  
1110 West Green Street  
Urbana, IL 61801

Prof. Charles A. Langston  
Geosciences Department  
403 Deike Building  
The Pennsylvania State University  
University Park, PA 16802

Prof. Thorne Lay  
Institute of Tectonics  
Earth Science Board  
University of California, Santa Cruz  
Santa Cruz, CA 95064

Prof. Arthur Lerner-Lam  
Lamont-Doherty Geological Observatory  
of Columbia University  
Palisades, NY 10964

Dr. Christopher Lynnes  
Teledyne Geotech  
314 Montgomery Street  
Alexandria, VA 22314

Prof. Peter Malin  
Department of Geology  
Old Chemistry Bldg.  
Duke University  
Durham, NC 27706

Dr. Randolph Martin, III  
New England Research, Inc.  
76 Olcott Drive  
White River Junction, VT 05001

Prof. Thomas V. McEvilly  
Seismographic Station  
University of California  
Berkeley, CA 94720

Dr. Keith L. McLaughlin  
S-CUBED  
A Division of Maxwell Laboratory  
P.O. Box 1620  
La Jolla, CA 92038-1620

Prof. William Menke  
Lamont-Doherty Geological Observatory  
of Columbia University  
Palisades, NY 10964

Stephen Miller  
SRI International  
333 Ravenswood Avenue  
Box AF 116  
Menlo Park, CA 94025-3493

Prof. Bernard Minster  
IGPP, A-025  
Scripps Institute of Oceanography  
University of California, San Diego  
La Jolla, CA 92093

Prof. Brian J. Mitchell  
Department of Earth & Atmospheric Sciences  
St. Louis University  
St. Louis, MO 63156

Mr. Jack Murphy  
S-CUBED, A Division of Maxwell Laboratory  
11800 Sunrise Valley Drive  
Suite 1212  
Reston, VA 22091 (2 copies)

Prof. John A. Orcutt  
IGPP, A-025  
Scripps Institute of Oceanography  
University of California, San Diego  
La Jolla, CA 92093

Prof. Keith Priestley  
University of Cambridge  
Bullard Labs, Dept. of Earth Sciences  
Madingley Rise, Madingley Rd.  
Cambridge CB3 0EZ, ENGLAND

Dr. Jay J. Pulli  
Radix Systems, Inc.  
2 Taft Court, Suite 203  
Rockville, MD 20850

Prof. Paul G. Richards  
Lamont Doherty Geological Observatory  
of Columbia University  
Palisades, NY 10964

Dr. Wilmer Rivers  
Teledyne Geotech  
314 Montgomery Street  
Alexandria, VA 22314

Prof. Charles G. Sammis  
Center for Earth Sciences  
University of Southern California  
University Park  
Los Angeles, CA 90089-0741

Prof. Christopher H. Scholz  
Lamont-Doherty Geological Observatory  
of Columbia University  
Palisades, NY 10964

Thomas J. Sereno, Jr.  
Science Application Int'l Corp.  
10260 Campus Point Drive  
San Diego, CA 92121

Prof. David G. Simpson  
Lamont-Doherty Geological Observatory  
of Columbia University  
Palisades, NY 10964

Dr. Jeffrey Stevens  
S-CUBED  
A Division of Maxwell Laboratory  
P.O. Box 1620  
La Jolla, CA 92038-1620

Prof. Brian Stump  
Institute for the Study of Earth & Man  
Geophysical Laboratory  
Southern Methodist University  
Dallas, TX 75275

Prof. Jeremiah Sullivan  
University of Illinois at Urbana-Champaign  
Department of Physics  
1110 West Green Street  
Urbana, IL 61801

Prof. Clifford Thurber  
University of Wisconsin-Madison  
Department of Geology & Geophysics  
1215 West Dayton Street  
Madison, WI 53706

Prof. M. Nafi Toksoz  
Earth Resources Lab  
Massachusetts Institute of Technology  
42 Carleton Street  
Cambridge, MA 02142

Prof. John E. Vidale  
University of California at Santa Cruz  
Seismological Laboratory  
Santa Cruz, CA 95064

Prof. Terry C. Wallace  
Department of Geosciences  
Building #77  
University of Arizona  
Tucson, AZ 85721

Dr. William Wortman  
Mission Research Corporation  
8560 Cinderbed Rd.  
Suite # 700  
Newington, VA 22122

Prof. Francis T. Wu  
Department of Geological Sciences  
State University of New York  
at Binghamton  
Vestal, NY 13901



OTHERS (United States)

Dr. Monem Abdel-Gawad  
Rockwell International Science Center  
1049 Camino Dos Rios  
Thousand Oaks, CA 91360

Michael Browne  
Teledyne Geotech  
3401 Shiloh Road  
Garland, TX 75041

Prof. Keiiti Aki  
Center for Earth Sciences  
University of Southern California  
University Park  
Los Angeles, CA 90089-0741

Mr. Roy Burger  
1221 Serry Road  
Schenectady, NY 12309

Prof. Shelton S. Alexander  
Geosciences Department  
403 Deike Building  
The Pennsylvania State University  
University Park, PA 16802

Dr. Robert Burrige  
Schlumberger-Doll Research Center  
Old Quarry Road  
Ridgefield, CT 06877

Dr. Kenneth Anderson  
BBNSTC  
Mail Stop 14/1B  
Cambridge, MA 02238

Dr. W. Winston Chan  
Teledyne Geotech  
314 Montgomery Street  
Alexandria, VA 22314-1581

Dr. Ralph Archuleta  
Department of Geological Sciences  
University of California at Santa Barbara  
Santa Barbara, CA 93102

Dr. Theodore Cherry  
Science Horizons, Inc.  
710 Encinitas Blvd., Suite 200  
Encinitas, CA 92024 (2 copies)

Dr. Susan Beck  
Department of Geosciences  
Bldg. # 77  
University of Arizona  
Tucson, AZ 85721

Prof. Jon F. Claerbout  
Department of Geophysics  
Stanford University  
Stanford, CA 94305

Dr. T.J. Bennett  
S-CUBED  
A Division of Maxwell Laboratory  
11800 Sunrise Valley Drive, Suite 1212  
Reston, VA 22091

Prof. Robert W. Clayton  
Seismological Laboratory  
Division of Geological & Planetary Sciences  
California Institute of Technology  
Pasadena, CA 91125

Mr. William J. Best  
907 Westwood Drive  
Vienna, VA 22180

Prof. F. A. Dahlen  
Geological and Geophysical Sciences  
Princeton University  
Princeton, NJ 08544-0636

Dr. N. Biswas  
Geophysical Institute  
University of Alaska  
Fairbanks, AK 99701

Mr. Charles Doll  
Earth Resources Laboratory  
Massachusetts Institute of Technology  
42 Carleton St.  
Cambridge, MA 02142

Dr. Stephen Bratt  
Center for Seismic Studies  
1300 North 17th Street  
Suite 1450  
Arlington, VA 22209

Prof. Adam Dziewonski  
Hoffman Laboratory, Harvard Univ.  
Dept. of Earth Atmos. & Planetary Sciences  
20 Oxford St  
Cambridge, MA 02138

Prof. John Ebel  
Department of Geology & Geophysics  
Boston College  
Chestnut Hill, MA 02167

Eric Fielding  
SNEE Hall  
INSTOC  
Cornell University  
Ithaca, NY 14853

Dr. John Foley  
Phillips Laboratory/LWH  
Hanscom AFB, MA 01731-5000

Prof. Donald Forsyth  
Department of Geological Sciences  
Brown University  
Providence, RI 02912

Dr. Cliff Frolich  
Institute of Geophysics  
8701 North Mopac  
Austin, TX 78759

Dr. Anthony Gangi  
Texas A&M University  
Department of Geophysics  
College Station, TX 77843

Dr. Freeman Gilbert  
IGPP, A-025  
Scripps Institute of Oceanography  
University of California  
La Jolla, CA 92093

Mr. Edward Giller  
Pacific Sierra Research Corp.  
1401 Wilson Boulevard  
Arlington, VA 22209

Dr. Jeffrey W. Given  
SAIC  
10260 Campus Point Drive  
San Diego, CA 92121

Prof. Stephen Grand  
University of Texas at Austin  
Department of Geological Sciences  
Austin, TX 78713-7909

Prof. Roy Greenfield  
Geosciences Department  
403 Deike Building  
The Pennsylvania State University  
University Park, PA 16802

Dan N. Hagedorn  
Battelle  
Pacific Northwest Laboratories  
Battelle Boulevard  
Richland, WA 99352

Dr. James Hannon  
Lawrence Livermore National Laboratory  
P. O. Box 808  
Livermore, CA 94550

Prof. Robert B. Herrmann  
Dept. of Earth & Atmospheric Sciences  
St. Louis University  
St. Louis, MO 63156

Ms. Heidi Houston  
Seismological Laboratory  
University of California  
Santa Cruz, CA 95064

Kevin Hutchenson  
Department of Earth Sciences  
St. Louis University  
3507 Laclede  
St. Louis, MO 63103

Dr. Hans Israelsson  
Center for Seismic Studies  
1300 N. 17th Street, Suite 1450  
Arlington, VA 22209-2308

Prof. Thomas H. Jordan  
Department of Earth, Atmospheric  
and Planetary Sciences  
Massachusetts Institute of Technology  
Cambridge, MA 02139

Prof. Alan Kafka  
Department of Geology & Geophysics  
Boston College  
Chestnut Hill, MA 02167

Robert C. Kemerait  
ENSCO, Inc.  
445 Pineda Court  
Melbourne, FL 32940

William Kikendall  
Teledyne Geotech  
3401 Shiloh Road  
Garland, TX 75041

Prof. Leon Knopoff  
University of California  
Institute of Geophysics & Planetary Physics  
Los Angeles, CA 90024

Prof. John Kuo  
Aldridge Laboratory of Applied Geophysics  
Columbia University  
842 Mudd Bldg.  
New York, NY 10027

Prof. L. Timothy Long  
School of Geophysical Sciences  
Georgia Institute of Technology  
Atlanta, GA 30332

Dr. Gary McCartor  
Department of Physics  
Southern Methodist University  
Dallas, TX 75275

Prof. Art McGarr  
Mail Stop 977  
Geological Survey  
345 Middlefield Rd.  
Menlo Park, CA 94025

Dr. George Mellman  
Sierra Geophysics  
11255 Kirkland Way  
Kirkland, WA 98033

Prof. John Nabelek  
College of Oceanography  
Oregon State University  
Corvallis, OR 97331

Prof. Geza Nagy  
University of California, San Diego  
Department of Ames, M.S. B-010  
La Jolla, CA 92093

Dr. Keith K. Nakanishi  
Lawrence Livermore National Laboratory  
L-205  
P. O. Box 808  
Livermore, CA 94550

Prof. Amos Nur  
Department of Geophysics  
Stanford University  
Stanford, CA 94305

Prof. Jack Oliver  
Department of Geology  
Cornell University  
Ithaca, NY 14850

Dr. Kenneth Olsen  
P. O. Box 1273  
Linwood, WA 98046-1273

Prof. Jeffrey Park  
Department of Geology and Geophysics  
Kline Geology Laboratory  
P. O. Box 6666  
New Haven, CT 06511-8130

Howard J. Patton  
Lawrence Livermore National Laboratory  
L-205  
P. O. Box 808  
Livermore, CA 94550

Prof. Robert Phinney  
Geological & Geophysical Sciences  
Princeton University  
Princeton, NJ 08544-0636

Dr. Paul Pomeroy  
Rondout Associates  
P.O. Box 224  
Stone Ridge, NY 12484

Dr. Norton Rimer  
S-CUBED  
A Division of Maxwell Laboratory  
P.O. Box 1620  
La Jolla, CA 92038-1620

Prof. Larry J. Ruff  
Department of Geological Sciences  
1006 C.C. Little Building  
University of Michigan  
Ann Arbor, MI 48109-1063

Dr. Richard Sailor  
TASC Inc.  
55 Walkers Brook Drive  
Reading, MA 01867

Dr. Susan Schwartz  
Institute of Tectonics  
1156 High St.  
Santa Cruz, CA 95064

Dr. David Taylor  
ENSCO, Inc.  
445 Pineda Court  
Melbourne, FL 32940

John Sherwin  
Teledyne Geotech  
3401 Shiloh Road  
Garland, TX 75041

Dr. Steven R. Taylor  
Lawrence Livermore National Laboratory  
L-205  
P. O. Box 808  
Livermore, CA 94550

Dr. Matthew Sibol  
Virginia Tech  
Seismological Observatory  
4044 Derring Hall  
Blacksburg, VA 24061-0420

Professor Ta-Liang Teng  
Center for Earth Sciences  
University of Southern California  
University Park  
Los Angeles, CA 90089-0741

Dr. Albert Smith  
Lawrence Livermore National Laboratory  
L-205  
P. O. Box 808  
Livermore, CA 94550

Dr. Gregory van der Vink  
IRIS, Inc.  
1616 North Fort Myer Drive  
Suite 1440  
Arlington, VA 22209

Prof. Robert Smith  
Department of Geophysics  
University of Utah  
1400 East 2nd South  
Salt Lake City, UT 84112

Professor Daniel Walker  
University of Hawaii  
Institute of Geophysics  
Honolulu, HI 96822

Dr. Stewart W. Smith  
Geophysics AK-50  
University of Washington  
Seattle, WA 98195

William R. Walter  
Seismological Laboratory  
University of Nevada  
Reno, NV 89557

Donald L. Springer  
Lawrence Livermore National Laboratory  
L-205  
P. O. Box 808  
Livermore, CA 94550

Dr. Raymond Willeman  
Phillips Laboratory - OL-AA/LWH  
Hanscom AFB, MA 01731-5000

Dr. George Sutton  
Rondout Associates  
P.O. Box 224  
Stone Ridge, NY 12484

Dr. Gregory Wojcik  
Weidlinger Associates  
4410 El Camino Real  
Suite 110  
Los Altos, CA 94022

Prof. L. Sykes  
Lamont-Doherty Geological Observatory  
of Columbia University  
Palisades, NY 10964

Dr. Lorraine Wolf  
Phillips Laboratory/LWH  
Hanscom AFB, MA 01731-5000

Prof. Pradeep Talwani  
Department of Geological Sciences  
University of South Carolina  
Columbia, SC 29208

Dr. Gregory B. Young  
ENSCO, Inc.  
5400 Port Royal Road  
Springfield, VA 22151-2388

Dr. Eileen Vergino  
Lawrence Livermore National Laboratory  
L-205  
P. O. Box 808  
Livermore, CA 94550

J. J. Zucca  
Lawrence Livermore National Laboratory  
P. O. Box 808  
Livermore, CA 94550

GOVERNMENT

Dr. Ralph Alewine III  
DARPA/NMRO  
1400 Wilson Boulevard  
Arlington, VA 22209-2308

Dr. Dale Glover  
DIA/DT-1B  
Washington, DC 20301

Mr. James C. Battis  
Phillips Laboratory/LWH  
Hanscom AFB, MA 01731-5000

Dr. T. Hanks  
USGS  
Nat'l Earthquake Research Center  
345 Middlefield Road  
Menlo Park, CA 94025

Harley Benz  
U.S. Geological Survey, MS-977  
345 Middlefield Rd.  
Menlo Park, CA 94025

Dr. Roger Hansen  
AFTAC/TT  
Patrick AFB, FL 32925

Dr. Robert Blandford  
AFTAC/TT  
Center for Seismic Studies  
1300 North 17th St. Suite 1450  
Arlington, VA 22209-2308

Paul Johnson  
ESS-4, Mail Stop J979  
Los Alamos National Laboratory  
Los Alamos, NM 87545

Eric Chael  
Division 9241  
Sandia Laboratory  
Albuquerque, NM 87185

Janet Johnston  
Phillips Laboratory/LWH  
Hanscom AFB, MA 01731-5000

Dr. John J. Cipar  
Phillips Laboratory/LWH  
Hanscom AFB, MA 01731-5000

Dr. Katharine Kadinsky-Cade  
Phillips Laboratory/LWH  
Hanscom AFB, MA 01731-5000

Cecil Davis  
Group P-15, Mail Stop D406  
P.O. Box 1663  
Los Alamos National Laboratory  
Los Alamos, NM 87544

Ms. Ann Kerr  
IGPP, A-025  
Scripps Institute of Oceanography  
University of California, San Diego  
La Jolla, CA 92093

Mr. Jeff Duncan  
Office of Congressman Markey  
2133 Rayburn House Bldg.  
Washington, DC 20515

Dr. Max Koontz  
US Dept of Energy/DP 5  
Forrestal Building  
1000 Independence Avenue  
Washington, DC 20585

Dr. Jack Evernden  
USGS - Earthquake Studies  
345 Middlefield Road  
Menlo Park, CA 94025

Dr. W.H.K. Lee  
Office of Earthquakes, Volcanoes,  
& Engineering  
345 Middlefield Road  
Menlo Park, CA 94025

Art Frankel  
USGS  
922 National Center  
Reston, VA 22092

Dr. William Leith  
U.S. Geological Survey  
Mail Stop 928  
Reston, VA 22092

Dr. Richard Lewis  
Director, Earthquake Engineering & Geophysics  
U.S. Army Corps of Engineers  
Box 631  
Vicksburg, MS 39180

James F. Lewkowicz  
Phillips Laboratory/LWH  
Hanscom AFB, MA 01731-5000

Mr. Alfred Lieberman  
ACDA/VI-OA State Department Bldg  
Room 5726  
320 - 21st Street, NW  
Washington, DC 20451

Stephen Mangino  
Phillips Laboratory/LWH  
Hanscom AFB, MA 01731-5000

Dr. Robert Masse  
Box 25046, Mail Stop 967  
Denver Federal Center  
Denver, CO 80225

Art McGarr  
U.S. Geological Survey, MS-977  
345 Middlefield Road  
Menlo Park, CA 94025

Richard Morrow  
ACDA/VI, Room 5741  
320 21st Street N.W.  
Washington, DC 20451

Dr. Carl Newton  
Los Alamos National Laboratory  
P.O. Box 1663  
Mail Stop C335, Group ESS-3  
Los Alamos, NM 87545

Dr. Bao Nguyen  
AFTAC/TTR  
Patrick AFB, FL 32925

Dr. Kenneth H. Olsen  
Los Alamos Scientific Laboratory  
P. O. Box 1663  
Mail Stop D-406  
Los Alamos, NM 87545

Mr. Chris Paine  
Office of Senator Kennedy  
SR 315  
United States Senate  
Washington, DC 20510

Colonel Jerry J. Perrizo  
AFOSR/NP, Building 410  
Bolling AFB  
Washington, DC 20332-6448

Dr. Frank F. Pilotte  
HQ AFTAC/TT  
Patrick AFB, FL 32925-6001

Katie Poley  
CIA-ACIS/TMC  
Room 4X16NHB  
Washington, DC 20505

Mr. Jack Rachlin  
U.S. Geological Survey  
Geology, Rm 3 C136  
Mail Stop 928 National Center  
Reston, VA 22092

Dr. Robert Reinke  
WL/NTESG  
Kirtland AFB, NM 87117-6008

Dr. Byron Ristvet  
HQ DNA, Nevada Operations Office  
Attn: NVCG  
P.O. Box 98539  
Las Vegas, NV 89193

Dr. George Rothe  
HQ AFTAC/TTR  
Patrick AFB, FL 32925-6001

Dr. Alan S. Ryall, Jr.  
DARPA/NMRO  
1400 Wilson Boulevard  
Arlington, VA 22209-2308

Dr. Michael Shore  
Defense Nuclear Agency/SPSS  
6801 Telegraph Road  
Alexandria, VA 22310

Mr. Charles L. Taylor  
Phillips Laboratory/LWH  
Hanscom AFB, MA 01731-5000

Phillips Laboratory  
Attn: XO  
Hanscom AFB, MA 01731-5000

Dr. Larry Turnbull  
CIA-OSWR/NED  
Washington, DC 20505

Phillips Laboratory  
Attn: LW  
Hanscom AFB, MA 01731-5000

Dr. Thomas Weaver  
Los Alamos National Laboratory  
P.O. Box 1663, Mail Stop C335  
Los Alamos, NM 87545

DARPA/PM  
1400 Wilson Boulevard  
Arlington, VA 22209

Phillips Laboratory  
Research Library  
ATTN: SULL  
Hanscom AFB, MA 01731-5000 (2 copies)

Defense Technical Information Center  
Cameron Station  
Alexandria, VA 22314 (5 copies)

Phillips Laboratory  
ATTN: SUL  
Kirtland AFB, NM 87117-6008

Defense Intelligence Agency  
Directorate for Scientific & Technical Intelligence  
Attn: DT1B  
Washington, DC 20340-6158

Secretary of the Air Force  
(SAFRD)  
Washington, DC 20330

AFTAC/CA  
(STINFO)  
Patrick AFB, FL 32925-6001

Office of the Secretary Defense  
DDR & E  
Washington, DC 20330

TACTEC  
Battelle Memorial Institute  
505 King Avenue  
Columbus, OH 43201 (Final Report Only)

HQ DNA  
Attn: Technical Library  
Washington, DC 20305

DARPA/RMO/RETRIEVAL  
1400 Wilson Boulevard  
Arlington, VA 22209

DARPA/RMO/Security Office  
1400 Wilson Boulevard  
Arlington, VA 22209



CONTRACTORS (FOREIGN)

Dr. Ramon Cabre, S.J.  
Observatorio San Calixto  
Casilla 5939  
La Paz, Bolivia

Prof. Hans-Peter Harjes  
Institute for Geophysik  
Ruhr University/Bochum  
P.O. Box 102148  
4630 Bochum 1, FRG

Prof. Eystein Husebye  
NTNF/NORSAR  
P.O. Box 51  
N-2007 Kjeller, NORWAY

Prof. Brian L.N. Kennett  
Research School of Earth Sciences  
Institute of Advanced Studies  
G.P.O. Box 4  
Canberra 2601, AUSTRALIA

Dr. Bernard Massinon  
Societe Radiomana  
27 rue Claude Bernard  
75005 Paris, FRANCE (2 Copies)

Dr. Pierre Mecheler  
Societe Radiomana  
27 rue Claude Bernard  
75005 Paris, FRANCE

Dr. Svein Mykkeltveit  
NTNF/NORSAR  
P.O. Box 51  
N-2007 Kjeller, NORWAY (3 copies)

FOREIGN (OTHERS)

Dr. Peter Basham  
Earth Physics Branch  
Geological Survey of Canada  
1 Observatory Crescent  
Ottawa, Ontario, CANADA K1A 0Y3

Dr. Eduard Berg  
Institute of Geophysics  
University of Hawaii  
Honolulu, HI 96822

Dr. Michel Bouchon  
I.R.I.G.M.-B.P. 68  
38402 St. Martin D'Heres  
Cedex, FRANCE

Dr. Hilmar Bungum  
NTNF/NORSAR  
P.O. Box 51  
N-2007 Kjeller, NORWAY

Dr. Michel Campillo  
Observatoire de Grenoble  
I.R.I.G.M.-B.P. 53  
38041 Grenoble, FRANCE

Dr. Kin Yip Chun  
Geophysics Division  
Physics Department  
University of Toronto  
Ontario, CANADA M5S 1A7

Dr. Alan Douglas  
Ministry of Defense  
Blacknest, Brimpton  
Reading RG7-4RS, UNITED KINGDOM

Dr. Manfred Henger  
Federal Institute for Geosciences & Nat'l Res.  
Postfach 510153  
D-3000 Hanover 51, FRG

Ms. Eva Johannisson  
Senior Research Officer  
National Defense Research Inst.  
P.O. Box 27322  
S-102 54 Stockholm, SWEDEN

Dr. Fekadu Kebede  
Geophysical Observatory, Science Faculty  
Addis Ababa University  
P. O. Box 1176  
Addis Ababa, ETHIOPIA

Dr. Tormod Kvaerna  
NTNF/NORSAR  
P.O. Box 51  
N-2007 Kjeller, NORWAY

Dr. Peter Marshall  
Procurement Executive  
Ministry of Defense  
Blacknest, Brimpton  
Reading FG7-4RS, UNITED KINGDOM

Prof. Ari Ben-Menahem  
Department of Applied Mathematics  
Weizman Institute of Science  
Rehovot, ISRAEL 951729

Dr. Robert North  
Geophysics Division  
Geological Survey of Canada  
1 Observatory Crescent  
Ottawa, Ontario, CANADA K1A 0Y3

Dr. Frode Ringdal  
NTNF/NORSAR  
P.O. Box 51  
N-2007 Kjeller, NORWAY

Dr. Jorg Schlittenhardt  
Federal Institute for Geosciences & Nat'l Res.  
Postfach 510153  
D-3000 Hannover 51, FEDERAL REPUBLIC OF  
GERMANY

Universita Degli Studi Di Trieste  
Facolta Di Ingegneria  
Istituto Di Miniere E. Geofisica Applicata, Trieste,  
ITALY

Dr. John Woodhouse  
Oxford University  
Dept of Earth Sciences  
Parks Road  
Oxford OX13PR, ENGLAND